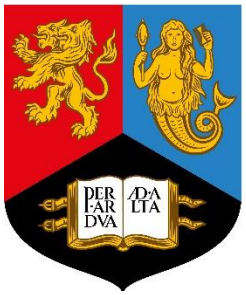

UNIVERSITY OF BIRMINGHAM

Investigations into transition metal dichalcogenides for electrocatalysis

by

Tshiamo Manyepedza

A thesis submitted to the University of Birmingham for the degree of DOCTOR OF PHILOSOPHY

School of Chemical Engineering

College of Engineering and Physical Sciences

University of Birmingham

September 2024

Abstract

Transition metal dichalcogenides have emerged as promising candidates for the hydrogen evolution reaction (HER) due to their unique properties and low costs compared to platinum-group metals (PGMs). Despite recent advancements, there is still a gap in reporting the electrochemical rate constants and detailed kinetics for improved HER activity due to transition metal dichalcogenides (TMDs) as well as the potential effects of mixing various TMDs for enhanced HER performance. This study investigated the HER electrocatalytic activity of TMDs as well as novel strategies for enhancing their catalytic activity and determining the reaction kinetics. Different structural morphologies (bulk and nanoparticle) of one TMD, MoS_2, were investigated to ascertain how it affects HER electrocatalytic activity. The impact electrochemistry technique was incorporated to study the nanoparticulate forms. The MoS_2 nanoparticles registered an improved onset potential of -0.10 V (vs RHE) through impact electrochemistry compared to 0.29 V (vs RHE) of the bulk MoS_2 for HER.

TMD heterostructures were also investigated, and they were synthesized using a method distinct from those that have been reported in the literature. Two methods were employed to create the heterolayers: utilising a drop-cast nanoparticle layer and an electrodeposited film. The heterolayers were evaluated for HER, and the heterostructures with an overlay of MoS_2 displayed superior stability compared to those with an overlay of $MoSe_2$. The stable heterolayers registered standard electrochemical rate constants (k_0) of $(3.20 \pm 0.10) \times 10^{-4}$ cm s^{-1} and $(1.73 \pm 0.03) \times 10^{-4}$ cm s^{-1} for WS_2/MoS_2 and $MoSe_2/MoS_2$ respectively, which was an overall improvement compared to reported rate constants for electrodeposited MoS_2. After evaluating the heterolayers, a novel mechanochemical approach was used to synthesize binary and ternary mixtures of TMDs to enhance the catalytic activity of the resulting hybrids. Electrochemical testing of the hybrids for HER exhibited improved HER performance in terms of onset potential and electrochemical rate constants compared to the individual TMDs. These ranged from 0.52×10^{-3} cm s^{-1} to 8.2×10^{-3} cm s^{-1}, with hybrids containing selenium having higher electrochemical rate constants. This improvement was due to the increased active sites, the exfoliation of the TMDs that generated 1T-monolayer components known for their higher activity in HER, and the combined effect of mixing two or more catalytically active materials.

Acknowledgements

I would like to express my deepest gratitude to my first supervisor, Dr. Neil V. Rees, for his invaluable guidance, support, and encouragement throughout the course of my research. His expertise, insightful feedback, and unwavering commitment have been crucial to the completion of this thesis. I am also sincerely grateful to my second supervisor, Dr. James M. Courtney, for his thoughtful advice, constructive criticism, and for always being available to discuss ideas and challenges. His support has been instrumental in shaping this work.

I would like to extend my heartfelt thanks to my family and friends for their endless support and encouragement throughout this journey. I am deeply grateful to my mom, whose unwavering belief in me has been a constant source of strength. Her sacrifices, love, and dedication to providing me with the best opportunities have shaped who I am today. She has been my inspiration and my anchor, always encouraging me to pursue my dreams and reminding me to stay resilient in the face of challenges. To my entire family, thank you for your patience, understanding, and encouragement during the most challenging times. You have been there for me every step of the way, providing not only practical support but also the emotional strength I needed to persevere. To my friends, thank you for the laughter, distractions, and camaraderie that helped me stay grounded and motivated.

Lastly, and most importantly, I would like to thank my wife, Maduo for her unwavering support, love, and belief in me have been my greatest strength throughout this journey. She has been my pillar, my confidant, and my partner in every sense, always standing by my side through both the highs and lows. Her patience, understanding, and encouragement have been invaluable, and for that, I am deeply thankful. This accomplishment would not have been possible without her unwavering presence and support. Thank you all for your tremendous support and encouragement, which have been fundamental to the completion of this thesis.

List of Publications

1) T. Manyepedza, J. M. Courtney, A. Snowdon, C. R. Jones and N. V. Rees. Impact Electrochemistry of MoS_2: Electrocatalysis and Hydrogen Generation at Low Overpotentials. *J. Phys. Chem. C*. 2022, **126**, 17942-17951.

2) T. Manyepedza, T. Auvray. T. Friščić and N. V. Rees. Electrochemically deposited transition metal dichalcogenide heterostructures as electrocatalysts: accelerated kinetics for the hydrogen evolution reaction. *Electrochem. Commun*. 2023, **160**, 107678.

3) T. Manyepedza, T. Auvray. T. Friščić and N. V. Rees. Novel electrocatalysts via mechanochemistry: binary & ternary mixed transition metal dichalcogenides. *Appl. Mater. Today*. 2024, under review.

Conference Presentations

1) Electrochem 2022 Conference (RSC), 4-6th September 2022, Edinburgh, UK, ***Poster Presentation*** "Impact Electrochemistry of MoS_2: Electrocatalysis and Hydrogen Generation at Low Overpotentials".
2) Electrochem 2023 Conference (RSC), 10-12th September 2023, Bristol, UK, ***Oral Presentation*** "Electrochemically deposited transition metal dichalcogenide heterostructures as electrocatalysts: accelerated kinetics for the hydrogen evolution reaction".
3) International Society of Electrochemistry (ISE) 74th Annual Meeting, 3-8th September 2023, Lyon, France, ***Poster Presentation*** "Impact Electrochemistry of MoS_2: Electrocatalysis and Hydrogen Generation at Low Overpotentials".

Table of Contents

1 Introduction 1

1.1 Background of the research 1

1.2 Hydrogen generation 3

1.2.1 Electrolyser 5

1.2.2 Hydrogen evolution reaction (HER) 7

1.3 General Electrochemistry 11

1.3.1 Electrochemical equilibrium: Nernst equation 14

1.3.2 Electrode kinetics 16

1.3.3 Electric Double Layer 17

1.3.4 Mass Transport: Diffusion 19

1.3.5 Linear sweep and cyclic voltammetry 19

1.4 Impact Electrochemistry 21

1.5 Research Aims and Objectives 23

1.6 Thesis Outline 24

1.7 References 25

2 Literature review 39

2.1 Transition Metal Dichalcogenides: Background 39

2.2 Transition Metal Dichalcogenide electrocatalysts for HER 42

2.3 Preparation methods of TMDs 43

2.3.1 Electrochemical deposition 43

2.3.2 Chemical vapour deposition 44

2.3.3 Mechanical and liquid exfoliation 45

2.4 Modification of TMDs for improved HER activity 47

2.4.1 Doping 47

2.4.2 Defect engineering 49

2.4.3 Nanostructured TMDs 50

2.4.4 Heterostructures 51

2.5 Conclusion 54

2.6 References 55

3 Experimental Methods 67

3.1 List of Chemicals 67

3.2 Electrochemical cell 67

3.2.1 Electrodes 68

3.3 Synthesis 69

3.3.1 Electrochemical Deposition of TMD films 69

3.3.2 Nanoparticle drop-casting 70

3.4 Electrochemistry 71

3.4.1 Hydrogen evolution reaction 71

3.4.2 Electrochemical Particle Impacts 72

3.4.3 Hydrogen generation 72

3.5 Characterization 73

3.5.1 Scanning electron microscope and energy dispersive spectroscopy (SEM-EDS) 73

3.5.2 Focused ion beam scanning electron microscope (FIB-SEM) 74

3.5.3 X-ray photoelectron spectroscopy (XPS) 74

3.5.4 Raman spectroscopy 75

3.5.5 Powder X-ray diffraction (XRD) 76

3.5.6 Gas chromatography 77

3.5.7 Atomic force microscope (AFM) 77

3.5.8 Spectroscopic Ellipsometry 78

3.6 References 80

4 Impact electrochemistry of MoS_2: electrocatalysis and hydrogen generation at low overpotentials 83

4.1 Introduction 84

4.2 Results and discussion 84

4.2.1 Electrodeposition and characterization of amorphous MoS_2 84

4.2.2 pH and kinetic study of HER on electrodeposited MoS_2 89

4.2.3 HER at MoS_2 particles via impact voltammetry 94

4.2.4 Hydrogen production 102

4.3 Conclusion 104

4.4 References 106

5 Electrochemically deposited transition metal dichalcogenide heterostructures as electrocatalysts: accelerated kinetics for the hydrogen evolution reaction 111

5.1 Introduction 112

5.2 Results and discussion 113

5.2.1 Heterolayer formation 113
5.2.2 HER activity 118
5.2.3 Heterolayer characterization 128
5.3 Conclusion 140
5.4 References 142
6 Novel electrocatalyst via mechanochemistry: binary & ternary mixed transition metal dichalcogenides 146
6.1 Introduction 147
6.2 Results and discussion 148
6.2.1 Characterization of mixed TMDs 148
6.2.2 HER activity 166
6.2.3 Kinetic analysis 171
6.3 Conclusion 178
6.4 References 180
7 Conclusion and Outlook 188
7.1 Summary 188
7.2 Future work 191
7.3 References 194
8 Appendix 195
8.1 Electrodeposition of MoS_2 195
8.2 Impact Electrochemistry 196
8.3 Tafel analysis 197
8.4 SEM characterisation of MoS_2 nanoparticles 199
8.5 Exfoliation of MoS_2 nanoparticles 200
8.6 AFM Imaging of MoS_2 Nanoparticles 202
8.7 References 202

List of figures

Figure 1.1. Schematic diagram of a fuel cell (PEMFC)……..2

Figure 1.2. Structure of an electrolyser……...6

Figure 1.3. Volcanic plot of the relationship between exchange current density and hydrogen binding energy of various materials. The peak of the volcano represents the optimal binding energy for the highest catalytic activity, highlighting the most efficient catalysts for the HER…….9

Figure 1.4. Diagrams of a two electrode (**A**) and three electrode (**B**) electrochemical cells…….13

Figure 1.5. Electric diffuse layer (EDL) formed on a positively charged electrode surface. Adapted from ref [105]…….18

Figure 1.6. (A) This voltammogram displays the characteristic curve, illustrating the current response as a function of the applied potential. The distinct shape provides insights into the electrochemical behaviour of the system under study, with specific regions corresponding to different electrochemical processes. **(B)** LSV plot from a microelectrode, divided into three regions: kinetically controlled, mixed control, and diffusion-controlled, highlighting the transition from electron transfer kinetics to diffusion-limited current……20

Figure 1.7. Illustration of a MoS_2 nanoparticle colliding with an electrode surface and acting as a surface for proton reduction. The process involves three main steps: (1) the nanoparticle collides with the electrode held at a sufficient potential, (2) protons on the nanoparticle surface are reduced to form hydrogen gas (H_2), and (3) the nanoparticle and the produced H_2 leave the electrode surface. This sequence illustrates the catalytic role of MoS_2 in the proton reduction reaction……22

Figure 2.1. Metal coordination and stacking sequences of transition metal dichalcogenides. Reproduced from ref [10,11]……..40

Figure 2.2 The energy band structures of the 2H, 3R, and 1T phases of MoS2 across the high-symmetry points. Reproduced from ref [16]……..…..41

Figure 3.1. Graphical representation of how the nanoparticle suspensions were dropcast onto the surfaces of glassy carbon electrodes…….…….71

Figure 3.2. Schematic diagram of the scaled up and modified three-electrode cell set-up for the nanoparticle impact study…….…..73

Figure 3.3. Graphical display of how an ellipsometer functions. Light produced from the light source is reflected by the heterolayer sample surface while a detector captures and measures the intensity of the reflected light……79

Figure 4.1. Cyclic voltammogram of the deposition of MoS_2 on a glassy carbon macroelectrode at a scan rate of 100 mV s^{-1} in a solution containing 2 mM $(NH_4)_2MoS_4$ and 0.1 M $NaClO_4$……...85

Figure 4.2. EDS spectra of the electrodeposited sample on glassy carbon. Molybdenum and sulfur were detected proving that the deposition resulted in some form of MoS_x……..……87

Figure 4.3. High resolution spectra of the Mo (A &C) and S (B&D) regions from the wide scan spectra. A and B spectra are from the modified electrode sample while C and D are from the nanoparticle sample……88

Figure 4.4. (A) LSVs recorded at a voltage scan rate of 20 mV s^{-1} in different pH solutions using a GC working electrode modified with electrodeposited MoS_2. The solutions contained sulfuric acid and sodium hydroxide of varying concentrations to achieve the pH required, along with 0.49 M of K_2SO_4 as supporting electrolyte. **(B)** A plot of the relationship between onset potentials and pH value, with a best-fit line, of equation $E = -(9.56 \times 10^{-2})pH - 0.112$, obtained by linear regression. The plot ends at pH 2.5 because of degradation of the electrodeposited layer started occurring at pH ≥3……..90

Figure 4.5. Repeated HER scans for electrodeposited MoS_2 in different pH solutions to investigate degradation: (A) pH 1.5, (B) pH 2, (C) pH 3, and (D) pH 4. In all cases a graphite counter and Ag/AgCl reference electrode were used and a voltage scan rate of 5 mV s^{-1}. A total of 10 successive scans for each modified GC electrode in a specific pH was carried out and the change recorded (the colour key shown in (A) applies to all plots)……91

Figure 4.6 (A) LSV scan of the HER at the MoS_2 modified carbon fibre microelectrode in a solution of 0.01 M H_2SO_4 and 0.49 M K_2SO_4 at a scan rate of 20 mV s^{-1}. **(B)** Experimental data (−) and best-fit plot of the waveshape fitting simulation (o) using DigiElch software……..92

Figure 4.7. (**A**) A voltammogram obtained using electrodeposited MoS_2 for HER and the Tafel slope (**B**) derived from this voltammogram……93

Figure 4.8. MoS_2 impact spikes for potentials held at **(A)** -0.25 V and **(B)** -0.50 V (vs RHE) for 30 seconds using a pH 2 suspension of 100 pM MoS_2 nanoparticles……94

Figure 4.9. Individual peaks were identified and separately analysed for peak height derivation. **A** and **C** show the overlaid peaks for scans carried out at potentials -0.2 V and -0.4 V (vs RHE) respectively. **B** and **D** displays the average peak height and shape for the peaks at -0.2 V and -0.4 V (vs RHE) respectively……95

Figure 4.10. Plots of (**A**) average frequency, and (**B**) average charge of nanoparticle impacts at different potentials. The 'switch on' potential at -0.10 V (vs RHE) of the MoS_2 nanoparticles for the HER is shown in both plots……96

Figure 4.11. Comparison of the resulting current-potential curves for HER in 0.01 M sulfuric acid solution from using (**A**) electrodeposited MoS_2 from Figure 4.4A and (**B**) drop-casted MoS_2 nanoparticles from Figure 4.6A. The peak heights from the nanoparticle impacts study have also been included (**C**) to highlight the shift in onset potential between the different scans (shown in more detail in Figure 4.11). The red dotted lines indicate the onset potentials, as identified in the main text, for ease of reference……97

Figure 4.12. Experimental data (■) and simulated waveshapes for impact signals of HER at MoS_2 particles. Simulations are for $D = 9.6 \times 10^{-5}$ cm s^{-2}, $\alpha = 0.67$, $E_f^0 = -0.120$ V (vs RHE), r = 8 nm and k_0 values (all in cm s^{-1}) of: 10^{-2} (- •• -), 0.1(- • -), 1.5 (- - -), 7.5 (• • •), and 250 (—)……..99

Figure 4.13. Rotating disk linear sweep voltammetry of a GC electrode in a solution containing 0.01 M H_2SO_4 and 0.49 M K_2SO_4 at 1600 rpm without MoS_2 NPs (—) and MoS_2 NPs (—)……...101

Figure 4.14. (A) AFM surface topography image of dropcast MoS_2 NPs on cleaved mica substrate, and **(B)** cross sectional height profile for 5 platelets representative of the overall scan area, showing thicknesses in multiples of ca. 0.65 nm……..…102

Figure 4.15. Schematic diagram of the electrolyser set up for the scaled-up nanoparticle impact study……....103

Figure 4.16. Gas chromatograms of the impact experiments at potentials (A) -0.15 V, and (B) -0.40 V (vs
RHE)……104

Figure 5.1. Cyclic voltammogram of the electrodeposition of MoS_2 onto $MoSe_2$ modified glassy carbon electrode in a solution of 2 mM $(NH_4)_2MoS_4$ and 0.1 M $NaClO_4$ at a scan rate of 50 mV s^{-1}…….114

Figure 5.2. Linear sweep voltammograms carried out using $MoSe_2/MoS_2$ (NP/L) heterolayers with varying electrochemical deposition cycles of MoS_2. The different cycles correspond to the thickness of the deposited MoS_2 layer…….115

Figure 5.3. Cyclic voltammetry of the deposition of $MoSe_2$ onto a modified glassy carbon electrode at a scan rate of 50 mV s^{-1} in a solution containing 0.05 M H_2MoO_4, 0.01 M Na_2SeO_3, 0.1 M $NaClO_4$ and adjusted to pH 6.5 with NaOH……..116

Figure 5.4. Stability of the different heterolayers in 10 mM H_2SO_4 and 0.1 M K_2SO_4 (**A**) $MoSe_2/MoS_2$(NP/L), (**B**) $MoS_2/MoSe_2$(NP/L), (**C**) WS_2/MoS_2(NP/L), (**D**) $MoS_2/MoSe_2$(L/L). Each heterolayer was subjected to 10 successive scans at a voltage scan rate of 20 mV s^{-1}…….117

Figure 5.5. Stability study of (**A**) electrodeposited $MoSe_2$ and (**B**) $WS_2/MoSe_2$ heterolayer in an acid solution of 10 mM H_2SO_4 and 0.1 M K_2SO_4. The TMDs were subjected to 10 successive scans at a voltage scan rate of 20 mV s^{-1}……..118

Figure 5.6. Linear sweep voltammograms of (**A**) $MoSe_2/MoS_2$, (**B**) $MoS_2/MoSe_2$, (**C**) WS_2/MoS_2 and (**D**) $WS_2/MoSe_2$ heterolayers as electrocatalysts for the hydrogen evolution reaction in comparison to the TMDs that make them up. This was done in a solution of 10 mM H_2SO_4 and 0.1 M K_2SO_4 at voltage scan rate of 20 mV s^{-1} for all the scans…….……120

Figure 5.7. Linear sweep voltammogram of the $MoS_2/MoSe_2$ heterolayer and the TMDs that make it up as electrocatalysts for HER in a solution of 10 mM H_2SO_4 and 0.1 M K_2SO_4……..121

Figure 5.8. Overlay of the different heterolayers and how they compare to each other. All conditions were kept the same and the voltammetry was carried out in a 10 mM H_2SO_4 and 0.1 M K_2SO_4 solution and with a Ag/AgCl reference electrode and a graphite rod counter at a scan rate of 20 mV s^{-1}……..122

Figure 5.9. HER scan rate study using the **(A)** $MoSe_2/MoS_2$ and **(C)** WS_2/MoS_2 heterolayer. The scan rate was varied from 10 to 250 mV s^{-1}. The Randles-Ševčík plots with linear fit for both $MoSe_2/MoS_2$ **(B)** with equation $I = (19.1v + 1.41) \times 10^{-4}$ and WS_2/MoS_2 **(D)** with equation $I = (18.6v + 2.96) \times 10^{-4}$ from the resulting scan rate studies……125

Figure 5.10. (A) A peak current vs scan rate plot comparing experimental results to those obtained theoretically. **(B)** Overlay of the Randles-Ševčík plots for the various heterolayers and those from theoretical results……..126

Figure 5.11. (A). HER voltammograms at various rotation rates using the WS_2/MoS_2 heterolayer electrocatalyst in a solution of 10 mM H_2SO_4 and 0.1 M K_2SO_4. **(B).** Koutecky-Levich plot resulting from the voltammograms in (A). **(C).** Tafel plot from using the intercepts and potentials data in (B). A best fit line was drawn with the resulting equation $log_{10}(I_k) = -2.32E - 4.36$, from which the electrochemical rate constant was calculated……127

Figure 5.12. (A). HER voltammograms at various rotation rates using the $MoSe_2/MoS_2$ heterolayer electrocatalyst in a solution of 10 Mm H_2SO_4 and 0.1 M K_2SO_4. **(B**). Koutecky-Levich plot resulting from the voltammograms in (A). **(C).** Tafel plot from using the intercepts and potentials data in (B). A best fit line was drawn with the resulting equation $log_{10}(I_k) = -2.05E - 4.63$, from which the electrochemical rate constant was calculated……128

Figure 5.13. (A&B) SEM top images of $MoSe_2/MoS_2$ hetero sample at different magnifications. **(C).** EDS spectra of the sample showing the detection of Mo, Se, and S elements in the sample……..129

Figure 5.14. (A&B) SEM top images of $MoS_2/MoSe_2$ hetero sample at different magnifications. **(C).** EDS spectra of the sample showing the detection of Mo, Se, and S elements in the sample……130

Figure 5.15. **(A&B)** SEM top images of WS_2/MoS_2 hetero sample at different magnifications. **(C).** EDS spectra of the sample showing the detection of Mo, W, and S elements in the sample…….131

Figure 5.16. (A&B) SEM top images of $WS_2/MoSe_2$ hetero sample at different magnifications. **(C).** EDS spectra of the sample showing the detection of Mo, W, Se, and S elements in the sample……132

Figure 5.17. (A&B) SEM top images of $MoS_2/MoSe_2$ (L/L) hetero sample at different magnifications. **(C).** EDS spectra of the sample showing the detection of Mo, Se, and S elements in the sample……133

Figure 5.18. Cross-sectional SEM image of the WS_2/MoS_2 heterolayer from which the film thickness was to be determined……134

Figure 5.19. (A) Wide area spectra of the $MoSe_2/MoS_2$ sample displaying all the elements in it. High resolution spectra of the **(B)** Mo 3d peak, **(C)** S 2p peak and the **(D)** Se 3d peaks from the sample $MoSe_2/MoS_2$……...……..135

Figure 5.20. (A) Wide area spectra of the WS_2/MoS_2 sample displaying all the elements in it. High resolution spectra of the **(B)** Mo 3d peak, **(C)** S 2p peak and the **(D)** W 4f peaks from the sample WS_2/MoS_2……136

Figure 5.21. (A) Wide area spectra of the $MoS_2/MoSe_2$ sample displaying all the elements in it. High resolution spectra of the **(B)** Mo 3d peak, **(C)** S 2p, Se 3p peaks and the **(D)** Se 3d peaks from the sample $MoS_2/MoSe_2$……137

Figure 5.23. (A) Wide area spectra of the $MoS_2/MoSe_2$ sample displaying all the elements in it. High resolution spectra of the **(B)** Mo 3d peak, **(C)** S 2p, Se 3p peaks and the **(D)** Se 3d peaks from the sample $MoS_2/MoSe_2$…….138

Figure 5.24. Model fitting result of the simulated data (---) against experimental data. The experimental data was collected at three different angles and then fitted using Tauc-Lorentz model to determine the sample thickness……..140

Figure 6.1. Wide area spectra of the MoS_2+WSe_2 mixture showing all the elements present in it…150

Figure 6.2. High resolution spectra of the MoS_2+WSe_2 mixture showing the **(A)** Mo 3d peak, **(B)** S 2p peak, **(C)** W 4f peak and **(D)** Se 3d peak regions from the wide area spectra. The coloured lines (red, blue, green and purple) represent the deconvolution of the peaks…….150

Figure 6.3. (A) Wide area spectra of the MoS_2+WS_2 mixture displaying all the elements present in it. High resolution spectra of the **(B)** Mo 3d, **(C)** W 4f and **(D)** S 2p peak regions. The coloured lines (red, blue, green, yellow and purple) represent the deconvolution of the peaks……..151

Figure 6.4. Wide area spectra of the $MoSe_2$+WS_2 sample highlighting all the elements detected in the sample……..152

Figure 6.5. High resolution spectra of the $MoSe_2$+WS_2 mixture showing the **(A)** Mo 3d peak, **(B)** S 2p peak, **(C)** W 4f peak and **(D)** Se 3d peak regions from the wide spectra. The coloured lines (red, blue, green and purple) represent the deconvolution of the peaks……152

Figure 6.6. (A) Wide area spectra of the $MoSe_2$+WSe_2 mixture displaying all the elements present in it. High resolution spectra of the **(B)** Mo 3d, **(C)** W 4f and **(D)** Se 3d peak regions from the wide spectra. The coloured lines (red, blue, green and purple) represent the deconvolution of the peaks……...153

Figure 6.7. (A) Wide area spectra of the MoSSe sample showing all the elements present in it. High resolution spectra of the **(B)** Mo 3d peak, **(C)** S 2p peak and **(D)** Se 3d peak regions from the wide spectra. The coloured lines (red, blue, green and purple) represent the deconvolution of the peaks…154

Figure 6.8. Wide area spectra of the MoS_2+$MoSe_2$+WS_2 sample highlighting all the elements detected in the sample…….154

Figure 6.9. High resolution spectra of the MoS_2+$MoSe_2$+WS_2 mixture showing the **(A)** Mo 3d peak, **(B)** Se 3d peak, **(C)** W 4f peak and **(D)** S 2p peak regions from the wide spectra. The coloured lines (red, blue, green and purple) represent the deconvolution of the peaks……155

Figure 6.10. (A) Wide area spectra of the MoS_2+$MoTe_2$+WSe_2 mixture showing all the elements present in it. High resolution spectra of the **(B)** Mo 3d peak, **(C)** Se 3d peak, **(D)** S 2p peak, **(E)** W 4f peak and **(F)** Te 3d peak regions from the wide spectra. The coloured lines (red, blue, green and purple) represent the deconvolution of the peaks……..156

Figure 6.11. (A) Wide area spectra of the MoSSe+WTe_2+WS_2 mixture showing all the elements present in it. High resolution spectra of the **(B)** Mo 3d peak, **(C)** W 4f peak, **(D)** Se 3d peak, **(E)** Te 3d peak and **(F)** S 2p peak regions from the wide spectra. The coloured lines (red, blue, green and purple) represent the deconvolution of the peaks……157

Figure 6.12. X-ray powder diffraction patterns of the binary TMD mixtures and the individual TMD components **(A-D)**……159

Figure 6.13. X-ray powder diffraction patterns of the MoSSe sample and the individual TMDs making it up……..160

Figure 6.14. X-ray powder diffraction patterns of the MoS_2+$MoSe_2$+WS_2 mixture and the individual TMDs making it up…….160

Figure 6.15. X-ray powder diffraction patterns of the MoS_2+$MoTe_2$+WSe_2 mixture and the individual TMDs making it up…….161

Figure 6.16. X-ray powder diffraction patterns of the MoSSe+WTe_2+WS_2 mixture and the individual TMDs making it up…….161

Figure 6.17. Raman spectra of the various TMD mixtures along with the spectra of individual TMD components **(A-D)**……163

Figure 6.18. Raman spectra of the MoSSe sample along with the spectra of individual TMDs making them up…….164

Figure 6.19. Raman spectra of the MoS_2+$MoSe_2$+WS_2 TMD mixtures along with the spectra of individual TMDs making them up……164

Figure 6.20. Raman spectra of the MoS_2+$MoTe_2$+WSe_2 TMD mixtures along with the spectra of individual TMDs making them up……165

Figure 6.21. Raman spectra of the MoSSe+WTe_2+WS_2 TMD mixtures along with the spectra of individual TMDs making them up……165

Figure 6.22. Voltammograms showing the change in onset potential between the TMD mixtures and the individual TMD components as electrocatalysts for the hydrogen evolution reaction **(A-D)**. An aqueous supporting electrolyte containing 10 mM H_2SO_4 and 0.1 M K_2SO_4 was used for the measurements with a scan rate of 50 mV s^{-1}……166

Figure 6.23. Voltammograms showing the change in onset potential between the TMD mixtures and the individual TMDs making them up as electrocatalysts for the hydrogen evolution reaction **(A-C)**. A solution of 10 mM H_2SO_4 with 0.1 M K_2SO_4 supporting electrolyte was used for the measurements with a scan rate of 50 mV s^{-1}..…….168

Figure 6.24. Comparison of the different TMD mixtures as electrocatalysts for HER. The conditions were kept the same for all the scans and the voltammetry was conducted in a 10 mM H_2SO_4 and 0.1 M K_2SO_4 aqueous electrolyte. The cells consisted of a Ag/AgCl (saturated KCl) reference electrode and graphite rod counter electrode along with modified glassy carbon as the working electrode……170

Figure 1.25. Tafel slope values for the different TMD mixtures. The Tafel slopes for the pure TMDs are: 104 mV dec^{-1} (MoS_2), 143 mV dec^{-1} (WS_2), 97 mV dec^{-1} ($MoSe_2$), 130 mV dec^{-1} (WSe_2), 66 mV dec^{-1} ($MoTe_2$) and 84 mV dec^{-1} (WTe_2)…….172

Figure 6.26. Reaction kinetics modelling of the resulting voltammograms from the HER scans using the TMD mixtures. Best-fit plot of the waveshape fitting simulation (o) and experimental data (-) for **(A)** MoS_2+WS_2, **(B)** MoS_2+WSe_2, **(C)** $MoSe_2$+WS_2 and **(D)** $MoSe_2$+WSe_2……173

Figure 6.27. Reaction kinetics modelling of the resulting voltammograms from the HER scans using the MoS_2+WSe_2 TMD mixture. Best-fit plot of the waveshape fitting simulation (o) and experimental data (-) for two HER scans **(A-B)**……174

Figure 6.28. Reaction kinetics modelling of the resulting voltammograms from the HER scans using the MoS_2+WS_2 TMD mixture. Best-fit plot of the waveshape fitting simulation (o) and experimental data (-) for two HER scans **(A-B)**……174

Figure 6.29. Reaction kinetics modelling of the resulting voltammograms from the HER scans using the $MoSe_2$+WS_2 TMD mixture. Best-fit plot of the waveshape fitting simulation (o) and experimental data (-) for two HER scans **(A-B)**……175

Figure 6.30. Reaction kinetics modelling of the resulting voltammograms from the HER scans using the $MoSe_2$+WSe_2 TMD mixture. Best-fit plot of the waveshape fitting simulation (o) and experimental data (-) for two HER scans **(A-B)**……175

Figure 6.31. Reaction kinetics modelling of the resulting voltammograms from the HER scans using the MoS_2+$MoSe_2$+WS_2 TMD mixture. Best-fit plot of the waveshape fitting simulation (o) and experimental data (-) for two HER scans **(A-B)**……176

Figure 6.32. Reaction kinetics modelling of the resulting voltammograms from the HER scans using the MoS_2+$MoTe_2$+WSe_2 TMD mixture. Best-fit plot of the waveshape fitting simulation (o) and experimental data (-) for two HER scans **(A-B)**……..176

Figure 6.33. Reaction kinetics modelling of the resulting voltammograms from the HER scans using the MoSSe+WTe_2+WS_2 TMD mixture. Best-fit plot of the waveshape fitting simulation (o) and experimental data (-) for two HER scans **(A-B)**……177

Figure 8.1. Cyclic voltammetry of the deposition of MoS_2 onto a glassy carbon electrode at a scan rate of 50 mV s^{-1} in a solution containing 2 mM $(NH_4)_2MoS_4$ and 0.1 M $NaClO_4$……..……195

Figure 8.2. (A, B) Chronoamperometry scans without any spikes for potentials held at -0.25 V and -0.50 V (vs RHE) for 30 seconds with a pH 2 solution of 0.01 M H_2SO_4 and 0.01 M NaOH. **(C, D)** MoS_2 impact spikes for potentials held at -0.25 V and -0.50 V for 30 seconds using a 100 pM MoS_2……..196

Figure 8.3. Tafel slope derivation for the electrodeposited (B) and nanoparticle (D) MoS_2 towards HER. An LSV (A) obtained using the electrodeposited MoS_2 and the nanoparticle impact height (C) scan were used for deriving the Tafel plots……198

Figure 8.4. Scanning electron micrograph of MoS_2 nanoparticles. Scale bar of 10 µm……..199

Figure 8.5. XRD spectra of the raw and ultrasonicated nanoparticles. The 2H-MoS_2 spectra from ICSD (https://icsd.psds.ac.uk/search/basic.xhtml) is also shown for comparison…….201

Figure 8.6. AFM image of MoS_2 on mica (A&B). (C) 3D image of the region shown in B……..202

List of Tables

Table 2.1 Comparison of synthesis methods for TMDs highlighting their advantages, limitations and achievable catalytic activity range (HER overpotential)……46

Table 2.2. HER performance of various doped TMDs. All potentials were corrected for the pH used in each solution ……..….49

Table 2.3. Comparison of the HER activity of different nanoparticulate forms of various TMDs…...51

Table 2.4. HER performance of various TMD heterostructures in comparison to the individual TMDs making them up…….….52

Table 2.5. Comparison of modification methods for TMDs, highlighting advantages, limitations and achievable catalytic activity ranges……53

Table 4.1. HER mechanism. Data from [18–20]……....93

Table 5.1. HER mechanism steps…….123

Table 5.2. Onset potential and Tafel slope values for the various TMDs and their heterolayers.……124

Table 5.3. Percentage composition of the different elemental states of the various components in each heterolayer……139

Table 6.1. Atomic percentages of the different elements in the TMD mixtures…….…..158

Table 6.2. HER onset potentials for the various TMD mixtures used as electrocatalysts. Onset potentials were determined at a current density of 0.5 mA cm^{-2} for all materials…….....169

Table 6.3. Rate determining steps in the hydrogen evolution reaction and their respective Tafel slope…….171

Table 6.3. The calculated standard electrochemical rate constants (k_0) and transfer coefficients (α) for HER from modelling the voltammograms using DigiElch software…….…..178

1 Introduction

1.1 Background of the research

The dangers of global warming are becoming increasingly prominent due to the rise in global average temperatures of approximately 1.0 ºC above pre-industrial levels, with an increase of 0.2 ºC per decade.[1,2] This increase is associated with human activity, which has produced an increase in greenhouse gas emissions (GHG) that have had a direct effect on global warming.[3-5] Of these greenhouse gas emissions, fossil fuel usage accounts for over 75% of their global emissions and carbon dioxide (CO_2) emissions.[6] The GHG and CO_2 emissions, alongside the reality of running out of fossil fuels, have sparked the need for alternative green energy sources with very low to no CO_2 and GHG emissions. This led to the emergence of renewable energy generation technologies such as wind, solar, hydropower and biofuels to transition to less carbon-intensive, or clean energy.[7-10]

These alternative energy generation techniques have their own drawbacks, which makes it challenging to fully phase out fossil fuel technologies and be fully dependent on renewable energy. For solar energy generation, the intermittent energy production along with the high costs of the systems and large areas to site them are proving to be taxing towards developing and expanding solar energy techniques, hence the need for alternative clean energy sources or technologies.[11,12] Wind energy, in contrast, has issues of low-level noise and limited locations for wind turbines, which limits full utilisation of wind energy technologies to provide sufficient energy to compete with fossil fuels.[13-15]

The limitations of renewable energy technologies led to the exploration of alternative methods to achieve clean energy generation such as fuel cells, energy storage systems, and hydrogen as an alternative fuel. Energy storage systems (ESS) are technologies designed to collect energy from different sources, transform and store it for later use, helping to balance supply and demand, enhance grid stability, and support renewable energy integration.[16] These can be divided into electrical, chemical, and thermal energy storage systems to suit different applications and environments. Energy storage is being explored for a variety of applications, some of which include controlling and tackling the intermittent power supply issue in the distributed generation of power. These are usually used for

load levelling, that is, to store the excess energy generated that can be later converted to electricity when demand increases, and the supply is low. Other applications include the automotive industry, utility grids, manufacturing, and aerospace industries. Like many energy technologies, energy storage systems face challenges of high initial investment, lifecycle costs, safety issues and durability (limited life cycle and performance degradation over time), which hinder most of their applications.[17,18]

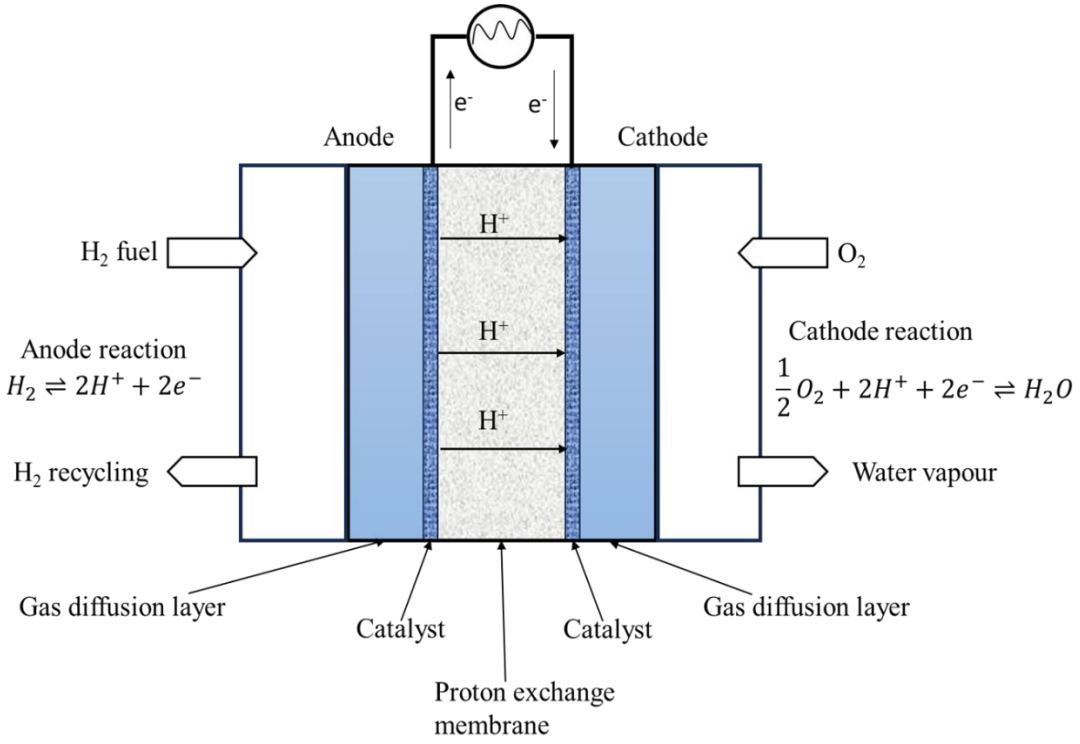

Figure 1.1. Schematic diagram of a fuel cell (PEMFC)

Fuel cells are electrochemical devices that convert chemical energy directly into electrical energy through reactions between a fuel and an oxidant, typically hydrogen and oxygen.[19-21] These consist of an anode where the fuel undergoes oxidation and releases electrons and protons which migrate to the cathode where they combine with oxygen to create water and produce heat, as shown in figure 1.1. The protons pass through the membrane from the anode to the cathode while the electrons get blocked by it thereby being forced to take an alternate route through the external circuit, generating a current in the process.[21] Different types of fuel cells have been developed for various purposes and these include proton exchange membrane fuel cells (PEMFCs), solid oxide fuel cells (SOFCs), alkaline fuel cells (AFCs), phosphoric acid fuel cells (PAFCs) and molten carbonate fuel cells (MCFCs).[22-24] These offer

high efficiency, low emissions, and versatility in fuel options. Fuel cells are gaining traction in the automotive industry as low or zero emission alternatives to combustion engines due to extensive research into the field as a way of tackling the CO_2 emissions challenge.[25,26]

The main challenge for commercialising fuel cells is their relatively high production costs due to catalyst materials like platinum and platinum alloys which are usually used at either the anode or cathode. In addition, the stable production and supply of hydrogen are other challenges that are incurred. The efficient production, storage and transportation of hydrogen safely also remain a challenge due to its properties: primarily its low volumetric energy density, and flammability. Thus, widespread adoption of hydrogen as a fuel requires innovative storage solutions with advanced materials to ensure safety and durability.[27-29]

Despite these challenges, hydrogen remains a promising fuel in the pursuit of a sustainable and low-carbon energy future. Efficient and cost-effective hydrogen production is crucial for this goal, with economical electrocatalyst materials playing a significant role. Consequently, there is a strong interest in exploring various materials that are affordable, durable, and possess excellent catalytic activity for hydrogen production. This study aims to investigate a group of 2D semiconductors called transition metal dichalcogenides (TMDs) as potential economical electrocatalyst materials for hydrogen production.

1.2 Hydrogen generation

Hydrogen has been recognised as a clean energy carrier with the potential to become a cornerstone of the global energy system.[30-32] It has various applications ranging from energy production and transportation to industrial processes while contributing to decreasing greenhouse gas emissions and transitioning to a sustainable energy future. As an energy carrier, it can store excess renewable energy and deliver usable energy efficiently during peak times, making it an essential part of the energy system.[33-35] It is also used as a clean fuel in fuel cells to produce electrical energy, and the by-product of the reaction is only water, as such, it is an environmentally friendly alternative to fossil fuels.

Hydrogen utilization in various industries is increasing, and with this, the demand for hydrogen is also growing, hence the need for efficient and environmentally friendly hydrogen production methods. The current production methods include steam reforming, partial oxidation and gasification, biomass-based hydrogen production and electrolysis, to name a few.

Steam reforming is the most common method used to produce hydrogen and it mainly consists of reacting steam with a hydrocarbon in the presence of a catalysts at temperatures of 750-1000 ºC to produce hydrogen and carbon dioxide.[36,37] The catalyst used is usually nickel-based and typical hydrocarbons used include natural gas (methane), liquid petroleum gas (LPG), methanol, and ethanol for the reforming process. Methane steam reforming is the most commonly used method to produce hydrogen, and it accounts for 48% of world hydrogen production.[38] It is an endothermic reaction of methane and steam at temperatures of 700-1000 ºC in a cobalt-nickel (Co-Ni) catalysed reactor at a pressure of 3-25 bar. Methane is converted to hydrogen following the reaction:[38]

$$CH_4(g) + H_2O(g) \rightleftharpoons CO(g) + 3H_2(g) \qquad \Delta H_{298} = 206\ kJ\ mol^{-1} \qquad (1.1)$$

$$CO(g) + H_2O(g) \rightleftharpoons CO_2(g) + H_2(g) \qquad \Delta H_{298} = -41\ kJ\ mol^{-1} \qquad (1.2)$$

where reaction 1.2 is the water gas shift (WGS) reaction. This reaction converts the carbon monoxide (CO) produced from methane reformation to carbon dioxide (CO_2) and water. This is where the main issue with methane steam reformation to produce hydrogen stems from: the generation of significant amounts of carbon dioxide, and hence the need for carbon capture and storage (CCS) technologies to reduce CO_2 emissions.

Partial oxidation and gasification are techniques used to produce hydrogen by breaking down hydrocarbon feedstocks such as coal, biomass, and natural gas into simpler molecules like hydrogen and carbon dioxide through high-temperature reactions.[39,40] With partial oxidation, the hydrocarbon is reacted with a limited amount of oxygen to produce hydrogen, carbon monoxide, carbon dioxide and water. This is an exothermic reaction, and the heat generated by the oxidation reaction is used to sustain the process, eliminating the need for external heating.[38,41] The main benefit of this method is the flexibility to use various hydrocarbon feedstocks, and it has a high efficiency which makes it suitable

for large-scale hydrogen production. On the other hand, gasification reacts the hydrocarbon materials with a controlled amount of oxygen or steam at high temperatures to produce hydrogen and carbon monoxide.[37,42,43] This is an endothermic reaction and requires external heat for the reaction to occur. The gases produced from the reaction (syngas) must be cleaned of particulate matter, sulfur compounds and other impurities before hydrogen is extracted from the mixture. The main advantage of the method is that a variety of hydrocarbon feedstocks can be used, including low-grade fuels and waste, which makes it more economical. However, both partial oxidation and gasification produce significant amounts of carbon dioxide, necessitating the use of carbon capture and storage technologies which can have a huge impact on capital costs for both methods.

Electrolysis is another technique used to generate hydrogen and it utilises electricity to split water into hydrogen and oxygen. The water-splitting reaction is very endothermic, hence the need for electricity to supply the required energy:[44-47]

$$2H_2O(l) \rightarrow 2H_2(g) + O_2(g) \qquad E^0 = -1.23\,V \qquad (1.3)$$

The main advantage of this method over other hydrogen production methods is that there is no direct emission of greenhouse gases, but it is more expensive in comparison to them. When powered by renewable energy, it produces hydrogen without any direct CO_2 emissions thus making it a completely green and environmentally friendly hydrogen production method.

1.2.1 Electrolyser

An electrolyser is a device that performs the electrolysis of water into hydrogen and oxygen and comprises an anode, the positive electrode where oxidation occurs; and a cathode, the negative electrode where the reduction of protons occurs to produce hydrogen, as shown in figure 1.2. Additionally, there is an electrolyte that acts as a medium for conducting ions between the anode and cathode and a membrane separating the two.[48,49]

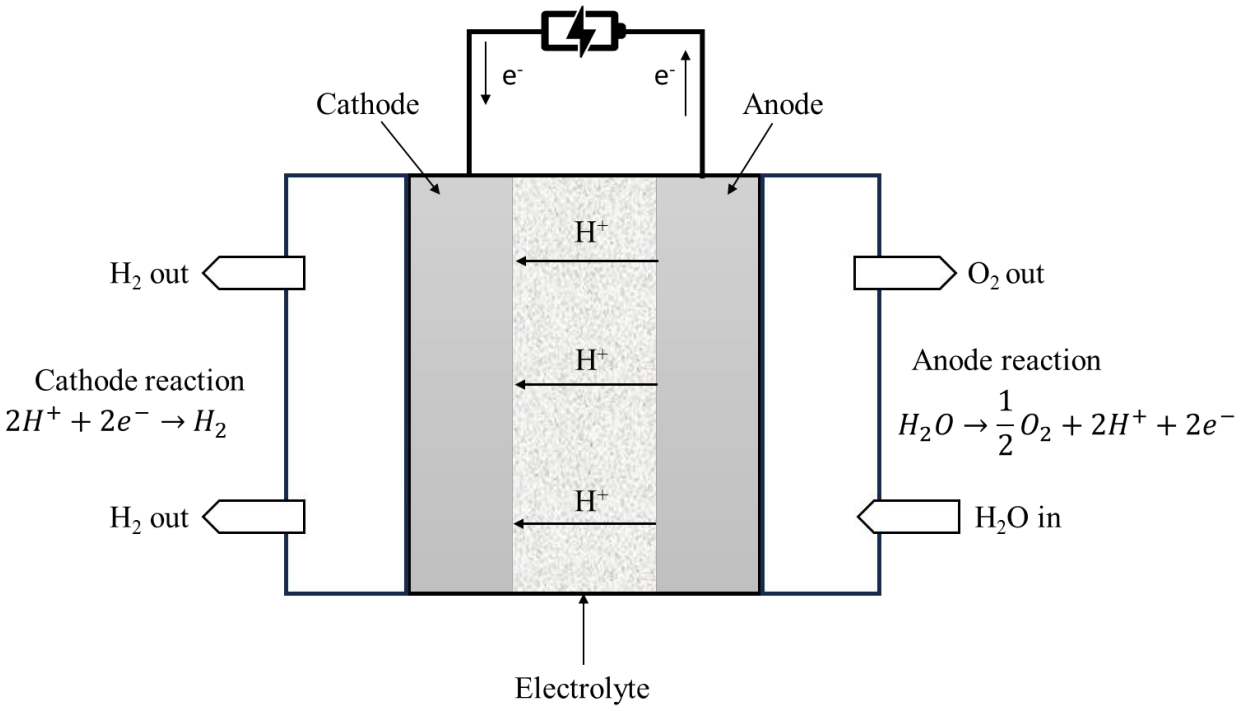

Figure 1.2. Structure of an electrolyser

Different types of electrolysers are being developed with various anode and cathode materials, the primary distinction being the type of electrolyte used. Alkaline electrolysers (AEL) use an alkaline solution, typically potassium hydroxide, as the electrolyte to conduct hydroxide ions.[50] They are relatively inexpensive compared to other types but are less efficient at higher pressures, which can limit their application. Proton exchange membrane electrolysers (PEM) utilize a solid polymer membrane electrolyte, which conducts protons from the anode to the cathode during water splitting.[50,51] They are highly efficient in hydrogen production and responds quickly to load changes. However, the membrane degrades over time, and using expensive materials like platinum group metal (PGM) catalysts makes them costly.[51] The last type is the solid oxide electrolyser (SOE), which uses a solid ceramic electrolyte that conducts oxide ions at high temperatures (700-1000°C).[52,53] SOEs offer high hydrogen production efficiency and can utilize waste heat from industrial processes. Their main disadvantage is the high operating temperatures, which can lead to durability issues.

An electrolyser produces hydrogen through the water-splitting process, involving two main reactions: the hydrogen evolution reaction (HER) at the cathode and the oxygen evolution reaction (OER) at the

anode shown in figure 1.2. These half-cell reactions have high overpotentials, resulting from slow reaction kinetics, which poses a challenge for the practical use of water splitting to produce hydrogen.[54] Effective catalysis is essential to address this issue, necessitating highly efficient catalyst materials for both OER and HER to reduce the overpotentials of these reactions.

Different catalysts are required for the HER and OER due to the varying operating conditions of the electrolysis cell, leading to the use of different catalytic materials for the anode and cathode electrodes. For example, the OER often requires noble metal and noble metal oxide electrocatalysts when water electrolysis is conducted under acidic conditions.[1] However, under alkaline conditions, the range of suitable electrocatalysts expands to include non-noble metals and metal oxides. Using noble metal and metal oxide electrocatalysts increases the cost of the electrolytic cell while using non-noble metals and metal oxides requires alkaline conditions, which lowers the activity of the HER compared to acidic conditions.[55,56]

This creates a challenge in water electrolysis: the need for low-cost, durable, and highly effective electrocatalysts for both the OER and HER, that can function well under the same conditions. Current research focuses on finding suitable electrocatalyst materials for both reactions to improve the efficiency and economic feasibility of the electrolysers for hydrogen production. This study contributes to this research by focusing on the HER half-cell reaction and investigating potential electrocatalyst materials that could enhance hydrogen production in the industry.

1.2.2 Hydrogen evolution reaction (HER)

The hydrogen evolution reaction is an electrochemical reaction that produces hydrogen gas (H_2) from the reduction of protons.[46,57,58] It is a two-electron transfer process that occurs at the cathode during water electrolysis. The reaction is highly dependent on environmental conditions, but the general equations are as follows in both acidic (eqn. 1.4) and alkaline media (eqn. 1.5):[57,59,60]

$$2H^+ + 2e^- \rightarrow H_2 \qquad (1.4)$$

$$2H_2O + 2e^- \rightarrow 2OH^- + H_2 \qquad (1.5)$$

The reactions consist of a series of steps that vary depending on the reaction conditions and catalysts used. When HER is conducted in acidic media, the reaction mechanism generally involves the following steps:[58,61,62]

$H^+ + e^- \rightarrow H_{ad}$ Volmer step (1.6)

$H^+ + e^- + H_{ad} \rightarrow H_2$ Heyrovsky step (1.7)

$H_{ad} + H_{ad} \rightarrow H_2$ Tafel step (1.8)

The Volmer step is the first step which produces the adsorbed hydrogen from the reduction and adsorption of a proton on the catalyst surface, after which the hydrogen evolution reaction proceeds either by the Heyrovsky or Tafel steps.[46] The Heyrovsky step produces hydrogen gas by combining the adsorbed hydrogen with a proton and an electron via equation 1.7, while the Tafel step combines the adsorbed hydrogens to produce hydrogen gas (H_2). During HER, one of these steps becomes the rate-determining step due to kinetically limiting the electrochemical reaction, thereby controlling the speed at which the reaction occurs.[57] These kinetics are linked to the adsorption and desorption speeds of the hydrogen atoms on the active sites of the catalysts thus making them dependent on the catalyst material used. First shown experimentally by Trasatti, the activity of the hydrogen evolution reaction is closely related to the hydrogen adsorption properties of the electrocatalyst.[63] The Gibbs energy of hydrogen adsorption (ΔG_H) is used as a key measure of the electrocatalytic activity of a material towards HER. Ideally, an optimal ΔG_H value close to zero indicates that the material has a balanced ability to adsorb and desorb hydrogen, leading to high catalytic efficiency.[63-65]

The energy of chemisorption of hydrogen as a descriptor of HER has been used to draw up a volcano curve/plot (figure 1.3), which provides a comparison of the catalytic activities of different metals in acidic media. The left side of the peak corresponds to metals (e.g. Mo, W and Ti) that have a larger negative ΔG_H and bind hydrogen strongly, therefore making the desorption more difficult while the metals on the right side of the volcano plot (e.g. Au, Ag and Ni) weakly binds hydrogen, which prevents the formation of stable intermediates on the catalyst surface, thereby limiting HER.[66-70] From figure 1.3,

it can be seen that platinum and the platinum group metals (PGM) are located at the top of the volcano plot, indicating their high catalytic activity for HER.

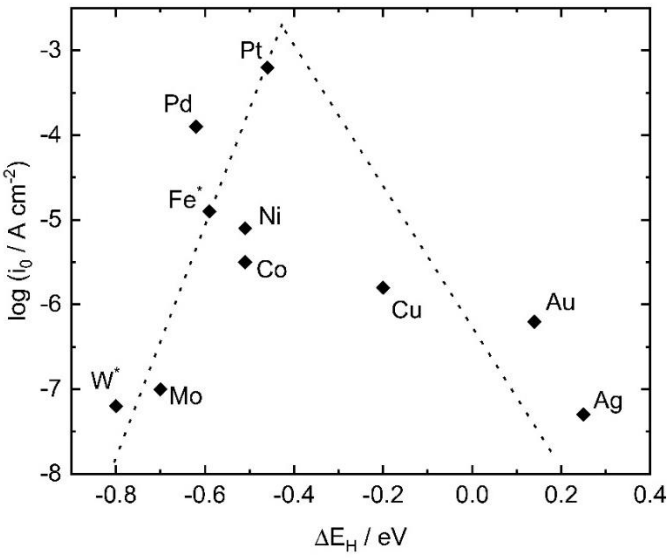

Figure 1.3. Volcanic plot of the relationship between exchange current density and hydrogen binding energy of various materials (recreated from ref. [67]). The peak of the volcano represents the optimal binding energy for the highest catalytic activity, highlighting the most efficient catalysts for the HER.

Platinum group metals (Pt, Pd, Ir, Ru, and Rh) are the most effective electrocatalysts for HER due to their favourable electronic properties, stability, and catalytic activity. Despite their excellent performance, the high cost and limited availability of these noble metal-based electrocatalysts drive ongoing research into alloying and alternative materials to achieve cost-effective and efficient HER electrocatalysis. Studies are being conducted on ways of reducing noble metal loading and achieving high metal utilization for optimum HER catalytic performance. One approach involved alloying platinum with other low-cost transition metals to enhance platinum utilization.[46,71]

Some research efforts are directed towards non-noble metal-based materials as alternative electrocatalysts for HER. These materials have shown great promise as efficient HER electrocatalysts and offer the advantage of being more affordable than noble metal-based electrocatalysts.[72-74] Examples

include transition metal carbides (TMCs) like Mo_2C and WC which have been shown to display high catalytic activity for HER due to their excellent electrical conductivity, favourable hydrogen adsorption properties and suitable d-band electronic density state similar to that of Pt.[46] Density functional theory (DFT) calculations and experimental analysis of the physical, chemical, and electronic structures of TMCs have shown that embedding carbon atoms into the lattice interstices gives them d-band electronic density OF states comparable to those of platinum hence the improved HER catalytic activity.[75,76] Another interest group is the transition metal phosphides (TMPs), which have been gaining attention due to their high catalytic activity for HER and stability in both acidic and alkaline media. Their catalytic activity is attributed to the synergy between transition metals and phosphorus atoms, which generates active sites and enhances the electronic structure of the material.[46,77] TMPs possess a mix of covalent and ionic interactions, imparting them with unique electronic properties, enabling both metallic conductivity and semiconducting behaviour, which further supports their catalytic performance.

Non-metal electrocatalysts, such as carbon-based electrocatalysts, have also been explored for HER. Carbon is an inert material for most electrochemical reactions, but certain measures have been developed to improve catalytic activity. One of these is to introduce heteroatoms to the carbon matrix through doping, which modifies the electronic properties of the doped carbon and produces active sites for HER.[78,79] Non-metal atoms such as P, S and N have been used as dopants to improve HER catalytic activity of the carbon.[80-83] Hybrid carbon structures have also been proven to produce enhanced HER performance. Zheng et. al. synthesised a layer of $CoSe_2$ nanobelts on carbon fibre felt ($CoSe_2$/CFF), and this resulted in an overpotential of 141 mV at 10 mA cm^{-2}, a great improvement from the 252 mV recorded for the physical mixture of $CoSe_2$ and CFF.[84]

MXenes are some of the latest groups of non-PGM catalysts to be investigated for HER activity due to their potential as HER electrocatalysts, large surface area, adjustable structure and superior electrical conductivity.[85-87] These are a group of two-dimensional inorganic compounds that consist of transition metal carbides, nitrides or carbonitrides. Their structures comprise two or more layers of transition metal atoms arranged in a 2D lattice, with carbon and/or nitrogen layers filling the octahedral sites

between the adjacent transition metal layers.[86,88,89] Yuan et al. investigated a novel synthesis method for highly active MXene nanofibers (Ti_3C_2) which displayed enhanced HER electrocatalytic activity with a low overpotential of 160 mV at a current density of 10 mA cm^{-2}.[90] This was due to the high specific surface area and exposed active sites of the MXene nanofiber.

Lastly, transition metal dichalcogenides (TMDs) represent another promising group of non-noble metal-based electrocatalysts for the hydrogen evolution reaction. TMDs, such as MoS_2, WS_2, and others, have shown significant potential due to their unique layered structures, which provide abundant active sites for hydrogen adsorption and evolution.[91,92] This study specifically focuses on TMDs as HER electrocatalysts. The following chapters will delve into the detailed mechanisms of hydrogen evolution on TMDs, explore the various synthesis methods, and evaluate their performance compared to other non-noble metal-based catalysts. The goal is to identify the most promising TMD candidates and optimize their properties for efficient and sustainable hydrogen production. By concentrating on TMDs, this research aims to contribute to the development of cost-effective and high-performance electrocatalysts that can facilitate the widespread adoption of hydrogen as a clean energy carrier.

1.3 General Electrochemistry

Electrochemistry encompasses a variety of processes that have wide-ranging applications, including electrolysis, batteries, fuel cells, electroplating, and corrosion control. The electrochemical processes conducted in these applications can generally be categorized into galvanic and faradaic processes. A galvanic process involves a spontaneous redox reaction that generates electrical energy, whereas a faradaic process refers to a non-spontaneous reaction where there is a direct transfer of electrons between an electrode and a species in solution due to an external potential bias.[93] This constitutes a heterogeneous electrochemical process since the electron transfer occurs at the interface of two different phases, that is, a solid-liquid interface which will be the case for reactions investigated in this study. During these reactions, electrons move between two distinct phases (electrode and solution species), leading to a net charge separation as equilibrium is approached.[94,95] This creates a potential difference

at the interface, and if E_m is electrode potential and E_s is solution potential, then the potential drop at the interface is:

$$\Delta E_{m/s} = E_m - E_s \qquad (1.9)$$

This quantity has a precise finite value for any system, but its direct measurement is not experimentally feasible unless an additional electrode is added to complete the electrical circuit thereby creating a two-electrode electrochemical cell (Fig. 1.4A).[94] This additional electrode, should have a constant known potential drop so that the potential difference (*E*) between the two electrodes can be measured and it is given by:

$$E = (E_m - E_s) + constant \qquad (1.10)$$

where the constant refers to counter electrode potential and the term in brackets is the potential drop of the electrode of interest. A reference electrode is added to the previously described two-electrode cell to form the conventional three-electrode electrochemical cell setup shown in figure 1.4B. This three-electrode system isolates the potential control and current measurements, allowing for more precise and accurate electrochemical measurements.

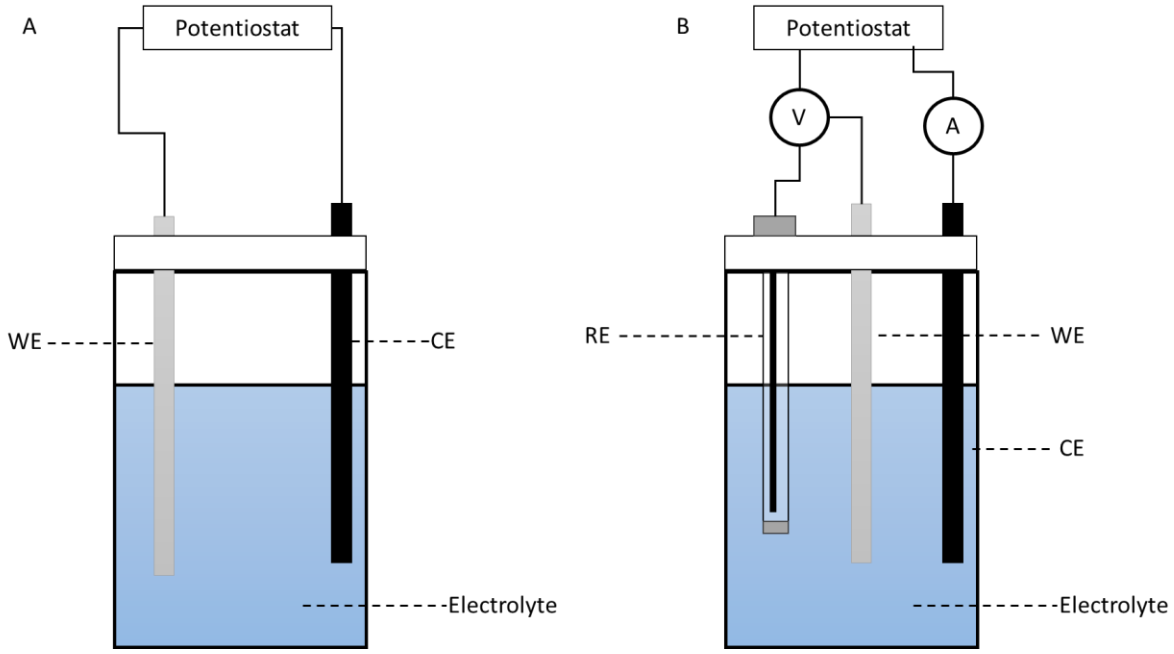

Figure 1.4. Diagrams of a two-electrode (**A**) and three-electrode (**B**) electrochemical cells.

For a two-electrode cell, the potential difference E is given by:

$$E = E_{WE} - E_{CE} \qquad (1.11)$$

Where E_{WE} is the potential at the working electrode and E_{CE} is the potential at the counter electrode. However, E_{CE} can vary because the counter electrode also carries the current required for the reaction, leading to potential drops due to solution resistance (iR drop):

$$E_{CE} = E_{ref} + iR_{sol} \qquad (1.12)$$

with E_{ref} being the reference potential of the counter electrode, i is the current and R_{sol} is the solution resistance. When a reference electrode is added to the system, to make it a three-electrode cell, it provides a stable and known potential (E_{RE}) due to the potentiostat providing infinite impedance, which ensures no current flows through it. Infinite impedance ensures that the reference electrode is not disturbed by the electrochemical reactions occurring in the cell, thereby preventing any drift in the reference potential that could affect the accuracy of the measurements. The potential difference of the cell then becomes:

$$E = E_{WE} - E_{RE} \quad (1.13)$$

The counter electrode carries the current, thereby completing the electrical circuit and it is typically constructed from materials that are electrochemically inert in the system under study.[96] It should also possess a high surface area and excellent electrical conductivity to ensure that it does not limit the electrode kinetics at the working electrode. The working electrode is where the desired electrochemical reactions take place, with its potential accurately controlled and measured against the reference electrode by a potentiostat. The working electrode is essential to the operation of an electrochemical cell, with its material, surface area, and conductivity being crucial for the efficiency and precision of electrochemical measurements.[97]

1.3.1 Electrochemical equilibrium: Nernst equation

The Nernst equation relates the reduction potential of a half-cell to activities (or concentrations) of the electroactive species involved. It connects chemical thermodynamics with practical measurements in electrochemistry, providing insight into the behaviour of cells and the properties of the involved species under various conditions. For a given reduction process where an oxidized species gains *n* electrons to form a reduced species:

$$ox + ne^{-} \rightleftharpoons red \quad (1.14)$$

the Gibbs energy is given by:[98]

$$\Delta G = \Delta G^{o} + RT \ln \frac{(a_{red})}{(a_{ox})} \quad (1.15)$$

where ΔG^{o} is the standard Gibbs energy, R is the gas constant (8.314 J K^{-1} mol^{-1}), T is the temperature (K) while a_{red} and a_{ox} are the activities of the reduced and oxidised species, respectively. The Gibbs energy for the half-reaction is connected to the electrode potential E through the following equation:

$$\Delta G = -nFE \quad (1.16);$$

$$\Delta G^{o} = -nFE^{o} \quad (1.17)$$

where F is the Faraday constant (96485 C mol^{-1}) and n is the stoichiometric number of electrons transferred. The standard electrode potential E^o corresponds to the standard Gibbs energy (ΔG^o), which occurs when the activities of products and reactants are equal to unity.[99] From equation 1.16, it can be deduced that positive electrode potential values are thermodynamically favourable. In contrast, negative electrode potential values indicate that the electrochemical cell would require an external driving force to initiate the reaction.

When equations 1.15, 1.16 and 1.17 are combined, it results in the following expression, known as the Nernst equation:

$$E = E^o - \frac{RT}{nF} \ln \frac{(a_{red})}{(a_{ox})} \qquad (1.18)$$

For the hydrogen evolution reaction:

$$H^+ + e^- \rightarrow \frac{1}{2} H_2 \qquad (1.19)$$

The Nernst equation takes the form:

$$E = E^o - \frac{RT}{F} \ln \frac{\left(f_{H_2}^{1/2}\right)}{(a_{H^+})} \qquad (1.20)$$

When accounting for the fugacity of hydrogen $f_{H_2}^{1/2}$ which is 1 under ideal gas conditions, and converting from natural logarithm, we obtain the expression:[98,100]

$$E = E^o - \frac{2.303RT}{F} \log_{10} \frac{1}{a_{H^+}} \qquad (1.21)$$

At 298 K, $pH = \log_{10}\left(\frac{1}{a_{H^+}}\right)$, and when substituting for that in eqn 1.21, we finally get:

$$E = E_f^o - 0.059pH \qquad (1.22)$$

with the formal potential E_f^o replacing the standard potential E^o to account for non-ideal behaviour and practical conditions. This quantitatively illustrates the pH sensitivity of the HER, showing that for each unit change in pH, the electrode potential shifts by 59 mV at 298 K.

1.3.2 Electrode kinetics

Electrochemical reactions involve electron transfer, and a quantitative model can be developed to describe the rate of electron transfer as a function of overpotential. Considering the following electrochemical reaction:

$$Ox(aq) + e^{-}(m) \underset{k_{ox}}{\overset{k_{red}}{\rightleftarrows}} Red(aq) \qquad (1.23)$$

where k_{red} and k_{ox} are the first-order heterogeneous rate constants of the forward (reductive) and backward (oxidative) electron transfer reactions. The net current *I* for the reaction, which is the sum of the reductive (I_{red}) and oxidative (I_{ox}) component, is expressed as:

$$I = I_{ox} - I_{red} = FA(k_{ox}[Red]_o - k_{red}[Ox]_o) \quad (1.24)$$

given that $I_{ox} = FAk_{ox}[Red]_o$ and $I_{red} = FAk_{red}[Ox]_o$. $[Red]_o$ and $[Ox]_o$ are the bulk concentrations of the reductive and oxidative species, respectively, while A is the electrode area (cm^2).

The electrode overpotential (η), defined as the difference between the applied potential E and the formal potential E_f^o, is linked to the activation Gibbs energies of the reductive and oxidative reactions, which results in:

$$k_{ox} = k^o exp\left(\frac{(1-\alpha)zF\eta}{RT}\right) \quad (1.25);$$

$$k_{red} = k^o exp\left(\frac{-\alpha zF\eta}{RT}\right) \quad (1.26)$$

where k^o is the standard rate constant, while α is the charge transfer coefficient, and z is the number of electrons. The charge transfer coefficient ($0 < \alpha < 1$) is sometimes referred to as the symmetry factor as it reflects the symmetry of the energy barrier for the electrochemical reaction. For α values close to 1, the energy barrier is significantly lowered by the applied potential, while for values close to 0, the energy barrier for the reaction is largely unaffected by the applied overpotential.

Equations 1.25 and 1.26 can be included in equation 1.24 to form:

$$I = FAk^0\left\{[Red]_o exp\left(\frac{(1-\alpha)zF\eta}{RT}\right) - [Ox]_o exp\left(\frac{-\alpha zF\eta}{RT}\right)\right\} \quad (1.27)$$

Normalizing the above equation by the electrode area *A* and rearranging the above equation using $j_o = Fk^o[Red]_o$ and $j_o = Fk^o[Ox]_o$, we get the Butler-Volmer equation:[101]

$$j = j_o\left\{exp\left(\frac{(1-\alpha)zF\eta}{RT}\right) - exp\left(\frac{-\alpha zF\eta}{RT}\right)\right\} \quad (1.28)$$

The Butler-Volmer equation can be transformed into the Tafel equation under conditions of high overpotential, where one of the exponential terms (reductive or oxidative) dominates. This results in one of the terms being negligible, and for the case of high anodic overpotential ($\eta \gg 0$) and taking natural logarithms, this results in:

$$\ln(j) = \ln(j_o) + \left(\frac{(1-\alpha)zF\eta}{RT}\right) \quad (1.29)$$

while for high cathodic overpotential ($\eta \ll 0$), we get:

$$\ln|j| = \ln|j_0| - \left(\frac{\alpha zF\eta}{RT}\right) \quad (1.30)$$

These Tafel equations provide a linear relationship between the overpotential η and the logarithm of the current density j. The slope of the resulting line, known as the Tafel slope is related to a and the y-intercept value relates to the exchange current density j_o. The application of these equations will be outlined in the results chapters. At low overpotentials, a Tafel expression can be derived from a series expansion of eqn 1.28 which would describe the current density (j) as a function of overpotential (η):

$$\eta = a + b\log(j) \quad (1.31)$$

where a is a constant, and b is the Tafel slope.

1.3.3 Electric Double Layer

The electric double layer (EDL) is a layer that forms at the interface of an electrode and electrolyte solution when a potential difference is applied due to charges on the electrode surface attracting oppositely charged ions from the electrolyte. It consists of two layers (inner and outer layer) of charges

with opposite polarity, creating a region where electrical potential and charge distribution are significantly different from those in bulk phases.[102,103] The inner layer, also known as the Helmholtz or Stern layer is immediately adjacent to the electrode surface and includes adsorbed ions (counter-ions) which are strongly bound to the surface and solvated ions.[94,102] This layer can be further divided into the Inner Helmholtz Plane (IHP) where the specifically adsorbed ions reside and the Outer Helmholtz Plane (OHP), where solvated ions approach the electrode surface but do not adsorb, as shown on figure 1.5.[104] Beyond the Helmholtz layer, is the outer layer (diffuse or Gouy-Chapman layer) which contains ions that are influenced by the electric field of the electrode. These ions are distributed in a gradient, forming a diffuse cloud of charges that gradually balances the charge of the electrode.[105] The electrical potential varies across the EDL, and it drops sharply in the Stern layer and more gradually in the diffuse layer until the boundary of the diffuse layer, where this potential is referred to as the zeta potential.

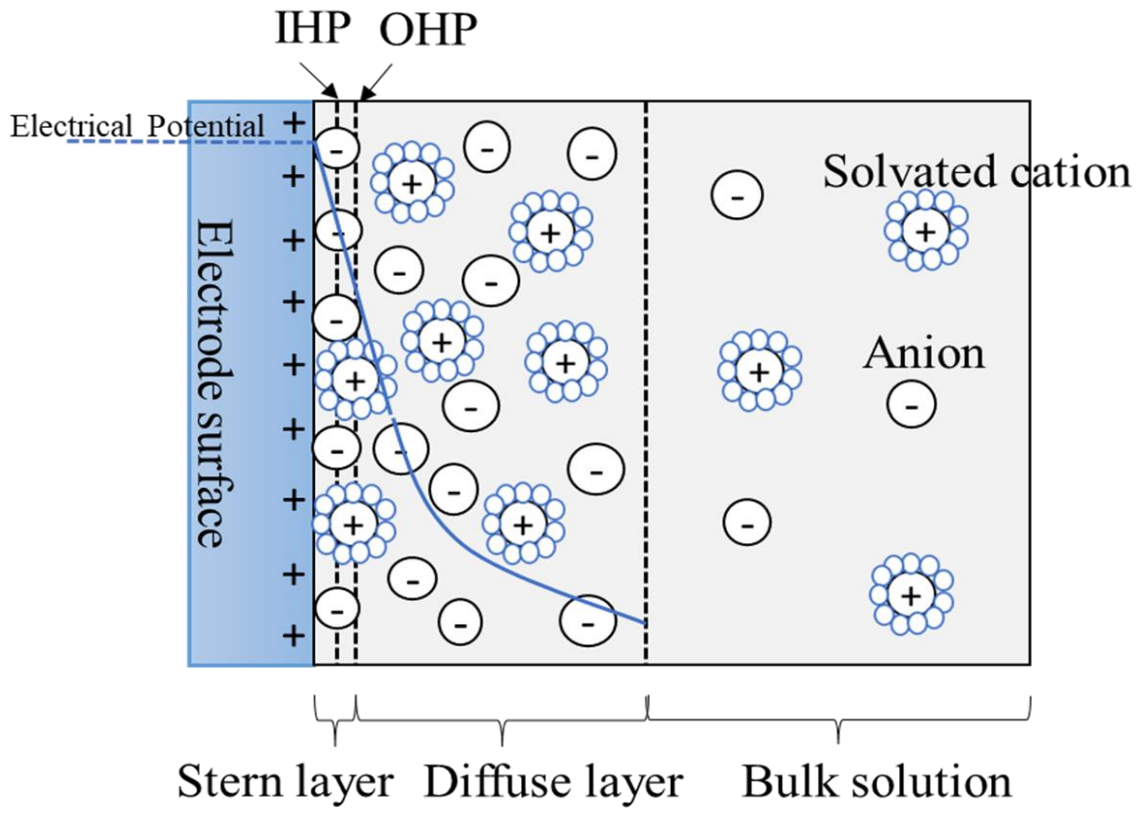

Figure 1.5. Electric double layer (EDL) formed on a positively charged electrode surface (adapted from ref [105]).

1.3.4 Mass Transport: Diffusion

Mass transport significantly affects the efficiency, rate, and overall performance of electrochemical systems. When mass transport is slow, it can become rate-limiting, controlling the observed current rather than the intrinsic kinetics of the reaction.[106] The primary forms of mass transport are diffusion, convection, and migration,[95,107] although the latter two are often eliminated experimentally, thereby allowing diffusion to be the primary mode of transport for electroactive species. Adding an excess of inert electrolyte to the solution compresses the electric double layer (EDL), thereby regulating the distance over which the electrical potential decreases from the electrode surface to the bulk solution.[94] This is crucial because eliminating potential gradients outside the narrow EDL prevents migration effects, while the short distance supports electron tunnelling between the electrode surface and reactant ions. Additionally, limiting the timescale of the experiments to approximately 20-30 s can mitigate the effects of natural convection. With convection and migration mitigated, only diffusion remains to transport the electroactive species to the electrode-electrolyte interface, driven by a concentration gradient. The rate of diffusion for the electroactive species can be determined and incorporated into kinetics calculations for accurate analysis of electrochemical cells. This rate of diffusion, according to Fick's first law, is proportional to the concentration gradient and is expressed as:[94,108]

$$J = -D\frac{\partial C}{\partial x} \qquad (1.32)$$

where J is the diffusion flux, D is the diffusion coefficient and $\frac{\partial C}{\partial x}$ is the concentration gradient. The second law goes on to describe how the concentration of electroactive species changes over time ($\frac{\partial C}{\partial t}$) due to diffusion and is given by:[108]

$$\frac{\partial C}{\partial t} = D\frac{\partial^2 C}{\partial x^2} \qquad (1.33)$$

1.3.5 Linear sweep and cyclic voltammetry

Linear sweep (LSV) and cyclic voltammetry (CV) are fundamental electrochemical techniques used to investigate redox properties, reaction mechanisms, and kinetics of electrochemical systems. LSV has

the potential of the working electrode linearly ramped at a constant rate over time while measuring the resulting current, while with CV, the potential is swept linearly between two set values and then reversed back to the starting potential point as shown in figure 1.6 A&B.[94] Figure 1.6A shows the usual transient voltammogram resulting from a CV from which two distinct current peaks are observed.

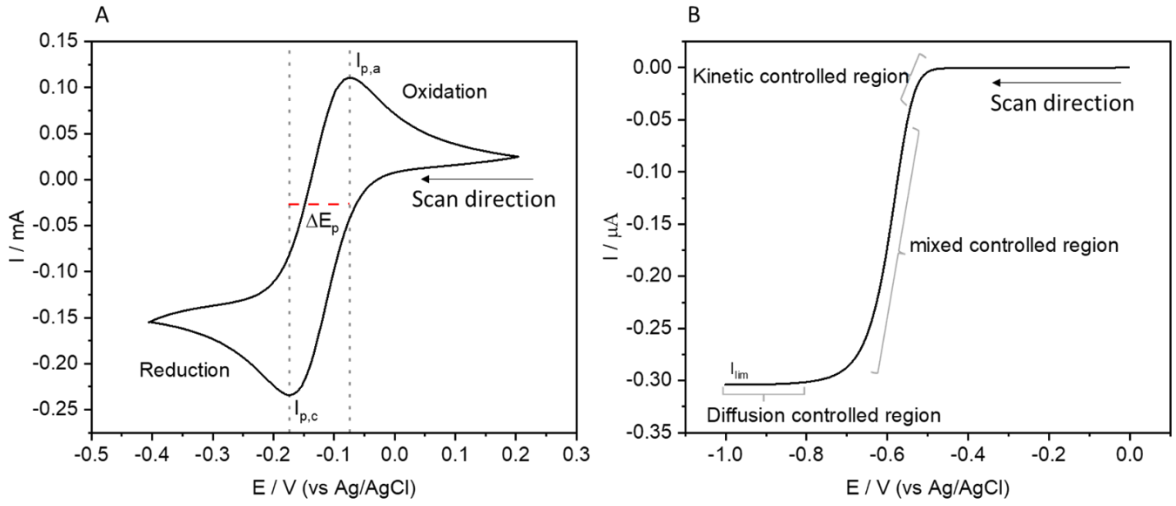

Figure 1.6. (A) This voltammogram displays the characteristic curve, illustrating the current response as a function of the applied potential. The distinct shape provides insights into the electrochemical behaviour of the system under study, with specific regions corresponding to different electrochemical processes. **(B)** LSV plot from a microelectrode, divided into three regions: kinetically controlled, mixed control, and diffusion-controlled, highlighting the transition from electron transfer kinetics to diffusion-limited current.

These are the anodic and cathodic peaks which have a peak-to-peak separation (ΔE_p) of 59/n mV (n being the number of electrons) for a reversible redox couple.[96,109] For irreversible or quasi-reversible reactions, the peak-to-peak separation is larger (ΔE_p> 120/n mV) if the reverse peak is present, indicating slower electron transfer kinetics. The size of the peak current (I_p in A) is proportional to the rate at which the potential is swept (voltage scan rate v in V s^{-1}) and this correlation brings forth the Randles-Ševčík equation:[94]

Reversible: $I_p = 2.69 \times 10^5 n^{3/2} A C D^{1/2} v^{1/2}$ (1.34)

Irreversible: $I_p = 2.99 \times 10^5 a^{1/2} A C D^{1/2} v^{1/2}$ (1.35)

where α is the transfer coefficient, C is the concentration (mol cm^{-3}), D is the diffusion coefficient (cm^2 s^{-1}) and A is the electrode area (cm^2). This equation enables the determination of diffusion coefficients (D) and other kinetic parameters like the transfer coefficients and number of electrons transferred in an electrochemical reaction.

Figure 1.6B shows an LSV plot obtained from a microelectrode, illustrating the electrochemical behaviour of the system under investigation. The curve is divided into three distinct regions: the kinetically controlled region, where the reaction rate is determined by the electron transfer kinetics; the mixed region, where both kinetics and mass transport influence the current; and the diffusion-controlled region, where the current (I_{lim}) is limited by the rate at which the reactants diffuse to the electrode surface.[110] The steady state limiting current (I_{lim}) is given by the following equation:[93,111]

$I_{lim} = 4nFC_{bulk}Dr$ (1.36)

where n is the number of electrons, F is the Faraday constant, C_{bulk} is the bulk concentration of the electroactive species, D is the diffusion coefficient, and r is the radius of the microelectrode.

1.4 Impact Electrochemistry

Impact electrochemistry or single-entity electrochemistry as it is sometimes known, is a branch of electrochemistry that focuses on studying the behaviour of individual nanoparticles, droplets or other small entities when they interact with an electrode surface. It focuses on single nanoparticles colliding with an electrode surface, where this interaction can result in electron transfer processes if the electrode material is suitable for the reaction and is held at an adequate potential.[112-115] When the particle collides with the electrode, it can either serve as a surface for the reduction or oxidation of electroactive species (indirect impacts) or undergo reduction or oxidation itself (direct impacts).

In terms of hydrogen evolution reaction, indirect impacts (figure 1.7) occur with the nanoparticle colliding with an electrode surface held at a sufficiently negative overpotential, leading to proton

reduction on the nanoparticle surface.[116-118] When successful collision occurs, a current signal is generated and from this current spike, information regarding the kinetics of the system under investigation can be extracted. The main benefit of the technique is that detailed information on the heterogeneity and individual behaviour of particles can be determined, which is not possible with bulk methods. In this study, the technique will be used to investigate the HER kinetics at the nanoparticle level, allowing for a comparison with bulk methods.

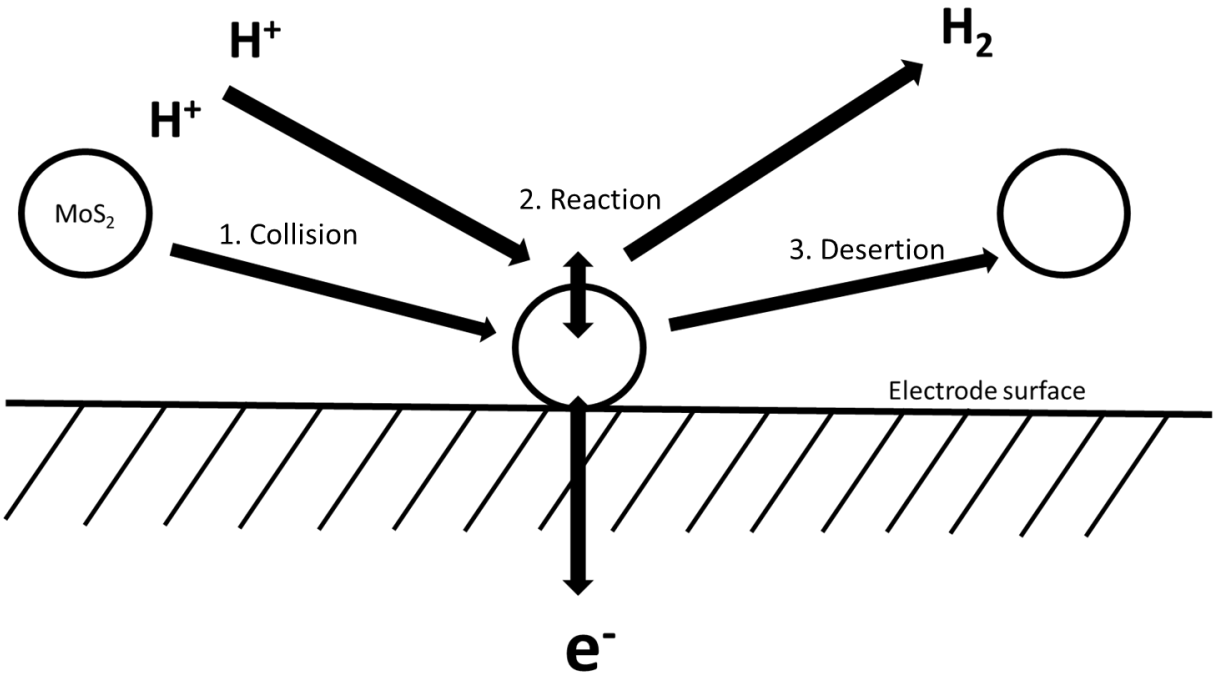

Figure 1.7. Illustration of a MoS_2 nanoparticle colliding with an electrode surface and acting as a surface for proton reduction. The process involves three main steps: (1) the nanoparticle collides with the electrode held at a sufficient potential, (2) protons on the nanoparticle surface are reduced to form hydrogen gas (H_2), and (3) the nanoparticle and the produced H_2 leave the electrode surface. This sequence illustrates the catalytic role of MoS_2 in the proton reduction reaction.

1.5 Research Aims and Objectives

The global push towards sustainable and renewable energy sources necessitates advancements in green energy technologies, with efficient hydrogen production being pivotal to this energy transition. Although platinum group metals are highly effective catalysts for the hydrogen evolution reaction, their scarcity and high cost drive the need for alternative materials that are both efficient and economically viable. Transition metal dichalcogenides have emerged as promising candidates for HER due to their unique properties and low costs compared to PGMs. Research on TMDs has evolved from initial studies on bulk materials to exploring few-layer TMDs, doping strategies, phase engineering, and heterostructuring to enhance catalytic activity. Despite these advancements, there is a significant gap in reporting the electrochemical rate constants and detailed kinetics, and the potential effects of mixing various TMDs for enhanced HER catalysis have not been thoroughly investigated. This study aims to fill these gaps by investigating TMDs to a further degree in order to enhance their HER electrocatalytic performance as well as determining the reaction kinetics due to these improved TMDs. The focus is on the hydrogen evolution reaction (HER) because it directly impacts hydrogen production efficiency and complements existing efforts to address the more kinetically challenging oxygen evolution reaction (OER), enabling a balanced and efficient water-splitting system.

This research aims to investigate the catalytic performance of bulk and nanoparticulate forms of transition metal dichalcogenides by utilizing impact electrochemistry to gain kinetic insights at the nanoscale. Additionally, the study will explore alternative synthesis methods for creating TMD heterostructures, with a focus on evaluating the stability of the resulting heterolayers and their effectiveness in the hydrogen evolution reaction (HER). The electrochemical rate constants and reaction kinetics of these enhanced TMDs will be studied and reported, providing a deeper understanding of their catalytic behaviours. Furthermore, the research will examine the potential synergistic effects of combining different TMDs to enhance HER catalytic activity.

1.6 Thesis Outline

- Chapter 2- Literature Review
- Chapter 3- Experimental Methods
- Chapter 4- Impact electrochemistry of MoS_2: electrocatalysis and hydrogen generation at low overpotentials
- Chapter 5- Electrochemically deposited transition metal dichalcogenide heterostructures as electrocatalysts: accelerated kinetics for the hydrogen evolution reaction
- Chapter 6- Novel electrocatalyst via mechanochemistry: binary & ternary mixed transition metal dichalcogenides
- Chapter 7- Conclusion and Outlook
- Chapter 8- Appendix

1.7 References

(1) Nieto, M. J. Whatever It Takes to Reach Net Zero Emissions Around 2050 and Limit Global Warming to 1.5C: The Cases of United States, China, European Union and Japan. *SSRN Electron. J. 2022*, https://doi.org/10.2139/ssrn.4007974.

(2) Masson-Delmotte, V.; Zhai, P.; Pörtner, H.-O.; Roberts, D.; Skea, J.; Shukla, P. R.; Pirani, A.; Moufouma-Okia, W.; Péan, C.; Pidcock, R.; Connors, S.; Matthews, J. B. R.; Chen, Y.; Zhou, X.; Gomis, M. I.; Lonnoy, E.; Maycock, T.; Tignor, M.; Waterfield, T. Global Warming of 1.5°C An IPCC Special Report on the Impacts of Global Warming of 1.5°C above Pre-Industrial Levels and Related Global Greenhouse Gas Emission Pathways, in the Context of Strengthening the Global Response to the Threat of Climate Change, Sustainable Development, and Efforts to Eradicate Poverty. *IPCC*, 2018, https://doi.org/10.1017/9781009157940

(3) Cassia, R.; Nocioni, M.; Correa-Aragunde, N.; Lamattina, L. Climate Change and the Impact of Greenhouse Gasses: CO_2 and NO, Friends and Foes of Plant Oxidative Stress. *Front. Plant Sci.* 2018, **9**, 273. https://doi.org/10.3389/fpls.2018.00273.

(4) Kweku, D.; Bismark, O.; Maxwell, A.; Desmond, K.; Danso, K.; Oti-Mensah, E.; Quachie, A.; Adormaa, B. Greenhouse Effect: Greenhouse Gases and Their Impact on Global Warming. *J. Sci. Res. Rep.* 2018, **17**, 1–9. https://doi.org/10.9734/jsrr/2017/39630.

(5) Yoro, K. O.; Daramola, M. O. CO_2 Emission Sources, Greenhouse Gases, and the Global Warming Effect. In *Advances in Carbon Capture: Methods, Technologies and Applications*; Woodhead Publishing, 2020, 3–28. https://doi.org/10.1016/B978-0-12-819657-1.00001-3.

(6) Osman, A. I.; Chen, L.; Yang, M.; Msigwa, G.; Farghali, M.; Fawzy, S.; Rooney, D. W.; Yap, P. S. Cost, Environmental Impact, and Resilience of Renewable Energy under a Changing Climate: A Review. *Environ. Chem. Lett.* 2023, **21**, 741–764. https://doi.org/10.1007/s10311-022-01532-8.

(7) Ang, T. Z.; Salem, M.; Kamarol, M.; Das, H. S.; Nazari, M. A.; Prabaharan, N. A Comprehensive Study of Renewable Energy Sources: Classifications, Challenges and Suggestions. *Energy Strategy Rev*. 2022, **43**, 100939. https://doi.org/10.1016/j.esr.2022.100939.

(8) Seminario-Córdova, R.; Rojas-Ortega, R. Renewable Energy Sources and Energy Production: A Bibliometric Analysis of the Last Five Years. *Sustainability* 2023, **15**, 10499. https://doi.org/10.3390/su151310499.

(9) Candra, O.; Chammam, A.; Alvarez, J. R. N.; Muda, I.; Aybar, H. The Impact of Renewable Energy Sources on the Sustainable Development of the Economy and Greenhouse Gas Emissions. *Sustainability* 2023, **15**, 214. https://doi.org/10.3390/su15032104.

(10) Neha; Rambeer, J. Renewable Energy Sources: A Review. *J. Phys.: Conf. Ser.* 2021, **1979**. https://doi.org/10.1088/1742-6596/1979/1/012023.

(11) Shahabuddin, M.; Alim, M. A.; Alam, T.; Mofijur, M.; Ahmed, S. F.; Perkins, G. A Critical Review on the Development and Challenges of Concentrated Solar Power Technologies. *Sustainable Energy Technol. Assess*. 2021, **47**, 101434. https://doi.org/10.1016/j.seta.2021.101434.

(12) Bouich, A.; Pradas, I. G.; Khan, M. A.; Khattak, Y. H. Opportunities, Challenges, and Future Prospects of the Solar Cell Market. *Sustainability* 2023, **15**, 15445. https://doi.org/10.3390/su152115445.

(13) Rahaman, K.; Hassan, Q. Prospects and Challenges of Wind Energy: A Comprehensive Anatomy. *International Conference on Mechanical Engineering*, Dhaka, December 2011.

(14) Roga, S.; Bardhan, S.; Kumar, Y.; Dubey, S. K. Recent Technology and Challenges of Wind Energy Generation: A Review. *Sustainable Energy Technol. Assess.* 2022, **52**, 102239. https://doi.org/10.1016/j.seta.2022.102239.

(15) Chen, Z. Challenges and Perspectives of Wind Energy Technology. *Wind* 2023, **3**, 545–547. https://doi.org/10.3390/wind3040030.

(16) Mitali, J.; Dhinakaran, S.; Mohamad, A. A. Energy Storage Systems: A Review. *Energy Storage Sav*. 2022, **1**,166–216. https://doi.org/10.1016/j.enss.2022.07.002.

(17) Yao, L.; Yang, B.; Cui, H.; Zhuang, J.; Ye, J.; Xue, J. Challenges and Progresses of Energy Storage Technology and Its Application in Power Systems. *J. Modern Power Sys. Clean Energy* 2016, **4**, 519–528. https://doi.org/10.1007/s40565-016-0248-x.

(18) Dehghani-Sanij, A. R.; Tharumalingam, E.; Dusseault, M. B.; Fraser, R. Study of Energy Storage Systems and Environmental Challenges of Batteries. *Renewable Sustainable Energy Rev*. 2019, **104**, 192–208. https://doi.org/10.1016/j.rser.2019.01.023.

(19) Staffell, I.; Scamman, D.; Velazquez Abad, A.; Balcombe, P.; Dodds, P. E.; Ekins, P.; Shah, N.; Ward, K. R. The Role of Hydrogen and Fuel Cells in the Global Energy System. *Energy Environ. Sci*. 2019, **12**, 463–491. https://doi.org/10.1039/c8ee01157e.

(20) Sazali, N.; Salleh, W. N. W.; Jamaludin, A. S.; Razali, M. N. M. New Perspectives on Fuel Cell Technology: A Brief Review. *Membranes*. 2020, **10**, 99. https://doi.org/10.3390/membranes10050099.

(21) Giorgi, L. Fuel Cells: Technologies and Applications. *Open Fuel Cells J.* 2013, **6**, 1–20. https://doi.org/10.2174/1875932720130719001.

(22) Jawad, N. H.; Yahya, A. A.; Al-Shathr, A. R.; Salih, H. G.; Rashid, K. T.; Al-Saadi, S.; Abdulrazak, A. A.; Salih, I. K.; Zrelli, A.; Alsalhy, Q. F. Fuel Cell Types, Properties of Membrane, and Operating Conditions: A Review. *Sustainability* 2022, **14**, 14653. https://doi.org/10.3390/su142114653.

(23) Eg&g Technical Services Inc. *Fuel Cell Handbook (Seventh Edition)*, Lulu Press 2004.

(24) Yatoo, M. A.; Habib, F.; Malik, A. H.; Qazi, M. J.; Ahmad, S.; Ganayee, M. A.; Ahmad, Z. Solid-Oxide Fuel Cells: A Critical Review of Materials for Cell Components. *MRS Commun*. 2023, **13**, 378–384. https://doi.org/10.1557/s43579-023-00371-0.

(25) Hassan, Q.; Azzawi, I. D. J.; Sameen, A. Z.; Salman, H. M. Hydrogen Fuel Cell Vehicles: Opportunities and Challenges. *Sustainability* 2023, **15**, 11501. https://doi.org/10.3390/su151511501.

(26) Muthukumar, M.; Rengarajan, N.; Velliyangiri, B.; Omprakas, M. A.; Rohit, C. B.; Raja, U. K. The Development of Fuel Cell Electric Vehicles - A Review. *Mater. Today: Proc.* 2021, **45**, 1181–1187. https://doi.org/10.1016/j.matpr.2020.03.679.

(27) Hassanpouryouzband, A.; Joonaki, E.; Edlmann, K.; Heinemann, N.; Yang, J. Thermodynamic and Transport Properties of Hydrogen Containing Streams. *Sci. Data* 2020, **7**, 222. https://doi.org/10.1038/s41597-020-0568-6.

(28) Keçebaş, A.; Kayfeci, M. Chapter 1-Hydrogen Properties. Francesco Calise, Massimo Dentice D'Accadia, Massimo Santarelli, Andrea Lanzini, Domenico Ferrero, *Solar Hydrogen Production: Processes, Systems and Technologies*, Academic Press, 2019, 3–29. https://doi.org/10.1016/B978-0-12-814853-2.00001-1.

(29) Momirlan, M.; Veziroglu, T. N. The Properties of Hydrogen as Fuel Tomorrow in Sustainable Energy System for a Cleaner Planet. *Int. J. Hydrogen Energy* 2005, **30**, 795–802. https://doi.org/10.1016/j.ijhydene.2004.10.011.

(30) Marbán, G.; Valdés-Solís, T. Towards the Hydrogen Economy? *Int. J. Hydrogen Energy* 2007, **32**, 1625–1637. https://doi.org/10.1016/j.ijhydene.2006.12.017.

(31) Dutta, S. A Review on Production, Storage of Hydrogen and Its Utilization as an Energy Resource. *J. Ind. Eng. Chem.* 2014, **20**, 1148–1156. https://doi.org/10.1016/j.jiec.2013.07.037.

(32) Hennicke, P.; Fischedick, M. Towards Sustainable Energy Systems: The Related Role of Hydrogen. *Energy Policy* 2006, **34**, 1260–1270. https://doi.org/10.1016/j.enpol.2005.12.016.

(33) Dunn, S. Hydrogen Futures: Toward a Sustainable Energy System. *Int. J. Hydrogen Energy* 2002, **27**, 235-264. www.elsevier.com/locate/ijhydene.

(34) Zeng, K.; Zhang, D. Recent Progress in Alkaline Water Electrolysis for Hydrogen Production and Applications. *Prog. Energy Combust. Sci.* 2010, **36**, 307–326. https://doi.org/10.1016/j.pecs.2009.11.002.

(35) Ni, M.; Leung, M. K. H.; Sumathy, K.; Leung, D. Y. C. Potential of Renewable Hydrogen Production for Energy Supply in Hong Kong. *Int. J. Hydrogen Energy* 2006, **31**, 1401–1412. https://doi.org/10.1016/j.ijhydene.2005.11.005.

(36) El-Shafie, M.; Kambara, S.; Hayakawa, Y. Hydrogen Production Technologies Overview. *J. Power Energy Eng.* 2019, **7**, 107–154. https://doi.org/10.4236/jpee.2019.71007.

(37) Gunawardane, K. Evolution of Hydrogen Energy and Its Potential Opportunities around the Globe. In *Hydrogen Energy Conversion and Management*, Khan, M.; Azad A. K.; Than Oo, A. M. Elsevier, 2023, 3–33. https://doi.org/10.1016/B978-0-443-15329-7.00007-7.

(38) Kayfeci, M.; Keçebaş, A.; Bayat, M. Hydrogen Production. In *Solar Hydrogen Production: Processes, Systems and Technologies*, Calise, F.; D'Accadia, M. D.; Santarelli, M.; Lanzini, A.; Ferrero, D. Academic Press, 2019, 45–83. https://doi.org/10.1016/B978-0-12-814853-2.00003-5.

(39) Fakeeha, A.; Ibrahim, A. A.; Aljuraywi, H.; Alqahtani, Y.; Alkhodair, A.; Alswaidan, S.; Abasaeed, A. E.; Kasim, S. O.; Mahmud, S.; Al-Fatesh, A. S. Hydrogen Production by Partial Oxidation Reforming of Methane over Ni Catalysts Supported on High and Low Surface Area Alumina and Zirconia. *Processes* 2020, **8**, 499. https://doi.org/10.3390/PR8050499.

(40) Wu, Q. Analysis of Several Main Hydrogen Production Technologies. *IOP Conference Series: Earth Environ. Sci.* 2021, **1011**, 012005. https://doi.org/10.1088/1755-1315/1011/1/012005.

(41) Dincer, I. Green Methods for Hydrogen Production. *Int. J. Hydrogen Energy*, 2012, **37**, 1954–1971. https://doi.org/10.1016/j.ijhydene.2011.03.173.

(42) Rubinsin, N. J.; Karim, N. A.; Timmiati, S. N.; Lim, K. L.; Isahak, W. N. R. W.; Pudukudy, M. An Overview of the Enhanced Biomass Gasification for Hydrogen Production. *Int. J. Hydrogen Energy* 2024, **49**, 1139–1164. https://doi.org/10.1016/j.ijhydene.2023.09.043.

(43) Song, H.; Yang, G.; Xue, P.; Li, Y.; Zou, J.; Wang, S.; Yang, H.; Chen, H. Recent Development of Biomass Gasification for H_2 Rich Gas Production. *Appl. Energy Combust. Sci.* 2022, **10**, 100059. https://doi.org/10.1016/j.jaecs.2022.100059.

(44) Chatenet, M.; Pollet, B. G.; Dekel, D. R.; Dionigi, F.; Deseure, J.; Millet, P.; Braatz, R. D.; Bazant, M. Z.; Eikerling, M.; Staffell, I.; Balcombe, P.; Shao-Horn, Y.; Schäfer, H. Water Electrolysis: From Textbook Knowledge to the Latest Scientific Strategies and Industrial Developments. *Chem. Soc. Rev*. 2022, **51**, 4583–4762. https://doi.org/10.1039/d0cs01079k.

(45) Shiva Kumar, S.; Lim, H. An Overview of Water Electrolysis Technologies for Green Hydrogen Production. *Energy Rep*. 2022, **8**,13793–13813. https://doi.org/10.1016/j.egyr.2022.10.127.

(46) Wang, S.; Lu, A.; Zhong, C. J. Hydrogen Production from Water Electrolysis: Role of Catalysts. *Nano Convergence* 2021, **8**, 4. https://doi.org/10.1186/s40580-021-00254-x.

(47) Thomassen, M. S.; Reksten, A. H.; Barnett, A. O.; Khoza, T.; Ayers, K. PEM Water Electrolysis. In *Electrochemical Power Sources: Fundamentals, Systems, and Applications Hydrogen Production by Water Electrolysis*, Smolinka, T.; Garche, J., Elsevier, 2022, 199–228. https://doi.org/10.1016/B978-0-12-819424-9.00013-6.

(48) Zhang, F.; Zhao, P.; Niu, M.; Maddy, J. The Survey of Key Technologies in Hydrogen Energy Storage. *Int. J. Hydrogen Energy* 2016, **41**, 14535–14552. https://doi.org/10.1016/j.ijhydene.2016.05.293.

(49) Chisholm, G.; Cronin, L. Hydrogen from Water Electrolysis. In *Storing Energy: With Special Reference to Renewable Energy Sources*, Letcher, T. M., Elsevier, 2016, 315–343. https://doi.org/10.1016/B978-0-12-803440-8.00016-6.

(50) El-Shafie, M.; Kambara, S.; Hayakawa, Y. Hydrogen Production Technologies Overview. *J. Power Energy Eng.* 2019, **07**, 107–154. https://doi.org/10.4236/jpee.2019.71007.

(51) Ursúa, A.; Gandía, L. M.; Sanchis, P. Hydrogen Production from Water Electrolysis: Current Status and Future Trends. In *Proceedings of the IEEE*, 2012, **100**, 410–426. https://doi.org/10.1109/JPROC.2011.2156750.

(52) Hino, R.; Haga, K.; Aita, H.; Sekita, K. 38. R&D on Hydrogen Production by High-Temperature Electrolysis of Steam. *Nucl. Eng. Des.* 2004, **233**, 363–375. https://doi.org/10.1016/j.nucengdes.2004.08.029.

(53) Utgikar, V.; Thiesen, T. Life Cycle Assessment of High Temperature Electrolysis for Hydrogen Production via Nuclear Energy. *Int. J. Hydrogen Energy* 2006, **31**, 939–944. https://doi.org/10.1016/j.ijhydene.2005.07.001.

(54) Suen, N. T.; Hung, S. F.; Quan, Q.; Zhang, N.; Xu, Y. J.; Chen, H. M. Electrocatalysis for the Oxygen Evolution Reaction: Recent Development and Future Perspectives. *Chem. Soc. Rev*. 2017, **46**, 337–365. https://doi.org/10.1039/c6cs00328a.

(55) Sardar, K.; Petrucco, E.; Hiley, C. I.; Sharman, J. D. B.; Wells, P. P.; Russell, A. E.; Kashtiban, R. J.; Sloan, J.; Walton, R. I. Water-Splitting Electrocatalysis in Acid Conditions Using Ruthenate-Iridate Pyrochlores. *Angew. Chem.- Inter. Edi.* 2014, **53**, 10960–10964. https://doi.org/10.1002/anie.201406668.

(56) Strmcnik, D.; Uchimura, M.; Wang, C.; Subbaraman, R.; Danilovic, N.; Van Der Vliet, D.; Paulikas, A. P.; Stamenkovic, V. R.; Markovic, N. M. Improving the Hydrogen Oxidation Reaction Rate by Promotion of Hydroxyl Adsorption. *Nat. Chem.* 2013, **5**, 300–306. https://doi.org/10.1038/nchem.1574.

(57) Dubouis, N.; Grimaud, A. The Hydrogen Evolution Reaction: From Material to Interfacial Descriptors. *Chem. Sci*. 2019, **10**, 9165–9181. https://doi.org/10.1039/c9sc03831k.

(58) Conway, B. E.; Tilak, B. V. Interfacial Processes Involving Electrocatalytic Evolution and Oxidation of H_2, and the Role of Chemisorbed H. *Electrochim. Acta* 2002, **47**, 3571-3594.

(59) Mahmood, N.; Yao, Y.; Zhang, J. W.; Pan, L.; Zhang, X.; Zou, J. J. Electrocatalysts for Hydrogen Evolution in Alkaline Electrolytes: Mechanisms, Challenges, and Prospective Solutions. *Adv. Sci*. 2018, 5, 1700464. https://doi.org/10.1002/advs.201700464.

(60) Danilovic, N.; Subbaraman, R.; Strmcnik, D.; Stamenkovic, V. R.; Markovic, N. M. Electrocatalysis of the HER in Acid and Alkaline Media. *J. Serb. Chem. Soc.* 2013, **78**, 2007–2015. https://doi.org/10.2298/JSC131118136D.

(61) Tan, S. M.; Pumera, M. Bottom-up Electrosynthesis of Highly Active Tungsten Sulfide (WS_{3-x}) Films for Hydrogen Evolution. *ACS Appl. Mater. Interfaces* 2016, **8**, 3948–3957. https://doi.org/10.1021/acsami.5b11109.

(62) Li, Y.; Wang, H.; Xie, L.; Liang, Y.; Hong, G.; Dai, H. MoS_2 Nanoparticles Grown on Graphene: An Advanced Catalyst for the Hydrogen Evolution Reaction. *J. Am. Chem. Soc.* 2011, **133**, 7296–7299. https://doi.org/10.1021/ja201269b.

(63) Trasatti, S. Work function, electronegativity, and electrochemical behaviour of metals. *J. Electroanal. Chem.* 1972, **39**, 163-184.

(64) Cook, T. R.; Dogutan, D. K.; Reece, S. Y.; Surendranath, Y.; Teets, T. S.; Nocera, D. G. Solar Energy Supply and Storage for the Legacy and Nonlegacy Worlds. *Chem. Rev.* 2010, **110**, 6474–6502. https://doi.org/10.1021/cr100246c.

(65) Sheng, W.; Myint, M.; Chen, J. G.; Yan, Y. Correlating the Hydrogen Evolution Reaction Activity in Alkaline Electrolytes with the Hydrogen Binding Energy on Monometallic Surfaces. *Energy Environ. Sci.* 2013, **6**, 1509–1512. https://doi.org/10.1039/c3ee00045a.

(66) Morales-Guio, C. G.; Stern, L. A.; Hu, X. Nanostructured Hydrotreating Catalysts for Electrochemical Hydrogen Evolution. *Chem. Soc. Rev.* 2014, **43**, 6555–6569. https://doi.org/10.1039/c3cs60468c.

(67) Pomerantseva, E.; Resini, C.; Kovnir, K.; Kolen'ko, Y. V. Emerging Nanostructured Electrode Materials for Water Electrolysis and Rechargeable beyond Li-Ion Batteries. *Adv. Phys.* 2017, **2**, 211–253. https://doi.org/10.1080/23746149.2016.1273796.

(68) Calle-Vallejo, F.; Koper, M. T. M. First-Principles Computational Electrochemistry: Achievements and Challenges. *Electrochim. Acta* 2012, **84**, 3–11. https://doi.org/10.1016/j.electacta.2012.04.062.

(69) Faber, M. S.; Jin, S. Earth-Abundant Inorganic Electrocatalysts and Their Nanostructures for Energy Conversion Applications. *Energy Environ. Sci*. 2014, **7**, 3519–3542. https://doi.org/10.1039/c4ee01760a.

(70) Greeley, J.; Markovic, N. M. The Road from Animal Electricity to Green Energy: Combining Experiment and Theory in Electrocatalysis. *Energy Environ. Sci*. 2012, **5**, 9246–9256. https://doi.org/10.1039/c2ee21754f.

(71) Xie, L.; Liu, Q.; Shi, X.; Asiri, A. M.; Luo, Y.; Sun, X. Superior Alkaline Hydrogen Evolution Electrocatalysis Enabled by an Ultrafine PtNi Nanoparticle-Decorated Ni Nanoarray with Ultralow Pt Loading. *Inorg. Chem. Front.* 2018, **5**, 1365–1369. https://doi.org/10.1039/c8qi00120k.

(72) Khan, M. A.; Zhao, H.; Zou, W.; Chen, Z.; Cao, W.; Fang, J.; Xu, J.; Zhang, L.; Zhang, J. Recent Progresses in Electrocatalysts for Water Electrolysis. *Electrochem. Energy Rev*. 2018, **1**, 483–530. https://doi.org/10.1007/s41918-018-0014-z.

(73) Wu, H.; Feng, C.; Zhang, L.; Zhang, J.; Wilkinson, D. P. Non-Noble Metal Electrocatalysts for the Hydrogen Evolution Reaction in Water Electrolysis. *Electrochem. Energy Rev*. 2021, **4**, 473–507. https://doi.org/10.1007/s41918-020-00086-z.

(74) Ali, A.; Shen, P. K. Recent Progress in Graphene-Based Nanostructured Electrocatalysts for Overall Water Splitting. *Electrochem. Energy Rev*. 2020, **3**, 370–394. https://doi.org/10.1007/s41918-020-00066-3.

(75) Kitchin, J. R.; Nørskov, J. K.; Barteau, M. A.; Chen, J. G. Trends in the Chemical Properties of Early Transition Metal Carbide Surfaces: A Density Functional Study. *Catal. Today* 2005, **105**, 66–73. https://doi.org/10.1016/j.cattod.2005.04.008.

(76) Vrubel, H.; Hu, X. Molybdenum Boride and Carbide Catalyze Hydrogen Evolution in Both Acidic and Basic Solutions. *Angew. Chem., Int. Ed.* 2012, **51**, 12703–12706. https://doi.org/10.1002/anie.201207111.

(77) Liu, P.; Rodriguez, J. A. Catalysts for Hydrogen Evolution from the [NiFe] Hydrogenase to the Ni_2P(001) Surface: The Importance of Ensemble Effect. *J. Am. Chem. Soc.* 2005, **127**, 14871–14878. https://doi.org/10.1021/ja0540019.

(78) Duan, J.; Chen, S.; Jaroniec, M.; Qiao, S. Z. Porous C_3N_4 Nanolayers@N-Graphene Films as Catalyst Electrodes for Highly Efficient Hydrogen Evolution. *ACS Nano* 2015, **9**, 931–940. https://doi.org/10.1021/nn506701x.

(79) Zhang, L.; Xiao, J.; Wang, H.; Shao, M. Carbon-Based Electrocatalysts for Hydrogen and Oxygen Evolution Reactions. *ACS Catal.* 2017, **7**, 7855–7865. https://doi.org/10.1021/acscatal.7b02718.

(80) Shervedani, R. K.; Amini, A. Sulfur-Doped Graphene as a Catalyst Support: Influences of Carbon Black and Ruthenium Nanoparticles on the Hydrogen Evolution Reaction Performance. *Carbon* 2015, **93**, 762–773. https://doi.org/10.1016/j.carbon.2015.05.088.

(81) Zheng, Y.; Jiao, Y.; Zhu, Y.; Li, L. H.; Han, Y.; Chen, Y.; Du, A.; Jaroniec, M.; Qiao, S. Z. Hydrogen Evolution by a Metal-Free Electrocatalyst. *Nat. Commun.* 2014, **5**, 3783. https://doi.org/10.1038/ncomms4783.

(82) Wang, J.; Kong, H.; Zhang, J.; Hao, Y.; Shao, Z.; Ciucci, F. Carbon-Based Electrocatalysts for Sustainable Energy Applications. *Prog. Mater. Sci*. 2021, **116**, 100717. https://doi.org/10.1016/j.pmatsci.2020.100717.

(83) Duan, J.; Chen, S.; Jaroniec, M.; Qiao, S. Z. Heteroatom-Doped Graphene-Based Materials for Energy-Relevant Electrocatalytic Processes. *ACS Catal.* 2015, **5**, 5207–5234. https://doi.org/10.1021/acscatal.5b00991.

(84) Zheng, Y. R.; Gao, M. R.; Yu, Z. Y.; Gao, Q.; Gao, H. L.; Yu, S. H. Cobalt Diselenide Nanobelts Grafted on Carbon Fiber Felt: An Efficient and Robust 3D Cathode for Hydrogen Production. *Chem. Sci.* 2015, **6**, 4594–4598. https://doi.org/10.1039/c5sc01335f.

(85) Mohammadi, A. V.; Rosen, J.; Gogotsi, Y. The World of Two-Dimensional Carbides and Nitrides (MXenes). *Science* 2021, **372**, 1165. https://doi.org/10.1126/science.abf1581.

(86) Naguib, M.; Kurtoglu, M.; Presser, V.; Lu, J.; Niu, J.; Heon, M.; Hultman, L.; Gogotsi, Y.; Barsoum, M. W. Two-Dimensional Nanocrystals Produced by Exfoliation of Ti_3AlC_2. *Adv. Mater.* 2011, **23**, 4248–4253. https://doi.org/10.1002/adma.201102306.

(87) Naguib, M.; Mochalin, V. N.; Barsoum, M. W.; Gogotsi, Y. 25th Anniversary Article: MXenes: A New Family of Two-Dimensional Materials. *Adv. Mater.* 2014, **26**, 992–1005. https://doi.org/10.1002/adma.201304138.

(88) Naguib, M.; Mashtalir, O.; Carle, J.; Presser, V.; Lu, J.; Hultman, L.; Gogotsi, Y.; Barsoum, M. W. Two-Dimensional Transition Metal Carbides. *ACS Nano* 2012, **6**, 1322–1331. https://doi.org/10.1021/nn204153h.

(89) Bai, S.; Yang, M.; Jiang, J.; He, X.; Zou, J.; Xiong, Z.; Liao, G.; Liu, S. Recent Advances of MXenes as Electrocatalysts for Hydrogen Evolution Reaction. *npj 2D Mater. Appl.* 2021, **5**, 78. https://doi.org/10.1038/s41699-021-00259-4.

(90) Yuan, W.; Cheng, L.; An, Y.; Wu, H.; Yao, N.; Fan, X.; Guo, X. MXene Nanofibers as Highly Active Catalysts for Hydrogen Evolution Reaction. *ACS Sustain. Chem. Eng.* 2018, **6**, 8976–8982. https://doi.org/10.1021/acssuschemeng.8b01348.

(91) Chia, X.; Eng, A. Y. S.; Ambrosi, A.; Tan, S. M.; Pumera, M. Electrochemistry of Nanostructured Layered Transition-Metal Dichalcogenides. *Chem. Rev*. 2015, **115**, 11941–11966. https://doi.org/10.1021/acs.chemrev.5b00287.

(92) Chia, X.; Pumera, M. Layered Transition Metal Dichalcogenide Electrochemistry: Journey across the Periodic Table. *Chem. Soc. Rev*. 2018, **47**, 5602–5613. https://doi.org/10.1039/c7cs00846e.

(93) Bard, A. J.; Faulkner, L. R. *Electrochemical Methods: Fundamentals and Applications*, John Wiley & Sons, New York, 2000.

(94) Fisher, A. C. *Electrode Dynamics*, Oxford University Press, New York, 1996.

(95) Compton, R. G.; Banks, C. E. *Understanding Voltammetry*, Third., World Scientific Publishing Europe Ltd, Singapore, 2018.

(96) Elgrishi, N.; Rountree, K. J.; McCarthy, B. D.; Rountree, E. S.; Eisenhart, T. T.; Dempsey, J. L. A Practical Beginner's Guide to Cyclic Voltammetry. *J. Chem. Educ.* 2018, **95**, 197–206. https://doi.org/10.1021/acs.jchemed.7b00361.

(97) Komorsky-Lovrić, Š. Working Electrodes. In *Electroanalytical Methods*, Scholz. F. Springer Berlin Heidelberg, Berlin, 2010, 273–290. https://doi.org/10.1007/978-3-642-02915-8_14.

(98) Bekmezci, M.; Altuner, E. E.; Erduran, V.; Bayat, R.; Isik, I.; Şen, F. Fundamentals of Electrochemistry. In *Nanomaterials for Direct Alcohol Fuel Cells: Characterization, Design, and Electrocatalysis*, Sen, F. Elsevier, 2021, 1–15. https://doi.org/10.1016/B978-0-12-821713-9.00023-8.

(99) Swayer, D. T.; Sobkowiak, A.; Roberts, J. L. J. *Electrochemistry for Chemists*, 2nd ed., John Wiley & Sons Inc, New York, 1995.

(100) Compton, R. G.; Sanders, G. H. W. *Electrode Potentials*, Oxford University Press, Oxford, 1996.

(101) Batchelor-McAuley, C. Defining the Onset Potential. *Curr. Opin. Electrochem*. 2023, **37**, 101176. https://doi.org/10.1016/j.coelec.2022.101176.

(102) Martinsen, Ø. G.; Heiskanen, A. Electrodes. In *Bioimpedance and Bioelectricity Basics*, Elsevier, 2023, 175–248. https://doi.org/10.1016/B978-0-12-819107-1.00005-4.

(103) Wu, J. Understanding the Electric Double-Layer Structure, Capacitance, and Charging Dynamics. *Chem. Rev*. 2022, **122**, 10821–10859. https://doi.org/10.1021/acs.chemrev.2c00097.

(104) Liu, N.; Chen, R.; Wan, Q. Recent Advances in Electric-Double-Layer Transistors for Bio-Chemical Sensing Applications. *Sensors* 2019, **19**, 3425. https://doi.org/10.3390/s19153425.

(105) Zhang, L.; Zhao, X. S. Carbon-Based Materials as Supercapacitor Electrodes. *Chem. Soc. Rev.* 2009, **38**, 2520–2531. https://doi.org/10.1039/b813846j.

(106) Batchelor-McAuley, C.; Li, D.; Compton, R. G. Mass-Transport-Corrected Transfer Coefficients: A Fully General Approach. *ChemElectroChem.* 2020, **7**, 3844–3851. https://doi.org/10.1002/celc.202001107.

(107) Compton, R. G.; Laborda, E.; Ward, K. R. *Understanding Voltammetry: Simulation of Electrode Processes*. World Scientific Publishing, London, 2018.

(108) Tyrrell, H. J. V. The Origin and Present Status of Fick's Diffusion Law. *J. Chem. Educ*.1964, **41**, 397-400.

(109) Yamada, H.; Yoshii, K.; Asahi, M.; Chiku, M.; Kitazumi, Y. Cyclic Voltammetry Part 1: Fundamentals†. *Electrochemistry* 2022, **90**, 102005. https://doi.org/10.5796/ELECTROCHEMISTRY.22-66082.

(110) Wang, J.; Zhao, C. X.; Liu, J. N.; Ren, D.; Li, B. Q.; Huang, J. Q.; Zhang, Q. Quantitative Kinetic Analysis on Oxygen Reduction Reaction: A Perspective. *Nano Mater. Sci.* 2021, **3**, 313–318. https://doi.org/10.1016/j.nanoms.2021.03.006.

(111) Pumera, M. Impact Electrochemistry: Measuring Individual Nanoparticles. *ACS Nano*. 2014, **8**, 7555–7558. https://doi.org/10.1021/nn503831r.

(112) Shan Lim, C.; Min Tan, S.; Sofer, Z.; Pumera, M. Impact Electrochemistry of Layered Transition Metal Dichalcogenides. *ACS Nano* 2015, **9**, 8474-8483.

(113) Keal, M. E.; Courtney, J. M.; Rees, N. V. Redox Electrochemistry of Mn(II) via Carbon Black Nanoparticle Impacts. *J. Phys. Chem. C* 2023, **127**, 13380–13388. https://doi.org/10.1021/acs.jpcc.3c02964.

(114) Keal, M. E.; Rees, N. V. Recent Advances in Nanomaterial Fabrication and Electrocatalysis Applications of Single-Entity Nano-Impact Electrochemistry. *Curr. Opin. Electrochem*. 2024, **45**, 101525. https://doi.org/10.1016/j.coelec.2024.101525.

(115) Giovanni, M.; Ambrosi, A.; Sofer, Z.; Pumera, M. Impact Electrochemistry of Individual Molybdenum Nanoparticles. *Electrochem. Commun.* 2015, **56**, 16–19. https://doi.org/10.1016/j.elecom.2015.04.002.

(116) Azimzadeh Sani, M.; Tschulik, K. Nanoparticle Impact Electrochemistry. *Front. Nanosci*. 2021 **18**, 203–252. https://doi.org/10.1016/B978-0-12-820055-1.00007-1.

(117) Xiao, X.; Bard, A. J. Observing Single Nanoparticle Collisions at an Ultramicroelectrode by Electrocatalytic Amplification. *J. Am. Chem. Soc.* 2007, **129**, 9610–9612. https://doi.org/10.1021/ja072344w.

(118) Zhou, Y. G.; Rees, N. V.; Compton, R. G. The Electrochemical Detection and Characterization of Silver Nanoparticles in Aqueous Solution. *Angew. Chem., Int. Ed.* 2011, **50**, 4219–4221. https://doi.org/10.1002/anie.201100885.

2 Literature review

This chapter introduces transition metal dichalcogenides by touching on their background, structural properties, and their applications. It also investigates how they are synthesised as well as their electrocatalytic activity for the hydrogen evolution reaction, focusing mostly on what makes them suitable for this application and how they compare to other electrocatalysts. Lastly, strategies used to enhance the catalytic activities of TMDs by exposing more active edge sites, activating the basal plane sites and improving electronic properties are explored.

2.1 Transition Metal Dichalcogenides: Background

Green energy technologies are increasingly attracting attention because of the move away from methods that emit large amounts of carbon dioxide and other pollutants. A critical element of these green technologies is the use of catalyst materials, with platinum group metals (PGMs) being the most prevalent. However, their high cost and limited availability have driven research into alternatives, leading to the development of various catalytic materials, including transition metal dichalcogenides (TMDs). TMDs have important applications in energy storage, semiconductors, and photo- and electrocatalysis, particularly in catalysing the hydrogen evolution reaction (HER).[1-4] TMDs are a class of materials composed of transition metals and chalcogen elements (sulfur, selenium, tellurium etc) with the general formula MX_2, where M is a transition metal and X is a chalcogen.[5,6] They have garnered significant interest due to their unique chemical, physical and electronic properties. These have a two-dimensional tri-layered crystalline structure similar to that of graphite, with the layers held together by weak van der Waals forces (vdW).[5] This kind of structure allows them to be easily exfoliated into thin layers or even monolayers for various applications.

The individual tri-layers consist of three atomic planes with a typical thickness of 6-7 Å, featuring a hexagonally packed plane of metal atoms positioned between two planes of chalcogen atoms (figure 2.1).[7] The local coordination of the metal atoms within the tri-layer can either be trigonal prismatic or octahedral as shown in figure 2.1. The tri-layers are stacked together to form the bulk structural forms

of the TMDs, and these can exist in three different polymorphs being the 1*T* (trigonal), 2*H* (hexagonal) and the 3*R* (rhombohedral) forms.[7-9] TMDs can exist in different phases and can be converted from one phase to the other. For example, MoS_2 can exist as 1*T*-MoS_2 or as 2*H*-MoS_2 and it can be transformed to either phase via intralayer atomic gliding.[10,11] 1*T*-MoS_2 is thermodynamically unstable, and it will gradually transform to the more stable 2*H*-MoS_2 phase.[7,9] These phases have different electronic properties, that is, 1*T*-MoS_2 is metallic and more active catalyst for HER than 2*H*-MoS_2 which is semiconducting.[12-14] The altered electronic and physical properties resulting from phase transformations make TMDs particularly intriguing as HER electrocatalysts. This opens up numerous possibilities for modifying these properties to enhance the HER activities of the resulting materials.

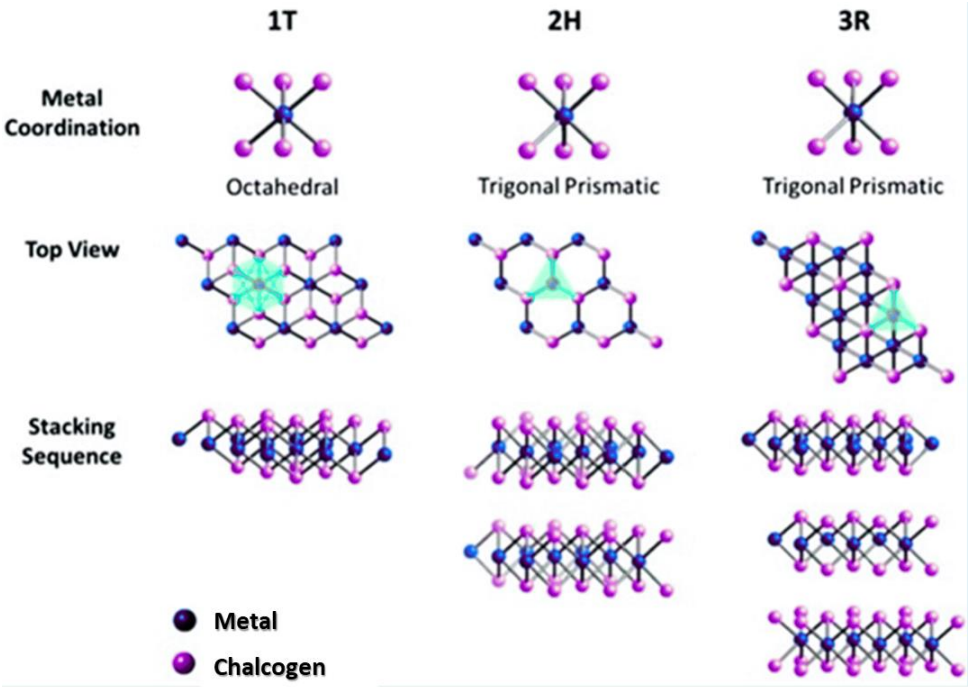

Figure 2.1. Metal coordination and stacking sequences of transition metal dichalcogenides. Reproduced from ref [10,11]

The phases of TMDs are determined by their electronic properties, which are influenced by the filling of the non-bonding d-bands for groups 4 to 10 TMDs. When these d-band orbitals are partially filled, TMDs exhibit metallic properties. Conversely, when the d-band orbitals are fully filled, TMDs display semiconducting properties.[9,15] The partial filling allows for free movement of electrons, contributing to high electrical conductivity while the fully occupied d-bands leads to a bandgap between the valence

and conduction bands, restricting electron flow and enabling semiconducting behaviour. XiaoBo et al investigated the energy band structure of different phases of MoS_2 and this is illustrated in figure 2.2.[16] For the 2*H* phase, an indirect band gap of 0.93 eV was determined, which was smaller than the experimentally calculated one of 1.29 eV.[16,17] The valence band maximum (VBM) is located at Γ, while the conduction band minimum (CBM) is positioned halfway between Γ and K for the 2*H* phase in figure 2.2. The 3R phase also has an indirect band gap of 0.86 eV, but the VBM is shifted from Γ to A, and the CBM moves from midway between Γ and K to H, due to the band folding effect caused by the increased stacking periodicity. Unlike the 2*H* and 3*R* phases, the 1*T* phase exhibits metallic characteristics.

The different phases of TMDs make them versatile for various applications: their 2*H*-phase properties make them suitable as semiconductors, their high surface area makes them ideal for supercapacitors in energy storage, and their tunable and direct bandgaps in monolayer form (1*T*-phase) make them excellent for optoelectronics and photovoltaic cells.[13,15,18-20] Lastly, the electronic structure, high surface area, stability and durability and the presence of catalytic active sites makes TMDs effective electrocatalysts for the hydrogen evolution reaction.

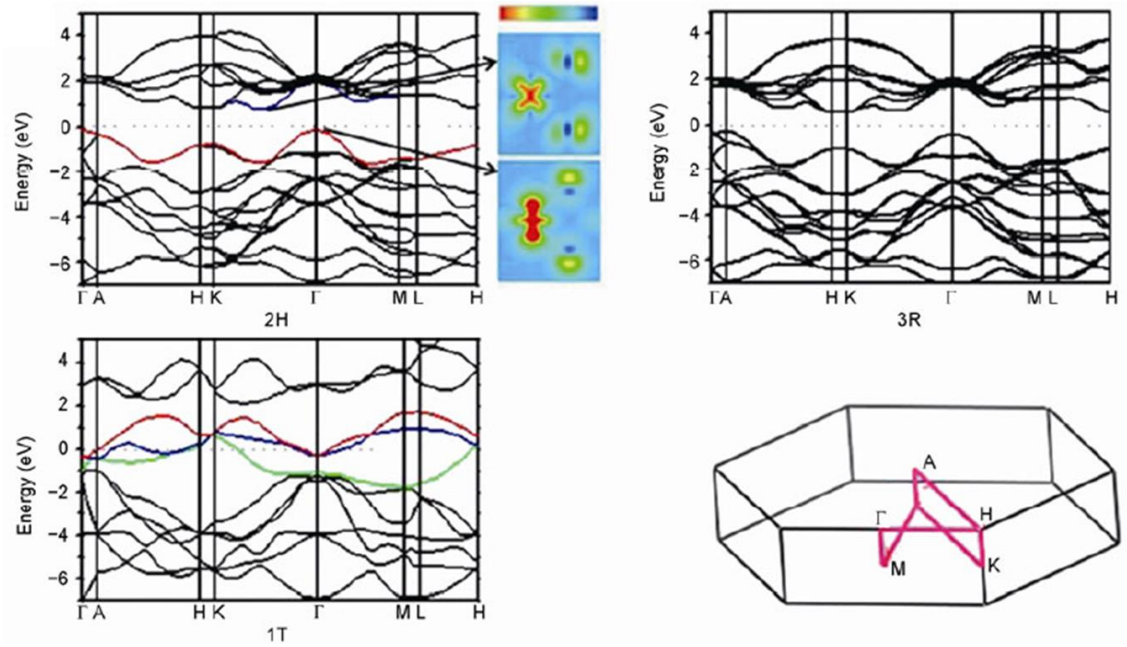

Figure 2.2 The energy band structures of the 2H, 3R, and 1T phases of MoS2 across the high-symmetry points. Reproduced from ref [16].

2.2 Transition Metal Dichalcogenide electrocatalysts for HER

TMDs have active edge sites that are highly reactive and provide efficient catalytic activity for HER.[5,21-23] These edge sites provide a favourable environment for the adsorption and reduction of protons which makes it possible for TMDs to act as electrocatalysts for the hydrogen evolution reaction. Research on MoS_2 has aimed to identify the nature of its active sites using scanning tunnelling microscopy (STM) and catalytic performance testing.[24] The findings indicated a correlation between the reaction rate and the edges of the sample/electrocatalyst, rather than its area, suggesting that the edges of MoS_2 are the catalytically active sites for HER and this has been proven for other TMDs such as WS_2, $MoSe_2$ and WSe_2.[25,26] The basal planes of the TMD and more especially for the 2*H* phases, are relatively inert compared to the edge sites. However, modifying the basal planes can enhance their catalytic activity thereby improving the overall activity of the TMD for HER.[27-29]

Several TMDs have been explored as potential HER electrocatalysts and the most widely researched is molybdenum disulfide (MoS_2), which has demonstrated promise due to its stability and high catalytic activity for HER.[12,30-32] Similarly, molybdenum diselenide ($MoSe_2$), with its narrow bandgap and low Gibbs energy, is also well-suited for HER.[33-36] Metallic tungsten diselenide (WSe_2) has also been reported to exhibit improved electrocatalytic activity for the hydrogen evolution reaction (HER). Additionally, WSe_2 has demonstrated excellent long-term durability, maintaining its performance over extended periods.[37] This combination of high activity and stability makes it a promising candidate for efficient and durable HER electrocatalysis. The reported enhanced HER activities of various TMDs as well as their large abundance and being relatively cheap, is what makes them much more promising as HER electrocatalysts compared to other earth-abundant electrocatalysts with the possibility of replacing PGMs. Among these, molybdenum disulfide (MoS_2) has been reported to have a hydrogen binding energy of 0.08 eV at 50% hydrogen coverage, which is nearly zero.[32,38] This binding energy is comparable to that of active noble metal catalysts like platinum (Pt), highlighting the potential of MoS_2 as an effective and economical HER electrocatalyst.

2.3 Preparation methods of TMDs

Several methods have been reported for preparing TMDs, each with its own advantages and disadvantages. These synthesis techniques can produce TMDs with varying levels of HER catalytic activity and different physical forms, ranging from bulk structures to monolayers, depending on the intended application. The following sections describe some common methods used to synthesize various TMDs.

2.3.1 Electrochemical deposition

This a technique that involves the reduction of metal and chalcogen precursors from an electrolyte solution onto a conductive substrate such as glassy carbon (GC) or indium tin oxide (ITO), forming a film of the TMD through either cyclic voltammetry or chronoamperometry.[39-41] This is one of the most cost-effective and versatile method for synthesizing TMDs. The main advantages of this method are that it can be easily scaled up for large-area deposition along with offering precise control over film thickness, composition and morphology.[31,42] Parameters such as deposition time, temperature and applied potential can be adjusted to control the thickness and morphology of the resulting TMD film. The electrochemically deposited layer is amorphous in structure with some complex surface groups. These can include molybdenum oxysulfides (MoO_xS_y), free terminal sulfur groups, and bridging sulfur groups for electrodeposited MoS_2.[31,43] These make it difficult to control the stoichiometry of the electrodeposited layer and often results in sulfur-poor products (MoS_{2-x}).[31] The technique has been used to produce TMDs with enhanced HER catalytic activity such as MoS_2, WS_2 and $MoSe_2$ among others and their usual precursors are ammonium tetrathiomolybdate ($(NH_4)_2MoS4$), ammonium tetrathiotungstate ($(NH_4)_2WS_4$) and molybdic acid and sodium selenite respectively.[39,42,44-47] This is the technique mainly used in this study to synthesize the various TMDs used.

For MoS_2, the deposition reactions are as follows:[46,47]

$$[MoS_4]^{2-} \rightarrow MoS_3 + \frac{1}{8}S_8 + 2e^- \quad (2.1)$$

$$[MoS_4]^{2-} + 2H_2O + 2e^- \rightarrow MoS_2 + 2HS^- + 2OH^- \quad (2.2)$$

For $MoSe_2$, the deposition reactions are as follows:[39]

$$H_2MoO_4 + 6H^+ + 6e^- \rightarrow Mo + 4H_2O \quad (2.3)$$

$$H_2SeO_3 + 4H^+ + 4e^- \rightarrow Se + 3H_2O \quad (2.4)$$

For WS_2, the deposition follows the reactions:[44]

$$[WS_4]^{2-} \rightarrow WS_3 + \frac{1}{8}S_8 + 2e^- \quad (2.5)$$

$$WS_3 + 2e^- + 2H^+ \rightarrow WS_2 + H_2S(g) \quad (2.6)$$

2.3.2 Chemical vapour deposition

Chemical vapour deposition is a technique that involves the chemical reaction of gaseous precursors at temperatures between 600-1000 ºC, to form a thin film of TMDs on a substrate.[48] The method follows one of two routes, one in which the metal-based precursors are initially deposited on the substrate and then followed by the chalcogen-based precursors.[5] The second route involves both the metal and chalcogen precursors being processed and reacted at the same time to form the TMD on the substrate. In both synthesis routes, the precursors are transported into the reaction chamber by using carrier gases like argon or hydrogen and they react at the surface of the substrate, forming a thin film of TMDs. After this process, post-deposition annealing is performed to improve the crystallinity and phase of the films.[5,7,15,48] The technique produces TMD films with excellent crystallinity, purity and sometimes sulfur rich results ideal for HER electrocatalytic activity. It also allows for precise control over film thickness, composition and morphology. The main drawback is the high operational costs and safety when it comes to handling gaseous precursors.

This technique has been frequently employed to produce multi-layered MoS_2. In one study, a three-layered MoS_2 film was synthesized by dip-coating a substrate in ammonium thiomolybdate [$(NH_4)_2MoS_4$], then annealing it at 500°C to convert it to MoS_2, followed by sulfurization at 1000°C in sulfur vapor to improve the crystallinity.[9,49] The conversion of [$(NH_4)_2MoS_4$] to MoS_2 is reported to follow the chemical reaction below:[49]

$$(NH_4)_2MoS_4 + H_2 \rightarrow 2NH_3 + 2H_2S + MoS_2 \quad (2.7)$$

Other alternative CVD methods have been reported where monolayer MoS_2 was synthesized from a gas phase reaction of MoO_3 and S powders through sulfurization.[50] This demonstrates how the CVD method is being continually explored and modified to produce a wide range of TMDs, from monolayers to bulk forms. These advancements highlight the versatility and adaptability of the CVD process in the synthesis of various TMD structures.

2.3.3 Mechanical and liquid exfoliation

Exfoliation is a technique used to obtain thin layers or monolayers of TMDs from their bulk materials by leveraging the weak van der Waals forces between the layers, making it possible to separate them into thinner sheets.[5,7] The commonly used methods are mechanical exfoliation and liquid exfoliation to obtain the thin layer TMDs. Mechanical exfoliation involves physically peeling off layers from the bulk TMD crystal using adhesive tape or other mechanical means.[15,51,52] This method is simple and does not require any chemical reagents while producing high-quality monolayers. Its main disadvantage is the low yield and scalability making it mostly suitable for small scale application and laboratory research.

Liquid phase exfoliation, on the other hand, entails dispersing TMD powder in a solvent and applying ultrasonic energy to separate the TMD layers. This process is facilitated by the structure of TMDs, which allows intercalation by organic molecules, lithium ions, and transition metal halides, among other intercalates. Once intercalated, the compound can be exfoliated into monolayer or few-layer TMD sheets through ultrasonication.[15,53-55] TMDs such as MoS_2, $MoSe_2$, $MoTe_2$, and WS_2 have been exfoliated using this method using *N*-methyl-2-pyrrolidone as the solvent and this produced single layer and multilayer nanosheets of these materials.[56] Lithium ions solutions have also been extensively used for exfoliation of 2D TMDs. The lithium ions are inserted into the interlayer spacing of the TMD crystals and this increases the interlayer distance, thereby weakening the van der Waals forces and this combined with sonication successfully exfoliates the TMD into few layers and even 1T monolayer TMDs.[57,58] Exfoliation method is advantageous due to being able to produce large quantities of

exfoliated TMDs but this comes at the cost of having mixed layer thicknesses and lower crystallinity compared to mechanical exfoliation.

Table 2.1 below summarise the discussed synthesis methods and how they compare to each other.

Table 2.1. Comparison of synthesis methods for transition metal dichalcogenides (TMDs) highlighting their advantages, limitations and achievable catalytic activity range (HER overpotential).

TMD synthesis method	**Activity range (HER overpotential at -10 mA cm^{-2})**	**Benefits**	**Limitations**	**Additional information**
Electrochemical deposition	150-400 mV[31,39-47]	• Simple and scalable setup. • Tunable deposition conditions • Results in increased edge sites and defects that benefits HER catalysis. • Cost-effective method for producing TMDs.	• May produce mixed phases of TMDs. • Difficult to control stoichiometry of resulting products. • Limited to conductive substrates.	• Enables direct deposition on electrodes.
Chemical vapour deposition (CVD)	200-400 mV[5,7,9,15,48,49]	• Produces high quality, pure crystalline TMDs. • Can produce monolayer and few-layers TMDs. • Can result in sulfur rich TMDs, which are ideal for HER.	• High operational costs. • Safety consideration due to the possibility of releasing toxic gases such as H_2S.	• High crystalline TMD products. • Can be adjusted to conduct doping of TMDs.
Mechanical exfoliation	300-400 mV[5,7,15,51,52]	• Produces high quality monolayers. • Cheap method of producing TMD.	• Limited scalability. • Low yield.	• Ideal for fundamental studies requiring few or monolayer TMDs

Liquid phase exfoliation	200-350 mV[15,53-58]	• Large scale production of few to monolayer TMDs.	• Random size distribution of particles. • Extra steps required to separate and clean the final TMD products.	

2.4 Modification of TMDs for improved HER activity

The two-dimensional structure of TMDs permits structural modifications to enhance their catalytic activity for the hydrogen evolution reaction. Additionally, their basal plane sites can be activated and utilized for HER catalysis through various techniques such as doping, defect and strain engineering. These capabilities have created numerous possibilities for optimizing TMDs to improve their catalytic performance, which has become a primary focus of research. Below are some strategies employed to modify TMDs for enhanced HER activity:

2.4.1 Doping

Doping entails incorporating different atoms into the TMD lattice in order to change its electronic properties and creating more active sites for HER. Doping is typically examined from two perspectives. The first involves doping with elements to induce crystal distortion, which subsequently improves the electronic structure.[59] The second focuses on the dopant element itself becoming new active sites, thereby increasing the overall number of adsorption sites.[60] Doping can be divided into two, namely metal element doping and non-metal element doping, with each having its own benefits. With metal element doping, there is a change in physical properties such as electrical conductivity and magnetic properties of the resulting TMD.[61-64] Tsai et al. conducted plane-wave DFT employing ultrasoft-pseudopotentials for calculations on HER activities of MoS_2 doped by a variety of transition metal atoms such as Co, Fe, V, Mn and Ta.[65] It was observed that there were binding strength modifications for the sulfur and metal atoms close to the doped atoms which became optimised for HER. Non-metal doping differs in that it requires greater consideration to be taken to determine suitable doping sites and

for a more stable configuration, replacing the S atoms or fitting the dopant in the S-vacancies in the basal plane has been shown to have better effect.[52] It causes crystal distortion and formation of an amorphous structure which results in additional active sites. Table 2.2 below shows the HER performance of various TMDs resulting from both metal and non-metal doping. Both metal and non-metal doping can enhance the HER catalytic activity of TMDs, and other times leads to poor HER performance, and this shows how selection of appropriate dopants is key in achieving TMD modification.

Table 2.2. HER performance of various doped TMDs. All potentials were corrected for the pH used in each solution.

TMD	Dopant	HER overpotential at -10 mA cm^{-2} / mV (vs RHE)	Tafel / mV dec^{-1}	Synthesis method
Bulk MoS_2 powder	-	-900	-	Commercial powder[66]
Exfoliated MoS_2 powder	-	-580	-	Lithium intercalation[66]
MoS_2	Zn	-194	80-125	Defect engineering and heteroatom doping[67]
MoS_2	Ni	-400		Hydrothermal method[68]
MoS_2	Co	-350	101	Wetness impregnation followed by sulfurization with H_2S[23]
MoS_2	V	-130	60-75	Solid state reaction and liquid exfoliation[69]
Bulk WS_2 powder	-	-830	-	Commercial powder[66]
Exfoliated WS_2 powder	-	-380	-	Lithium intercalation[66]
WS_2	Te	-213	94	Spin coating, sulfuration and tellurization[70]
WS_2	Co	-350	132	Wetness impregnation followed by sulfurization with H_2S[23]
WS_2	N	-197	69.7	Sol-gel process[71]

2.4.2 Defect engineering

Defect engineering is one of the methods that has been devised to improve the number of active edge sites in TMDs by introducing defects to the TMD structure by means of crack formation among other ways.[26] Recent studies have investigated introduction of defects to TMDs to modify them through plasma treatment. One study investigated Ar and O_2 plasma treated MoS_2, and this was done by treating the MoS_2 with Ar plasma and O_2 plasma for varying time periods before conducting HER studies with

the resulting plasma treated MoS_2.[72] There was an improved HER performance for the Ar plasma treated MoS_2, registering a current density of 16.3 mA cm^{-2} at -35 mV which was approximately 11.7 times higher than the 1.39 mA cm^{-2} of pristine MoS_2. Another study reported on how cracks due to oxygen plasma created defects which resulted in increased concentrations of exposed edge sites which ultimately improved HER performance.[73] Engineering defects in the TMD structures can have both negative and positive effects for HER performance but it has been proved to influence number of exposed active sites this can be studied further to improve the catalytic activity of various TMDs.

2.4.3 Nanostructured TMDs

Synthesis of nanostructured TMDs maximizes the exposure of the TMD edges thereby exposing more of the edge sites that are catalytically active. Nanostructuring involves formation of nanoparticles, vertical nanoflakes, and nanowires which significantly increases the surface area-to-volume ratio, thereby proving more active sites for HER. The fabrication of $MoSe_2$ and WSe_2 on carbon microfibers and Si nanowires was investigated by Wang et al, and this vertical layer configurations maximised the exposure of layer edges which in turn enhanced the HER catalytic activity.[74] Another study created a mesoporous, high surface area and double gyroid MoS_2 bicontinuous network which had a higher ratio of edge sites, and this enhanced the catalytic activity for HER.[75] The large number of active sites and improved electron transport pathways in nanostructured TMDs result in improved catalytic performance compared to the bulk TMDs. The enhanced HER activity of the nanostructure TMDs is shown in table 2.3, where a reduction in overpotential and Tafel slope values can be observed in relation to the bulk forms of the corresponding TMDs in table 2.2. When comparing nano and bulk materials, it is worth noting that the normalisation of surface area is usually done using the geometric surface area of the substrate electrode which might be different from the actual surface area of the amorphous or porous catalyst material. This is a widespread problem in the field and one way of tackling this is to use the Brunauer-Emmett-Teller (BET) method for accurate determination of surface area.[76] This is a technique that measures the amount of nitrogen adsorbed on a surface as a function of pressure and this allows for calculation of the specific surface area of the material. Using this technique for surface area

normalisation would greatly improve the accuracy of reported values for amorphous and porous TMD electrocatalysts.

Table 2.3. Comparison of the HER activity of different nanoparticulate forms of various TMDs.

TMD	**HER overpotential at -10 mA cm^{-2} / mV (vs RHE)**	**Tafel / mV dec^{-1}**	**Synthesis method**
MoS_2 nanosheets	-200	40	Commercial obtained[12]
MoS_2 nanosheets	-187	43	CVD followed by chemical intercalation[77]
WS_2 nanosheets	-142	70	CVD followed by microwave assisted chemical intercalation[78]
$MoSe_2$ nanosheets	-350	82	Commercial obtained followed by Li intercalation[66]
$MoSe_2$ nanofilm	-250	59	CVD[74]
WSe_2 nanofilm	-300	77	CVD[74]

2.4.4 Heterostructures

Recent studies have explored TMD heterolayered structures, which consist of two stacked TMD layers, to modify the bandgap and enhance photoelectrocatalysis for HER.[79-82] Computational methods have been employed to predict how stacking different TMDs could impact the bandgap, either positively or negatively, depending on the location of the valence band maximum and conduction band minimum in the layers.[81,82] For water splitting, a bandgap of 1.2-2.5 eV is desirable for to balance light absorption and charge carrier dynamics. Hydrothermal and chemical vapor deposition methods have been utilized to create these heterostructures, which have demonstrated improved electrocatalytic hydrogen evolution performance.[83,84] Additionally, some TMD heterolayers can be fabricated from electrodeposited TMD films; for instance, heterolayers formed from electrodeposited MoS_2 and $MoSe_2$ films have shown enhanced proton reduction activity.[39] Table 2.4 highlights some of the HER improvements in terms of overpotential and Tafel slopes values for TMD heterostructures. It highlights the various heterostructure methods reported in literature and how each result in different heterostructures with varying HER

performance hence the diverse nature of the synthesis methods. Creating TMD heterostructures results in increased number of active sites and facilitates efficient charge transfer between the layers, reducing recombination losses and improving the overall catalytic performance of the heterostructure. A synergistic effect can arise between the two TMD layers that can result in unique electronic properties such as enhanced conductivity or fine-tuning adsorption energy to enhance catalytic activity and selectivity, which would aid in electrocatalytic behaviour.

Table 2.4. HER performance of various TMD heterostructures in comparison to the individual TMDs making them up.

TMD heterostructures	**HER overpotential at -10 mA cm^{-2} / mV (vs RHE)**	**Tafel / mV dec^{-1}**	**Synthesis method**
$MoSe_2/WS_2$	-75	60	Chemical bath and CVD sputtering[83]
$MoSe_2$	-112	136	Chemical bath[83]
WS_2	-158	114	CVD[83]
$MoSe_2/MoS_2$	-186	71	Exfoliation and microwave assisted[85]
MoS_2	-214	109	Exfoliation[85]
$MoSe_2$	-254	73	Hydrothermal and exfoliation[85]
MoS_2/WS_2	-157	44	Microwave assisted solvothermal reaction[86]
MoS_2	-214	81	Microwave assisted solvothermal reaction[86]
MoS_2/CoS_2	-69	62	Hydrothermal, electrodeposition and sulfurization[87]
MoS_2	-147	77	Hydrothermal synthesis[87]
CoS_2	-107	63	Electrodeposition and sulfurization[87]

Table 2.5 below summarise the discussed TMD modification methods and how they compare to each other.

Table 2.5. Comparison of modification methods for TMDs, highlighting advantages, limitations and achievable catalytic activity ranges.

Modification method	Activity range (HER overpotential at -10 mA cm^{-2})	Benefits	Limitations	Additional information
Doping	100-400 mV[23,59-71]	• Improves conductivity and catalytic activity. • Tailoring electronic properties for HER. • Enhances edge activity and carrier mobility.	• Can negatively affect stability of the resulting TMD. • Precise control of dopant distribution and location is challenging.	• Can cause crystal distortions and formation of an amorphous structure.
Defect engineering	35-200 mV[26,72,73]	• Creates active sites. • Enhances intrinsic activity of the TMD.	• Can cause a reduction in material stability.	• Defects are balanced in such a way that it avoids structural degradation.
Nanostructuring	80-350 mV[12,66,74-77]	• Increases surface area of TMD. • Increases exposed active sites.	• Aggregation of nanoparticles can occur and negatively affect catalytic activity. • Requires complex synthesis processes.	• Ideal for HER due to high edge to surface ratios.
Heterostructures	50-200 mV[39,78-86]	• Enhances charge transfer. • Increases number of exposed active sites. • Enables synergistic effects between materials.	• Requires precise layer control. • Interfacial instability may arise during fabrication.	• Improves the bandgap of the resulting heterostructure.

2.5 Conclusion

This chapter provides a comprehensive overview of transition metal dichalcogenides (TMDs), covering their fundamental background, structural properties, and HER applications. It delves into the synthesis methods and HER electrocatalytic performance of TMDs, highlighting their advantages and potential. Furthermore, the chapter examines various strategies to enhance the catalytic efficiency of TMDs by increasing the exposure of active edge sites, activating basal plane sites, and improving their electronic properties, thereby underscoring their promise as efficient and tunable materials for HER catalytic applications.

2.6 References

(1) Bradac, C.; Xu, Z. Q.; Aharonovich, I. Quantum Energy and Charge Transfer at Two-Dimensional Interfaces. *Nano Lett.* 2021, **21**, 1193–1204. https://doi.org/10.1021/acs.nanolett.0c04152.

(2) Shi, Y.; Li, H.; Li, L. J. Recent Advances in Controlled Synthesis of Two-Dimensional Transition Metal Dichalcogenides via Vapour Deposition Techniques. *Chem. Soc. Rev*. 2015, **44**, 2744–2756. https://doi.org/10.1039/c4cs00256c.

(3) Zhang, Q.; Wee, A. T. S.; Liang, Q.; Zhao, X.; Liu, M. Defect Engineering of Two-Dimensional Transition-Metal Dichalcogenides: Applications, Challenges, and Opportunities. *ACS Nano*. 2021, **15**, 2165–2181. https://doi.org/10.1021/acsnano.0c09666.

(4) Lv, Q.; Wu, X.; Tan, J.; Liu, B.; Gan, L.; Li, J.; Huang, Z. H.; Kang, F.; Lv, R. Ultrasensitive Molecular Sensing of Few-Layer Niobium Diselenide. *J. Mater. Chem. A* 2021, **9,** 2725–2733. https://doi.org/10.1039/d0ta09520f.

(5) Kolobov, A. V.; Tominaga, J. *Two-Dimensional Transition-Metal Dichalcogenides*, Springer International Publishing, 2016.

(6) Fu, Q.; Han, J.; Wang, X.; Xu, P.; Yao, T.; Zhong, J.; Zhong, W.; Liu, S.; Gao, T.; Zhang, Z.; Xu, L.; Song, B. 2D Transition Metal Dichalcogenides: Design, Modulation, and Challenges in Electrocatalysis. *Adv. Mater.* 2021, **33**, 1907818. https://doi.org/10.1002/adma.201907818.

(7) Lv, R.; Robinson, J. A.; Schaak, R. E.; Sun, D.; Sun, Y.; Mallouk, T. E.; Terrones, M. Transition Metal Dichalcogenides and beyond: Synthesis, Properties, and Applications of Single- and Few-Layer Nanosheets. *Acc. Chem. Res.* 2015, **48**, 56–64. https://doi.org/10.1021/ar5002846.

(8) Zhang, W.; Zhang, Y.; Qiu, J.; Zhao, Z.; Liu, N. Topological Structures of Transition Metal Dichalcogenides: A Review on Fabrication, Effects, Applications, and Potential. *InfoMat*. 2021, **3**, 133–154. https://doi.org/10.1002/inf2.12156.

(9) Chhowalla, M.; Shin, H. S.; Eda, G.; Li, L. J.; Loh, K. P.; Zhang, H. The Chemistry of Two-Dimensional Layered Transition Metal Dichalcogenide Nanosheets. *Nat. Chem*. 2013, **5**, 263–275. https://doi.org/10.1038/nchem.1589.

(10) Saliba, M.; Atanas, J. P.; Howayek, T. M.; Habchi, R. Molybdenum Disulfide, Exfoliation Methods and Applications to Photocatalysis: A Review. *Nanoscale Adv*. 2023, **5**, 6787–6803. https://doi.org/10.1039/d3na00741c.

(11) Thomas, N.; Mathew, S.; Nair, K. M.; O'Dowd, K.; Forouzandeh, P.; Goswami, A.; McGranaghan, G.; Pillai, S. C. 2D MoS_2: Structure, Mechanisms, and Photocatalytic Applications. *Mater. Today Sustain.* 2021, **13**, 100073. https://doi.org/10.1016/j.mtsust.2021.100073.

(12) Voiry, D.; Salehi, M.; Silva, R.; Fujita, T.; Chen, M.; Asefa, T.; Shenoy, V. B.; Eda, G.; Chhowalla, M. Conducting MoS_2 Nanosheets as Catalysts for Hydrogen Evolution Reaction. *Nano Lett.* 2013, **13**, 6222–6227. https://doi.org/10.1021/nl403661s.

(13) Lin, Y. C.; Dumcenco, D. O.; Huang, Y. S.; Suenaga, K. Atomic Mechanism of the Semiconducting-to-Metallic Phase Transition in Single-Layered MoS_2. *Nat. Nanotechnol.* 2014, **9**, 391–396. https://doi.org/10.1038/nnano.2014.64.

(14) Wang, H.; Lu, Z.; Kong, D.; Sun, J.; Hymel, T. M.; Cui, Y. Electrochemical Tuning of MoS_2 Nanoparticles on Three-Dimensional Substrate for Efficient Hydrogen Evolution. *ACS Nano* 2014, **8**, 4940–4947. https://doi.org/10.1021/nn500959v.

(15) Han, S. A.; Bhatia, R.; Kim, S. W. Synthesis, Properties and Potential Applications of Two-Dimensional Transition Metal Dichalcogenides. *Nano Convergence* 2015, 5, 17. https://doi.org/10.1186/s40580-015-0048-4.

(16) Chen, X. B.; Chen, Z. L.; Li, J. Critical Electronic Structures Controlling Phase Transitions Induced by Lithium-Ion Intercalation in Molybdenum Disulphide. *Chin. Sci. Bull.* 2013, **58**, 1632–1641. https://doi.org/10.1007/s11434-013-5834-y.

(17) Kugler, H. K.; Keller, C. *Gmelin Handbook of Inorganic and Organometallic Chemistry*; Springer: Dordrecht, 1995.

(18) Wang, Q. H.; Kalantar-Zadeh, K.; Kis, A.; Coleman, J. N.; Strano, M. S. Electronics and Optoelectronics of Two-Dimensional Transition Metal Dichalcogenides. *Nat. Nanotechnol.* 2012, **7**, 699–712. https://doi.org/10.1038/nnano.2012.193.

(19) Ejigu, A.; Kinloch, I. A.; Prestat, E.; Dryfe, R. A. W. A Simple Electrochemical Route to Metallic Phase Trilayer MoS_2: Evaluation as Electrocatalysts and Supercapacitors. *J. Mater. Chem. A* 2017, **5**, 11316–11330. https://doi.org/10.1039/c7ta02577g.

(20) Bissett, M. A.; Worrall, S. D.; Kinloch, I. A.; Dryfe, R. A. W. Comparison of Two-Dimensional Transition Metal Dichalcogenides for Electrochemical Supercapacitors. *Electrochim. Acta* 2016, **201**, 30–37. https://doi.org/10.1016/j.electacta.2016.03.190.

(21) Velický, M.; Dryfe, R. A. W. Electrochemistry of 2D Nanomaterials. *Front. Nanosci.* Elsevier 2021, **18**, 485–536. https://doi.org/10.1016/B978-0-12-820055-1.00009-5.

(22) Shan Lim, C.; Min Tan, S.; Sofer, Z.; Pumera, M. Impact Electrochemistry of Layered Transition Metal Dichalcogenides. *ACS Nano* 2015, **9**, 8474-8483.

(23) Bonde, J.; Moses, P. G.; Jaramillo, T. F.; Norskov, J. K.; Chorkendorff, I. Hydrogen Evolution on Nano-Particulate Metal Sulfides. *Faraday Discuss*. 2008, **140**, 9–10. https://doi.org/10.1039/b814058h.

(24) Jaramillo, T. F.; Jørgensen, K. P.; Bonde, J.; Nielsen, J. H.; Horch, S.; Chorkendorff, I. Identification of Active Edge Sites for Electrochemical H_2 Evolution from MoS_2 Nanocatalysts. *Science* 2007, **317**, 100–102. https://doi.org/10.1126/science.1141483.

(25) Tsai, C.; Chan, K.; Abild-Pedersen, F.; Nørskov, J. K. Active Edge Sites in $MoSe_2$ and WSe_2 Catalysts for the Hydrogen Evolution Reaction: A Density Functional Study. *Phys. Chem. Chem. Phys.* 2014, **16**, 13156–13164. https://doi.org/10.1039/C4CP01237B.

(26) Zhu, J.; Yang, R.; Zhang, G. Atomically Thin Transition Metal Dichalcogenides for the Hydrogen Evolution Reaction. *ChemPhysMater*. 2022, **1**, 102–111. https://doi.org/10.1016/j.chphma.2021.11.005.

(27) Li, H.; Tsai, C.; Koh, A. L.; Cai, L.; Contryman, A. W.; Fragapane, A. H.; Zhao, J.; Han, H. S.; Manoharan, H. C.; Abild-Pedersen, F.; Nørskov, J. K.; Zheng, X. Activating and Optimizing MoS_2 Basal Planes for Hydrogen Evolution through the Formation of Strained Sulphur Vacancies. *Nat. Mater.* 2016, **15**, 48–53. https://doi.org/10.1038/nmat4465.

(28) Lau, T. H. M.; Lu, X.; Kulhavý, J.; Wu, S.; Lu, L.; Wu, T. S.; Kato, R.; Foord, J. S.; Soo, Y. L.; Suenaga, K.; Tsang, S. C. E. Transition Metal Atom Doping of the Basal Plane of MoS_2 Monolayer Nanosheets for Electrochemical Hydrogen Evolution. *Chem. Sci.* 2018, **9**, 4769–4776. https://doi.org/10.1039/c8sc01114a.

(29) Li, H.; Du, M.; Mleczko, M. J.; Koh, A. L.; Nishi, Y.; Pop, E.; Bard, A. J.; Zheng, X. Kinetic Study of Hydrogen Evolution Reaction over Strained MoS_2 with Sulfur Vacancies Using Scanning Electrochemical Microscopy. *J. Am. Chem. Soc.* 2016, **138**, 5123–5129. https://doi.org/10.1021/jacs.6b01377.

(30) Merki, D.; Fierro, S.; Vrubel, H.; Hu, X. Amorphous Molybdenum Sulfide Films as Catalysts for Electrochemical Hydrogen Production in Water. *Chem. Sci.* 2011, **2**, 1262–1267. https://doi.org/10.1039/c1sc00117e.

(31) Escalera-López, D.; Lou, Z.; Rees, N. V. Benchmarking the Activity, Stability, and Inherent Electrochemistry of Amorphous Molybdenum Sulfide for Hydrogen Production. *Adv. Energy Mater.* 2019, **9**, 1802614. https://doi.org/10.1002/aenm.201802614.

(32) Hinnemann, B.; Moses, P. G.; Bonde, J.; Jørgensen, K. P.; Nielsen, J. H.; Horch, S.; Chorkendorff, I.; Nørskov, J. K. Biomimetic Hydrogen Evolution: MoS_2 Nanoparticles as Catalyst for Hydrogen Evolution. *J. Am. Chem. Soc.* 2005, **127**, 5308–5309. https://doi.org/10.1021/ja0504690.

(33) Wazir, M. B.; Daud, M.; Safeer, S.; Almarzooqi, F.; Qurashi, A. Review on 2D Molybdenum Diselenide ($MoSe_2$) and Its Hybrids for Green Hydrogen (H_2) Generation Applications. *ACS Omega* 2022, **7**, 16856-16865. https://doi.org/10.1021/acsomega.2c00330.

(34) Xia, X.; Wang, L.; Sui, N.; Colvin, V. L.; Yu, W. W. Recent Progress in Transition Metal Selenide Electrocatalysts for Water Splitting. *Nanoscale* 2020, **12**, 12249–12262. https://doi.org/10.1039/d0nr02939d.

(35) Eftekhari, A. Molybdenum Diselenide ($MoSe_2$) for Energy Storage, Catalysis, and Optoelectronics. *Appl. Mater. Today*. 2017, **8**, 1–17. https://doi.org/10.1016/j.apmt.2017.01.006.

(36) Xiao, D.; Huang, C.; Luo, Y.; Tang, K.; Ruan, Q.; Wang, G.; Chu, P. K. Atomic-Scale Intercalation of Graphene Layers into $MoSe_2$ Nanoflower Sheets as a Highly Efficient Catalyst for Hydrogen Evolution Reaction. *ACS Appl. Mater. Interfaces* 2020, **12**, 2460–2468. https://doi.org/10.1021/acsami.9b18302.

(37) Wang, W.; Li, Y.; Li, M.; Shen, H.; Zhang, W.; Zhang, J.; Liu, T.; Kong, X.; Bi, H. Metallic Phase WSe_2 Nanoscrolls for the Hydrogen Evolution Reaction. *New J. Chem.* 2022, **46**, 8381-8384. https://doi.org/10.1039/d2nj01598f.

(38) Laursen, A. B.; Kegnæs, S.; Dahl, S.; Chorkendorff, I. Molybdenum Sulfides - Efficient and Viable Materials for Electro - And Photoelectrocatalytic Hydrogen Evolution. *Energy Environ. Sci.* 2012, **5**, 5577–5591. https://doi.org/10.1039/c2ee02618j.

(39) Strange, L. E.; Garg, S.; Kung, P.; Ashaduzzaman, M.; Szulczewski, G.; Pan, S. Electrodeposited Transition Metal Dichalcogenides for Use in Hydrogen Evolution Electrocatalysts. *J. Electrochem. Soc.* 2022, **169**, 026510. https://doi.org/10.1149/1945-7111/ac4f25.

(40) Noori, Y. J.; Thomas, S.; Ramadan, S.; Smith, D. E.; Greenacre, V. K.; Abdelazim, N.; Han, Y.; Beanland, R.; Hector, A. L.; Klein, N.; Reid, G.; Bartlett, P. N.; Kees De Groot, C. H. Large-Area Electrodeposition of Few-Layer MoS_2 on Graphene for 2D Material Heterostructures. *ACS Appl. Mater. Interfaces* 2020, **12**, 49786–49794. https://doi.org/10.1021/acsami.0c14777.

(41) Bartlett, P. N.; Benjamin, S. L.; Kees De Groot, C. H.; Hector, A. L.; Huang, R.; Jolleys, A.; Kissling, G. P.; Levason, W.; Pearce, S. J.; Reid, G.; Wang, Y. Non-Aqueous Electrodeposition of Functional Semiconducting Metal Chalcogenides: $Ge_2Sb_2Te_5$ Phase Change Memory. *Mater. Horiz.* 2015, **2**, 420–426. https://doi.org/10.1039/c5mh00030k.

(42) Mabayoje, O.; Liu, Y.; Wang, M.; Shoola, A.; Ebrahim, A. M.; Frenkel, A. I.; Mullins, C. B. Electrodeposition of MoS_x Hydrogen Evolution Catalysts from Sulfur-Rich Precursors. *ACS Appl. Mater. Interfaces* 2019, **11**, 32879–32886. https://doi.org/10.1021/acsami.9b07277.

(43) Tran, P. D.; Tran, T. V.; Orio, M.; Torelli, S.; Truong, Q. D.; Nayuki, K.; Sasaki, Y.; Chiam, S. Y.; Yi, R.; Honma, I.; Barber, J.; Artero, V. Coordination Polymer Structure and Revisited Hydrogen Evolution Catalytic Mechanism for Amorphous Molybdenum Sulfide. *Nat. Mater.* 2016, **15**, 640–646. https://doi.org/10.1038/nmat4588.

(44) Tan, S. M.; Pumera, M. Bottom-up Electrosynthesis of Highly Active Tungsten Sulfide (WS_{3-x}) Films for Hydrogen Evolution. *ACS Appl. Mater. Interfaces* 2016, **8**, 3948–3957. https://doi.org/10.1021/acsami.5b11109.

(45) Chia, X.; Ambrosi, A.; Sofer, Z.; Luxa, J.; Pumera, M. Catalytic and Charge Transfer Properties of Transition Metal Dichalcogenides Arising from Electrochemical Pretreatment. *ACS Nano* 2015, **9**, 5164–5179. https://doi.org/10.1021/acsnano.5b00501.

(46) Belanger, D.; Laperribre, G.; Marsan, B. The Electrodeposition of Amorphous Molybdenum Sulfide, *J. Electroanal. Chem.* 1993, **347**, 165-183.

(47) Vrubel, H.; Hu, X. Growth and Activation of an Amorphous Molybdenum Sulfide Hydrogen Evolving Catalyst. *ACS Catal.* 2013, **3**, 2002–2011. https://doi.org/10.1021/cs400441u.

(48) Aras, F. G.; Yilmaz, A.; Tasdelen, H. G.; Ozden, A.; Ay, F.; Perkgoz, N. K.; Yeltik, A. A Review on Recent Advances of Chemical Vapor Deposition Technique for Monolayer Transition Metal Dichalcogenides (MX_2: Mo, W; S, Se, Te). *Mater. Sci. Semicond. Process*. 2022, **148**, 106829. https://doi.org/10.1016/j.mssp.2022.106829.

(49) Liu, K. K.; Zhang, W.; Lee, Y. H.; Lin, Y. C.; Chang, M. T.; Su, C. Y.; Chang, C. S.; Li, H.; Shi, Y.; Zhang, H.; Lai, C. S.; Li, L. J. Growth of Large-Area and Highly Crystalline MoS_2 Thin Layers on Insulating Substrates. *Nano Lett.* 2012, **12**, 1538–1544. https://doi.org/10.1021/nl2043612.

(50) Lee, Y. H.; Zhang, X. Q.; Zhang, W.; Chang, M. T.; Lin, C. Te; Chang, K. Di; Yu, Y. C.; Wang, J. T. W.; Chang, C. S.; Li, L. J.; Lin, T. W. Synthesis of Large-Area MoS_2 Atomic Layers with Chemical Vapor Deposition. *Adv. Mater.* 2012, **24**, 2320–2325. https://doi.org/10.1002/adma.201104798.

(51) Novoselov, K. S.; Jiang, D.; Schedin, F.; Booth, T. J.; Khotkevich, V. V; Morozov, S. V; Geim, A. K. Two-Dimensional Atomic Crystals, *Proc. Natl. Acad. Sci. U. S. A.* 2005, **102**, 10451-10453. https://www.pnas.org.

(52) Deng, Q.; Li, Z.; Huang, R.; Li, P.; Gomaa, H.; Wu, S.; An, C.; Hu, N. Research Progress of Transition-Metal Dichalcogenides for the Hydrogen Evolution Reaction. *J. Mater. Chem. A*. 2023, **11**, 24434–24453. https://doi.org/10.1039/d3ta04475k.

(53) Ramakrishna Matte, H. S. S.; Gomathi, A.; Manna, A. K.; Late, D. J.; Datta, R.; Pati, S. K.; Rao, C. N. R. MoS_2 and WS_2 Analogues of Graphene. *Angew. Chem., Int. Ed.* 2010, **49**, 4059–4062. https://doi.org/10.1002/anie.201000009.

(54) Eda, G.; Yamaguchi, H.; Voiry, D.; Fujita, T.; Chen, M.; Chhowalla, M. Photoluminescence from Chemically Exfoliated MoS_2. *Nano Lett.* 2011, **11**, 5111–5116. https://doi.org/10.1021/nl201874w.

(55) Joensen, P.; Frindt, R. F.; Morrison, S. R. SINGLE-LAYER MoS_2, *Mat. Res. Bull*. 1986, **21**, 457-461.

(56) Coleman, J. N.; Lotya, M.; O'neill, A.; Bergin, S. D.; King, P. J.; Khan, U.; Young, K.; Gaucher, A.; De, S.; Smith, R. J.; Shvets, I. V; Arora, S. K.; Stanton, G.; Kim, H.-Y.; Lee, K.; Kim, G. T.; Duesberg, G. S.; Hallam, T.; Boland, J. J.; Wang, J. J.; Donegan, J. F.; Grunlan, J. C.; Moriarty,

G.; Shmeliov, A.; Nicholls, R. J.; Perkins, J. M.; Grieveson, E. M.; Theuwissen, K.; Mccomb, D. W.; Nellist, P. D.; Nicolosi, V. Two-Dimensional Nanosheets Produced by Liquid Exfoliation of Layered Materials. *Science* 2011, **331**, 568-571.

(57) Chavalekvirat, P.; Hirunpinyopas, W.; Deshsorn, K.; Jitapunkul, K.; Iamprasertkun, P. Liquid Phase Exfoliation of 2D Materials and Its Electrochemical Applications in the Data-Driven Future. *Precis. Chem*. 2024, **2**, 300-329.

(58) Mayorga-Martinez, C. C.; Ambrosi, A.; Sheng Eng, A. Y.; Sofer, Z.; Pumera, M. Transition metal dichalcogenides (MoS_2, $MoSe_2$, WS_2 and WSe_2) exfoliation technique has strong influence upon their capacitance. *Electrochem. Commun*. 2015, **56**, 24-28

(59) Ding, Q.; Zhai, J.; Cabán-Acevedo, M.; Shearer, M. J.; Li, L.; Chang, H. C.; Tsai, M. L.; Ma, D.; Zhang, X.; Hamers, R. J.; He, J. H.; Jin, S. Designing Efficient Solar-Driven Hydrogen Evolution Photocathodes Using Semitransparent MoQxCly (Q = S, Se) Catalysts on Si Micropyramids. *Adv. Mater.* 2015, **27**, 6511–6518. https://doi.org/10.1002/adma.201501884.

(60) Xie, J.; Zhang, J.; Li, S.; Grote, F.; Zhang, X.; Zhang, H.; Wang, R.; Lei, Y.; Pan, B.; Xie, Y. Controllable Disorder Engineering in Oxygen-Incorporated MoS_2 Ultrathin Nanosheets for Efficient Hydrogen Evolution. *J. Am. Chem. Soc.* 2013, **135**, 17881–17888. https://doi.org/10.1021/ja408329q.

(61) Wei, J.; Zhou, M.; Long, A.; Xue, Y.; Liao, H.; Wei, C.; Xu, Z. J. Heterostructured Electrocatalysts for Hydrogen Evolution Reaction Under Alkaline Conditions. *Nano-Micro Lett*. 2018, **10**, 75. https://doi.org/10.1007/s40820-018-0229-x.

(62) Wang, L.; Xu, C.; Liu, Z.; Chen, L.; Ma, X.; Cheng, H. M.; Ren, W.; Kang, N. Magnetotransport Properties in High-Quality Ultrathin Two-Dimensional Superconducting Mo_2C Crystals. *ACS Nano* 2016, **10**, 4504–4510. https://doi.org/10.1021/acsnano.6b00270.

(63) Nair, N. L.; Maniv, E.; John, C.; Doyle, S.; Orenstein, J.; Analytis, J. G. Electrical Switching in a Magnetically Intercalated Transition Metal Dichalcogenide. *Nat. Mater*. 2020, **19**, 153–157. https://doi.org/10.1038/s41563-019-0518-x.

(64) Tiwari, S.; Van de Put, M. L.; Sorée, B.; Vandenberghe, W. G. Magnetic Order and Critical Temperature of Substitutionally Doped Transition Metal Dichalcogenide Monolayers. *npj 2D Mater. Appl.* 2021, **5**, 54. https://doi.org/10.1038/s41699-021-00233-0.

(65) Tsai, C.; Chan, K.; Nørskov, J. K.; Abild-Pedersen, F. Rational Design of MoS_2 Catalysts: Tuning the Structure and Activity via Transition Metal Doping. *Catal. Sci. Technol.* 2015, **5**, 246–253. https://doi.org/10.1039/c4cy01162g.

(66) Ambrosi, A.; Sofer, Z.; Pumera, M. 2H → 1T Phase Transition and Hydrogen Evolution Activity of MoS_2, $MoSe_2$, WS_2 and WSe_2 Strongly Depends on the MX_2 Composition. *Chem. Commun.* 2015, **51**, 8450–8453. https://doi.org/10.1039/c5cc00803d.

(67) Wu, W.; Niu, C.; Wei, C.; Jia, Y.; Li, C.; Xu, Q. Activation of MoS_2 Basal Planes for Hydrogen Evolution by Zinc. *Angew. Chem.* 2019, **131**, 2051–2055. https://doi.org/10.1002/ange.201812475.

(68) Martinez, L. M.; Delgado, J. A.; Saiz, C. L.; Cosio, A.; Wu, Y.; Villagrán, D.; Gandha, K.; Karthik, C.; Nlebedim, I. C.; Singamaneni, S. R. Magnetic and Electrocatalytic Properties of Transition Metal Doped MoS_2 Nanocrystals. *J. Appl. Phys.* 2018, **124**, 153903. https://doi.org/10.1063/1.5043208.

(69) Sun, X.; Dai, J.; Guo, Y.; Wu, C.; Hu, F.; Zhao, J.; Zeng, X.; Xie, Y. Semimetallic Molybdenum Disulfide Ultrathin Nanosheets as an Efficient Electrocatalyst for Hydrogen Evolution. *Nanoscale* 2014, **6**, 8359–8367. https://doi.org/10.1039/c4nr01894j.

(70) Pan, Y.; Zheng, F.; Wang, X.; Qin, H.; Liu, E.; Sha, J.; Zhao, N.; Zhang, P.; Ma, L. Enhanced Electrochemical Hydrogen Evolution Performance of WS_2 Nanosheets by Te Doping. *J. Catal.* 2020, **382**, 204–211. https://doi.org/10.1016/j.jcat.2019.12.031.

(71) Sun, C.; Zhang, J.; Ma, J.; Liu, P.; Gao, D.; Tao, K.; Xue, D. N-Doped WS_2 Nanosheets: A High-Performance Electrocatalyst for the Hydrogen Evolution Reaction. *J. Mater. Chem. A* 2016, **4**, 11234–11238. https://doi.org/10.1039/c6ta04082a.

(72) Tao, L.; Duan, X.; Wang, C.; Duan, X.; Wang, S. Plasma-Engineered MoS_2 Thin-Film as an Efficient Electrocatalyst for Hydrogen Evolution Reaction. *Chem. Commun.* 2015, **51**, 7470–7473. https://doi.org/10.1039/c5cc01981h.

(73) Ye, G.; Gong, Y.; Lin, J.; Li, B.; He, Y.; Pantelides, S. T.; Zhou, W.; Vajtai, R.; Ajayan, P. M. Defects Engineered Monolayer MoS_2 for Improved Hydrogen Evolution Reaction. *Nano Lett.* 2016, **16**, 1097–1103. https://doi.org/10.1021/acs.nanolett.5b04331.

(74) Wang, H.; Kong, D.; Johanes, P.; Cha, J. J.; Zheng, G.; Yan, K.; Liu, N.; Cui, Y. $MoSe_2$ and WSe_2 Nanofilms with Vertically Aligned Molecular Layers on Curved and Rough Surfaces. *Nano Lett.* 2013, **13**, 3426–3433. https://doi.org/10.1021/nl401944f.

(75) Kibsgaard, J.; Chen, Z.; Reinecke, B. N.; Jaramillo, T. F. Engineering the Surface Structure of MoS_2 to Preferentially Expose Active Edge Sites for Electrocatalysis. *Nat. Mater.* 2012, **11**, 963–969. https://doi.org/10.1038/nmat3439.

(76) Huang, S.; You, Z.; Jiang, Y.; Zhang, F.; Liu, K.; Liu, Y.; Chen, X.; Lv, Y. Fabrication of Ultrathin MoS_2 Nanosheets and Application on Adsorption of Organic Pollutants and Heavy Metals. *Processes* 2020, **8**, 504.

(77) Lukowski, M. A.; Daniel, A. S.; Meng, F.; Forticaux, A.; Li, L.; Jin, S. Enhanced Hydrogen Evolution Catalysis from Chemically Exfoliated Metallic MoS_2 Nanosheets. *J. Am. Chem. Soc.* 2013, **135**, 10274–10277. https://doi.org/10.1021/ja404523s.

(78) Lukowski, M. A.; Daniel, A. S.; English, C. R.; Meng, F.; Forticaux, A.; Hamers, R. J.; Jin, S. Highly Active Hydrogen Evolution Catalysis from Metallic WS_2 Nanosheets. *Energy Environ. Sci.* 2014, **7**, 2608–2613. https://doi.org/10.1039/c4ee01329h.

(79) Terrones, H.; López-Urías, F.; Terrones, M. Novel Hetero-Layered Materials with Tunable Direct Band Gaps by Sandwiching Different Metal Disulfides and Diselenides. *Sci. Rep.* 2013, **3**, 1549. https://doi.org/10.1038/srep01549.

(80) Amin, B.; Singh, N.; Schwingenschlögl, U. Heterostructures of Transition Metal Dichalcogenides. *Phys. Rev. B* 2015, **92**, 075439. https://doi.org/10.1103/PhysRevB.92.075439.

(81) He, J.; Hummer, K.; Franchini, C. Stacking Effects on the Electronic and Optical Properties of Bilayer Transition Metal Dichalcogenides MoS_2, $MoSe_2$, WS_2, and WSe_2. *Phys. Rev. B* 2014, **89**, 075409. https://doi.org/10.1103/PhysRevB.89.075409.

(82) Komsa, H. P.; Krasheninnikov, A. V. Electronic Structures and Optical Properties of Realistic Transition Metal Dichalcogenide Heterostructures from First Principles. *Phys. Rev. B* 2013, **88**, 085318. https://doi.org/10.1103/PhysRevB.88.085318.

(83) Vikraman, D.; Hussain, S.; Patil, S. A.; Truong, L.; Arbab, A. A.; Jeong, S. H.; Chun, S. H.; Jung, J.; Kim, H. S. Engineering $MoSe_2/WS_2$ Hybrids to Replace the Scarce Platinum Electrode for Hydrogen Evolution Reactions and Dye-Sensitized Solar Cells. *ACS Appl. Mater. Interfaces* 2021, **13**, 5061–5072. https://doi.org/10.1021/acsami.0c19890.

(84) Zhao, G.; Li, P.; Rui, K.; Chen, Y.; Dou, S. X.; Sun, W. $CoSe_2/MoSe_2$ Heterostructures with Enriched Water Adsorption/Dissociation Sites towards Enhanced Alkaline Hydrogen Evolution Reaction. *Chem. - Eur. J.* 2018, **24**, 11158–11165. https://doi.org/10.1002/chem.201801693.

(85) Sharma, M. D.; Mahala, C.; Basu, M. 2D Thin Sheet Heterostructures of MoS_2 on $MoSe_2$ as Efficient Electrocatalyst for Hydrogen Evolution Reaction in Wide pH Range. *Inorg. Chem.* 2020, **59**, 4377–4388. https://doi.org/10.1021/acs.inorgchem.9b03445.

(86) Lee, H. J.; Lee, S. W.; Hwang, H.; Yoon, S. I.; Lee, Z.; Shin, H. S. Vertically Oriented MoS_2/WS_2 heterostructures on Reduced Graphene Oxide Sheets as Electrocatalysts for Hydrogen Evolution Reaction. *Mater. Chem. Front.* 2021, **5**, 3396–3403. https://doi.org/10.1039/d1qm00051a.

(87) Ouyang, C.; Feng, S.; Huo, J.; Wang, S. Three-Dimensional Hierarchical MoS_2/CoS_2 Heterostructure Arrays for Highly Efficient Electrocatalytic Hydrogen Evolution. *Green Energy Environ.* 2017, **2**, 134–141. https://doi.org/10.1016/j.gee.2017.01.004.

3 Experimental Methods

This chapter outlines the different materials and methods used along with the theory and purpose behind each technique used while investigating transition metal dichalcogenide materials for HER electrocatalysis.

3.1 List of Chemicals

The following chemicals were purchased commercially: ammonium tetrathiomolybdate (>99%, Sigma Aldrich), molybdenum (IV) sulfide nanoparticles (90 nm, 99% trace metal basis, Sigma Aldrich), ammonium tetrathiotungstate (>99% trace metal basis), tungsten (IV) sulfide nanoparticles (90 nm, 99% trace metal basis), sodium selenite (>99%, Fisher Chemical), molybdic acid (>85%, Honeywell), molybdenum (IV) selenide (powder form, Ossila Ltd), molybdenum sulfide selenide (powder form, Ossila Ltd), tungsten (IV) selenide (powder form, Ossila Ltd), molybdenum (IV) telluride (powder form, Ossila Ltd), tungsten (IV) telluride (powder form, Ossila Ltd), potassium sulfate (99.0%, Sigma Aldrich), sodium perchlorate (>98%, Sigma Aldrich), sodium hydroxide (97%, Alfa Aesar), potassium chloride (99.0-100%, Alfa Aesar), hydrochloric acid (37%, Honeywell), perchloric acid (60%, Fisher Scientific), and sulfuric acid (98%, Acros Organics). All solutions were made using ultrapure water with a resistivity of not less than 18.2 MΩ cm (MilliQ, Millipore), and were thoroughly degassed with nitrogen (oxygen-free, BOC Gases plc) before each experiment and a nitrogen atmosphere maintained throughout the experiment.

3.2 Electrochemical cell

A three-electrode electrochemical cell was used throughout this research for conducting electrochemical experiments. The set up consisted of a working, counter and reference electrode all connected to a computer-controlled potentiostat (Autolab PGSTAT302N), which applied the potential and measured the resulting current. The reference electrode was positioned as close as practicable to the working electrode (avoiding the counter electrode) to minimise Ohmic drop. Throughout the course of this study,

experiments were conducted in a solution of 10 mM H_2SO_4 with 0.1 M K_2SO_4 as the chosen supporting electrolyte unless stated otherwise.

3.2.1 Electrodes

For the purpose of this research, the working electrodes used were glassy carbon (GC) macroelectrodes (3 and 5 mm diameter, BASi Inc), and carbon fibre (CF) microelectrodes (9 and 33 μm diameter). The 33 μm microelectrodes were purchased (IJ Cambria Scientific Ltd) while the 9 μm microelectrodes were produced in-house using pitch-derived carbon fibres (Goodfellow Cambridge Ltd) embedded in epoxy resin (RS Components). These electrodes were rigorously polished with alumina slurries of decreasing size from 3 μm to 0.5 μm successively on microcloth lapping pads (Buehler Inc, USA). Both the GC and CF electrodes were later modified by either electrodepositing or dropcasting a transition metal dichalcogenide on the surface and then used as working electrodes in further electrochemical experiments for the hydrogen evolution reaction.

A graphite rod (6 mm diameter) was used as the counter electrode in this study for all electrochemical experiments unless stated otherwise. This ensured that the surface area of the counter electrode was always over 10× greater than the surface area of the working electrode.

In this work, the reference electrodes used were either a saturated silver/silver chloride electrode or a saturated calomel electrode (SCE), with standard electrode potentials of 0.197 V and 0.242 V at room temperature and pressure, respectively.[1] Their corresponding redox couples are:

$$AgCl + e^- \rightarrow Ag + Cl^- \qquad (3.1)$$

$$\frac{1}{2}Hg_2Cl_2 + e^- \rightarrow Hg + Cl^- \qquad (3.2)$$

3.3 Synthesis

3.3.1 Electrochemical Deposition of TMD films

Electrochemical deposition of different TMD electrocatalysts was conducted via cyclic voltammetry in a covered (not airtight) three-electrode electrochemical cell. An oxygen-free atmosphere was maintained, to avoid forming transition metal oxides, by continuously pumping nitrogen gas into the cell. For most depositions, the cell consisted of a glassy carbon (3 mm diameter) working electrode, graphite rod counter and a saturated silver/silver chloride reference electrode along with the solution containing the analyte and supporting electrolyte. The voltammetry was performed using an Autolab PGSTAT302N potentiostat running Nova 2.1 software. For the electrochemical deposition of molybdenum disulfide (MoS_2) film onto a glassy carbon surface, a solution of 2 mM $(NH_4)_2MoS_4$ and 0.1 M $NaClO_4$ was used, and the potential was cycled between 0.4 V and -1.1 V (vs Ag/AgCl) for 50 cycles at a voltage scan rate of 50 mV s^{-1} for full coverage of the glassy carbon surface which was marked by the height of the oxidative and reductive current peaks reaching saturation (shown in chapter 4).[2-5] Equations 3.3 and 3.4 show the MoS_2 deposition routes.[3] The same cell set-up was used for the electrochemical deposition of tungsten (IV) sulfide (WS_2) film onto a glassy carbon surface but with a 10 mM $(NH_4)_2WS_4$ and 0.1 M KCl solution.[6] The deposition was conducted by cycling the potential between 1.1 V and -1.3 V (vs Ag/AgCl) at a voltage scan rate of 50 mV s^{-1} for 50 cycles. For the electrodeposition of molybdenum (IV) selenide ($MoSe_2$), the precursor solution used contained 0.05 M H_2MoO_4, 0.01 M Na_2SeO_3, 0.1 M $NaClO_4$ which was adjusted to pH 6.5 with NaOH and a saturated calomel electrode (SCE) reference electrode was used.[7] Cyclic voltammetry was also used for this deposition with the potential being scanned between 0.0 V and -1.2 V (vs SCE) for 50 cycles at a voltage scan rate of 50 mV s^{-1}.[7,8] Further details about the deposition as well as the deposition scans are provided in chapters 4 and 5.

$$[MoS_4]^{2-} \rightarrow MoS_3 + \frac{1}{8}S_8 + 2e^- \qquad (3.3)$$

$$[MoS_4]^{2-} + 2H_2O + 2e^- \rightarrow MoS_2 + 2HS^- + 2OH^- \qquad (3.4)$$

3.3.2 Nanoparticle drop-casting

Drop-casting is a technique whereby an aliquot of a suspension containing an insoluble material in a chosen solvent (e.g. water, water-propanol mixture) is pipetted onto an electrode surface and allowed to dry either at normal room temperature or under a light source, resulting in a deposited layer of material forming on the electrode surface. Whilst drop-casting often results in some layer roughness and is prone to 'coffee-ring' effects, it has the advantage of simplicity and does not suffer the restrictions on solvents of spin-coating.[9-11] The TMD nanoparticle powders were added to deionised water at 0.5 mg mL^{-1} and sonicated for 30 minutes to make well mixed suspensions. From the suspensions, a 5 μL aliquot of the nanoparticle suspension was drop-cast onto a glassy carbon (3 mm diameter) electrode and left to dry under a light source (shown in figure 3.1). Upon drying, a TMD layer was formed on the electrode surface and this modified electrode would be used as the working electrode during electrochemical experiments. MoS_2 and WS_2 were commercially bought as nanoparticles and could be readily made into suspensions. However, the other TMDs ($MoSe_2$, WSe_2, $MoTe_2$, WTe_2, and MoSSe), were purchased as powders (5 mm average size) and were subsequently crushed to submicron size through mechanochemical comminution. This technique uses a solvent-free sealed environment where comminution occurs to achieve particle breakdown and chemical transformations.[12,13] It is a physical process used to reduce bulk materials into nanoparticles by using mechanical energy to induce physical and chemical transformations on the sample material. This results in nanoparticles with a broad range of sizes and morphologies, depending on the milling parameters such as time, speed and media. The TMD powders (150 mg each) were ground using a 15 mL stainless steel jar from Form-Tech Scientific with two 7 mm stainless steel balls at 2500 rpm for 5 min using a FlackTek SpeedMixer™ (model DAC 330-100 Pro) and a custom-made jar holder.

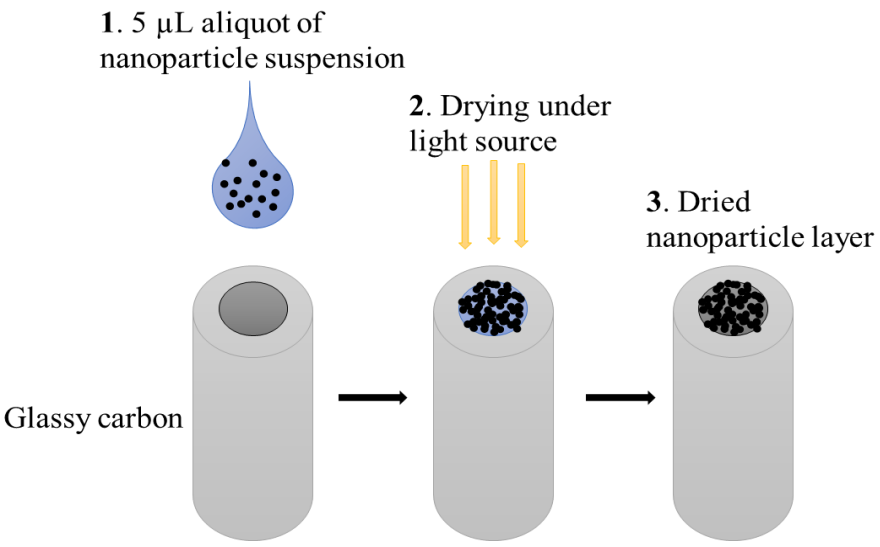

Figure 3.1. Graphical representation of how the nanoparticle suspensions were dropcast onto the surfaces of glassy carbon electrodes.

3.4 Electrochemistry

3.4.1 Hydrogen evolution reaction

The hydrogen evolution reaction (HER) is the cathodic half-reaction of the water splitting reaction. To facilitate the reaction and produce a significant amount of hydrogen requires electrocatalysts, hence the TMDs are used as working electrodes during the reaction. For all the HER experiments conducted in this study, a standard three-electrode electrochemical cell set up was used consisting of a graphite counter (Goodfellow Cambridge Ltd), a saturated Ag/AgCl (IJ Cambria Ltd) reference and either modified or unmodified glassy carbon (3mm diameter, BASi Inc) working electrodes. For determination of the standard electrochemical rate constant, a 33 µm diameter carbon fibre (IJ Cambria Ltd) microelectrode was used as the working electrode to conduct linear sweep voltammetry. The solution used throughout the course of this study was 10 mM H_2SO_4 with 0.1 M K_2SO_4 supporting electrode unless stated otherwise. Cyclic and linear sweep voltammetry were carried out using an Autolab PGSTAT302N potentiostat running Nova 2.1 software and the data obtained was analysed using Microsoft Excel and OriginPro 2022. Electrochemical simulation of the data to acquire kinetic data was performed using DigiElch v8 software (www.elchsoft.com).

3.4.2 Electrochemical Particle Impacts

Chronoamperometric particle-impact measurements were conducted using a specialized setup comprising a custom low-noise potentiostat with a high-speed variable-gain low-noise current amplifier (DHPCA-100, femto.de) controlled by PyFemto_0.8 software.[14,15] This achieved a sampling rate of 10^5 s^{-1} due to the amplifier bandwidth of 220 kHz and a rise time of 1.6 μs at an operating gain of 10^8, in conjunction with a National Instruments data acquisition card (NI-6003) with a bandwidth of 300 kHz. The nanoparticle impact scans generated very low current signals in the nanoampere (nA) range, necessitating the use of a low-noise potentiostat to minimize external noise effects during scanning.[16,17] To enhance signal quality and facilitate the identification of impact signals, a 250 Hz Bessel digital filter was applied to the chronoamperometry scans using PyFemto software, while preserving the raw data for subsequent analysis. In the experimental setup, the reference electrode was positioned in a fritted compartment to prevent contamination during impact experiments. This methodology ensured precise and reliable measurements of nanoparticle impacts with minimized interference from noise and contamination. Data analysis was carried out using Microsoft Excel and OriginPro 2022 for peak identification, background correction and peak analysis.

3.4.3 Hydrogen generation

To confirm that the detected impact signals during the nanoparticle impact study were indeed due to hydrogen evolution, a scaled-up and modified three-electrode cell (figure 3.2 below) was employed to capture and analyse any evolved gases using gas chromatography. The cell featured a graphite rod working electrode (6 mm diameter, 125 mm length) to provide a larger surface area for particle impacts, along with correspondingly larger graphite counter and Ag/AgCl reference electrodes housed in separate fritted compartments. The volume of the nanoparticle suspension was increased to 500 mL with a concentration of 3.0 nM to ensure sufficient gas production for testing. Chronoamperometric measurements were conducted at two potential values (-0.40 V and -0.15 V vs RHE) over a period of 4 hours to generate adequate gas quantities. The evolved gas was collected in a gas syringe via a shut-off valve connector and subsequently injected into a gas chromatograph for analysis to determine its

composition, specifically whether hydrogen was present or not. This experimental approach allowed for the identification and characterization of gases produced during the electrochemical measurements, providing valuable insights into the nature of the impact signals observed.

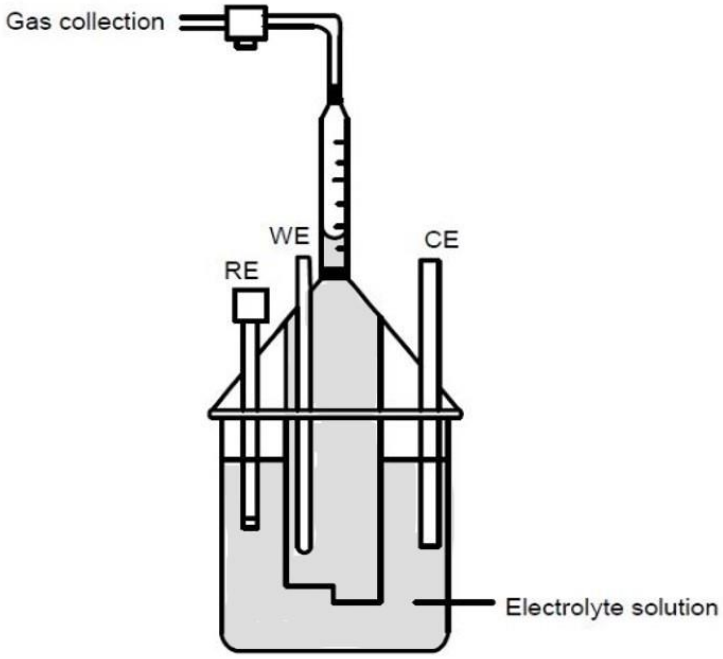

Figure 3.2. Schematic diagram of the scaled up and modified three-electrode cell set-up for the nanoparticle impact study.

3.5 Characterization

3.5.1 Scanning electron microscope and energy dispersive spectroscopy (SEM-EDS)

The characterization of transition metal dichalcogenide (TMD) samples was conducted using scanning electron microscopy with energy dispersive spectroscopy (SEM-EDS) utilizing a Hitachi TM3030 tabletop electron microscope. In this method, electron beams emitted from an electron gun are directed towards the sample and pass through a series of apertures and lenses for focusing before reaching the sample surface. The interaction of these electrons with atoms on the sample surface generates signals in the form of secondary and backscattered electrons, which are detected by sensors to produce high-resolution images.

Sample preparation involved dropcasting TMD suspensions onto a carbon conductive tab and allowing them to dry prior to imaging. For electrodeposited samples, glassy carbon studs were mounted on a stand and placed inside the microscope chamber for imaging. This approach facilitated detailed examination of TMD structures and elemental composition, enabling comprehensive characterization of sample morphology and chemical composition using SEM-EDS analysis.

3.5.2 Focused ion beam scanning electron microscope (FIB-SEM)

A focused ion beam scanning electron microscope (FIB-SEM) utilizes a beam of gallium ions to selectively remove material from a sample surface, enabling precise cross-sectioning, imaging, and analysis of internal structures. FIB-SEM analysis was conducted on TMD heterolayer samples to determine the thickness of individual TMD layers and the overall heterolayer thickness through cross-sectional imaging, by Dr Nigel Neate at Nanoscale and Microscale Research Centre (NMRC), University of Nottingham. The characterization process was performed using a Zeiss Crossbeam 550 FIB-FEG-SEM equipped with an Oxford Instruments EDS system. Sample preparation involved sputter coating with platinum to ensure electrical conductivity and protect against ion beam damage. Subsequently, an additional layer of platinum was deposited using the ion beam. A trench was then cut into the sample surface using the gallium ion beam operated at 30 kV and 700 pA. The back face of the trench was polished using the ion beam set to 30 kV and 50 pA. The cross-sectional image was obtained with the electron beam set to 5 kV and 200 pA, at a working distance of 5 mm, utilizing both Everhart-Thornley and In-lens secondary electron detectors for imaging. This enabled precise measurement and analysis of the TMD heterolayer structure, providing valuable insights into layer thicknesses and overall morphology at the nanoscale.

3.5.3 X-ray photoelectron spectroscopy (XPS)

X-ray photoelectron spectroscopy (XPS) is a surface-sensitive analytical technique employed to discern the elemental composition, as well as the chemical and electronic states of materials. XPS analysis was conducted by Dr Hannah Constantin and Dr Long Jiang at Nanoscale and Microscale Research Centre

(NMRC), University of Nottingham, using a Kratos Liquid Phase Photoelectron Spectroscopy (LiPPS) system equipped with a monochromated Al Kα X-ray source (1486.6 eV), operating at 10 mA emission current and 12 kV anode potential (120 W). Wide resolution scans were performed with a step size of 0.5 eV and a pass energy of 160 eV, while high-resolution scans utilized a step size of 0.1 eV and a pass energy of 20 eV. High-resolution scans focused on photoelectron peaks corresponding to the detected elements identified in the wide spectra. The acquired spectra were charge corrected relative to the C 1s peak (adventitious carbon) set at 285 eV. Data analysis was carried out using CASA XPS software (version 2.3.23), enabling detailed examination and interpretation of elemental composition and chemical states present in the TMD samples. This methodology provided valuable insights into the surface chemistry and electronic structure of the TMD materials.

3.5.4 Raman spectroscopy

Raman spectroscopy is an analytical technique used to study the vibrational, rotational and other low frequency modes in materials by examining the interaction between the sample and monochromatic light. It provides detailed information about the phase, chemical structure and molecular interactions based on the interaction of light with the chemical bonds of the material. In-plane vibrational mode (E_{2g}) and out-of-plane vibrational mode (A_{1g}) are the two primary vibrational modes commonly observed in many materials including TMDs. In-plane vibrational mode involves the vibration of atoms within the 2D plane of the materials while out-of-plane vibration mode involves the vibration of atoms perpendicular to the 2D plane of the material.[18] Raman spectroscopy has been used to determine layer thickness, interlayer interactions, strain and defects in various TMDs such as MoS_2, WS_2 and $MoSe_2$.[19,20]

Raman analysis was conducted on transition metal dichalcogenide (TMD) powder samples using a Renishaw InVia Raman Microscope equipped with a 532 nm laser, controlled by WiRE™ (Renishaw) software. Sample preparation involved depositing an appropriate amount of the TMD sample onto a microscope slide, which was then placed inside the microscope chamber for imaging. Careful positioning of the sample ensured optimal focus for the imaging process. The obtained Raman spectral data, which captured the vibrational modes and structural properties of the TMD samples, were

extracted and further analysed using OriginPro 2022 software. This analysis involved peak identification and characterization based on the Raman spectra, providing valuable insights into the composition and crystallographic features of the TMD samples. Raman spectroscopy served as an effective technique for the non-destructive characterization of TMD materials, offering detailed information about their molecular and structural properties based on light-matter interactions.

3.5.5 Powder X-ray diffraction (XRD)

Powder X-ray diffraction is a technique utilised to determine the crystal structure of materials and relies on the principle of Bragg's law, which explains that when X-rays interact with a crystal lattice, they undergo constructive interference and produce a diffraction pattern that is characteristic of the atomic arrangement of the crystal. The law states that when an X-ray hits a crystal surface at an incident angle, θ, it reflects at the same angle, θ and constructive interference occurs when the path difference, d, equals an integer multiple, n, of the wavelength, λ.[21,22] The expression for the law is as follows:

$$n\lambda = 2d\sin(\theta) \qquad (3.5)$$

XRD was conducted on the transition metal dichalcogenide (TMD) powder samples using the PANalytical Empyrean X-ray Diffractometer equipped with a copper (Cu) source and a Pixel Medipix 3D detector. The instrument was configured in reflection mode for the analysis. During the XRD analysis, the TMD samples were securely mounted on a clean stand and positioned within the X-ray chamber, which was then sealed for sample characterization. X-rays emitted by the Cu source were directed onto the sample, causing them to be diffracted based on the atomic arrangement and crystallographic properties of the TMD material. The diffracted X-rays were captured by the Pixel Medipix 3D detector. By moving the detector to vary the diffraction angle (the angle between the incident X-ray beam and the diffracted beam), the intensity of the diffracted X-rays was measured and recorded as diffraction data.

XRD analysis using this setup enabled the investigation of the crystalline structure and phase composition of the TMD samples. The resulting diffraction patterns provided valuable information

about the atomic arrangement and crystallographic properties of the TMD materials, allowing for detailed characterization and identification of specific phases present in the samples. This technique is essential for studying the structural properties and phase transitions of materials at the atomic level.

3.5.6 Gas chromatography

Gas identification was performed using a Shimadzu GC2014 gas chromatograph fitted with a thermal conductivity detector (TCD). Gas samples generated from the reaction cell were collected using a gas syringe and subsequently injected into the gas chromatograph for analysis. Nitrogen served as the carrier gas during the chromatographic separation process. The thermal conductivity detector was utilized to detect and identify the various gases present in the samples, allowing for accurate and reliable gas identification based on their retention times and thermal conductivity properties. This analytical approach facilitated the characterization and quantification of gases produced during the experimental reactions.

3.5.7 Atomic force microscope (AFM)

Surface topography imaging was conducted using Atomic Force Microscopy (AFM) by Dr Chris Jones, University of Birmingham, with a Flex AFM system from Nanosurf AG, Switzerland, operated in phase contrast (tapping) mode. Tap150DLC cantilevers (BudgetSensors, Bulgaria), featuring a diamond-like-carbon tip coating and a 15 nm nominal tip radius, were utilized for imaging. The AFM measurements were performed on particles deposited onto a freshly cleaved mica sheet (Agar Scientific Ltd, UK), which was positioned on the sample stage of an IX73 inverted microscope (Olympus, Japan). Care was taken to position the cantilever away from large, aggregated particles visible under the microscope. Images were captured over a 5 μm^2 area with 512 points recorded per line, and smaller scan sizes were employed in areas of interest. Image analysis was conducted using Gwyddion software (v2.58, http://gwyddion.net/)[23] to align rows within each image and quantify particle sizes, providing detailed surface topography data and particle size distributions of the examined samples.

3.5.8 Spectroscopic Ellipsometry

Spectroscopic ellipsometry was used to measure the thickness of transition metal dichalcogenide (TMD) heterolayers at three different angles (65°, 70°, and 75°) using an alpha-SE ellipsometer (J.A. Woollam Co. Inc). This non-destructive optical technique relies on changes in the polarization state of light as it reflects obliquely from a thin film sample, providing information about film thickness, surface roughness, and optical properties. Ellipsometry analyses changes in the polarisation state of light, represented by two parameters being the amplitude ratio of the reflected p-polarised and s-polarised light components (Psi Ψ) and the phase difference between these components (delta Δ). This technique has been used to for accurate determination of film thickness, bandgap as well as evaluating film homogeneity and crystallinity for thin films of TMDs like MoS_2.[24,25]

In the ellipsometry setup (figure 3.3), a light source emits a beam directed at the sample. Some of the light is absorbed by the sample while the rest is reflected towards a detector, which records the intensity of the reflected light beam. The acquired ellipsometry data was analysed and modelled using CompleteEASE software (J.A. Woollam Co. Inc), allowing for precise determination of layer thickness and structural parameters based on changes in polarized light. This characterization technique offered valuable insights into the thickness and optical properties of the TMD heterolayers, facilitating detailed analysis through advanced data analysis and modelling methods. Spectroscopic ellipsometry is a powerful tool for non-destructive characterization of thin film materials, providing essential information for understanding film properties and performance.

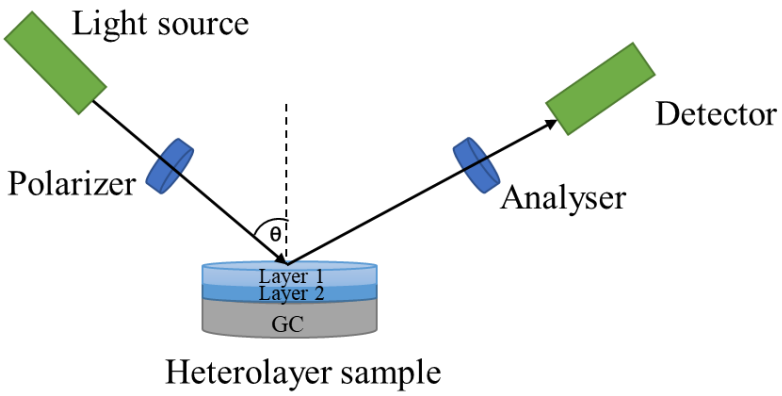

Figure 3.3. Graphical display of how an ellipsometer functions. Light produced from the light source is reflected by the heterolayer sample surface while a detector captures and measures the polarisation change.

3.6 References

(1) Ives, D. J. G.; Janz, G. J. *Reference Electrodes: Theory and Practice*; Academic Press: New York, 1961.

(2) Merki, D.; Fierro, S.; Vrubel, H.; Hu, X. Amorphous Molybdenum Sulfide Films as Catalysts for Electrochemical Hydrogen Production in Water. *Chem. Sci.* 2011, **2**, 1262–1267. https://doi.org/10.1039/c1sc00117e.

(3) Vrubel, H.; Hu, X. Growth and Activation of an Amorphous Molybdenum Sulfide Hydrogen Evolving Catalyst. *ACS Catal.* 2013, **3**, 2002–2011. https://doi.org/10.1021/cs400441u.

(4) Escalera-López, D.; Lou, Z.; Rees, N. V. Benchmarking the Activity, Stability, and Inherent Electrochemistry of Amorphous Molybdenum Sulfide for Hydrogen Production. *Adv. Energy Mater.* 2019, **9**, 1802614. https://doi.org/10.1002/aenm.201802614.

(5) Belanger, D.; Laperriere, G.; Marsan, B. The Electrodeposition of Amorphous Molybdenum Sulfide. *J. Electroanal. Chem*. 1993, **347**, 165-183.

(6) Tan, S. M.; Pumera, M. Bottom-up Electrosynthesis of Highly Active Tungsten Sulfide (WS_{3-x}) Films for Hydrogen Evolution. *ACS Appl. Mater. Interfaces,* 2016, **8**, 3948–3957. https://doi.org/10.1021/acsami.5b11109.

(7) Strange, L. E.; Garg, S.; Kung, P.; Ashaduzzaman, M.; Szulczewski, G.; Pan, S. Electrodeposited Transition Metal Dichalcogenides for Use in Hydrogen Evolution Electrocatalysts. *J. Electrochem. Soc.* 2022, **169**, 026510. https://doi.org/10.1149/1945-7111/ac4f25.

(8) Dukstiene, N.; Kazancev, K.; Prosicevas, I.; Guobiene, A. Electrodeposition of Mo-Se Thin Films from a Sulfamatic Electrolyte. *J. Solid State Electrochem.* 2004, **8**, 330–336. https://doi.org/10.1007/s10008-003-0457-x.

(9) Kaliyaraj Selva Kumar, A.; Zhang, Y.; Li, D.; Compton, R. G. A Mini-Review: How Reliable Is the Drop Casting Technique? *Electrochem. Commun*. 2020, **121**, 106867. https://doi.org/10.1016/j.elecom.2020.106867.

(10) Tschulik, K.; Batchelor-Mcauley, C.; Toh, H. S.; Stuart, E. J. E.; Compton, R. G. Electrochemical Studies of Silver Nanoparticles: A Guide for Experimentalists and a Perspective. *Phys. Chem. Chem. Phys*. 2014, **16**, 616–623. https://doi.org/10.1039/c3cp54221a.

(11) Zuo, C.; Ding, L. Drop-Casting to Make Efficient Perovskite Solar Cells under High Humidity. *Angew. Chem., Int. Ed.* 2021, **60**, 11242–11246. https://doi.org/10.1002/anie.202101868.

(12) Do, J. L.; Friščić, T. Mechanochemistry: A Force of Synthesis. *ACS Cent. Sci.* 2017, **3**, 13–19. https://doi.org/10.1021/acscentsci.6b00277.

(13) Cuccu, F.; De Luca, L.; Delogu, F.; Colacino, E.; Solin, N.; Mocci, R.; Porcheddu, A. Mechanochemistry: New Tools to Navigate the Uncharted Territory of "Impossible" Reactions. *ChemSusChem*. 2022, **15**, e202200362. https://doi.org/10.1002/cssc.202200362.

(14) Batchelor-McAuley, C.; Ellison, J.; Tschulik, K.; Hurst, P. L.; Boldt, R.; Compton, R. G. In Situ Nanoparticle Sizing with Zeptomole Sensitivity. *Analyst,* 2015, **140**, 5048–5054. https://doi.org/10.1039/c5an00474h.

(15) Schwuttke, G. H.; Yang, K.; Ciszek, T. F.; Bertocci, U. Applications of a Low Noise Potentiostat in Electrochemical Measurements. *J. Electrochem. Soc*. 1978, **127**, 1931-1934.

(16) Shideler, R. W.; Bertocci, U. A Low-Noise Potentiostat for the Study of Small Amplitude Signals in Electrochemistry. *J. Res. Natl. Bur. Stand*. 1980, **85**, 211-218.

(17) Oladeji, A. V.; Courtney, J. M.; Rees, N. V. Copper Deposition on Metallic and Non-Metallic Single Particles via Impact Electrochemistry. *Electrochim. Acta,* 2022, **405**, 139838. https://doi.org/10.1016/j.electacta.2022.139838.

(18) Berkdemir, A.; Gutiérrez, H. R.; Botello-Méndez, A. R.; Perea-López, N.; Elías, A. L.; Chia, C. I.; Wang, B.; Crespi, V. H.; López-Urías, F.; Charlier, J. C.; Terrones, H.; Terrones, M. Identification of Individual and Few Layers of WS_2 Using Raman Spectroscopy. *Sci. Rep.* 2013, **3**, 1755. https://doi.org/10.1038/srep01755.

(19) Fang, H.; Battaglia, C.; Carraro, C.; Nemsak, S.; Ozdol, B.; Kang, J. S.; Bechtel, H. A.; Desai, S. B.; Kronast, F.; Unal, A. A.; Conti, G.; Conlon, C.; Palsson, G. K.; Martin, M. C.; Minor, A. M.; Fadley, C. S.; Yablonovitch, E.; Maboudian, R.; Javey, A. Strong Interlayer Coupling in van Der Waals Heterostructures Built from Single-Layer Chalcogenides. *Proc. Natl. Acad. Sci.* 2014, **111**, 6198–6202. https://doi.org/10.1073/pnas.1405435111.

(20) Okada, M.; Kutana, A.; Kureishi, Y.; Kobayashi, Y.; Saito, Y.; Saito, T.; Watanabe, K.; Taniguchi, T.; Gupta, S.; Miyata, Y.; Yakobson, B. I.; Shinohara, H.; Kitaura, R. Direct and Indirect Interlayer Excitons in a van Der Waals Heterostructure of HBN/WS_2/MoS_2/HBN. *ACS Nano* 2018, **12**, 2498–2505. https://doi.org/10.1021/acsnano.7b08253.

(21) Kacher, J.; Landon, C.; Adams, B. L.; Fullwood, D. Bragg's Law Diffraction Simulations for Electron Backscatter Diffraction Analysis. *Ultramicroscopy,* 2009, **109**, 1148–1156. https://doi.org/10.1016/j.ultramic.2009.04.007.

(22) Pope, C. G. X-Ray Diffraction and the Bragg Equation. *J. Chem. Educ.* 1997, **74**, 129-131. https://pubs.acs.org/sharingguidelines.

(23) Nečas, D.; Klapetek, P. Gwyddion: An Open-Source Software for SPM Data Analysis. *Cent. Eur. J. Phys*. 2012, **10**, 181–188. https://doi.org/10.2478/s11534-011-0096-2.

(24) Yim, C.; O'Bren, M.; McEvoy, N.; Winters, S.; Mirza, I.; Lunney, J. G.; Duesberg, G. S. Investigation of the optical properties of MoS_2 thin films using spectroscopic ellipsometry. *Appl. Phys. Lett*. 2014, **104**, 103114.

(25) Navarro-Gamarra, K. E.; De Paoli, J. M.; Patrito, E. M. Ellipsometric Investigation of Thick Vertically Oriented MoS_2 Films Grown on Mo Foil at High Temperatures. *J. Phys. Chem. C* 2021, **125**, 2005-2014.

4 Impact electrochemistry of MoS_2: electrocatalysis and hydrogen generation at low overpotentials

This chapter is based on the publication:

T. Manyepedza, A. Snowdon, C. R. Jones, J. M. Courtney and N. V. Rees. Impact Electrochemistry of MoS_2: Electrocatalysis and Hydrogen Generation at Low Overpotentials. *J. Phys. Chem. C*. 2022, **126**, 17942-17951.

Credit authorship contribution statement

Tshiamo Manyepedza: Investigating, Conceptualization, Data curation, Formal analysis, Validation, Writing-original draft. **Abigail Snowdon**: Resources, Writing-Review and Editing. **Christopher R. Jones**: Resources, Writing-Review and Editing. **James M. Courtney**: Supervision, Writing-Review and Editing. **Neil V. Rees**: Conceptualization, Supervision, Writing-Review and Editing.

4.1 Introduction

The growing demand for alternative electrocatalyst materials has sparked research into molybdenum disulfide (MoS_2) as an economical and efficient electrocatalyst for the hydrogen evolution reaction. This 2D crystalline compound has edge sites that are catalytically active for HER while the basal sites are inert.[1,2] Studies have shown an improved catalytic activity towards HER for nanostructured forms of molybdenum disulfide as compared to its bulk crystalline form due to having more active edge sites exposed.[2,3] To fully explore the catalytic properties of nanoparticulate MoS_2, impact electrochemistry was used. The technique focuses on single nanoparticles colliding with an electrode surface which may result in electron transfer provided that the applied potential and choice of materials are suitable for a reaction to occur.[4-7]

This chapter investigates the amorphous film and nanoparticle forms of MoS_2 and their catalytic effect on the HER, as two different structural morphologies of the material. Electrochemical deposition was carried out to produce the bulk amorphous MoS_2 and its catalytic effect on the HER and its stability was tested through linear sweep voltammetry. Nanoparticle impact voltammetry was conducted stepwise across a range of potentials, from the non-active region (at positive overpotentials) to the active region (at negative overpotentials). The frequency of impact events was recorded, and the transient signal analysed to elucidate kinetic information. Tafel analysis of this data and modelling of kinetic behaviour was compared to gain further insight into the HER kinetics due to the different catalyst structures. The nanoparticle impact study was extended to explore the hydrogen producing capabilities of the nanoparticles via bulk electrolysis, using gas chromatography to confirm the earlier onset was due to the HER.

4.2 Results and discussion

4.2.1 Electrodeposition and characterization of amorphous MoS_2

The hydrogen evolution reaction was investigated using MoS_2 as electrocatalyst in two different structural forms, that is as electrodeposited amorphous and nanoparticles, in order to compare performance and kinetics. To establish a baseline of performance and to guide potentials of interest for

the impact electrochemistry study electrodeposited MoS_2 was studied. The electrochemical deposition of MoS_2 onto a glassy carbon electrode was carried out via cyclic voltammetry in a solution of 2 mM $(NH_4)_2MoS_4$ and 0.1 M $NaClO_4$ between 0.6 V to -0.9 V (vs RHE) at a voltage scan rate of 50 mV s^{-1} for 50 cycles (discussed further under Experimental Methods in section 3.3.1).

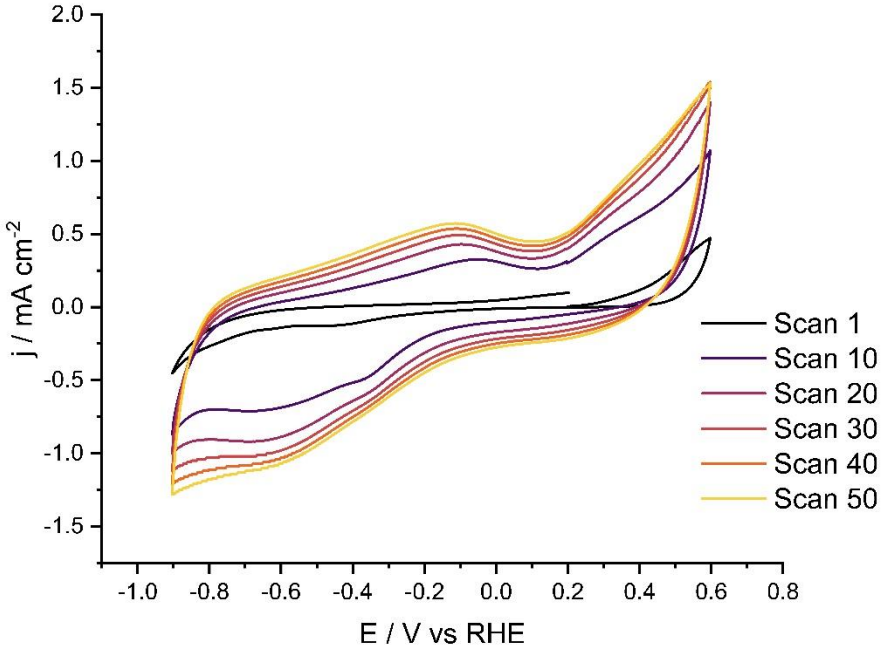

Figure 4.1. Cyclic voltammogram of the deposition of MoS_2 on a glassy carbon macroelectrode at a scan rate of 100 mV s^{-1} in a solution containing 2 mM $(NH_4)_2MoS_4$ and 0.1 M $NaClO_4$

The resulting voltammograms (Fig. 4.1) exhibited the expected broad oxidation and reductive peaks at -0.1 V and -0.6 V (vs RHE) respectively, due to the following redox processes:[8-12]

$$[MoS_4]^{2-} \rightarrow MoS_3 + \frac{1}{8}S_8 + 2e^- \qquad (4.1)$$

$$[MoS_4]^{2-} + 2H_2O + 2e^- \rightarrow MoS_2 + 2HS^- + 2OH^- \qquad (4.2)$$

The increased oxidative and reductive peaks indicate the growth of the MoS_2 film formed on the surface of the glassy carbon.[11] The deposition occurred via oxidation of $[MoS_4]^{2-}$ to form a film of MoS_3 as shown by equation 4.1 at potential -0.3 to 0.0 V and reduction of $[MoS_4]^{2-}$ to MoS_2 following equation 4.2 at potentials -0.4 to -0.7 V. This results in an amorphous film of MoS_2 and MoS_3 being created on the electrode surface. The increase in current during successive cycles indicates continuous nucleation and growth of MoS_2 and MoS_3 particles, which increase the electrochemically active surface area of the electrode. As the film grows, it facilitates faster electron transfer and enhances ion accessibility, leading to progressively higher peak currents.[11,12]

Scanning electron microscopy with energy dispersive spectroscopy (SEM-EDS) was used to determine the elemental composition of the electrodeposited MoS_2 film. The EDS detected small amounts of molybdenum and sulfur in the electrodeposited sample, shown on the spectra in Fig. 4.2 with the detected elements in the sample. It should be noted that the deposited layer of MoS_2 is estimated to be in the nano range in terms of thickness as reported by Merki et al, hence the low ratios in comparison to carbon in the spectrum.[8] This confirms that a layer of Mo and S exists on the glassy carbon after the electrochemical deposition process.

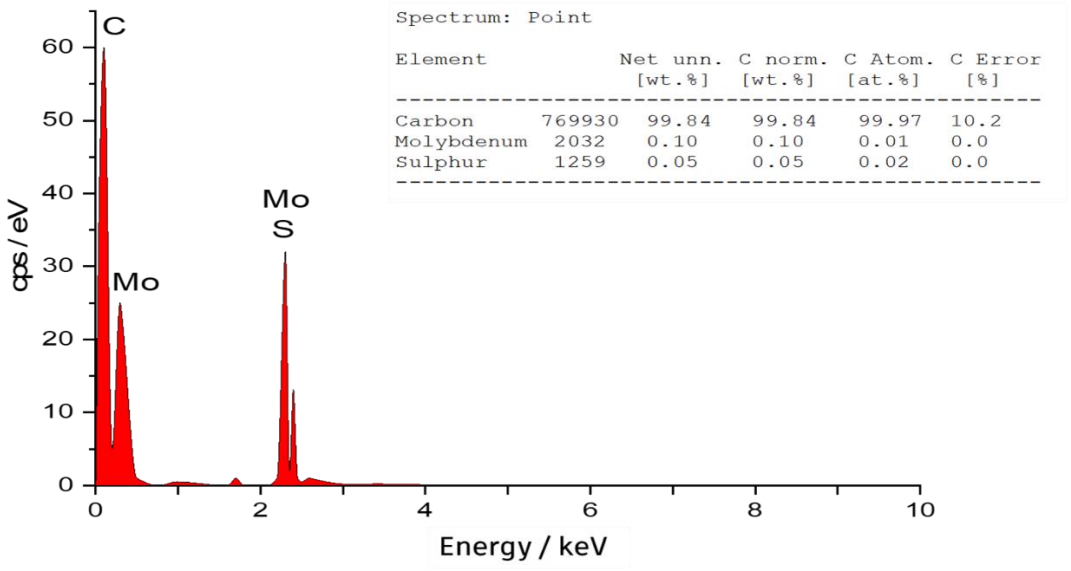

Figure 4.2. EDS spectra of the of the electrodeposited sample on glassy carbon. Molybdenum and sulfur were detected proving that the deposition resulted in some form of MoS_x.

Characterisation of the modified MoS_2/GC electrode and nanoparticle samples by X-ray photoelectron spectroscopy confirmed the presence of both Mo and S in both samples. High resolution XPS spectra of the S 2p and Mo 3d regions (see Fig. 4.3A)**,** indicates the presence of Mo^{4+} by the peaks at 228.8 eV and 232.6 eV, and Mo^{6+} is shown by the peaks at 232.5 eV and 235.6 eV, with the spin-orbit splitting of *ca* 3.8 eV and 3.1 eV respectively.[13,14] The Mo(VI) is believed to be due to the presence of MoO_3, and this is supported by the detection of a significant amount of oxygen (O 1s) in the sample. Ambrosi and Pumera also detected the Mo peak at ≈236 eV which they assigned to the Mo (VI) oxide species because of the presence of significant amounts of oxygen in their XPS spectra.[13]

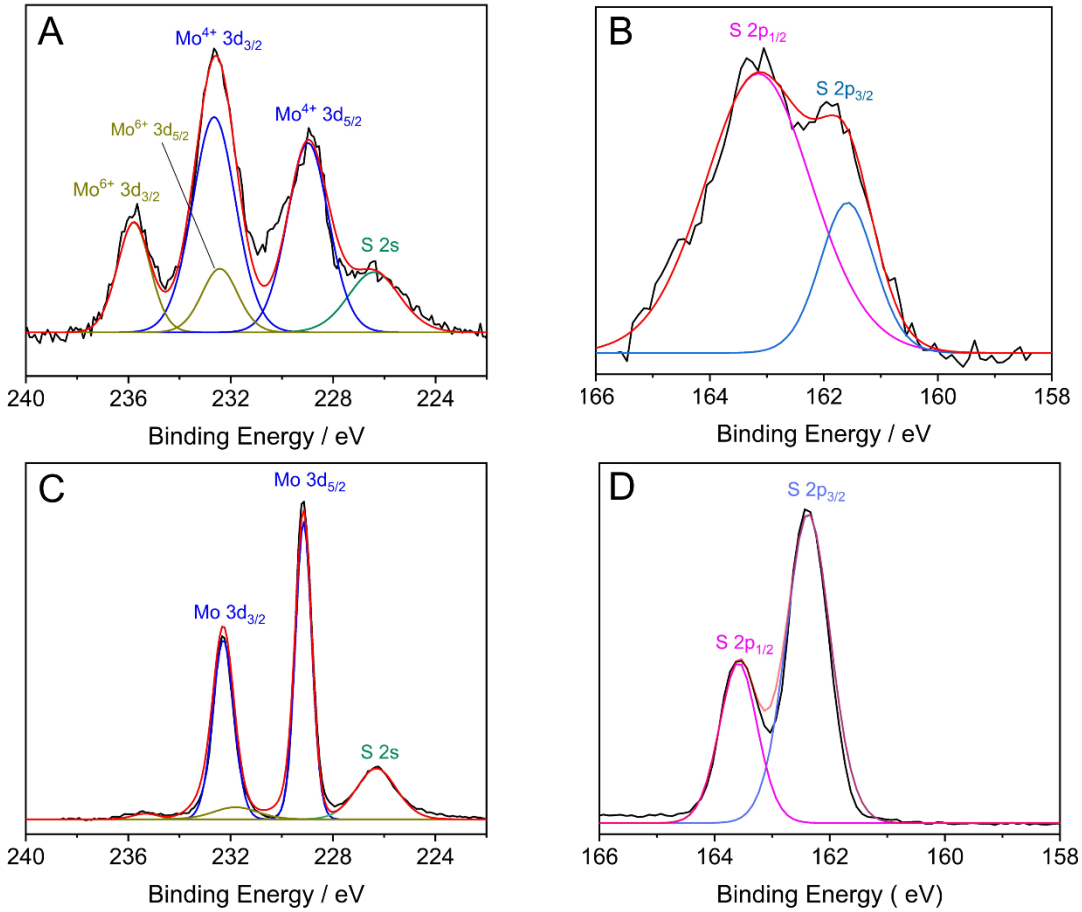

Figure 4.3. High resolution spectra of the Mo (A &C) and S (B&D) regions from the wide scan spectra. A and B spectra are from the modified electrode sample while C and D are from the nanoparticle sample.

The detection of a doublet peak for the S 2p signal indicates that the sulfur components present are S^{2-} and S_2^{2-}.[47] Detection of the S_2^{2-} species suggests the presence of MoS_3 in the sample which agrees with past structural studies that discovered the S_2^{2-}species and gave the formal composition as $Mo^{IV}(S^{2-})(S_2^{2-})$.[15] The formation of MoS_2 via cyclic voltammetry (involving both cathodic and anodic potentials) has been reported to create a mixed composition film of MoS_2 and MoS_3.[8,13] Accounting for the presence of Mo oxides, the Mo:S ratio obtained for the deposited layer resulted in a ratio of 1:2.2 from the wide spectra. XPS analysis of the nanoparticle sample, shown in Fig. 4.3 (C &D), shows a attenuation in the Mo oxide peak as compared to the electrodeposited sample thereby indicating a greater proportion of Mo^{4+}.

4.2.2 pH and kinetic study of HER on electrodeposited MoS_2

The electrodeposited MoS_2-modified electrode was then used to study the HER using linear sweep voltammetry at a range of pH values. The aim of the pH study was to determine a pH at which the HER signal from the deposited MoS_2 did not significantly degrade after continuous voltage scanning. This was to ensure that with the selected pH, the MoS_2 nanoparticles did not degrade over the timescale of the nanoparticle impact study. Linear sweep voltammetry was then carried out to study the HER. A potential sweep from 0.2 V towards negative potentials was run at a voltage scan rate of 20 mV s^{-1} in a pH 2 sulfuric acid solution and the resulting current change recorded. The pH of the solution was then changed, and the experiment repeated. Varying the pH resulted in a change in onset potential (defined here as the potential at which the current density was 0.5 mA cm^{-2}) for HER as shown in Fig. 4.4A confirming the varying HER activity according to specific pH regions, as reported in the literature.[9] The acidic region ($0 \leq \text{pH} < 4$), acidic to neutral ($4 \leq \text{pH} < 7$) and neutral to alkaline ($7 \leq \text{pH} \leq 10$) regions showed different HER mechanisms due to differences in the predominant HER active sites at the electrodeposited MoS_2 surface within each region.[16] For pH ≤ 2, the HER mechanism is operated by the electroreduction of hydronium ions while for pH ≥ 3 the HER occurs via the water reduction mechanism. Some pH display a peak/maximum in current and this result from non-uniform distribution of catalytic active sites on the MoS_2 film which leads to maximum activity or blockage by adsorbed species at specific pH levels and potentials, causing a peak in current density.

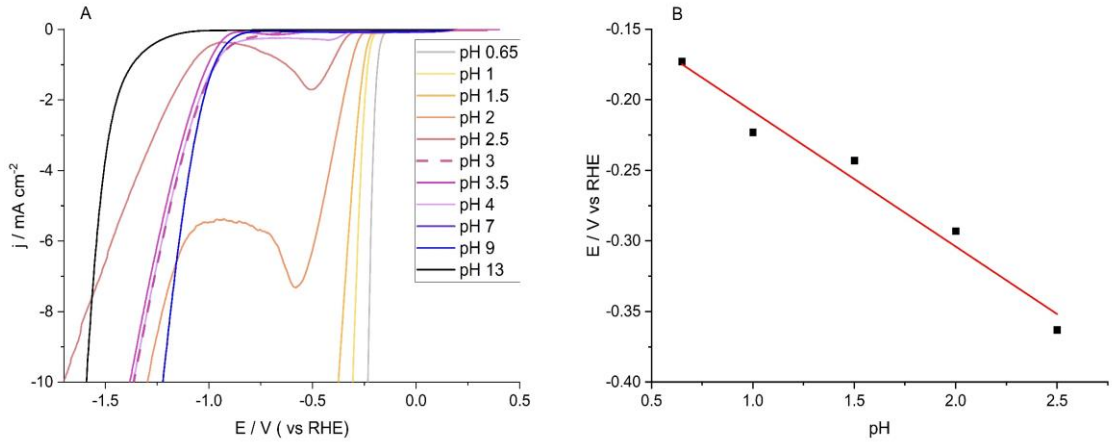

Figure 4.4. (A) LSVs recorded at a voltage scan rate of 20 mV s^{-1} in different pH solutions using a GC working electrode modified with electrodeposited MoS_2. The solutions contained sulfuric acid and sodium hydroxide of varying concentrations to achieve the pH required, along with 0.49 M of K_2SO_4 as supporting electrolyte. **(B)** A plot of the relationship between onset potentials and pH value, with a best-fit line, of equation $E = -(9.56 \times 10^{-2})pH - 0.112$, obtained by linear regression. The plot ends at pH 2.5 because of degradation of the electrodeposited layer started occurring at pH ≥3 (dashed line).

According to the Nernst equation (Eqn 1.22 in chapter 1), a potential change of 59 mV is expected per each pH unit for a single electron reaction. Based on this, a plot of onset potential against pH was drawn (see Figure 4.4B) and the gradient of the line of best fit was found to be 96 mV per pH unit. This suggests a mixture of a one electron one proton (59 mV/pH) and a one electron two protons (118 mV/pH) mechanisms for the proton coupled electron transfer mechanism. Overall, there is an onset potential increase with an increase in pH value but at pH 3 to 4 there is degradation of the MoS_2 substrate hence the huge shift in onset potential from pH 3. The degradation is a chemical process driven by pH and hydroxide ions that weakens the Mo-S bonds and HER electrochemical reactions exacerbate the degradation due to applied potential and accumulation of OH^- ions near the electrode surface.[17]

To further investigate the stability of the electrodeposited MoS_2 a series of LSV scans were recorded in different pH solutions. A total of 10 consecutive scans were completed for each modified electrode in

each pH solution. The degradation of MoS_2 is shown by the change in onset potential on the consecutive scans on Fig. 4.5. A solution of pH 2 was selected for further study of HER kinetics because the MoS_2 degradation is lower at this pH compared to pH >3. At pH 2, the onset potential for HER was -0.29 V (vs RHE).

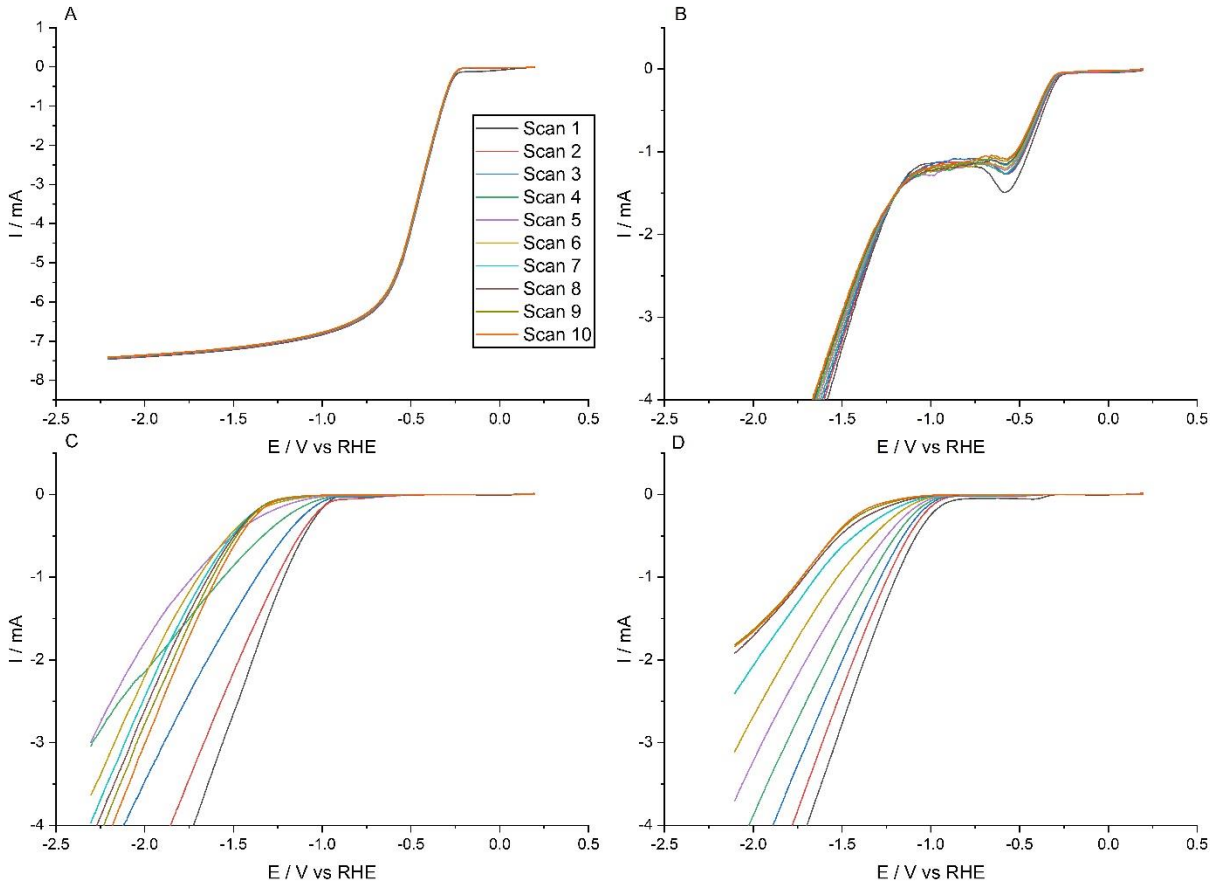

Figure 4.5. Repeated HER scans for electrodeposited MoS_2 in different pH solutions to investigate degradation: (A) pH 1.5, (B) pH 2, (C) pH 3, and (D) pH 4. In all cases a graphite counter and Ag/AgCl reference electrode were used and a voltage scan rate of 5 mV s^{-1}. A total of 10 successive scans for each modified GC electrode in a specific pH was carried out and the change recorded (the colour key shown in (A) applies to all plots).

To obtain data for kinetic analysis of HER experiments, LSV scans from 0.2 to -0.8 V (vs RHE) in a pH 2 sulfuric solution at a scan rate of 20 mV s^{-1}, were conducted on an MoS_2-modified (electrodeposited) carbon fibre microelectrode (shown in figure 4.6 below). Electrochemical deposition was carried out on the carbon fibre microelectrode (33 µm diameter) under the same conditions as for the electrodeposition on the GC electrode.

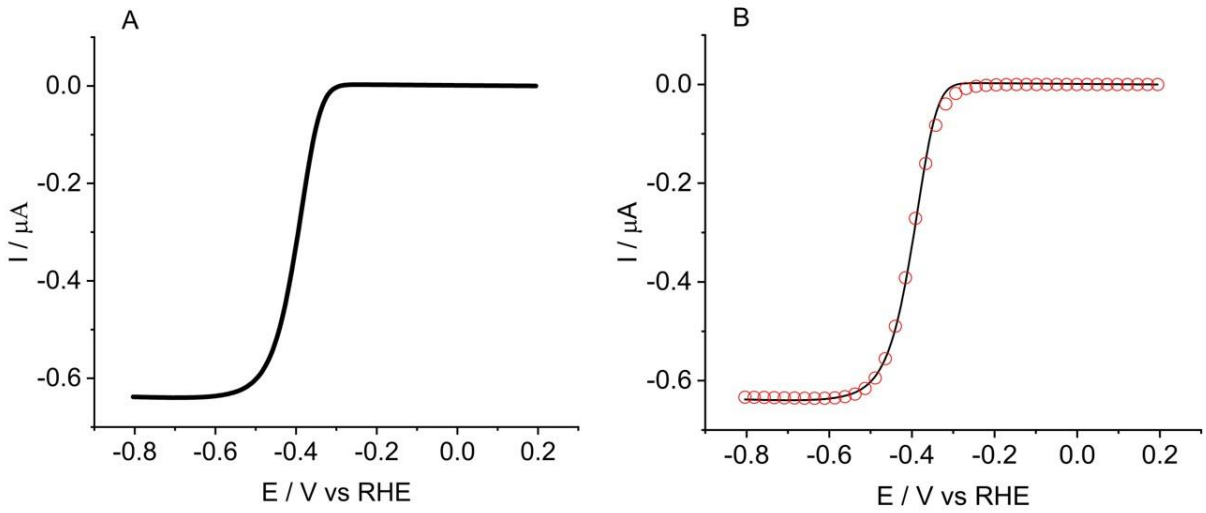

Figure 4.6 (A) LSV scan of the HER at the MoS_2 modified carbon fibre microelectrode in a solution of 0.01 M H_2SO_4 and 0.49 M K_2SO_4 at a scan rate of 20 mV s^{-1}. **(B)** Experimental data (−) and best-fit plot of the waveshape fitting simulation (○) using DigiElch software.

The MoS_2-modified microelectrode scans were then analysed to extract kinetic information. The Tafel slope for the electrodeposited MoS_2 was found to be 45 mV dec^{-1} with a transfer coefficient of 0.64 (Figure 4.7). Automated waveshape fitting was then performed using DigiElch software using a formal potential of -0.12 V (vs RHE), and diffusion coefficient of 9.6 × 10^{-5} cm^2 s^{-1}.[16] Grid parameters were varied in each coordinate to ensure the simulation result was independent of them (i.e. converged). This resulted in a standard electrochemical rate constant of (3.17 ± 0.3) × 10^{-5} cm s^{-1} and a transfer coefficient of α = 0.67 ± 0.02 which is in excellent agreement with the value derived from Tafel analysis. A

minimum of five voltammograms were used and Fig. 4.6B illustrates an example of the best-fit plots from the simulations.

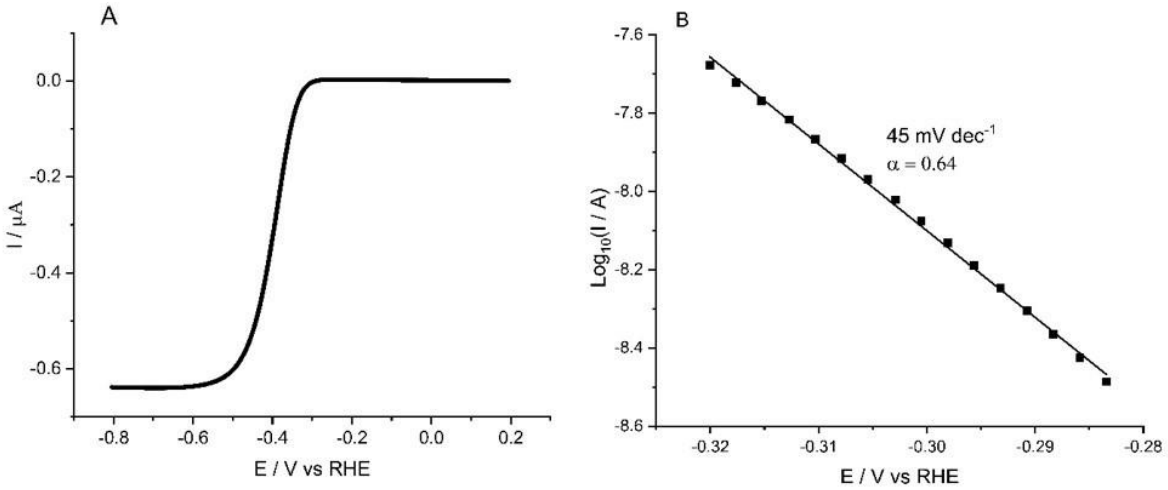

Figure 4.7. (**A**) A voltammogram obtained using electrodeposited MoS_2 for HER and the Tafel slope (**B**) derived from this voltammogram

The HER reaction mechanism is believed to involve a two-step process which may be restricted by any of the rate determining steps below:[18-20]

Table 4.1. HER mechanism. Data from [18-20]

Step	Equation	Tafel slope / mV dec^{-1}
Volmer	$H_3O^+ + e^- \rightarrow H_{ads} + H_2O$	120
Heyrovsky	$H_{ads} + H_3O^+ + e^- \rightarrow H_2 + H_2O$	40
Tafel	$H_{ads} + H_{ads} \rightarrow H_2$	30

The calculated Tafel slope value of ca 45 mV dec^{-1} for the MoS_2-modified electrode suggests that the Heyrovsky step is rate determining and falls within the literature range of Tafel slope values (40 to 50 mV dec^{-1}) reported for MoS_2 as an electrocatalyst for the hydrogen evolution reaction.[8,21,22]

4.2.3 HER at MoS_2 particles via impact voltammetry

Particle-impact electrochemistry was conducted with MoS_2 nanoparticles in pH 2 sulfuric acid solution (10 mM H_2SO_4 and 0.49 M K_2SO_4), using chronoamperometry at a range of potentials 0.3 V to -0.6 V (vs RHE) for 30 s duration using the low-noise potentiostat (discussed in detail under Experimental methods in section 3.4.2). Control experiments without nanoparticles were conducted at all potentials to confirm the absence of current transient signals, and no transient 'spikes' were detected in these scans (see Appendix 8.2). Next, analogous chronoamperograms were recorded using an identical solution containing 100 pM of MoS_2 nanoparticles. Reductive spikes were observed in chronoamperograms at potentials at (and more negative than) -0.10 V vs RHE. Figure 4.8 shows some typical current-time traces recorded with MoS_2 nanoparticles for potentials -0.25 V and -0.50 V (vs RHE). The spikes are due to the nanoparticles striking the surface of the working electrode at a sufficient overpotential at which the reduction of protons occurs at the MoS_2 particle surface.[7]

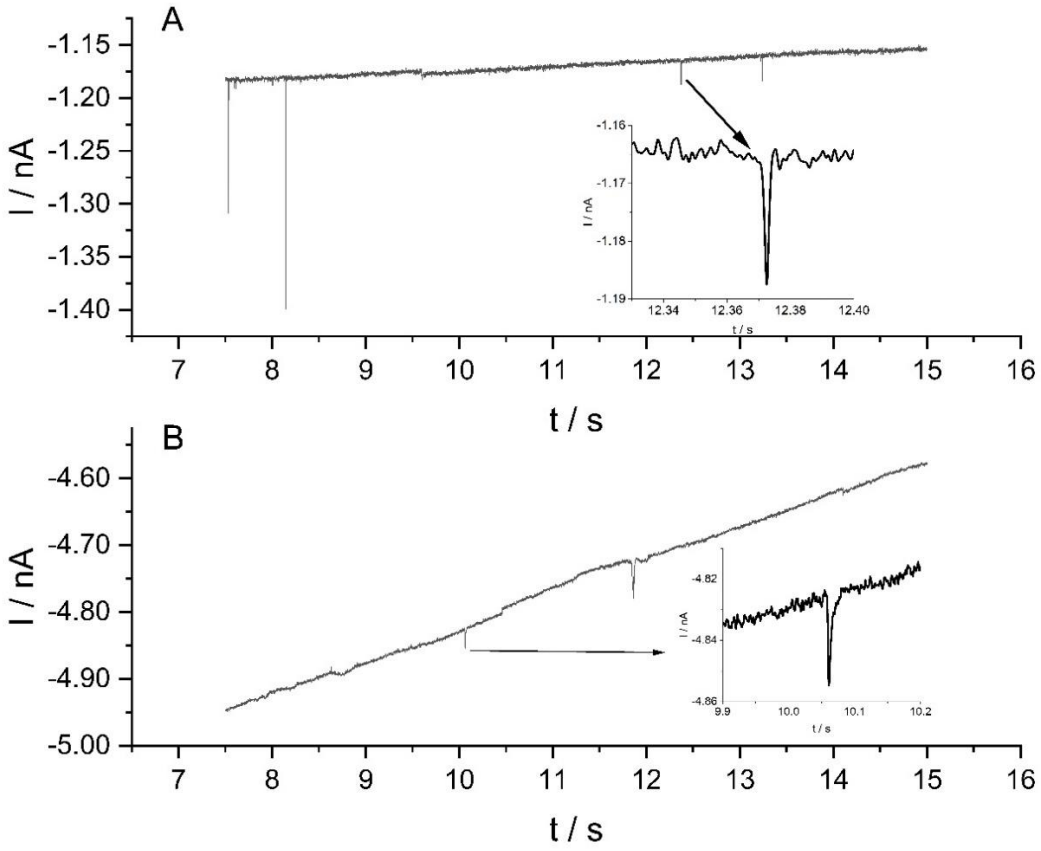

Figure 4.8. MoS_2 impact spikes for potentials held at **(A)** -0.25 V and **(B)** -0.50 V (vs RHE) for 30 seconds using a pH 2 suspension of 100 pM MoS_2 nanoparticles.

Analysis of the impact scans consisted of impact frequency determination and peak height calculations. Calculation of peak height involved separating the individual peaks in a scan and baseline correction for each of them. Figure 4.9 shows the overlaid individual peaks for scans at -0.2 V and -0.4 V (vs RHE). From the baseline corrected data, the peak height of each peak was derived, and this was done for all the scans at each potential from 0.2 V to -0.6 V (vs RHE). The overall average peak height at each potential was calculated and used in plotting the peak height graph in Fig. 4.10C. The frequency was calculated as the number of peaks recorded for the duration of that scan. For each potential from 0.2 V to -0.6 V (vs RHE), an average impact frequency was calculated and used in the impact frequency graph (see Fig. 4.9A)

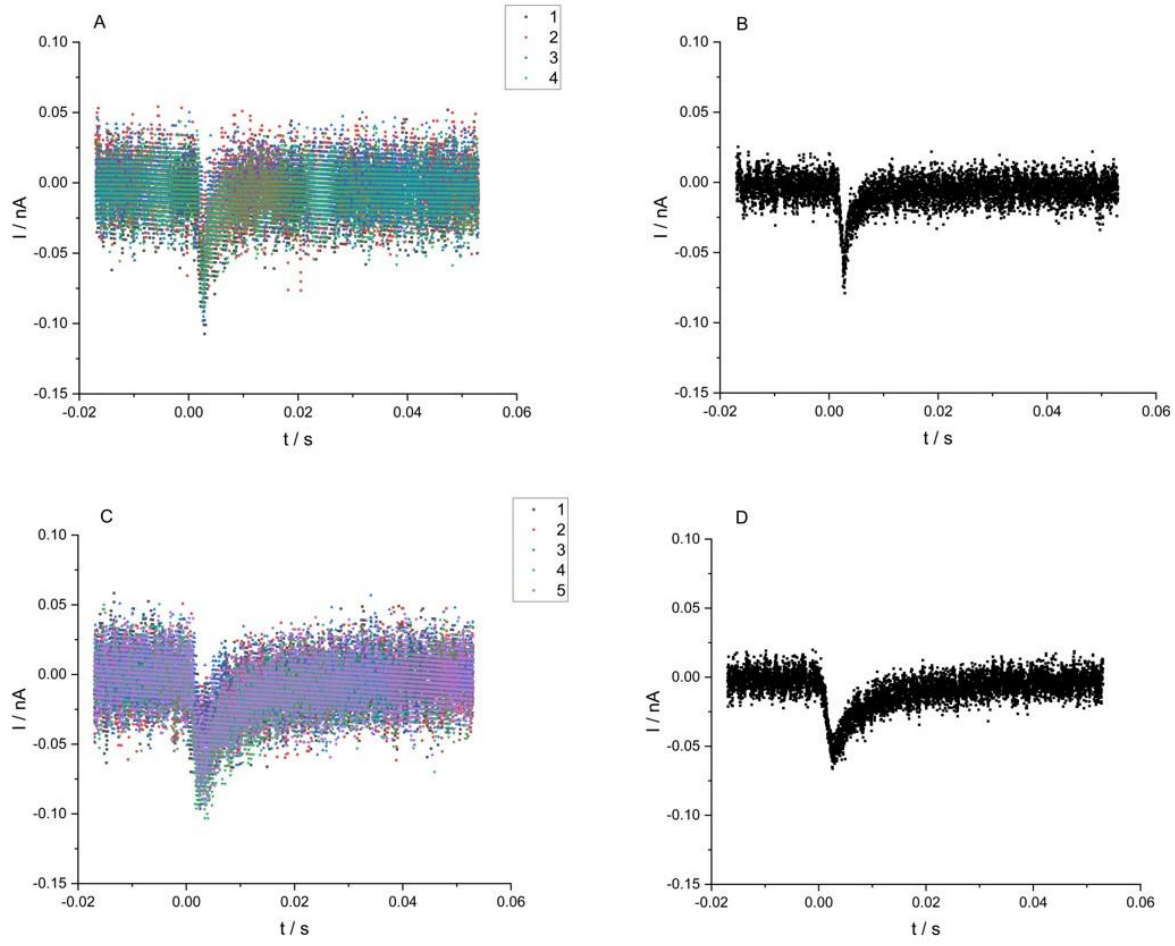

Figure 4.9. Individual peaks were identified and separately analysed for peak height derivation. **A** and **C** show the overlaid peaks for scans carried out at potentials -0.2 V and -0.4 V (vs RHE) respectively.

B and **D** displays the average peak height and shape for the peaks at -0.2 V and -0.4 V (vs RHE) respectively.

Figure 4.10 highlights the onset potential of MoS_2 for the HER impacts, shown in both impact signal frequency and average charge per impact, and was found to be -0.10 V (vs RHE). This is significantly different to the onset potential at the electrodeposited MoS_2 (-0.29 V vs RHE).

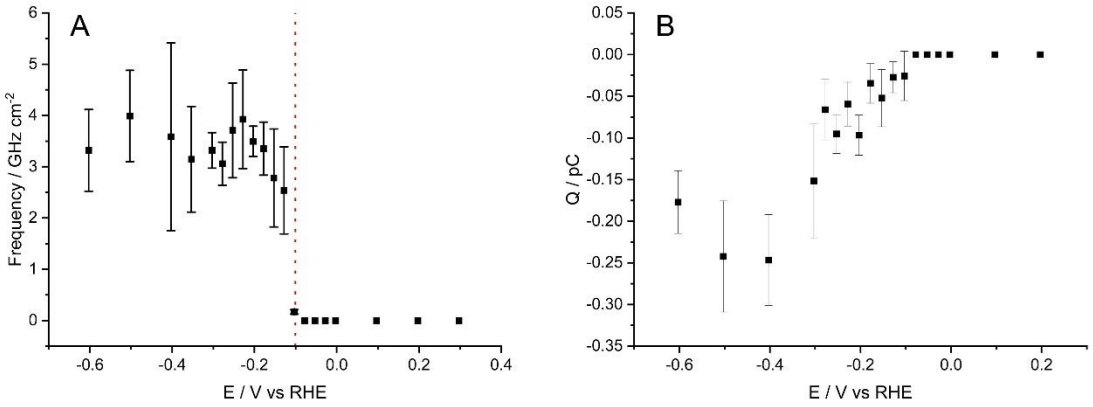

Figure 4.10. Plots of (**A**) average frequency, and (**B**) average charge of nanoparticle impacts at different potentials. The 'switch on' potential at -0.10 V (vs RHE) of the MoS_2 nanoparticles for the HER is shown in both plots.

To investigate the shift in onset potential between the electrodeposited and nanoparticle impacts, HER experiments were conducted using drop cast nanoparticles on the glassy carbon electrode. A 100 pM suspension of MoS_2 nanoparticles was made using ultrapure water and an aliquot of 10 µL was drop-cast onto a glassy carbon electrode and left to dry under a light source. The resulting coverage was sufficiently high to ensure planar diffusion to the NP-modified surface (average particle separation of 0.12 µm compared to approximate diffusion length >200 µm calculated from equation $L = \sqrt{Dt}$, where D is diffusion coefficient in cm^2/s and t is timescale of the experiment in seconds). This nanoparticle modified electrode was then used for HER in a solution of 0.01 M H_2SO_4 and 0.49 M K_2SO_4 at a scan rate of 20 mV s^{-1}. Figure 4.10B shows the resulting voltammogram, indicating an onset

for hydrogen evolution of ca -0.49 V (vs RHE) compared to electrodeposited MoS_2 (-0.29 V vs RHE) and the MoS_2 nano-impacts (-0.10 V vs RHE), which is within the range reported in literature of -0.30 V to -0.8 V (vs RHE), when adjusted for pH and reference electrode).[16,23,24] (Note here that the lower overpotential of the electrodeposited MoS_2 compared with the drop cast MoS_2 is due to the different surface moieties, structure and activity of these two forms[16])

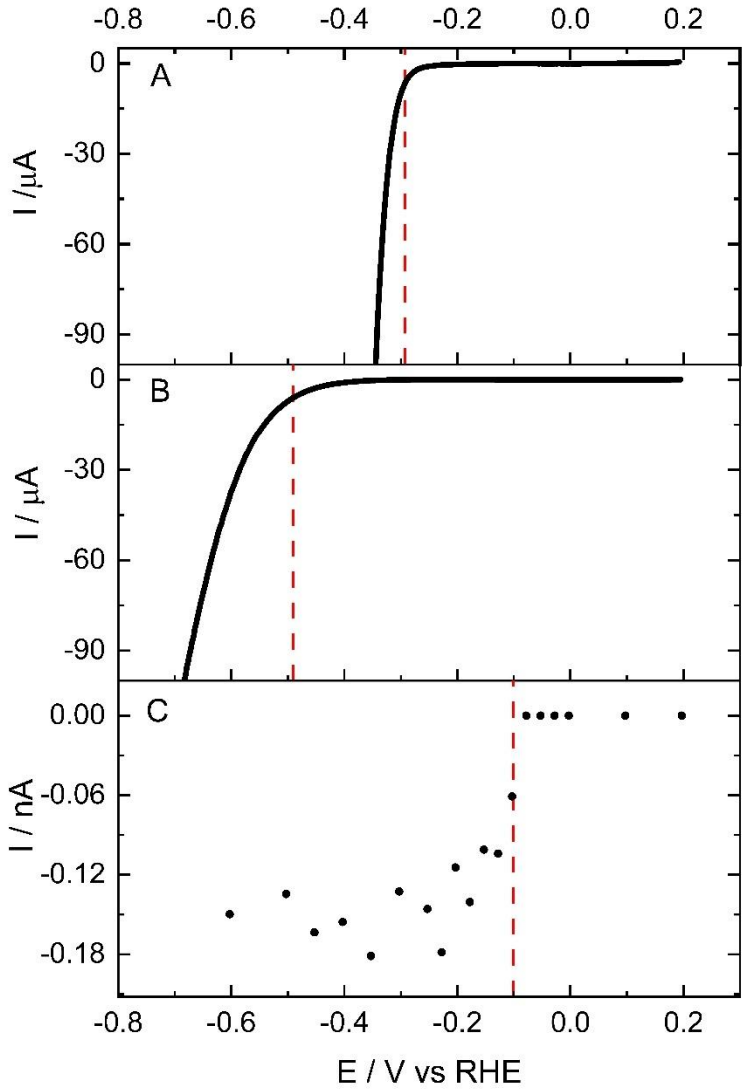

Figure 4.11. Comparison of the resulting current-potential curves for HER in 0.01 M sulfuric acid solution from using (**A**) electrodeposited MoS_2 from Figure 4.4A and (**B**) drop cast MoS_2 nanoparticles from Figure 4.6A. The peak heights from the nanoparticle impacts study have also been included (**C**)

to highlight the shift in onset potential between the different scans (shown in more detail in Figure 4.11). The red dotted lines indicate the onset potentials, as identified in the main text, for ease of reference.

Since the onset of HER for the drop cast MoS_2 NPs may be expected to be approximately the same as that recorded for the same NPs using the impact technique, the nano-impacts were analysed to gain kinetic information from the peak currents (shown on Fig. 4.11B). In conducting the analysis, care was required since the effects of electronic filtering on the transient current signals detected during impact experiments have been well-documented.[25,26] These effects can significantly distort the resulting data, and as such only minimal filtering was applied to the data for analysis[27] (here minimal filtering refers to only that inherent in the amplifier/DAC electronics, and no additional digital filtering). The nanoparticle spike currents were obtained from the unfiltered data and plotted versus potential to form an approximate voltammogram (Fig. 4.11C). Notwithstanding the approximate nature of interpreting the spike-derived voltammogram,[25-27] based on the known formal potential of -0.12 V (vs RHE), and α = 0.65 (taken as an average of the value determined from above), a range of k_0 values have been simulated in Figure 4.12.[28] The modelling of this data is necessarily approximate: the layered structure where thickness is likely to be the smallest dimension has been treated as a disc, and effective radius has been fitted as a variable, since the size of the nanoflake fragments in solution cannot be known.

The particularly large values for the standard electrochemical rate constant are due to the few trilayer to single trilayer MoS_2 as they have been shown to be more catalytical active for HER. These values are within the range reported by McKelvey et al, where values of k_0 were found to vary with the number of trilayers of MoS_2 from *ca* 1.5 cm s^{-1} for 3 trilayers to 250 cm s^{-1} for a single trilayer.[29] Based on their analysis, the results above indicate the impact signals commencing at the potential of ca -0.10 V (vs RHE) are derived from impacts of particles with approximately 2 trilayers,[29-31] which we ascribe to partial exfoliation of the commercial MoS_2 particles during the sample preparation involving dispersion in water via ultrasonication, given widespread literature reports on the use of ultrasound for exfoliating TMDs and other layered materials.[32-34]

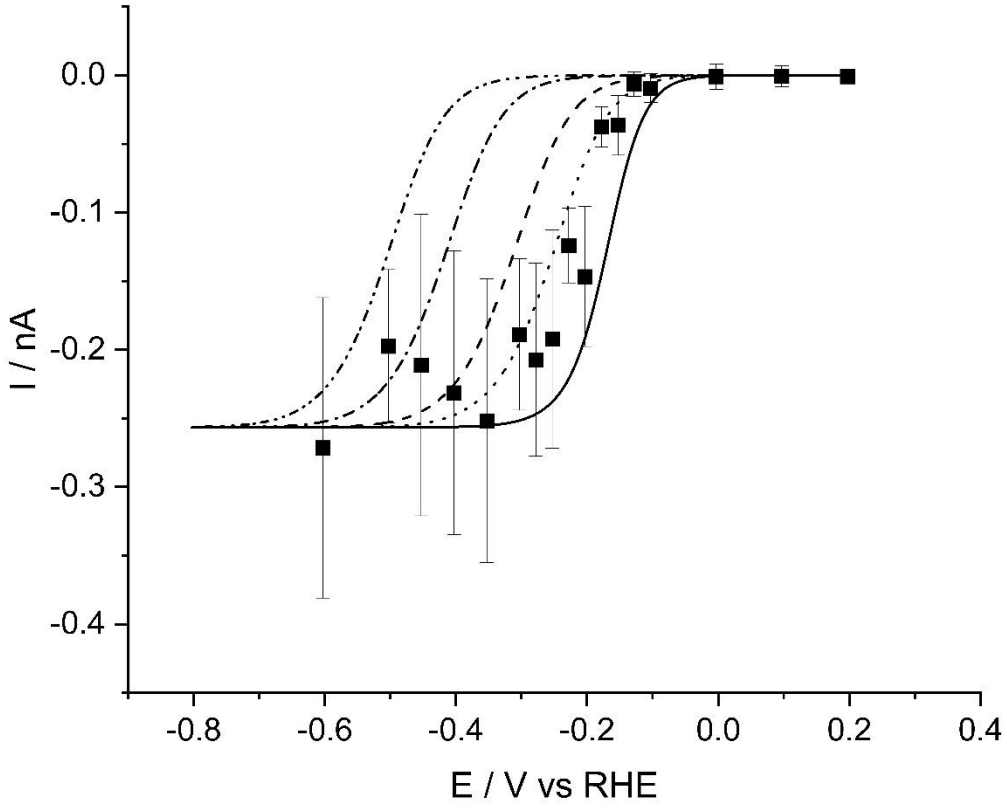

Figure 4.12. Experimental data (■) and simulated waveshapes for impact signals of HER at MoS_2 particles. Simulations are for D = 9.6 × 10^{-5} cm s^{-2}, α = 0.67, E_f^0 = -0.120 V (vs RHE), r = 8 nm and k_0 values (all in cm s^{-1}) of: 10^{-2} (- •• -), 0.1(- • -), 1.5 (- - -), 7.5 (• • •), and 250 (—).

We therefore postulate that the HER onset at -0.10 V (vs RHE) due to these few trilayer particles may be present in the drop cast voltammetry (due to similar preparation of the NP suspension) but are not visible on the current scale of the experiment due to the greater capacitance of the GC macroelectrode, hence the apparent onset of HER appears at greater overpotentials than either the NP impact or electrodeposited MoS_2 results.

The varying degrees of exfoliation caused by the sonication of the MoS_2 NP suspension will have resulted in a wide distribution of particle sizes, ranging from 1-2 trilayer nanoflakes to complete 90 nm particles. The rates of diffusion of these particles, and hence the frequency of impacts under diffusion-

only conditions, are expected to be inversely proportional to their size (via the Stokes-Einstein equation) as well as influenced by their shape (i.e. spherical, ellipsoidal, etc).[35] Hints of these effects may be seen in figure 4.10, where the impact frequency increases from the onset potential (-0.10 V vs RHE) before slightly decaying past an approximate maximum around -0.2 to -0.3 V (vs RHE), notwithstanding the error bars: this trend could result from a particle size distribution where the relative occurrence of small, rapidly diffusing, fragments is low increasing to more abundant, larger 90 nm particles, which diffuse more slowly. The impacts due to larger particles, with slower kinetics and an HER onset of ca -0.49 V (vs RHE), are not noticeable in figures 4.11C and 4.12 due to the relatively low number of impacts analysed (n=10-12) for each potential more negative than -0.49 V (vs RHE).

To probe this hypothesis, a rotating disk electrode (RDE) was used in the NP suspension containing 0.01 M H_2SO_4 and 0.49 M K_2SO_4, to record a voltammogram during rotation. In this way the high rates of convection due to the RDE would minimise capacitative charging currents, transport the different sizes of fragments at a more uniform rate than diffusion alone, and the HER kinetics (which become slower as the number of trilayers in the fragments increase) may manifest itself in different apparent onset potentials if the size distribution of MoS_2 fragments was unequal. Figure 4.13 shows the resulting linear sweep voltammogram, recorded at a rotation speed of 1600 rpm, where 3 onsets appear to be present: at approximately -0.10 V, -0.25 V, and -0.50 V (vs RHE). The aim of the RDE study was to show the various onset potentials related to the different trialyers of MoS_2 hence showing only a single rotation speed in figure 4.13.

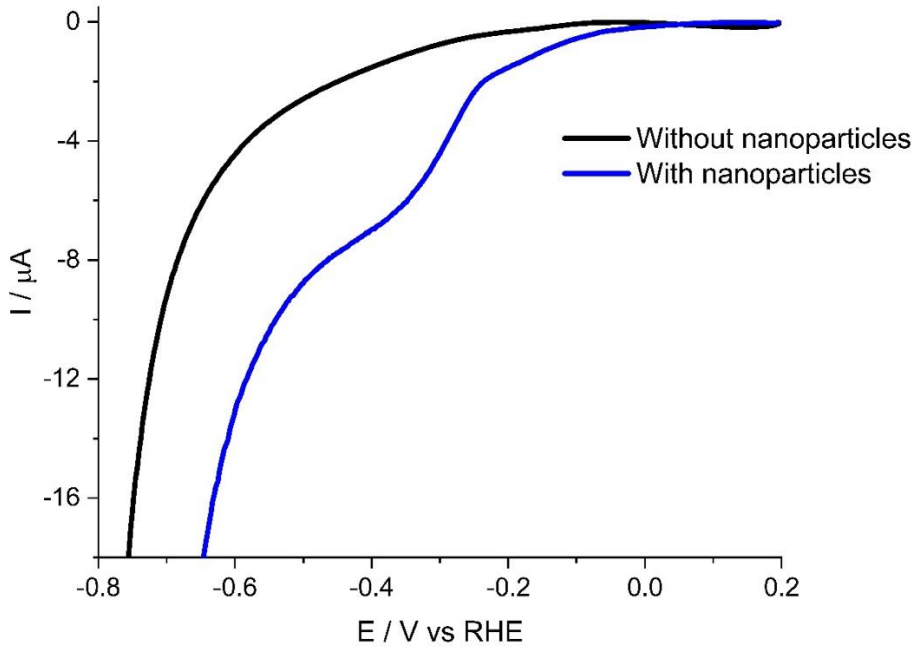

Figure 4.13. Rotating disk linear sweep voltammetry of a GC electrode in a solution containing 0.01 M H_2SO_4 and 0.49 M K_2SO_4 at 1600 rpm without MoS_2 NPs (—) and MoS_2 NPs (—).

To confirm the presence of few trilayer platelets of MoS_2, atom force microscopy images were recorded for a deposit of the ultrasonicated MoS_2 NPs, deposited onto a freshly cleaved mica surface. A wide range of particle sizes were observed (see Appendix 8.6 for further images), and figure 4.14 shows an area of deposit displaying smaller NP fragments. The smallest NPs observed had an approximate height of ca. 0.6 - 0.7 nm with the next smallest a factor of two larger, around 1.3 - 1.4 nm. This is in excellent agreement with literature values for the thickness of a trilayer of MoS_2 of 0.615 for single nanosheets,[36] and confirms the interpretation of the kinetic analysis of the electrochemical impacts.

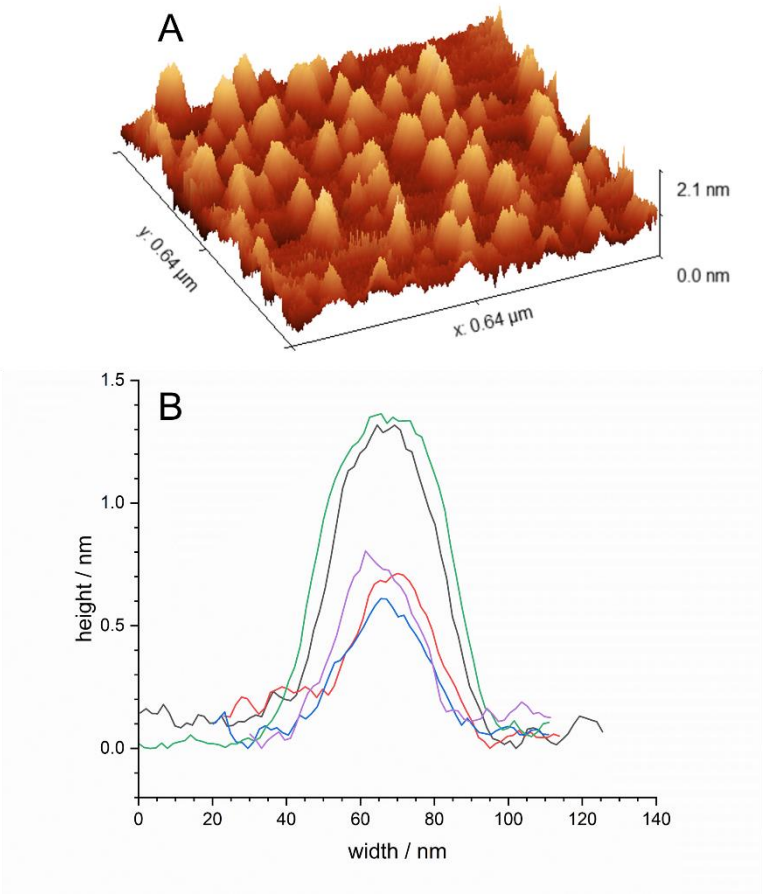

Figure 4.14. (A) AFM surface topography image of drop cast MoS_2 NPs on cleaved mica substrate, and **(B)** cross sectional height profile for 5 platelets representative of the overall scan area, showing thicknesses in multiples of ca. 0.65 nm.

4.2.4 Hydrogen production

To verify that impact signals detected at potentials negative of -0.10 V (vs RHE) were due to hydrogen evolution, the three-electrode cell was scaled-up and modified to capture any gases evolved for analysis and identification via gas chromatography (see figure 4.15 below).

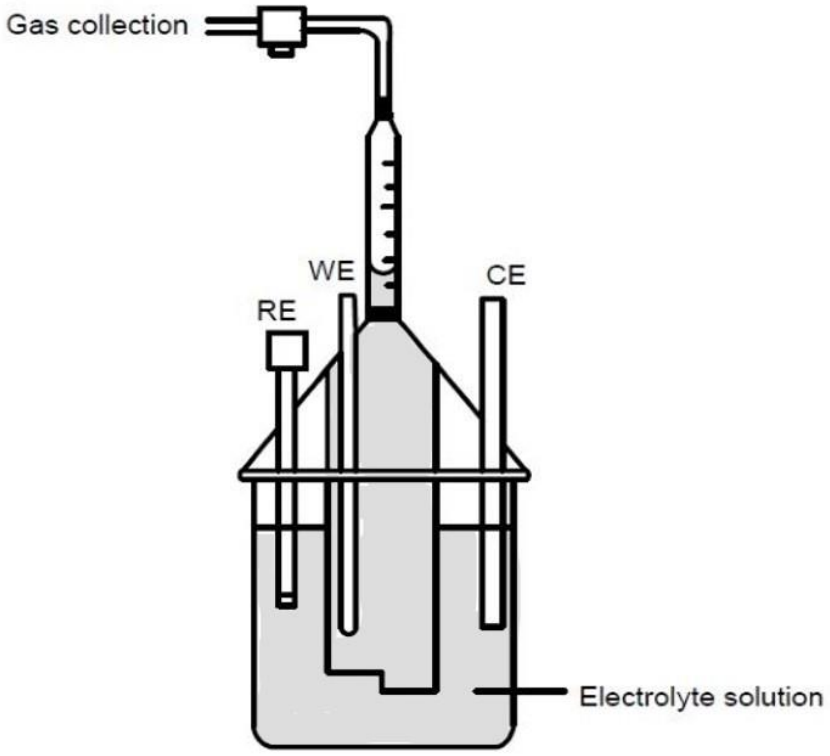

Figure 4.15. Schematic diagram of the electrolyser set up for the scaled-up nanoparticle impact study.

A graphite rod (6 mm diameter and 125 mm length) working electrode was used for an increased surface area for impacts to occur on, with a correspondingly larger graphite counter electrode and Ag/AgCl reference electrode which was housed in a separate fritted compartment. The volume of the nanoparticle suspension was increased to 500 mL and the concentration to 3.0 nM to ensure that a sufficient volume of gas for testing would be produced. A control experiment without the MoS_2 nanoparticles was initially conducted at -0.40 V and -0.15 V vs RHE for 4 hours and from this set-up, hydrogen gas was not detected when gas chromatography testing was conducted. Chronoamperometric measurements were then conducted in solution containing MoS_2 nanoparticles at two potential values (-0.40 V and -0.15 V vs RHE) for 4 hours for sufficient gas to be produced. The gas produced (0.9 mL by volume at -0.15 V and 2.1 mL at -0.40 V vs RHE) was collected in a gas syringe via a shut off valve connector (see figure 4.15) and injected into the gas chromatograph which confirmed it to be hydrogen (see Fig. 4.16). The faradaic efficiency was calculated at these two potentials and found to be 45% and 48% for -0.15 V and -0.40 V (vs RHE) respectively.

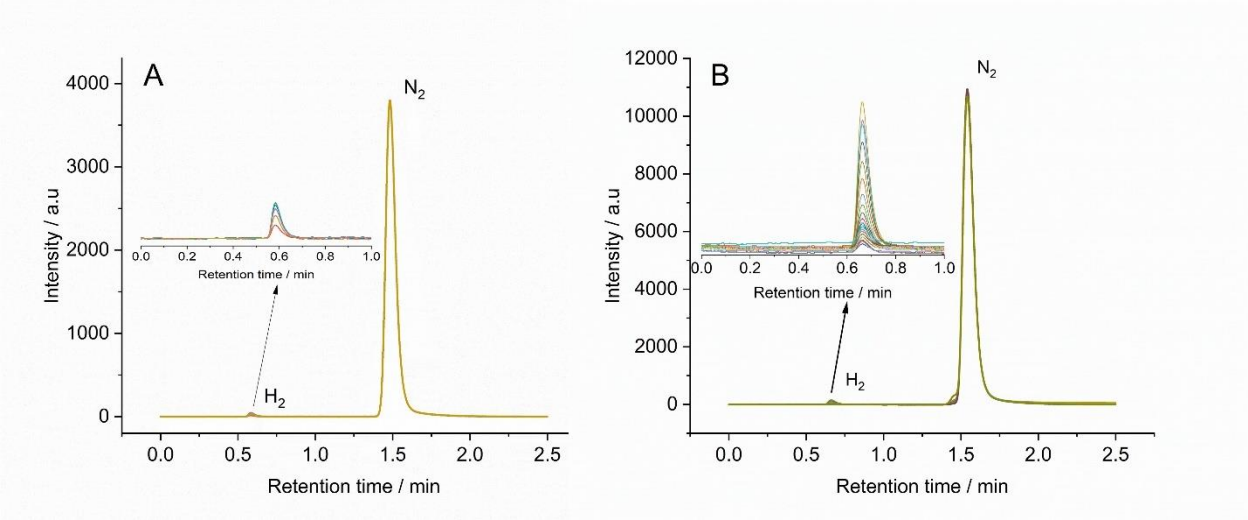

Figure 4.16. Gas chromatograms of the impact experiments at potentials (A) -0.15 V, and (B) -0.40 V (vs RHE).

4.3 Conclusion

In this chapter, the catalytic effects of amorphous and nanoparticulate forms of MoS_2 on the hydrogen evolution reaction (HER) were investigated as distinct structural morphologies of the material. An amorphous film of MoS_2 was electrodeposited onto a glassy carbon electrode, and its chemical composition was confirmed through energy-dispersive spectroscopy (EDS) and X-ray photoelectron spectroscopy (XPS) characterization. Subsequently, a stability study was conducted in various pH solutions, demonstrating that the MoS_2 film remained stable in pH 2 sulfuric acid solution. This stability finding suggests that the nanoparticles of MoS_2 would also exhibit stability under similar pH conditions.

The impact electrochemistry of MoS_2 nanoparticles was studied in comparison with the voltammetry of both dropcast MoS_2 nanoparticles and electrodeposited MoS_2. Each was found to have a different onset potential for the hydrogen evolution reaction in pH 2 sulfuric acid. The impact study revealed an onset potential of -0.10 V for HER, compared to -0.49 V and -0.29 V (vs RHE) for the dropcast and electrodeposited MoS_2 respectively. Scale-up of the impact experiment confirmed the impact production of H_2 gas via gas chromatography.

Analysis of the peak currents suggested that “few-trilayer” fragments were responsible for the low-overpotential for HER, with the apparent electrochemical rate constants for these 1-3 trilayer fragments in line with those reported by McKelvey et al.[28] The apparent absence of the -0.10 V (vs RHE) onset in the drop cast experiment is ascribed to the ultralow currents being lost within capacitative currents of the diffusion-only voltammogram. This hypothesis was supported by an experiment using a rotating electrode within the NP-suspension which appeared to indicate that an onset of ca -0.10 V (vs RHE) was present and confirmed by AFM imaging showing the presence of NPs of heights ca 0.65 nm and 1.30 nm corresponding to 1 and 2 trilayers in agreement with literature.[35]

4.4 References

(1) Jaramillo, T. F.; Jørgensen, K. P.; Bonde, J.; Nielsen, J. H.; Horch, S.; Chorkendorff, I. Identification of Active Edge Sites for Electrochemical H_2 Evolution from MoS_2 Nanocatalysts. *Science,* 2007, **317**, 100–102. https://doi.org/10.1126/science.1141483.

(2) Hinnemann, B.; Moses, P. G.; Bonde, J.; Jørgensen, K. P.; Nielsen, J. H.; Horch, S.; Chorkendorff, I.; Nørskov, J. K. Biomimetic Hydrogen Evolution: MoS_2 Nanoparticles as Catalyst for Hydrogen Evolution. *J. Am. Chem. Soc.* 2005, **127**, 5308–5309. https://doi.org/10.1021/ja0504690.

(3) Bonde, J.; Moses, P. G.; Jaramillo, T. F.; Norskov, J. K.; Chorkendorff, I. Hydrogen Evolution on Nano-Particulate Metal Sulfides. *Faraday Discuss*. 2008, **140**, 219–231. https://doi.org/10.1039/b814058h.

(4) Pumera, M. Impact Electrochemistry: Measuring Individual Nanoparticles. *ACS Nano*. 2014, **8**, 7555–7558. https://doi.org/10.1021/nn503831r.

(5) Oja, S. M.; Robinson, D. A.; Vitti, N. J.; Edwards, M. A.; Liu, Y.; White, H. S.; Zhang, B. Observation of Multipeak Collision Behaviour during the Electro-Oxidation of Single Ag Nanoparticles. *J. Am. Chem. Soc.* 2017, **139**, 708–718. https://doi.org/10.1021/jacs.6b11143.

(6) Oja, S. M.; Fan, Y.; Armstrong, C. M.; Defnet, P.; Zhang, B. Nanoscale Electrochemistry Revisited. *Anal. Chem*. 2016, **88**, 414–430. https://doi.org/10.1021/acs.analchem.5b04542.

(7) Lim, C. S.; Tan, S. M.; Sofer, Z.; Pumera, M. Impact Electrochemistry of Layered Transition Metal Dichalcogenides. *ACS Nano* 2015, **9**, 8474–8483. https://doi.org/10.1021/acsnano.5b03357.

(8) Merki, D.; Fierro, S.; Vrubel, H.; Hu, X. Amorphous Molybdenum Sulfide Films as Catalysts for Electrochemical Hydrogen Production in Water. *Chem. Sci.* 2011, **2**, 1262–1267. https://doi.org/10.1039/c1sc00117e.

(9) Hyun, C. M.; Choi, J. H.; Lee, S. W.; Park, J. H.; Lee, K. T.; Ahn, J. H. Synthesis Mechanism of MoS_2 Layered Crystals by Chemical Vapor Deposition Using MoO_3 and Sulfur Powders. *J. Alloys Compd.* 2018, **765**, 380–384. https://doi.org/10.1016/j.jallcom.2018.06.183.

(10) Luo, L.; Shi, M.; Zhao, S.; Tan, W.; Lin, X.; Wang, H.; Jiang, F. Hydrothermal Synthesis of MoS_2 with Controllable Morphologies and Its Adsorption Properties for Bisphenol A. *J. Saudi Chem. Soc.* 2019, **23**, 762–773. https://doi.org/10.1016/j.jscs.2019.01.005.

(11) Vrubel, H.; Hu, X. Growth and Activation of an Amorphous Molybdenum Sulfide Hydrogen Evolving. Catalyst. *ACS Catal.* 2013, **3**, 2002–2011. https://doi.org/10.1021/cs400441u.

(12) Belanger, D.; Laperriere, G.; Marsan, B. The Electrodeposition of Amorphous Molybdenum Sulfide, *J. Electoanal. Chem.* 1993, **347**, 165-183.

(13) Ambrosi, A.; Pumera, M. Templated Electrochemical Fabrication of Hollow Molybdenum Sulfide Microstructures and Nanostructures with Catalytic Properties for Hydrogen Production. *ACS Catal.* 2016, **6**, 3985–3993. https://doi.org/10.1021/acscatal.6b00910.

(14) Moulder, J. F.; Chastain, Jill. *Handbook of X-Ray Photoelectron Spectroscopy: A Reference Book of Standard Spectra for Identification and Interpretation of XPS Data*; Physical Electronics Division, Perkin-Elmer Corp, 1992.

(15) Weber, T.; Muijsers, J. C.; Niemantsverdriet, J. W. Structure of Amorphous MoS_3. *J. Phys. Chem.* 1995, **99**, 9194-9200. https://pubs.acs.org/sharingguidelines.

(16) Escalera-López, D.; Lou, Z.; Rees, N. V. Benchmarking the Activity, Stability, and Inherent Electrochemistry of Amorphous Molybdenum Sulfide for Hydrogen Production. *Adv. Energy Mater.* 2019, **9**, 1802614. https://doi.org/10.1002/aenm.201802614.

(17) Samy, O.; Zeng, S.; Birowosuto, M. D.; El Moutaouakil, A. A Review on MoS_2 Properties, Synthesis, Sensing Applications and Challenges. *Crystals* 2021, **11**, 355.

(18) Tan, S. M.; Pumera, M. Bottom-up Electrosynthesis of Highly Active Tungsten Sulfide (WS_{3-x}) Films for Hydrogen Evolution. *ACS Appl. Mater. Interfaces,* 2016, **8**, 3948–3957. https://doi.org/10.1021/acsami.5b11109.

(19) Li, Y.; Wang, H.; Xie, L.; Liang, Y.; Hong, G.; Dai, H. MoS_2 Nanoparticles Grown on Graphene: An Advanced Catalyst for the Hydrogen Evolution Reaction. *J. Am. Chem. Soc.* 2011, **133**, 7296–7299. https://doi.org/10.1021/ja201269b.

(20) Conway, B. E.; Tilak, B. V. Interfacial Processes Involving Electrocatalytic Evolution and Oxidation of H_2, and the Role of Chemisorbed H. *Electrochim. Acta,* 2002, **47**, 3571-3594.

(21) Shin, S.; Jin, Z.; Kwon, D. H.; Bose, R.; Min, Y. S. High Turnover Frequency of Hydrogen Evolution Reaction on Amorphous MoS_2 Thin Film Directly Grown by Atomic Layer Deposition. *Langmuir* 2015, **31**, 1196–1202. https://doi.org/10.1021/la504162u.

(22) Lukowski, M. A.; Daniel, A. S.; Meng, F.; Forticaux, A.; Li, L.; Jin, S. Enhanced Hydrogen Evolution Catalysis from Chemically Exfoliated Metallic MoS_2 Nanosheets. *J. Am. Chem. Soc.* 2013, 135, 10274–10277. https://doi.org/10.1021/ja404523s.

(23) Ambrosi, A.; Sofer, Z.; Pumera, M. 2H → 1T Phase Transition and Hydrogen Evolution Activity of MoS_2, $MoSe_2$, WS_2 and WSe_2 Strongly Depends on the MX_2 Composition. *Chem. Commun.* 2015, **51**, 8450–8453. https://doi.org/10.1039/c5cc00803d.

(24) Li, G.; Zhang, D.; Qiao, Q.; Yu, Y.; Peterson, D.; Zafar, A.; Kumar, R.; Curtarolo, S.; Hunte, F.; Shannon, S.; Zhu, Y.; Yang, W.; Cao, L. All the Catalytic Active Sites of MoS_2 for Hydrogen Evolution. *J. Am. Chem. Soc.* 2016, **138**, 16632–16638. https://doi.org/10.1021/jacs.6b05940.

(25) Sokolov, S. V.; Eloul, S.; Kätelhön, E.; Batchelor-McAuley, C.; Compton, R. G. Electrode–Particle Impacts: A Users Guide. *Phys. Chem. Chem. Phys.* 2017, **19**, 28–43. https://doi.org/10.1039/c6cp07788a.

(26) Stuart, E. J. E.; Tschulik, K.; Batchelor-McAuley, C.; Compton, R. G. Electrochemical Observation of Single Collision Events: Fullerene Nanoparticles. *ACS Nano,* 2014, **8**, 7648–7654. https://doi.org/10.1021/nn502634n.

(27) Batchelor-McAuley, C.; Ellison, J.; Tschulik, K.; Hurst, P. L.; Boldt, R.; Compton, R. G. In Situ Nanoparticle Sizing with Zeptomole Sensitivity. *Analyst,* 2015, **140**, 5048–5054. https://doi.org/10.1039/c5an00474h.

(28) Rees, N. V; Klymenko, O. V; Compton, R. G.; Oyama, M. The Electro-Oxidation of N, N-Dimethyl-p-Toluidine in Acetonitrile: A Microdisk Voltammetry Study. *J. Electroanal. Chem.* 2002, **531**, 33-34.

(29) Brunet Cabré, M.; Paiva, A. E.; Velický, M.; Colavita, P. E.; McKelvey, K. Electrochemical Kinetics as a Function of Transition Metal Dichalcogenide Thickness. *Electrochim. Acta* 2021, **393**, 139027. https://doi.org/10.1016/j.electacta.2021.139027.

(30) Yu, Y.; Huang, S. Y.; Li, Y.; Steinmann, S. N.; Yang, W.; Cao, L. Layer-Dependent Electrocatalysis of MoS_2 for Hydrogen Evolution. *Nano Lett.* 2014, **14**, 553–558. https://doi.org/10.1021/nl403620g.

(31) Velický, M.; Dryfe, R. A. W. Electrochemistry of 2D Nanomaterials. *Front. Nanosci.* 2021, **18**, 485–536. https://doi.org/10.1016/B978-0-12-820055-1.00009-5.

(32) Tan, X.; Kang, W.; Liu, J.; Zhang, C. Synergistic Exfoliation of MoS_2 by Ultrasound Sonication in a Supercritical Fluid Based Complex Solvent. *Nanoscale Res. Lett.* 2019, **14**, 317. https://doi.org/10.1186/s11671-019-3126-4.

(33) Qiao, W.; Yan, S.; He, X.; Song, X.; Li, Z.; Zhang, X.; Zhong, W.; Du, Y. Effects of Ultrasonic Cavitation Intensity on the Efficient Liquid-Exfoliation of MoS_2 Nanosheets. *RSC Adv.* 2014, **4**, 50981–50987. https://doi.org/10.1039/c4ra09001b.

(34) Sahoo, D.; Kumar, B.; Sinha, J.; Ghosh, S.; Roy, S. S.; Kaviraj, B. Cost Effective Liquid Phase Exfoliation of MoS_2 Nanosheets and Photocatalytic Activity for Wastewater Treatment Enforced by Visible Light. *Sci. Rep.* 2020, **10**, 10759. https://doi.org/10.1038/s41598-020-67683-2.

(35) Dill, K. A.; Bromberg, Sarina. Molecular Driving Forces: Statistical Thermodynamics in Biology, Chemistry, Physics, and Nanoscience, Garland Science, 2011.

(36) Fan, X.; Xu, P.; Li, Y. C.; Zhou, D.; Sun, Y.; Nguyen, M. A. T.; Terrones, M.; Mallouk, T. E. Controlled Exfoliation of MoS_2 Crystals into Trilayer Nanosheets. *J. Am. Chem. Soc.* 2016, **138**, 5143–5149. https://doi.org/10.1021/jacs.6b01502.

5 Electrochemically deposited transition metal dichalcogenide heterostructures as electrocatalysts: accelerated kinetics for the hydrogen evolution reaction

This chapter is based on the publication:

T. Manyepedza, T. Auvray. T. Friščić and N. V. Rees. Electrochemically deposited transition metal dichalcogenide heterostructures as electrocatalysts: accelerated kinetics for the hydrogen evolution reaction. *Electrochem. Commun*. 2023, **160**, 107678.

Credit authorship contribution statement

Tshiamo Manyepedza: Investigating, Conceptualization, Data curation, Formal analysis, Validation, Writing-original draft. **Thomas Auvray**: Investigation, Resources, Writing-Review and Editing. **Tomislav Friščić**: Supervision, Writing-Review and Editing. **Neil V. Rees**: Conceptualization, Supervision, Writing-Review and Editing.

5.1 Introduction

Several methods have been explored to enhance the hydrogen evolution reaction (HER) catalytic activity of transition metal dichalcogenides (TMDs), including doping, phase engineering, nanostructuring, and exfoliation aimed at increasing active edge sites.[1-3] Additionally, studies have investigated TMD heterolayer structures to modify band gaps, leading to improved photoelectrocatalysis for HER.[4-7] These heterolayers have demonstrated enhanced electrocatalytic hydrogen evolution behaviour.[8,9] Heterolayers can be fabricated using various methods such as hydrothermal synthesis, chemical vapor deposition, and electrochemical deposition.

Electrodeposition has been found to produce heterolayers with enhanced proton reduction activity. The cost-effectiveness of electrodeposition compared to more energy-intensive methods like chemical vapor deposition makes it an attractive method for synthesizing heterolayers as electrocatalysts for further investigation in HER applications.[10-12] This approach offers promising avenues for optimizing TMD heterolayer structures to achieve improved catalytic performance in hydrogen evolution.

This chapter investigates the hydrogen evolution reaction (HER) performance of various transition metal dichalcogenide (TMD) heterolayers prepared using nanoparticulate and electrodeposited forms. The experimental approach involved dropcasting a base layer of one type of TMD onto an ITO/glassy carbon substrate, followed by electrochemical deposition of a second TMD layer on top to create the heterolayer structure. For the electrodeposited form, a base layer of one type of TMD was first electrodeposited onto a glassy carbon substrate, followed by deposition of an overlayer of a different TMD. The catalytic effect of the resulting TMD heterolayers on the HER was evaluated using linear sweep voltammetry, and their stability in acidic media was assessed. Analysis of the voltammograms included Tafel and reaction kinetics analysis to gain insights into the HER kinetics and compare the catalytic activity of different heterolayers.

5.2 Results and discussion

5.2.1 Heterolayer formation

Heterolayer samples were fabricated from combinations of two different transition metal dichalcogenides (TMDs) to explore their HER catalytic activities compared to the individual layers of the starting TMDs. Two methods of forming the heterolayers were used: first, where the heterolayer consisted of a dropcast nanoparticle layer with an electrodeposited layer of a different TMD on top ('NP/L'), and second where the heterolayer was formed was by sequential electrodeposition of layers of the two different TMDs ('L/L'). Since the particulate and electrodeposited forms of the TMDs have different morphologies (crystalline vs amorphous), these two methods produced samples with potentially different interactions at the NP-L or L-L interface. The electrochemical deposition MoS_2 typically results in amorphous because the short time scales and local electrochemical environments favour the formation of disordered structures rather than crystalline MoS_2.[12,13] Other factors such as electrolyte composition, deposition potential and temperature can affect the degree of crystallinity achieved.

The first heterolayer fabricated was the $MoSe_2/MoS_2$ (NP/L) consisting of MoS_2 film electrodeposited on top of a layer of $MoSe_2$ particles on a glassy carbon (GC) electrode surface. An aliquot of 5 μL of a suspension of molybdenum diselenide powder in deionised water (concentration of 3.9 mM) was drop cast onto a 3 mm GC electrode and left to dry under light source (further explained in Experimental methods under section 3.3.2). $MoSe_2$ was mechanochemically milled using a 15 mL stainless steel jar with two 7 mm stainless steel balls at 2500 rpm for 5 min using a FlackTek SpeedMixer™ (model DAC 330-100 Pro) and a custom-made jar holder. The milled $MoSe_2$ particles had an average size of 240 nm with the size distribution ranging from 68 nm to 330 nm. The dropcast $MoSe_2$ particles had approximately 76% area coverage of the GC surface, calculated from the suspension concentration and volume dropcast. The modified electrode was then placed in a solution of 2 mM $(NH_4)_2MoS_4$ and 0.1 M $NaClO_4$ and cycled at a voltage scan rate of 50 mV s^{-1} for 50 cycles between 0.4 V and -1.1 V (vs Ag/AgCl) to electrodeposit a film of MoS_2 onto the $MoSe_2$ NP layer. Figure 1 shows the resulting

voltammogram with the expected oxidative and reductive peaks at -0.3 V and -0.8 V (vs Ag/AgCl) respectively as a result of the redox processes below:[12-14]

$$[MoS_4]^{2-} \rightarrow MoS_3 + {}^1/_8 S_8 + 2e^- \qquad (5.1)$$

$$[MoS_4]^{2-} + 2H_2O + 2e^- \rightarrow MoS_2 + 2HS^- + 2OH^- \qquad (5.2)$$

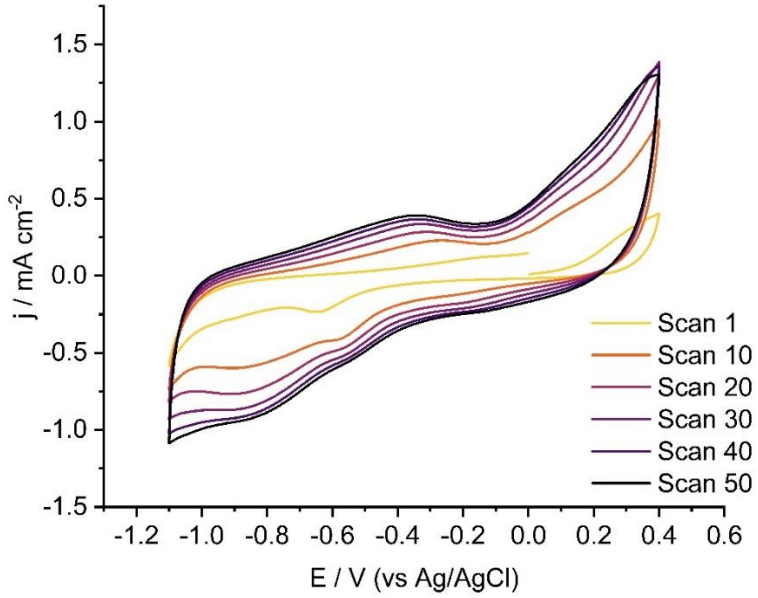

Figure 5.1. Cyclic voltammogram of the electrodeposition of MoS_2 onto $MoSe_2$ modified glassy carbon electrode in a solution of 2 mM $(NH_4)_2MoS_4$ and 0.1 M $NaClO_4$ at a scan rate of 50 mV s^{-1}.

The MoS_2 deposition voltammogram on $MoSe_2$ layer was identical to the voltammogram of MoS_2 deposition on bare GC (Appendix 8.1). A further study onto the MoS_2 deposition cycles was conducted to investigate the effects of deposition cycles/ film thickness on HER scans as well as determining the optimum number of cycles for full coverage of the electrode surface. The cycles were varied from 1, 2, 5, 10, 25 and 50 deposition cycles for the MoS_2 overlayer in the heterolayer samples. The resulting heterolayers were used for HER scans in a 10 mM H_2SO_4 and 0.1 M K_2SO_4 solution at a voltage scan rate of 20 mV s^{-1}. Figure 5.2 shows how the onset potential varied with the number of deposition cycles (which corresponds to film thickness) up until the 25th and 50th deposition cycles which have the same onset potential. At this point, full coverage of the GC-$MoSe_2$ layer is achieved and a stable $MoSe_2/MoS_2$

(NP/L) heterolayer is created. It was found that 50 CV cycles for the electrochemical deposition were sufficient for full coverage and forming a stable heterolayer.

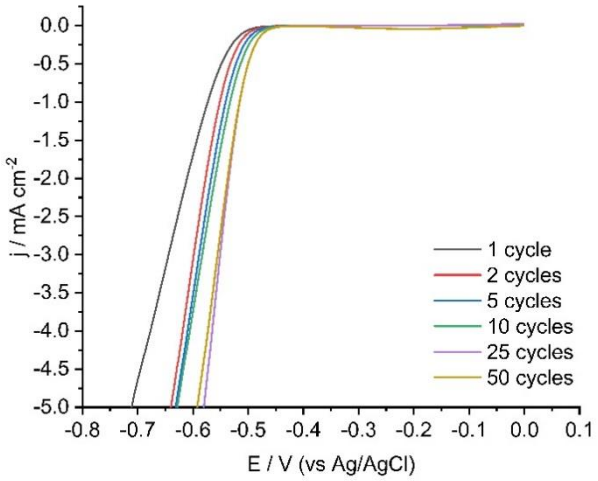

Figure 5.2. Linear sweep voltammograms carried out using $MoSe_2/MoS_2$ (NP/L) heterolayers with varying electrochemical deposition cycles of MoS_2. The different cycles correspond to the thickness of the deposited MoS_2 layer.

The formation of WS_2/MoS_2 (NP/L) heterolayer followed a similar procedure to that of $MoSe_2/MoS_2$ (NP/L) heterolayer, with the main difference being the use of WS_2 nanoparticles for the drop cast layer instead of $MoSe_2$. For the $MoS_2/MoSe_2$(NP/L) and $WS_2/MoSe_2$(NP/L) heterolayers, the nanoparticle underlayers were drop cast, and the $MoSe_2$ overlayer was electrodeposited onto them. The electrochemical deposition of $MoSe_2$ onto modified glassy carbon electrodes involved cyclic voltammetry carried out between 0 to -1.2 V (vs saturated calomel electrode, SCE) at a voltage scan rate of 50 mV s^{-1} for 50 cycles in a solution of 0.05 M H_2MoO_4, 0.01 M Na_2SeO_3 and 0.1 M $NaClO_4$ to ensure complete coverage of the electrode surface. Figure 5.3 illustrates the resulting voltammogram obtained during the $MoS_2/MoSe_2$ (NP/L) heterolayer formation process.[11]

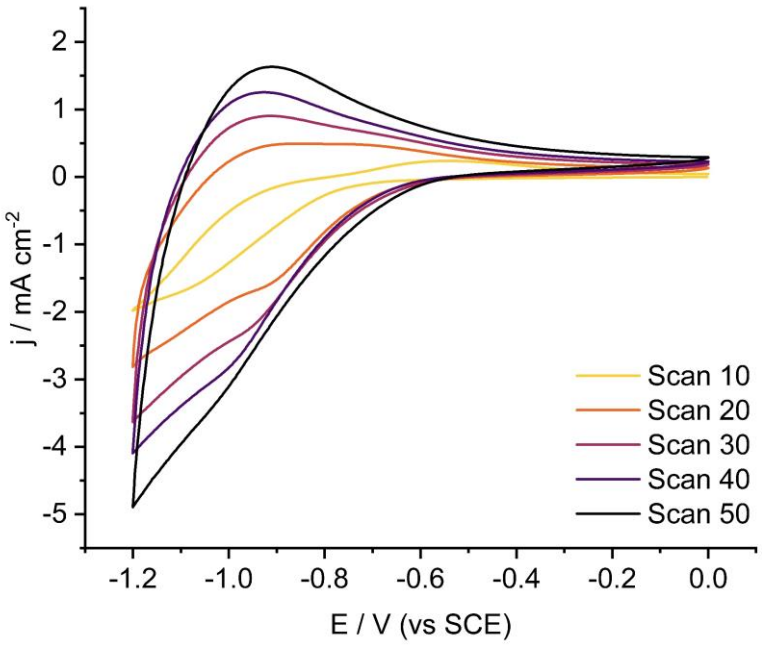

Figure 5.3. Cyclic voltammetry of the deposition of $MoSe_2$ onto a modified glassy carbon electrode at a scan rate of 50 mV s^{-1} in a solution containing 0.05 M H_2MoO_4, 0.01 M Na_2SeO_3, 0.1 M $NaClO_4$ and adjusted to pH 6.5 with NaOH.

The heterolayers were then tested for hydrogen evolution reaction (HER) catalytic activity and stability in acid solution through a series of cyclic voltammograms (CV). To determine the stability of the heterolayers, 10 successive CV scans were conducted in a solution of 10 mM H_2SO_4 and 0.1 M K_2SO_4 to observe any changes in the scan and onset potential for HER. Throughout this work, onset potential is defined as the potential (vs Ag/AgCl) at which current density is 0.5 mA cm^{-2}. Figure 5.4A shows that the onset potential remained approximately constant for the 10 scans of $MoSe_2/MoS_2$ (NP/L) heterolayer and no obvious degradation of the heterolayer was observed thus confirming that the previously reported high stability of electrodeposited MoS_2 in acidic conditions is not affected by the presence of the underlying drop cast $MoSe_2$ NPs.[14-16] These studies highlighted how stable an electrodeposited layer of MoS_2 is through repeated cycling in various conditions without observing any noticeable changes in overpotential during the scans. The electrochemical deposition of MoS_2 in this

study was conducted in a similar manner to these studies,[14,15] hence the similar high stability observed in sulfuric acid solution during HER scans. Another study was carried out to determine the stability of drop cast $MoSe_2$ particles during the hydrogen evolution reaction. The drop cast $MoSe_2$ particles were observed to be unstable in the acid solution when conducting HER voltammetry, where degradation of the layer was noticed as early as the second CV scan. The $MoSe_2$ layer dissolved into the solution with each scan until only the bare glassy carbon surface remained. This is not the case for the $MoSe_2/MoS_2$ (NP/L) heterolayer thanks to the stable overlayer of MoS_2 film which insulates the $MoSe_2$ layer thereby ensuring that the heterolayer remains intact during HER scans.

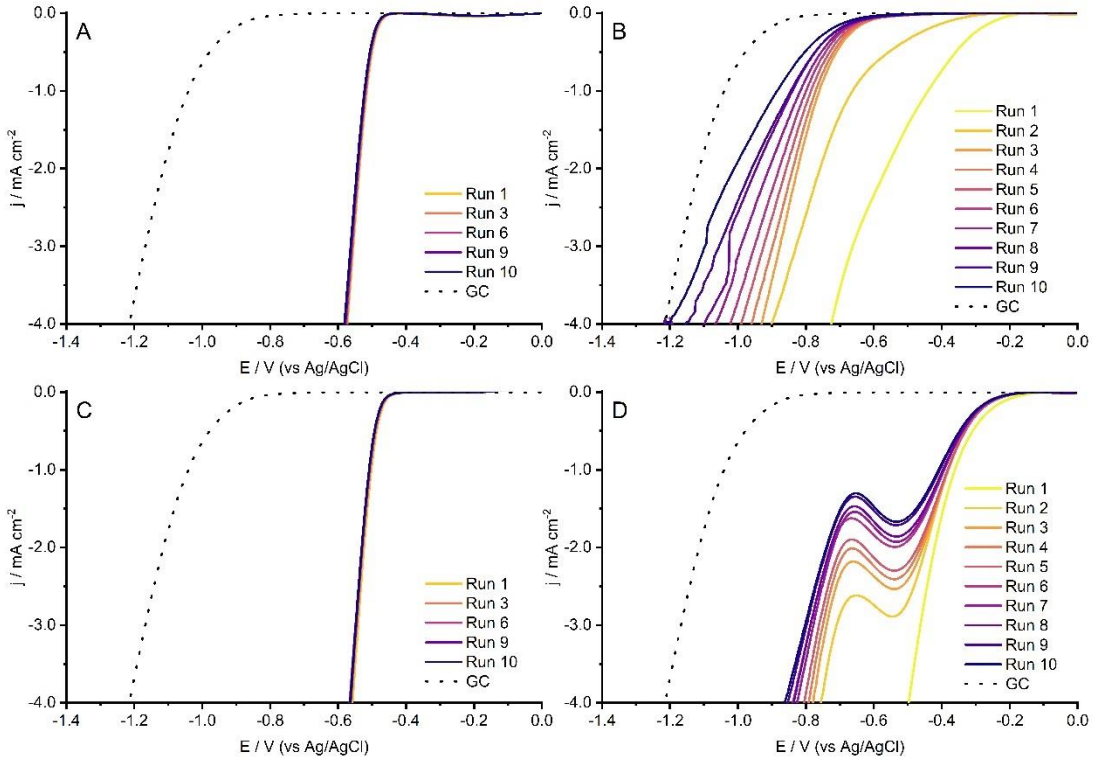

Figure 5.4. Stability of the different heterolayers in 10 mM H_2SO_4 and 0.1 M K_2SO_4 (**A**) $MoSe_2/MoS_2$(NP/L), (**B**) $MoS_2/MoSe_2$(NP/L), (**C**) WS_2/MoS_2(NP/L), (**D**) $MoS_2/MoSe_2$(L/L). Each heterolayer was subjected to 10 successive scans at a voltage scan rate of 20 mV s^{-1}.

The other TMD heterolayers investigated were $MoS_2/MoSe_2$ (NP/L), WS_2/MoS_2 (NP/L), $WS_2/MoSe_2$ (NP/L) and $MoS_2/MoSe_2$ (L/L). The stability of these heterolayers were also investigated in pH 2 solution for HER and the results are shown on figure 2 ($WS_2/MoSe_2$ is given in figure 5.5B). Those with an overlayer of $MoSe_2$ (B & D) have low stability compared to those with MoS_2 overlayers. The degradation of the heterolayer from the glassy carbon surface for both $MoS_2/MoSe_2$ and $WS_2/MoSe_2$ occurred after the first scan and continued with each run/scan. This degradation can be seen in figure 5.4 as the onset potential progressively moves to higher overpotentials with each cycle, tending towards the response for a bare GC surface. Electrodeposited $MoSe_2$ films have been observed to be less stable in acidic media for HER (Fig. 5.5A) and adding that to a dropcast layer of WS_2 and MoS_2 had no positive effect on the stability of the resulting heterolayer.

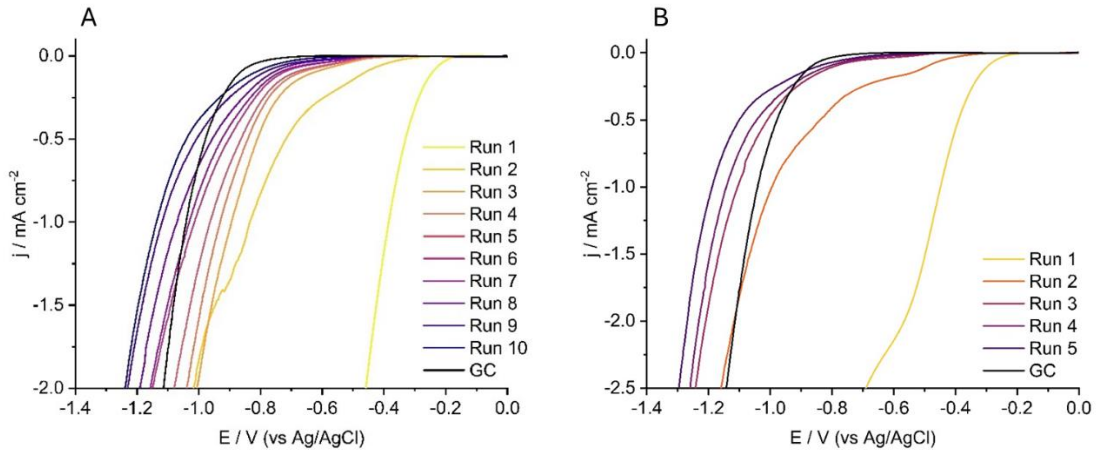

Figure 5.5. Stability study of (**A**) electrodeposited $MoSe_2$ and (**B**) $WS_2/MoSe_2$ heterolayer in an acid solution of 10 mM H_2SO_4 and 0.1 M K_2SO_4. The TMDs were subjected to 10 successive scans at a voltage scan rate of 20 mV s^{-1}.

5.2.2 HER activity

After determining the stability of the different heterolayers, their catalytic effects towards the HER were evaluated. The heterolayers were created with the aim of increasing active sites for adsorption of hydrogen as well improving charge transport due to the heterostructure.[9,16,17] Heterostructure formation has been reported to result in increased active edge sites and channels for charge transport thus

enhancing the electrical conductivity of the heterolayer, which all positively affects electrocatalytic activity.[8,18,19] The additional active edge sites are due to the increased surface area of the heterolayer as well as formation of defects at the heterointerfaces.[20] Catalytic activities of the two forms (particle-dropcast and electrodeposited forms) of TMDs making up the heterolayer were compared with that of the heterolayer, using linear sweep voltammetry (LSV) at a voltage scan rate of 20 mV s^{-1} in a solution of 10 mM H_2SO_4 and 0.1 M K_2SO_4 (see figure 5.6). Of the five combinations studied, $MoSe_2/MoS_2$ (NP/L) and WS_2/MoS_2 (NP/L) displayed a response indicative of improved kinetics over the electrodeposited layer (MoS_2) alone. MoS_2 has been the TMD of choice for most HER studies with its excellent catalytic activity and the ability to be modified to improve catalytic activity.[3,21] Of the many different structural forms of MoS_2, the electrodeposited form can be easily modified to change the thickness of the film formed by adjusting the cyclic voltammetry conditions. This combined with the formation of MoS_2 heterolayers results in improved HER activity thus showing the benefits of forming heterolayers.

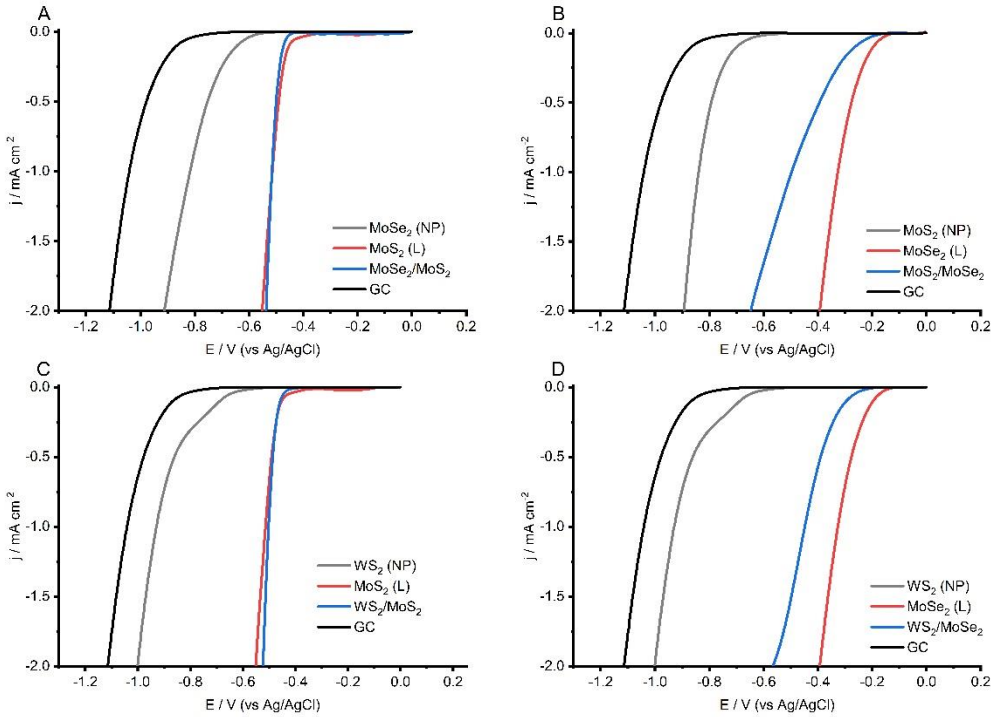

Figure 5.6. Linear sweep voltammograms of (**A**) $MoSe_2/MoS_2$, (**B**) $MoS_2/MoSe_2$, (**C**) WS_2/MoS_2 and (**D**) $WS_2/MoSe_2$ heterolayers as electrocatalysts for the hydrogen evolution reaction in comparison to the TMDs that make them up. This was done in a solution of 10 mM H_2SO_4 and 0.1 M K_2SO_4 at voltage scan rate of 20 mV s^{-1} for all the scans.

A similar heterolayer response was reported in previous studies looking into TMD heterostructures which revealed increased electrocatalytic ability for HER.[8,9,16] One study investigated $MoSe_2/MoS_2$ heterostructure fabricated from thin sheets of the TMDs and this heterostructure showed a lowered overpotential needed to generate 10 mA cm^{-2} as compared to the component layers as well as improved electrocatalytic activity.[16] For $MoS_2/MoSe_2$ (NP/L), $WS_2/MoSe_2$ (NP/L) and $MoS_2/MoSe_2$ (L/L) (Fig. 5.7), the current response (normalised by electrode surface area) was shifted to higher overpotentials (i.e., slower kinetics) compared to the electrodeposited layer ($MoSe_2$) alone. Electrodeposited $MoSe_2$ displays an earlier onset for HER than electrodeposited MoS_2 but is less stable in acid solutions (see below).

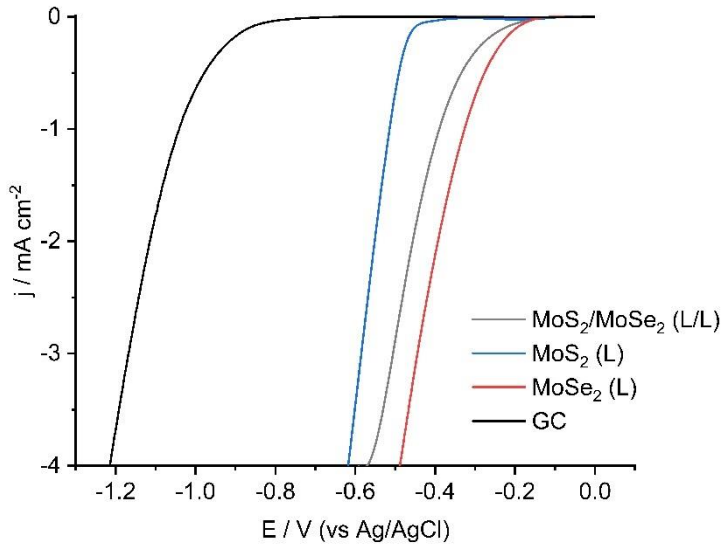

Figure 5.7. Linear sweep voltammogram of the $MoS_2/MoSe_2$ heterolayer and the TMDs that make it up as electrocatalysts for HER in a solution of 10 mM H_2SO_4 and 0.1 M K_2SO_4.

It was observed that the dropcast layers did not influence the stability of the electrodeposited overlayer, as degradation of the $MoS_2/MoSe_2$ and $WS_2/MoSe_2$ samples followed that of $MoSe_2$, with rapid increase of overpotential on consecutive CVs and reverting to a response akin to bare GC after less than 10 scans. Similarly, the samples with MoS_2 overlayers had similar stability to MoS_2 itself, albeit less catalytic than $MoSe_2$. A visual comparison of the heterolayers is shown on figure 5.8, having an overlay of the HER scans using the different heterolayers.

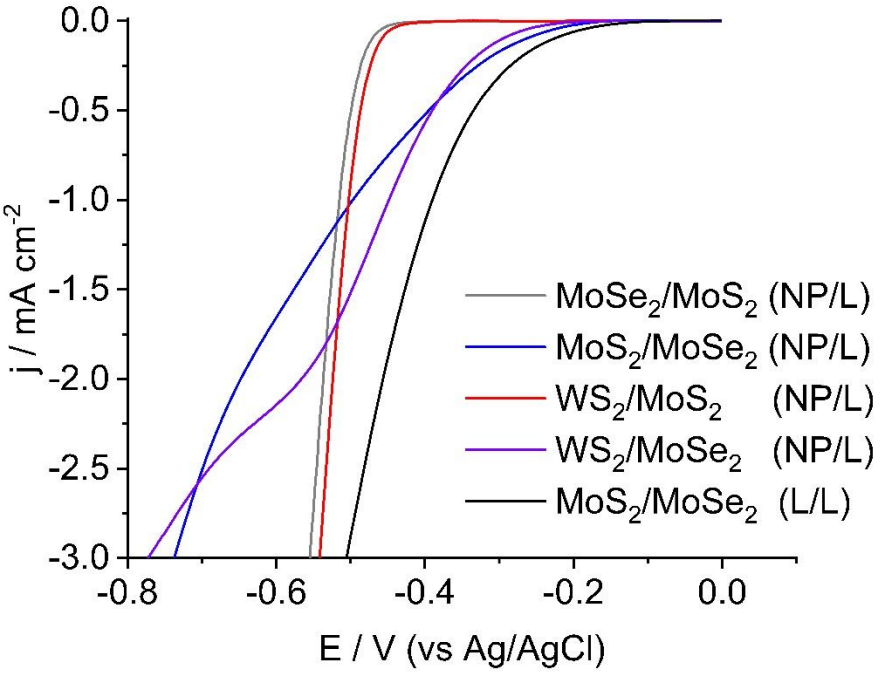

Figure 5.8. Overlay of the different heterolayers and how they compare to each other. All conditions were kept the same and the voltammetry was carried out in a 10 mM H_2SO_4 and 0.1 M K_2SO_4 solution and with a Ag/AgCl reference electrode and a graphite rod counter at a scan rate of 20 mV s^{-1}.

Tafel analysis was conducted for the heterolayers used and the resulting Tafel slopes along with onset potentials were determined. The reaction mechanism for HER is assumed to involve a series of steps which may be restricted by either the Volmer, Heyrovsky or Tafel steps as the rate determining steps and their associated Tafel slope values are as follows (table 5.1):[10,22-24]

Table 5.1. HER mechanism steps.

Step	Equation	Tafel slope / mV dec^{-1}
Volmer	$H_3O^+ + e^- \rightarrow H_{ads} + H_2O$	120
Heyrovsky	$H_{ads} + H_3O^+ + e^- \rightarrow H_2 + H_2O$	40
Tafel	$H_{ads} + H_{ads} \rightarrow H_2$	30

Table 5.2 highlights the calculated Tafel slope values for HER due to the heterolayers. These provide an indication of the rate determining step in the HER reaction mechanism as a result of catalysis from the heterolayers. WS_2/MoS_2 and $MoSe_2/MoS_2$ (NP/L) Tafel slope values are closer to the Heyrovsky step value thus indicating that the Heyrovsky is the rate determining step in the HER mechanism. The other heterolayers, that is $MoS_2/MoSe_2$ (L/L), $MoS_2/MoSe_2$ (NP/L) and $WS_2/MoSe_2$ (NP/L) have Tafel slope values which fall between the reported Tafel values for the Volmer and Heyrovsky steps. This suggests a mixture of the Volmer and Heyrovsky steps as rate determining steps in HER reaction mechanism involving these electrocatalysts. All the heterolayers yielded Tafel slopes values less than the previously reported values except for $WS_2/MoSe_2$ heterolayer. For most heterolayers, the HER onset value falls between the individual particle drop cast and electrodeposited form apart from the WS_2/MoS_2 (NP/L) heterolayer. It is worth noting that various methods used to create heterostructures impact crystallinity and defect density, which alters the electrochemical behaviour of the resulting heterostructures. This is showcased by the varying Tafel slope values in comparison to literature (table 5.2) as a result of different synthesis techniques.

Table 5.2. Onset potential and Tafel slope values for the various TMDs and their heterolayers.

Heterolayer	**Onset Potential at 0.5 mA cm^{-2} (± 0.01) / V**	**Tafel slope (± 0.5) / mV dec^{-1}**	**Reported Tafel slopes / mV dec^{-1}**	**Synthesis method for reported Tafel slopes**
$MoSe_2/MoS_2$ (NP/L)	-0.50	57	289 71	Electrodeposition[11] Hydrothermal and microwave-assisted method[16]
$MoS_2/MoSe_2$ (NP/L)	-0.39	94	315	Electrodeposition[11]
$MoS_2/MoSe_2$ (L/L)	-0.34	89	315	Electrodeposition[11]
WS_2/MoS_2 (NP/L)	-0.49	46	72	Chemical bath deposition and RF magnetron sputtering system[25]
$WS_2/MoSe_2$ (NP/L)	-0.39	98	60	Chemical bath and chemical vapor deposition sputtering[8]

Scan rate studies were carried out and a Randles-Ševčík plot derived to establish whether the reactions on the heterolayer surface were diffusion controlled or mass-transport limited. This study only worked for stable heterolayers such as $MoSe_2/MoS_2$ and WS_2/MoS_2 which could withstand several successive runs for HER in acidic media. An example of the $MoSe_2/MoS_2$ results with the Randles-Ševčík plot is displayed on figure 5.9A&B. Ideally the Randles-Ševčík plot has a zero intercept but with the obtained experimental results, a non-zero intercept was recorded. This was the case for the other heterolayers as well and suggested the surface of the heterolayers to have a non-homogenous nature.[26,27]

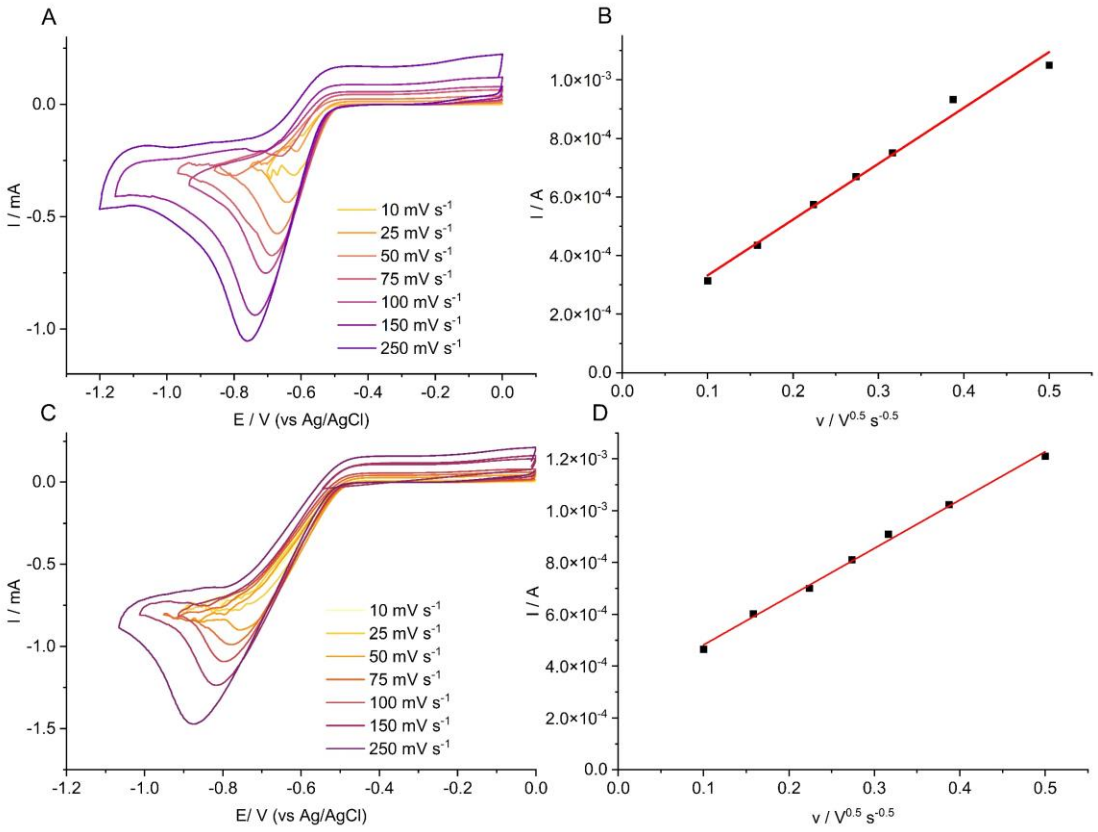

Figure 5.9. HER scan rate study using the **(A)** $MoSe_2/MoS_2$ and **(C)** WS_2/MoS_2 heterolayer. The scan rate was varied from 10 to 250 mV s^{-1}. The Randles-Ševčík plots with linear fit for both $MoSe_2/MoS_2$ **(B)** with equation $I = (19.1v + 1.41) \times 10^{-4}$ and WS_2/MoS_2 **(D)** with equation $I = (18.6v + 2.96) \times 10^{-4}$ from the resulting scan rate studies.

The Randles-Ševčík plot confirmed that a diffusion-controlled process is occurring on the surface of the heterolayers during the HER scans, from the linear relationship between the peak current and square root of the scan rate.[27] Figure 5.10 highlights the difference between theoretical and experimental results as well as proof of a diffusion-controlled process as opposed to a surface-controlled one. It also shows the non-zero intercepts of the other modified electrodes in the Randles-Ševčík plot which are a result of surface roughness of these electrocatalysts.

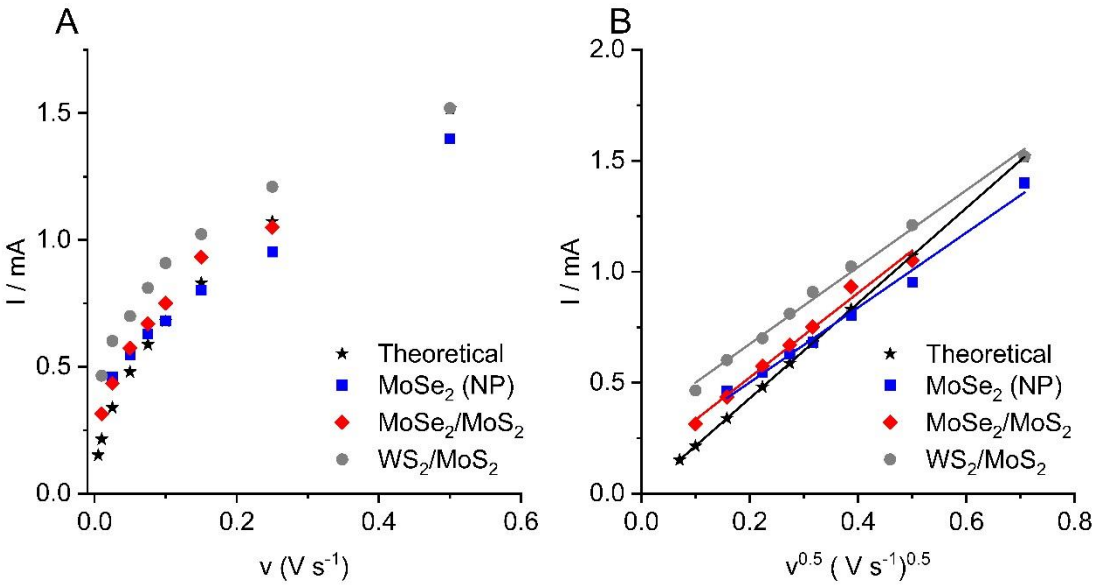

Figure 5.10. (A) A peak current vs scan rate plot comparing experimental results to those obtained theoretically. **(B)** Overlay of the Randles-Ševčík plots for the various heterolayers and those from theoretical results.

Next, the HER performance of the heterolayered electrodes were investigated via rotating disk voltammetry to determine kinetic performance. A surface modified glassy carbon rotating disk electrode was used to run LSV measurements from 0 to -1.6 V (vs Ag/AgCl) in an acid solution of 10 mM H_2SO_4 and 0.1 M K_2SO_4. Given the nature of the rotating disk electrode, only stable heterolayers such as $MoSe_2/MoS_2$ and WS_2/MoS_2 which could withstand the rotation were used in the study. The rotational speed was varied between 400 to 2000 rpm from 0 to -1.6 V (vs Ag/AgCl) at 20 mV s^{-1} and the resulting voltammograms used for the Koutecky-Levich analysis. Figure 5.11 displays the voltammogram resulting from WS_2/MoS_2 heterolayer along with the Koutecky-Levich plot (B) and Tafel graphs (C) used in calculating the rate constant. Plotting the Tafel plot resulted in a best-fit line from which the intercept corresponding to the exchange current density (j_0), was used to calculate the standard electrochemical rate constant (k_0) using Eq. 5.3 below:[28]

$$j_0 = nFk_0C_{bulk} \qquad (5.3)$$

Where F is the faraday constant (s A mol^{-1}), n is the number of electrons and C_{bulk} is the bulk concentration (mol cm^{-3}).

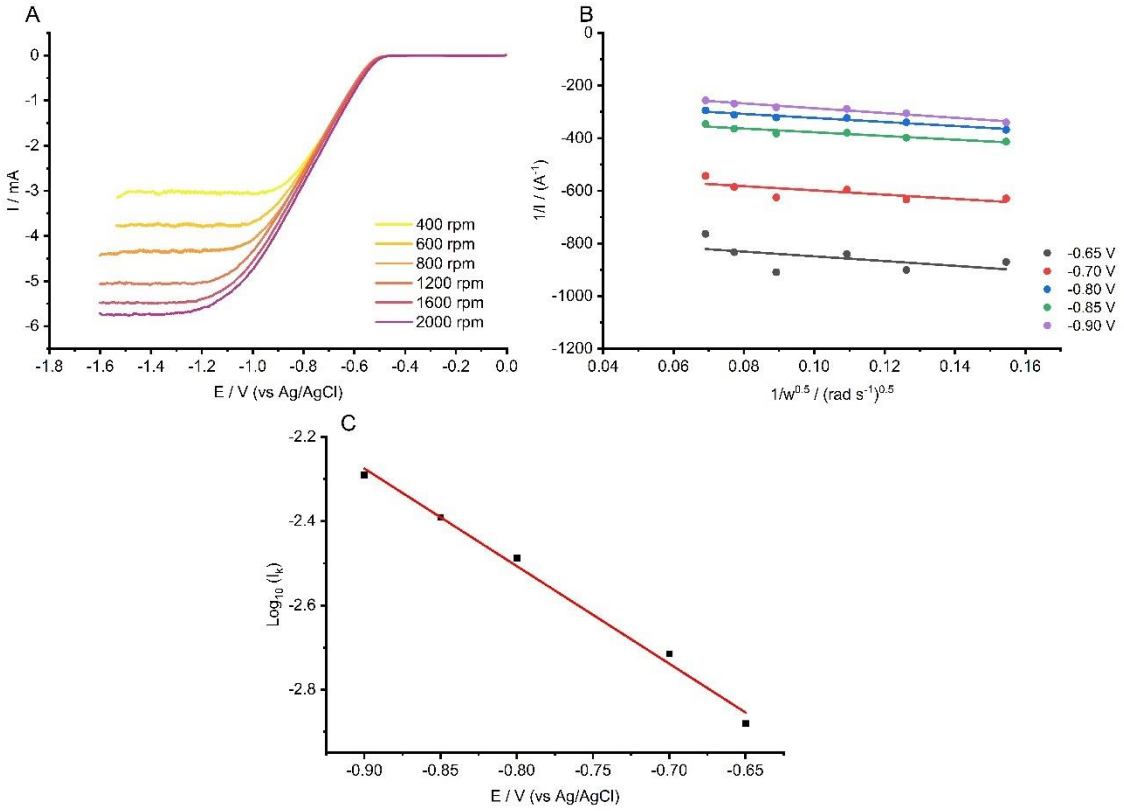

Figure 5.11. (A). HER voltammograms at various rotation rates using the WS_2/MoS_2 heterolayer electrocatalyst in a solution of 10 mM H_2SO_4 and 0.1 M K_2SO_4. **(B).** Koutecky-Levich plot resulting from the voltammograms in (A). **(C).** Tafel plot from using the intercepts and potentials data in (B). A best fit line was drawn with the resulting equation $log_{10}(I_k) = -2.32E - 4.36$, from which the electrochemical rate constant was calculated.

The standard electrochemical rate constant was calculated to be $k_0 = (3.20 \pm 0.10) \times 10^{-4}$ cm s^{-1} and a transfer coefficient of $\alpha = 0.62 \pm 0.02$. The same was done for $MoSe_2/MoS_2$ heterolayer (Fig. 5.12) and a rate constant of $k_0 = (1.73 \pm 0.03) \times 10^{-4}$ cm s^{-1} and a transfer coefficient of $\alpha = 0.85 \pm 0.02$ were calculated. Both WS_2/MoS_2 and $MoSe_2/MoS_2$ heterolayers have resulted in an improved rate constant by an order of magnitude compared to the reported MoS_2 rate constant of $k_0 = (3.17 \pm 0.30) \times 10^{-5}$ cm

s^{-1} which had the same preparative method via electrochemical deposition.[15] This highlights the improved catalytic activity of the two heterolayers for the hydrogen evolution reaction.

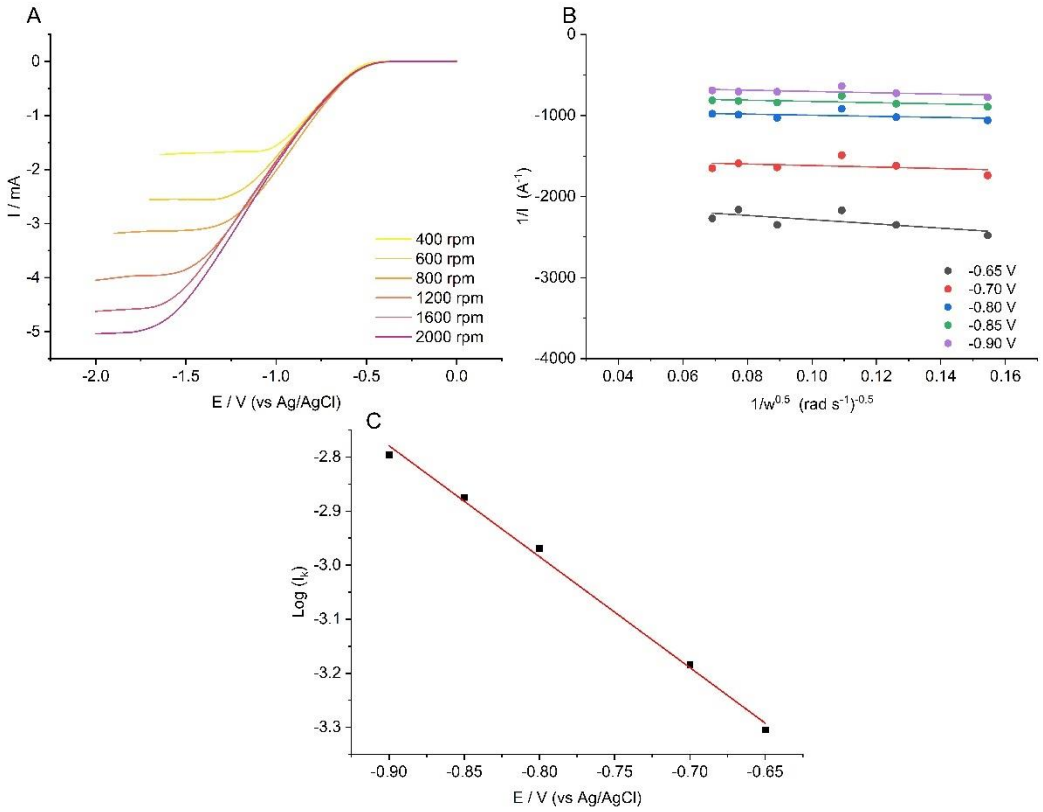

Figure 5.12. (A). HER voltammograms at various rotation rates using the $MoSe_2/MoS_2$ heterolayer electrocatalyst in a solution of 10 Mm H_2SO_4 and 0.1 M K_2SO_4. **(B)**. Koutecky-Levich plot resulting from the voltammograms in (A). **(C).** Tafel plot from using the intercepts and potentials data in (B). A best fit line was drawn with the resulting equation $log_{10}(I_k) = -2.05E - 4.63$, from which the electrochemical rate constant was calculated.

5.2.3 Heterolayer characterization

SEM and EDS characterization were used to gain insight into the atomic components and surface morphology of the heterolayers via imaging and spectrum analysis. SEM images and EDS spectra of the heterolayers are shown on Fig. 5.13-5.17. These show the top-view of the heterolayer surfaces: rough surfaces can be observed, and further magnification reveals particles of different sizes thus

supporting the non-homogeneity of the heterolayer surfaces. The EDS spectral results confirmed the presence of the different elements arising from the various TMDs used in making the heterolayers. For the $MoSe_2/MoS_2$ heterolayer, molybdenum, sulfur and selenium elements were detected during EDS. Detection of Se in the EDS spectra indicates that there might be dissolution and redeposition of the $MoSe_2$ layer during the electrochemical deposition of the MoS_2 layer.

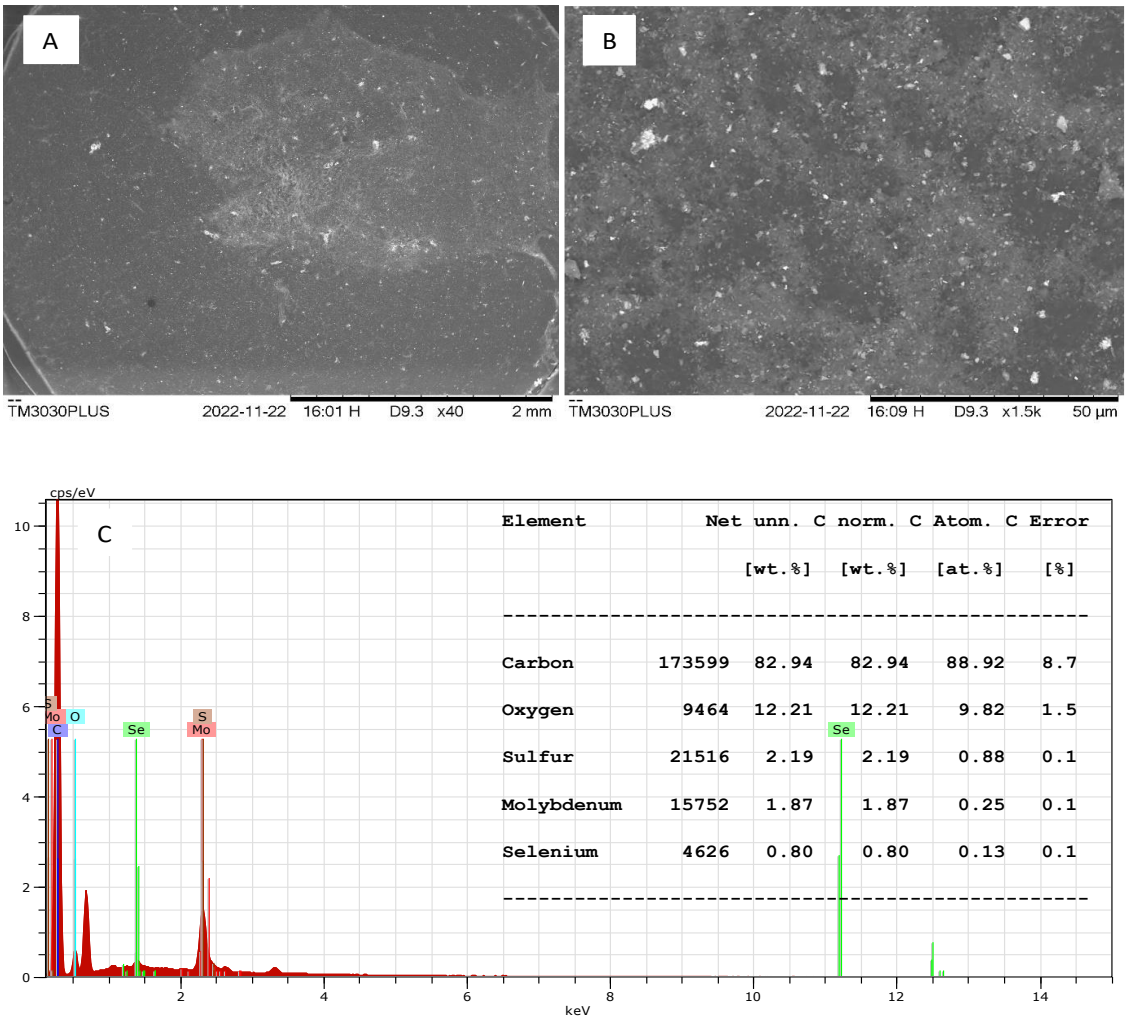

Figure 5.13. (A&B) SEM top images of $MoSe_2/MoS_2$ hetero sample at different magnifications. **(C).** EDS spectra of the sample showing the detection of Mo, Se, and S elements in the sample.

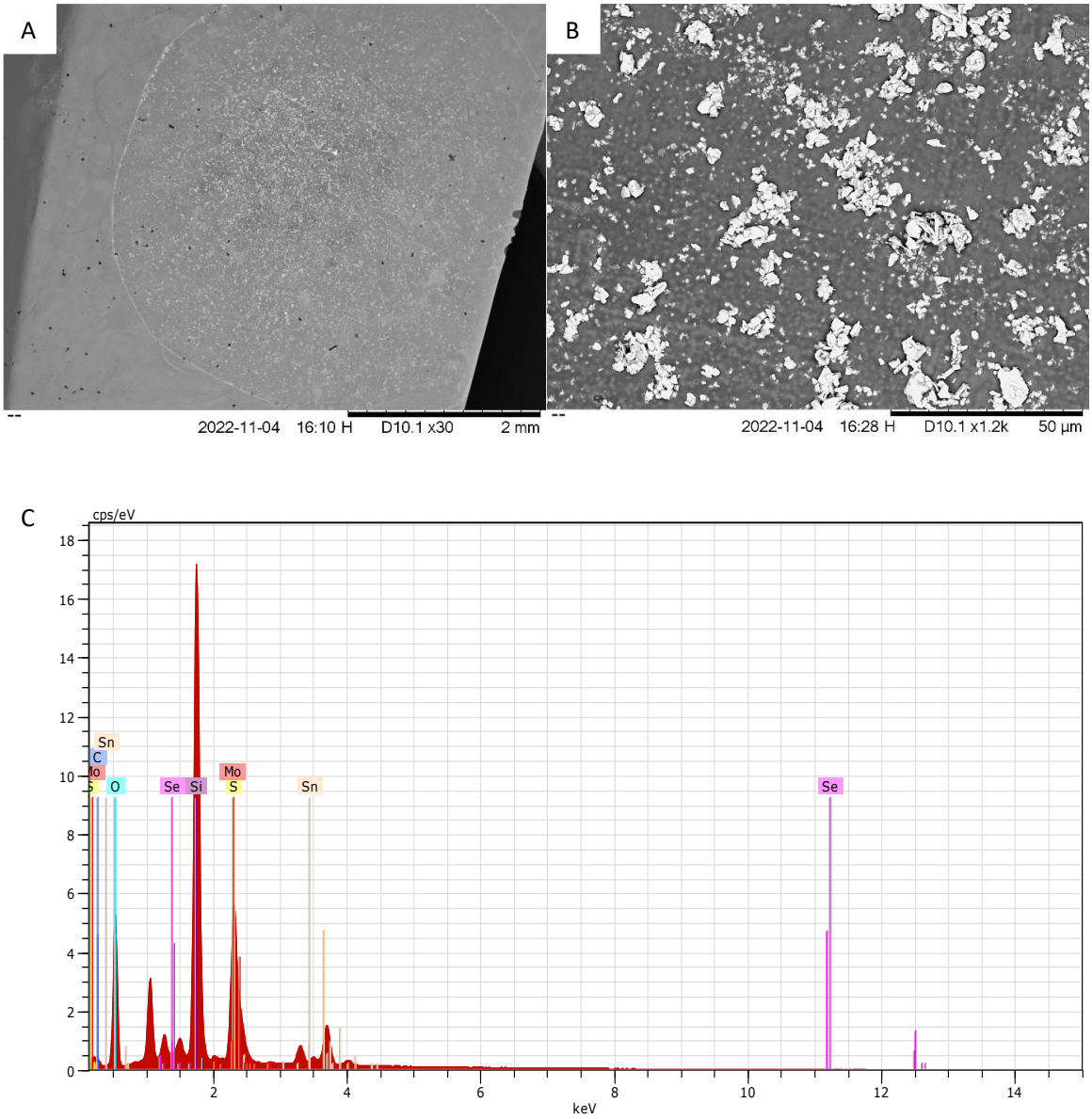

Figure 5.14. (A&B) SEM top images of $MoS_2/MoSe_2$ hetero sample at different magnifications. **(C).** EDS spectra of the sample showing the detection of Mo, Se, and S elements in the sample.

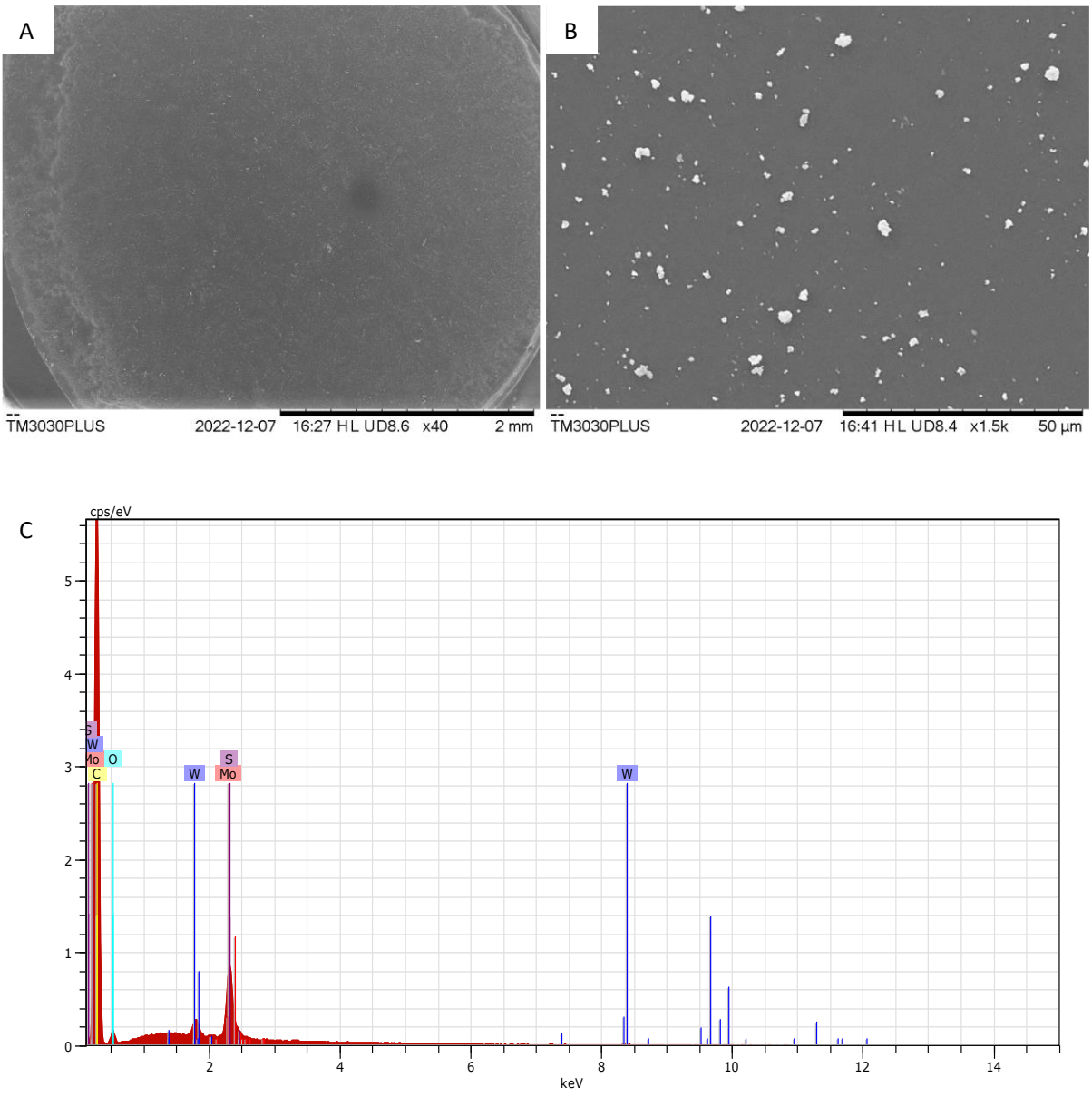

Figure 5.15. **(A&B)** SEM top images of WS_2/MoS_2 hetero sample at different magnifications. **(C).** EDS spectra of the sample showing the detection of Mo, W, and S elements in the sample.

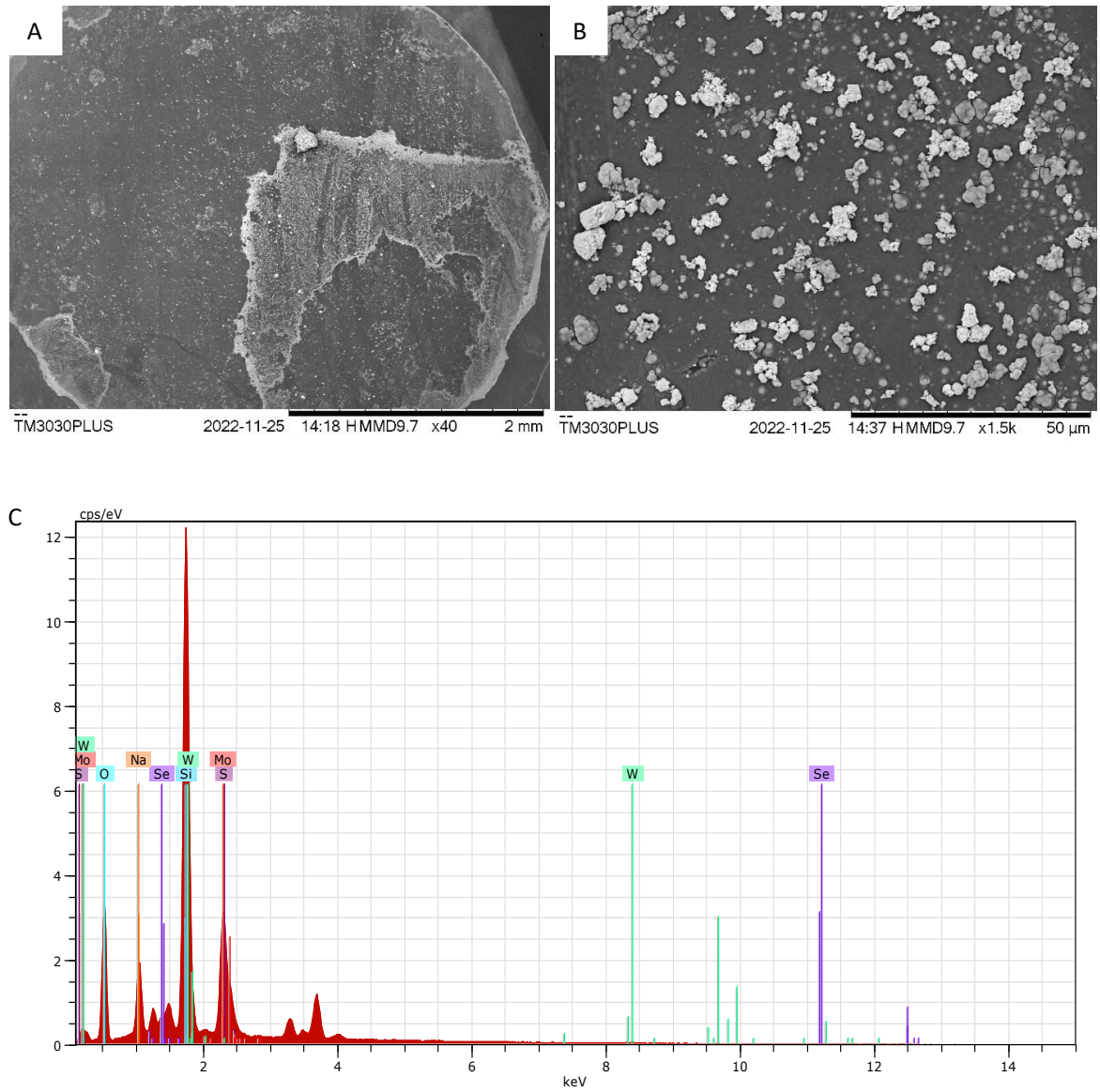

Figure 5.16. (A&B) SEM top images of $WS_2/MoSe_2$ hetero sample at different magnifications. **(C).** EDS spectra of the sample showing the detection of Mo, W, Se, and S elements in the sample.

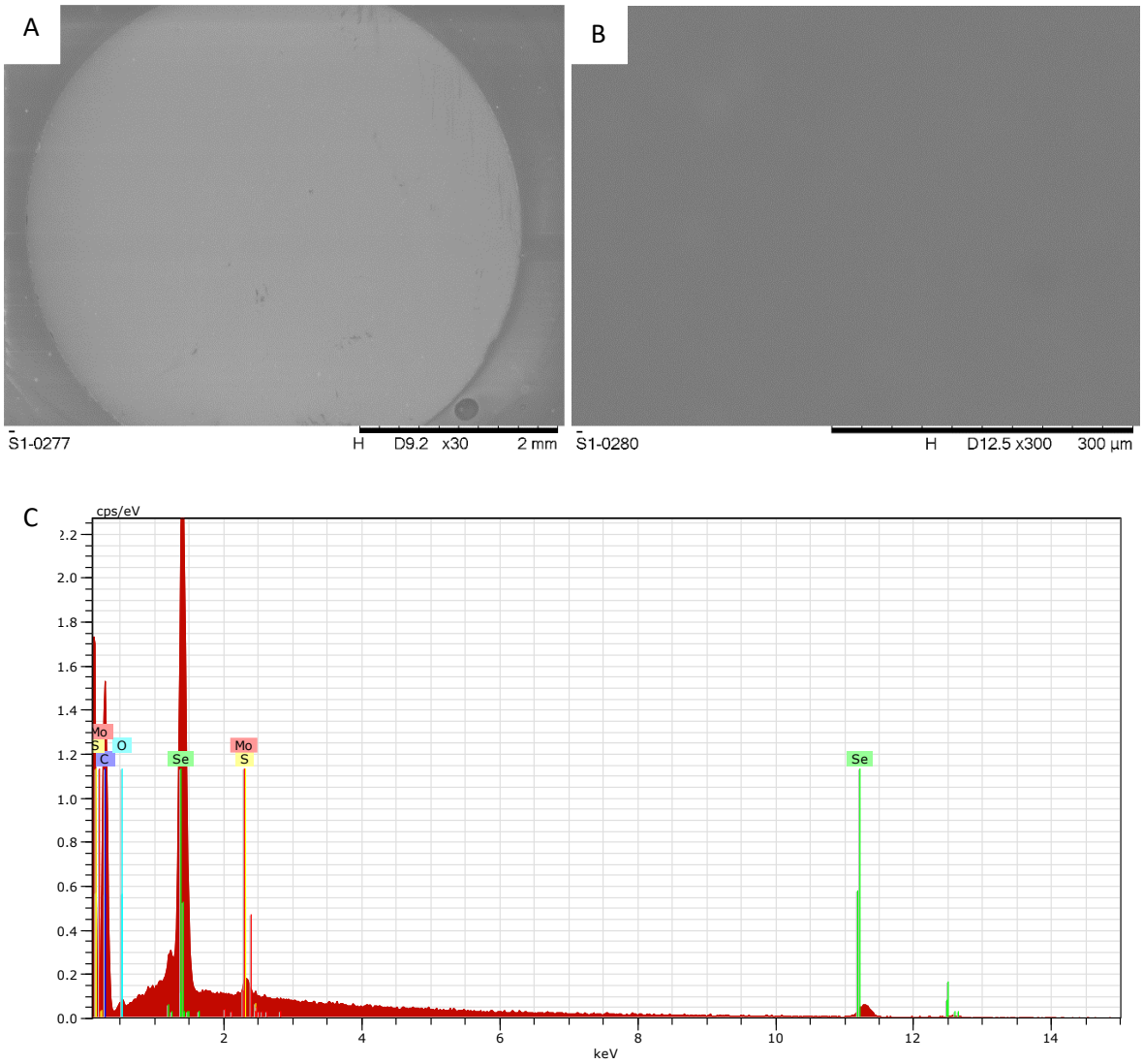

Figure 5.17. (A&B) SEM top images of $MoS_2/MoSe_2$ (L/L) hetero sample at different magnifications. **(C).** EDS spectra of the sample showing the detection of Mo, Se, and S elements in the sample.

Direct imaging of the WS_2/MoS_2 heterolayer cross-section by FIB-SEM (focused ion beam scanning electron microscopy) (Fig. 5.18B) showed a top layer of the deposited platinum and below it a single layer of material instead of two distinct layers. This may be due to the dissolution-deposition of the underlayer during the deposition of the overlayer forming a single "alloy-type" layer as reported by Strange.[11]

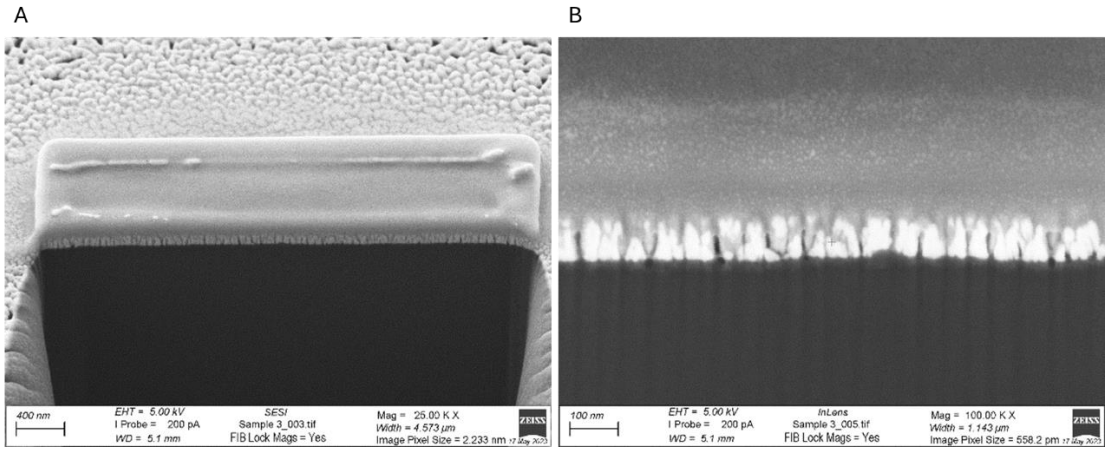

Figure 5.18. Cross-sectional SEM image of the WS_2/MoS_2 heterolayer from which the film thickness was to be determined.

Further characterization was conducted through XPS to determine the elemental compositions of the heterolayers. For the $MoSe_2/MoS_2$ sample, XPS confirmed the presence of Mo, S and Se in the sample as shown in the wide spectra on Fig 5.19A. High resolution spectra of these peaks revealed the Mo 3d, S 2s, S2p, Se 3s and Se 3d peaks. The Mo 3d peak area consisted of the Mo^{4+} at peaks 229 eV and 232 eV along with the Mo^{6+} at 236 eV.[14,29-31] The Mo^{6+} is attributed to the presence of MoO_3 in the sample and this is supported by the detection of significant amounts of oxygen in the sample. MoO_3 results from the partial oxidation of the layers when in contact with oxygen. S 2s and Se 3s were also detected in this spectrum at 228 eV and 232 respectively.[30,32] Two other chemical states of Se were detected, i.e., the Se 3d and Se 3p. For Se 3d, the peak of the spin-orbit doublet of Se $3d_{3/2}$ and Se $3d_{5/2}$ was detected with their peaks at 55.3 and 54.1 eV respectively.[16,33] To derive the elemental composition of the sample, accurate quantification would normally involve the analysis of the S 2p and Se 3p peaks. However, here these peaks overlap which makes peak deconvolution difficult: hence the S 2s and Se 3d peaks have been used for quantification.[11] This is also the case for the $MoSe_2/MoS_2$ sample. The S 2s: Se 3p peak area ratio for the $MoS_2/MoSe_2$ was calculated to be 1.0:1.9, while for the $MoSe_2/MoS_2$ it was 7.9:1.0. The difference is due to the amount of TMD film electrodeposited which is significantly more in comparison to the dropcast nanoparticles.

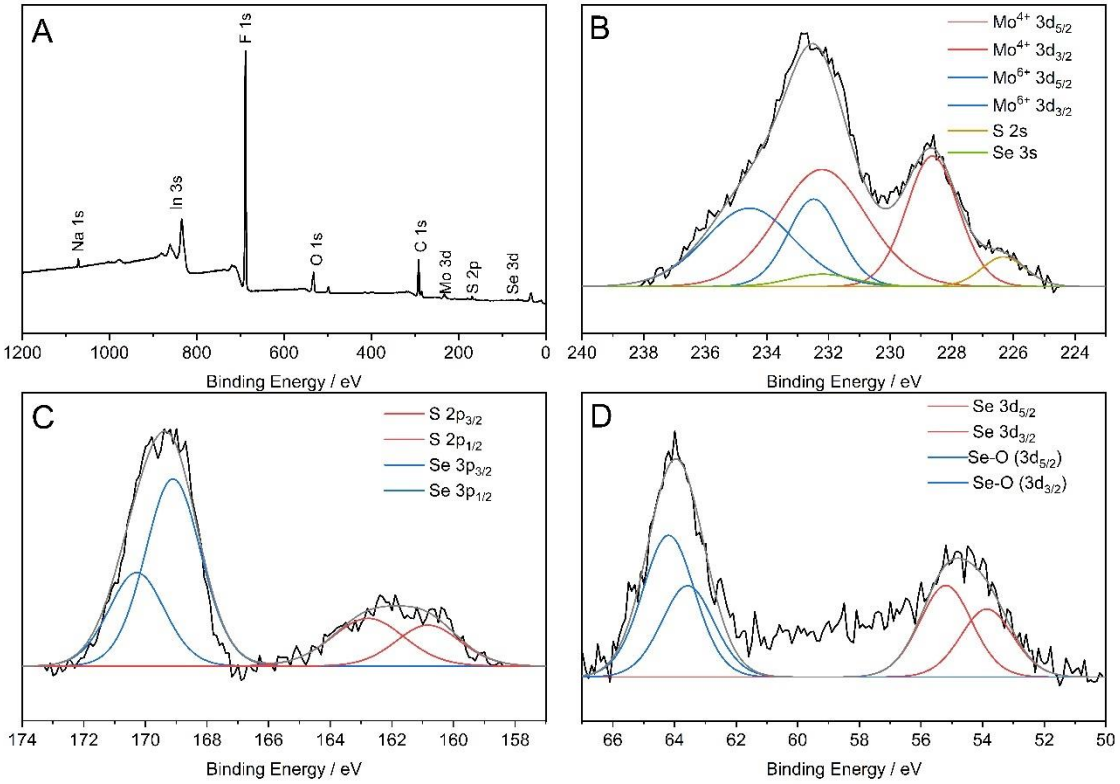

Figure 5.19. (A) Wide area spectra of the $MoSe_2/MoS_2$ sample displaying all the elements in it. High resolution spectra of the **(B)** Mo 3d peak, **(C)** S 2p peak and the **(D)** Se 3d peaks from the sample $MoSe_2/MoS_2$.

Analysis of the wide survey spectrum of the WS_2/MoS_2 heterolayer sample confirmed the presence of Mo, W and S elements which were detected via SEM-EDS. High resolution spectra of the Mo peak area also showed both Mo^{4+} and Mo^{6+} species along with the S 2s peak as displayed on Fig. 5.20. For this sample, partial oxidation also occurred hence the Mo^{6+} peaks observed. The chemical composition could not be determined since the S^{2-} was a common anion to both layers but the relative amounts of W^{4+} and Mo^{4+} could be used to determine the ratio of WS_2 to MoS_2 in the heterolayer sample. The ratio of W^{4+} to Mo^{4+} was calculated to be 1:2.7 thereby showing there is approximately 3 times more MoS_2 in the WS_2/MoS_2 heterolayer sample. The spectra of the other heterolayers are depicted in Figures 5.21 to 5.23, and from these spectra, the atomic percentage of each element was determined and is presented in Table 5.3.

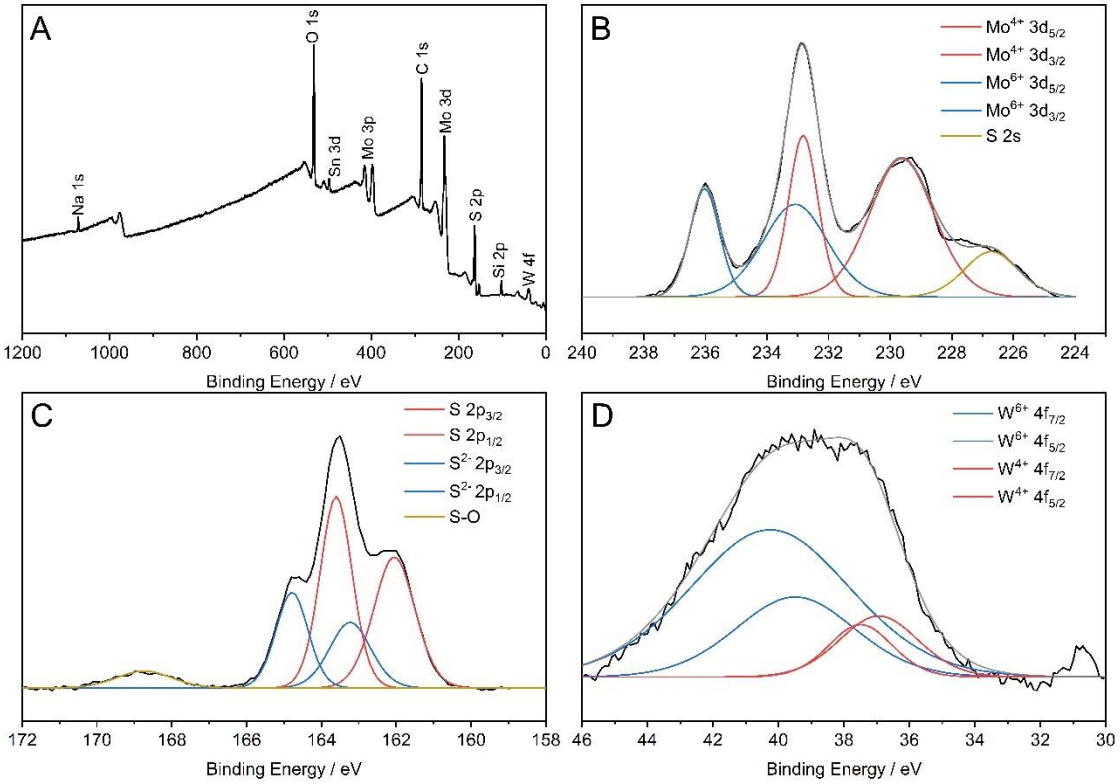

Figure 5.20. (A) Wide area spectra of the WS_2/MoS_2 sample displaying all the elements in it. High resolution spectra of the **(B)** Mo 3d peak, **(C)** S 2p peak and the **(D)** W 4f peaks from the sample WS_2/MoS_2.

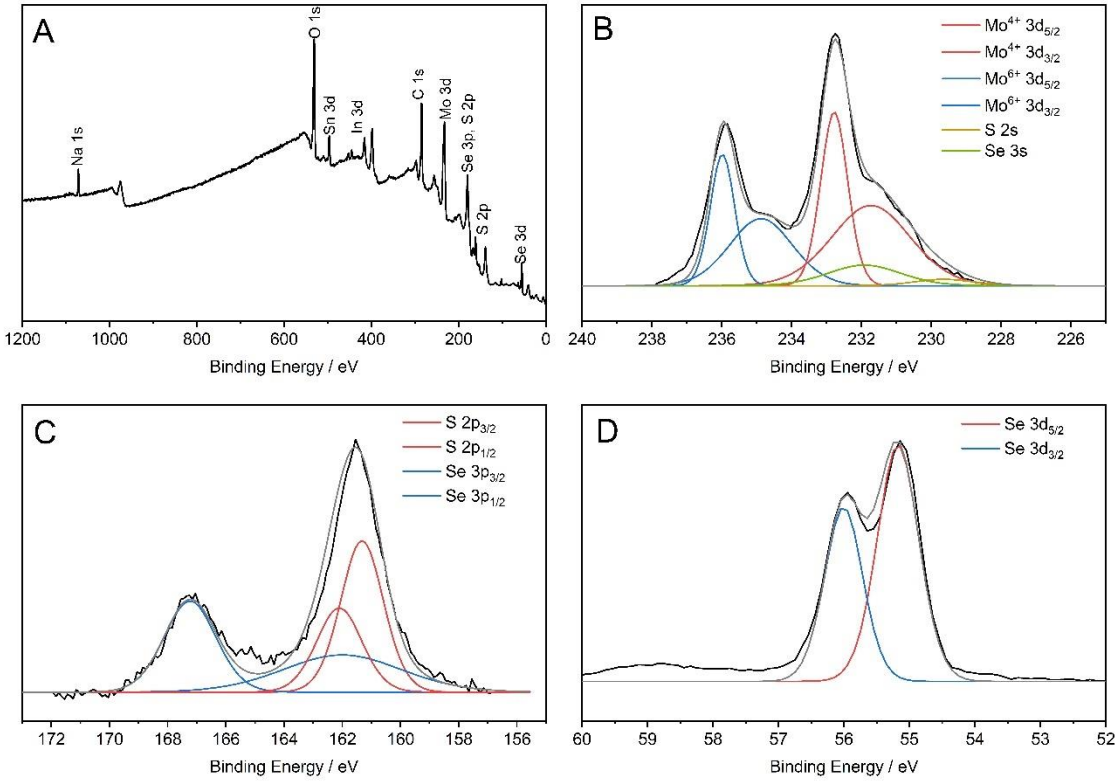

Figure 5.21. (A) Wide area spectra of the $MoS_2/MoSe_2$ sample displaying all the elements in it. High resolution spectra of the **(B)** Mo 3d peak, **(C)** S 2p, Se 3p peaks and the **(D)** Se 3d peaks from the sample $MoS_2/MoSe_2$.

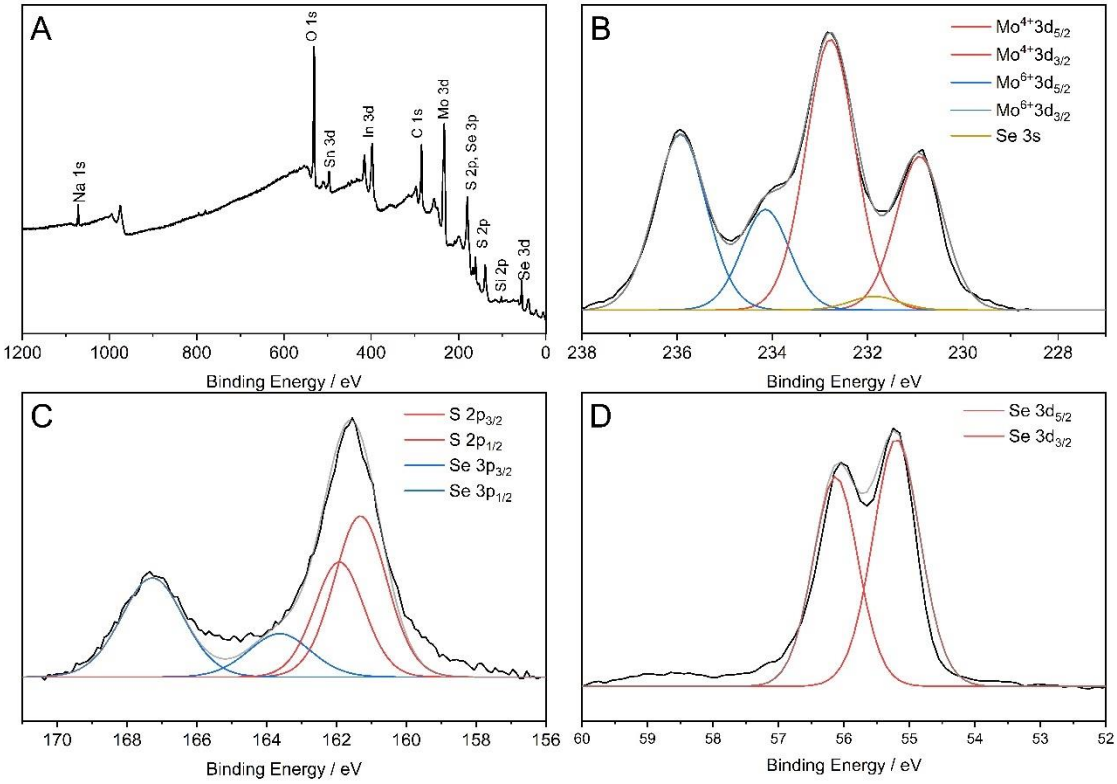

Figure 5.23. (A) Wide area spectra of the $MoS_2/MoSe_2$ sample displaying all the elements in it. High resolution spectra of the **(B)** Mo 3d peak, **(C)** S 2p, Se 3p peaks and the **(D)** Se 3d peaks from the sample $MoS_2/MoSe_2$.

Table 5.3. Percentage composition of the different elemental states of the various components in each heterolayer.

	XPS Percentage composition / %							
	Mo 3d region				**S 2p region**		**W 4f region**	
	Mo^{6+} 3d	**Mo^{4+} 3d**	**S 2s**	**Se 3s**	**S 2p**	**Se 3p**	**W^{6+} 4f**	**W^{4+} 4f**
$MoSe_2/MoS_2$ (NP/L)	37.35	55.76	4.25	2.63	28.15	71.85	-	-
$MoS_2/MoSe_2$ (NP/L)	36.51	54.16	1.89	7.43	52.98	47.02	-	-
$MoS_2/MoSe_2$ (L/L)	39.46	58.62	0	1.91	61.57	38.43	-	-
WS_2/MoS_2 (NP/L)	36.23	54.1	9.66	-	100	-	80.23	19.76

Spectroscopic ellipsometry was used to determine the thickness of the electrodeposited films. The experimental data, obtained through spectroscopic ellipsometry, was analysed using the Tauc-Lorentz model to determine the optical constants and ultimately the thickness of the sample. The model combines two approaches to accurately describe both the absorption edge (Tauc part) and the resonant response of bound electrons (Lorentz part) for amorphous materials or materials with some degree of disorder. For the $MoS_2/MoSe_2$ (L/L) heterolayer, a total layer thickness of (43.3 ± 4.4) nm with the MoS_2 film having a thickness of (25.5 ± 5.4) nm and (17.8 ± 3.4) nm for $MoSe_2$. The root mean squared error (MSE) value of 2.38 indicates a good fit of the model to the experimental data, as shown in figure 5.24.

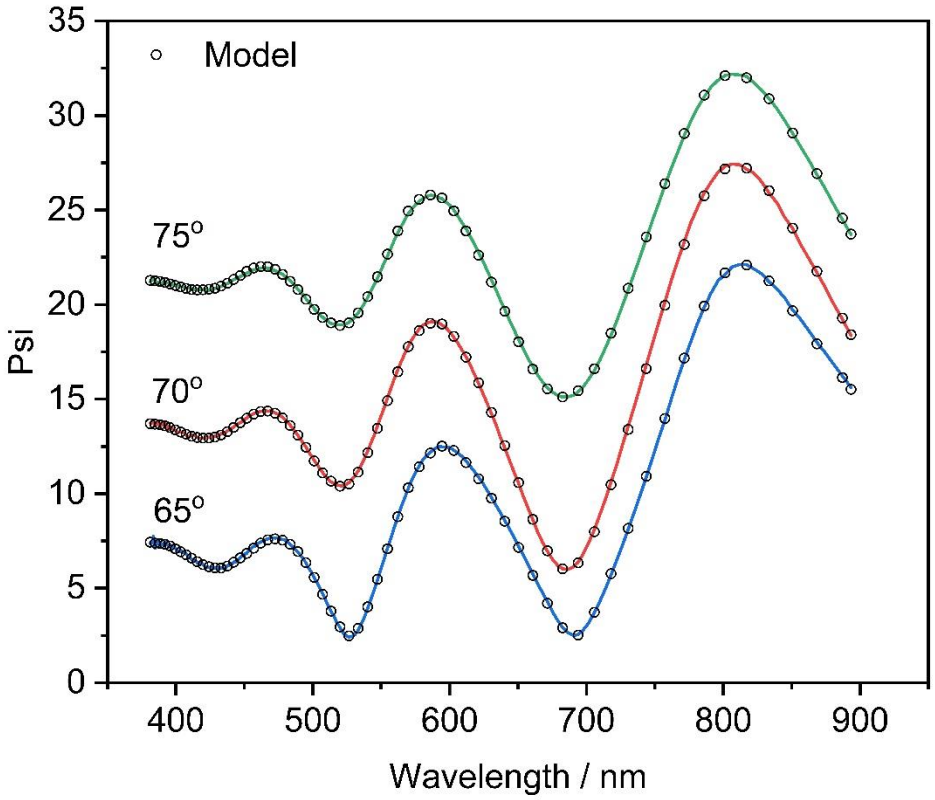

Figure 5.24. Model fitting result of the simulated data (---) against experimental data. The experimental data was collected at three different angles and then fitted using Tauc-Lorentz model to determine the sample thickness.

5.3 Conclusion

Transition metal dichalcogenide (TMD) heterostructures were investigated for their hydrogen evolution reaction (HER) catalytic activity and the resulting reaction kinetics. Two methods were used to form the heterolayers: one involved drop casting a nanoparticle layer of one TMD followed by electrodeposition of a different TMD on top ('NP/L'), while the second method involved sequential electrodeposition of layers of two different TMDs ('L/L'). The formation of these heterolayers on a glassy carbon substrate was confirmed through X-ray photoelectron spectroscopy (XPS) and scanning electron microscopy with energy-dispersive X-ray spectroscopy (SEM-EDS) characterization.

However, accurately determining the chemical compositions of the heterolayer samples proved challenging due to peak overlaps in the S 2*p* and Se 3*p* spectra, making peak deconvolution difficult. Some heterolayer samples contained sulfur chalcogen in both TMD layers, complicating the derivation of atomic percentages of S 2*p* for each TMD layer within the heterolayer sample. This analytical limitation highlights the complexity of characterizing TMD heterostructures and underscores the need for advanced spectroscopic techniques to resolve overlapping peaks and accurately quantify elemental compositions in such systems.

The stability of the resulting heterolayers was tested in an acidic solution and it was observed that those with a film of $MoSe_2$ had low stability while those with a film of MoS_2 were very stable even after 10 consecutive CV scans. Heterolayers with a film of MoS_2 displayed an improved HER ability when compared to the starting TMD materials. An earlier onset potential for HER was also observed for them. The resulting reaction kinetics due to the heterolayers was investigated and these included Tafel analysis and electrochemical rate constant calculation. WS_2/MoS_2 and $MoSe_2/MoS_2$ heterolayers registered rate constants of $(3.20 \pm 0.10) \times 10^{-4}$ cm s^{-1} and $(1.73 \pm 0.03) \times 10^{-4}$ cm s^{-1} respectively, which was an improvement of an order of magnitude compared to the reported rate constant of electrodeposited MoS_2. This further showed the improved HER catalytic activity of the heterolayers and how there is still room for improvement when it comes to TMDs.

5.4 References

(1) Chhowalla, M.; Shin, H. S.; Eda, G.; Li, L. J.; Loh, K. P.; Zhang, H. The Chemistry of Two-Dimensional Layered Transition Metal Dichalcogenide Nanosheets. *Nat. Chem.* 2013, **5**, 263–275. https://doi.org/10.1038/nchem.1589.

(2) Kolobov, A. V; Tominaga, J. Two-Dimensional Transition-Metal Dichalcogenides. Springer International Publishing, 2016.

(3) Lau, T. H. M.; Lu, X.; Kulhavý, J.; Wu, S.; Lu, L.; Wu, T. S.; Kato, R.; Foord, J. S.; Soo, Y. L.; Suenaga, K.; Tsang, S. C. E. Transition Metal Atom Doping of the Basal Plane of MoS_2 Monolayer Nanosheets for Electrochemical Hydrogen Evolution. *Chem. Sci.* 2018, **9**, 4769–4776. https://doi.org/10.1039/c8sc01114a.

(4) Terrones, H.; López-Urías, F.; Terrones, M. Novel Hetero-Layered Materials with Tunable Direct Band Gaps by Sandwiching Different Metal Disulfides and Diselenides. *Sci. Rep.* 2013, **3***,* 1549. https://doi.org/10.1038/srep01549.

(5) Amin, B.; Singh, N.; Schwingenschlögl, U. Heterostructures of Transition Metal Dichalcogenides. *Phys. Rev. B.* 2015, **92,** 075439. https://doi.org/10.1103/PhysRevB.92.075439.

(6) Komsa, H. P.; Krasheninnikov, A. V. Electronic Structures and Optical Properties of Realistic Transition Metal Dichalcogenide Heterostructures from First Principles. *Phys. Rev. B.* 2013, **88**, 085318. https://doi.org/10.1103/PhysRevB.88.085318.

(7) He, J.; Hummer, K.; Franchini, C. Stacking Effects on the Electronic and Optical Properties of Bilayer Transition Metal Dichalcogenides MoS_2, $MoSe_2$, WS_2, and WSe_2. *Phys. Rev. B.* 2014, **89**, 075409. https://doi.org/10.1103/PhysRevB.89.075409.

(8) Vikraman, D.; Hussain, S.; Patil, S. A.; Truong, L.; Arbab, A. A.; Jeong, S. H.; Chun, S. H.; Jung, J.; Kim, H. S. Engineering $MoSe_2$/WS_2 Hybrids to Replace the Scarce Platinum Electrode for Hydrogen Evolution Reactions and Dye-Sensitized Solar Cells. *ACS Appl. Mater. Interfaces,* 2021, **13**, 5061–5072. https://doi.org/10.1021/acsami.0c19890.

(9) Zhao, G.; Li, P.; Rui, K.; Chen, Y.; Dou, S. X.; Sun, W. $CoSe_2/MoSe_2$ Heterostructures with Enriched Water Adsorption/Dissociation Sites towards Enhanced Alkaline Hydrogen Evolution Reaction. *Chem. - Eur. J.* 2018, **24**, 11158–11165. https://doi.org/10.1002/chem.201801693.

(10) Tan, S. M.; Pumera, M. Bottom-up Electrosynthesis of Highly Active Tungsten Sulfide (WS_{3-x}) Films for Hydrogen Evolution. *ACS Appl. Mater. Interfaces,* 2016, **8**, 3948–3957. https://doi.org/10.1021/acsami.5b11109.

(11) Strange, L. E.; Garg, S.; Kung, P.; Ashaduzzaman, M.; Szulczewski, G.; Pan, S. Electrodeposited Transition Metal Dichalcogenides for Use in Hydrogen Evolution Electrocatalysts. *J. Electrochem. Soc.* 2022, **169**, 026510. https://doi.org/10.1149/1945-7111/ac4f25.

(12) Belanger, D.; Laperriere, G.; Marsan, B. The Electrodeposition of Amorphous Molybdenum Sulfide. *J. Electroanal. Chem.* 1993, **347**, 165-183.

(13) Merki, D.; Fierro, S.; Vrubel, H.; Hu, X. Amorphous Molybdenum Sulfide Films as Catalysts for Electrochemical Hydrogen Production in Water. *Chem. Sci.* 2011, **2**, 1262–1267. https://doi.org/10.1039/c1sc00117e.

(14) Escalera-López, D.; Lou, Z.; Rees, N. V. Benchmarking the Activity, Stability, and Inherent Electrochemistry of Amorphous Molybdenum Sulfide for Hydrogen Production. *Adv. Energy Mater.* 2019, **9**, 1802614. https://doi.org/10.1002/aenm.201802614.

(15) Manyepedza, T.; Courtney, J. M.; Snowden, A.; Jones, C. R.; Rees, N. V. Impact Electrochemistry of MoS_2: Electrocatalysis and Hydrogen Generation at Low Overpotentials. *J. Phys. Chem. C,* 2022, **126**, 17942–17951. https://doi.org/10.1021/acs.jpcc.2c06055.

(16) Sharma, M. D.; Mahala, C.; Basu, M. 2D Thin Sheet Heterostructures of MoS_2 on $MoSe_2$ as Efficient Electrocatalyst for Hydrogen Evolution Reaction in Wide PH Range. *Inorg. Chem.* 2020, **59**, 4377–4388. https://doi.org/10.1021/acs.inorgchem.9b03445.

(17) Gao, M. R.; Liang, J. X.; Zheng, Y. R.; Xu, Y. F.; Jiang, J.; Gao, Q.; Li, J.; Yu, S. H. An Efficient Molybdenum Disulfide/Cobalt Diselenide Hybrid Catalyst for Electrochemical Hydrogen Generation. *Nat. Commun.* 2015, **6**, 5982. https://doi.org/10.1038/ncomms6982.

(18) Yang, J.; Wang, C.; Ju, H.; Sun, Y.; Xing, S.; Zhu, J.; Yang, Q. Integrated Quasiplane Heteronanostructures of $MoSe_2/Bi_2Se_3$ Hexagonal Nanosheets: Synergetic Electrocatalytic Water Splitting and Enhanced Supercapacitor Performance. *Adv. Funct. Mater.* 2017, **27**, 1703864. https://doi.org/10.1002/adfm.201703864.

(19) Li, S.; Zang, W.; Liu, X.; Pennycook, S. J.; Kou, Z.; Yang, C.; Guan, C.; Wang, J. Heterojunction Engineering of $MoSe_2/MoS_2$ with Electronic Modulation towards Synergetic Hydrogen Evolution Reaction and Supercapacitance Performance. *Chem. Eng. J.* 2019, **359**, 1419–1426. https://doi.org/10.1016/j.cej.2018.11.036.

(20) Zhang, L.; Zhu, J.; Wang, Z.; Zhang, W. 2D $MoSe_2$/CoP Intercalated Nanosheets for Efficient Electrocatalytic Hydrogen Production. *Int. J. Hydrogen Energy* 2020, **45**, 19246–19256. https://doi.org/10.1016/j.ijhydene.2020.05.059.

(21) Zhang, Q.; Wee, A. T. S.; Liang, Q.; Zhao, X.; Liu, M. Defect Engineering of Two-Dimensional Transition-Metal Dichalcogenides: Applications, Challenges, and Opportunities. *ACS Nano*, 2021, **15**, 2165–2181. https://doi.org/10.1021/acsnano.0c09666.

(22) Li, Y.; Wang, H.; Xie, L.; Liang, Y.; Hong, G.; Dai, H. MoS_2 Nanoparticles Grown on Graphene: An Advanced Catalyst for the Hydrogen Evolution Reaction. *J. Am. Chem. Soc.* 2011, **133**, 7296–7299. https://doi.org/10.1021/ja201269b.

(23) Conway, B. E.; Tilak, B. V. Interfacial Processes Involving Electrocatalytic Evolution and Oxidation of H_2, and the Role of Chemisorbed H. *Electrochim. Acta*, 2002, **47**, 3571-3594.

(24) Dubouis, N.; Grimaud, A. The Hydrogen Evolution Reaction: From Material to Interfacial Descriptors. *Chem. Sci.* 2019, **10**, 9165–9181. https://doi.org/10.1039/c9sc03831k.

(25) Vikraman, D.; Hussain, S.; Akbar, K.; Truong, L.; Kathalingam, A.; Chun, S. H.; Jung, J.; Park, H. J.; Kim, H. S. Improved Hydrogen Evolution Reaction Performance Using MoS_2-WS_2 Heterostructures by Physicochemical Process. *ACS Sustain. Chem. Eng.* 2018, **6**, 8400–8409. https://doi.org/10.1021/acssuschemeng.8b00524.

(26) Elgrishi, N.; Rountree, K. J.; McCarthy, B. D.; Rountree, E. S.; Eisenhart, T. T.; Dempsey, J. L. A Practical Beginner's Guide to Cyclic Voltammetry. *J. Chem. Educ.* 2018, **95**, 197–206. https://doi.org/10.1021/acs.jchemed.7b00361.

(27) Yamada, H.; Yoshii, K.; Asahi, M.; Chiku, M.; Kitazumi, Y. Cyclic Voltammetry Part 1: Fundamentals†. *Electrochemistry* 2022, **90**, 102005. https://doi.org/10.5796/electrochemistry.22-66082.

(28) Treimer, S.; Tang, A.; Johnson, D. C. A Consideration of the Application of Koutecky -Levich Plots in the Diagnoses of Charge-Transfer Mechanisms at Rotated Disk Electrodes. *Electroanalysis*, 2002, **14**, 165-171.

(29) Vrubel, H.; Hu, X. Growth and Activation of an Amorphous Molybdenum Sulfide Hydrogen Evolving Catalyst. *ACS Catal.* 2013, **3**, 2002–2011. https://doi.org/10.1021/cs400441u.

(30) Ambrosi, A.; Pumera, M. Templated Electrochemical Fabrication of Hollow Molybdenum Sulfide Microstructures and Nanostructures with Catalytic Properties for Hydrogen Production. *ACS Catal.* 2016, **6**, 3985–3993. https://doi.org/10.1021/acscatal.6b00910.

(31) Moulder, J. F.; Chastain, Jill. Handbook of X-Ray Photoelectron Spectroscopy, Perkin-Elmer Corp, Minnesota, 1992.

(32) Weber, T.; Muijsers, J. C.; Niemantsverdriet, J. W. Structure of Amorphous MoS_3, *J. Phys. Chem.* 1995, **99**, 9194-9200.

(33) Rodriguez-Pereira, J.; Zazpe, R.; Charvot, J.; Bureš, F.; Macak, J. M. Molybdenum Diselenide Thin Films Grown by Atomic Layer Deposition: An XPS Analysis. *Surf. Sci. Spectra,* 2020, **27**, 024006. https://doi.org/10.1116/6.0000354

6 Novel electrocatalyst via mechanochemistry: binary & ternary mixed transition metal dichalcogenides

This chapter is based on a manuscript undergoing review for publication:

T. Manyepedza, T. Auvray, R. Hendi, G. N. Aliev, T. Friščić and N. V. Rees. Novel electrocatalysts via mechanochemistry: binary & ternary mixed transition metal dichalcogenides. *Appl. Mater. Today*. 2024, under review.

Credit authorship contribution statement

Tshiamo Manyepedza: Investigating, Conceptualization, Data curation, Formal analysis, Validation, Writing-original draft. **Thomas Auvray**: Investigation, Resources, Writing-Review and Editing. **Ruba Hendi**: Imaging, analysis and review. **Gazi N. Aliev**: STEM imaging. **Tomislav Friščić:** Supervision, Writing-Review and Editing. **Neil V. Rees**: Conceptualization, Supervision, Writing-Review and Editing.

6.1 Introduction

TMDs have been studied extensively to enhance HER catalytic activity and methods such as exfoliation to reduce the number of tri-layers, nano-structuring, phase transition and doping to increase the number of active edge sites have been employed.[1-8] From the previous chapter, heterostructure formation was explored as one of the methods to improve TMD catalytic activity for HER and an improvement was recorded thereby highlighting the significance of bringing two TMDs together and to continue on this, the next step would be to mix two or more different TMDs to create a TMD mixture or hybrid. This would combine the HER capabilities of two or more TMDs which could potentially boost the overall HER activity of the resulting hybrid.

A more environmentally friendly method for producing TMD mixtures is mechanochemistry, which serves as an alternative to traditional TMD synthesis techniques. This approach leverages mechanical energy to induce physical and chemical transformations, enabling the preparation of various materials.[9,10] Mechanochemistry involves applying mechanical forces such as impact and shear to materials, thereby initiating chemical reactions.[11] During this process, the sample may undergo phase and structural alterations, change in crystallinity and surface activation due to energy fluctuations caused by impact, shearing, and friction through techniques like manual grinding, ball-milling, pan-milling or ultrasonication.[12-16] Mixed TMD materials can be synthesized mechanochemically from bulk TMD particles or crystals in a solvent-free, enclosed environment where mixing or comminution facilitates chemical transformations and particle breakdown.[17,18] This technique has been used to synthesize various TMDs, including MoS_2, and some studies have even produced TMD heterostructures for example a MoS_2-C_{60} hybrid,[19,20] and varying the milling speed and time when synthesizing MoS_2 using a planetary ball mill, impacted the formation and size of the resulting MoS_2.[19]

This chapter explores the synthesis of binary and ternary transition metal dichalcogenide mixtures by mechanochemical milling to develop electrocatalysts for the hydrogen evolution reaction. The produced TMD hybrids were then characterized using XPS, XRD and Raman spectroscopy and followed by electrochemical testing through linear sweep and cyclic voltammetry to evaluate their catalytic activity for the hydrogen evolution reaction in acidic media. The resulting voltammograms were analysed to

obtain HER reaction kinetics and Tafel information, allowing for a comparison of the catalytic activity of the TMD mixtures with recent literature.

The various TMD powders and nanoparticles were combined and milled to submicron sizes mechanochemically to create hybrid mixtures. For the binary hybrids, four combinations were produced: MoS_2+WS_2, MoS_2+WSe_2, $MoSe_2$+WS_2, and $MoSe_2$+WSe_2. For the ternary hybrids, three mixtures were formed: MoS_2+$MoSe_2$+WS_2, MoS_2+$MoTe_2$+WSe_2, and MoSSe+WTe_2+WS_2. Equal masses (0.15 g each) of the individual TMD powders were used to prepare the mixtures. 150 mg of the chosen mixture powder was milled to submicron size in a 15 mL stainless steel jar from Form-Tech Scientific, using two 7 mm stainless steel balls at 2500 rpm for 5 minutes in a FlackTek SpeedMixerTM (model DAC 330-100 Pro) with a custom jar holder. The resulting materials were suspended in ultrapure water for dropcasting. Glassy carbon electrodes were modified by dropcasting 5 µL of the hybrid TMD nanoparticle suspension onto the surface, then drying under a light source before using them as electrocatalysts in hydrogen evolution reaction (HER) studies (further discussed in Experimental Methods under section 3.3.2). The mechanochemical processing was also performed on individual TMD powders to compare their HER effects with those of the TMD hybrids.

6.2 Results and discussion

6.2.1 Characterization of mixed TMDs

6.2.1.1 X-ray photoelectron spectroscopy

X-ray photoelectron spectroscopy (XPS) was conducted to obtain the elemental composition of the mixed TMDs as well as to detect any changes in chemical composition after mechanochemical mixing. For the MoS_2+WSe_2 mixture, XPS confirmed the presence of Mo, W, S and Se elements in the wide survey spectra (Fig. 6.1) and high-resolution spectra of these peaks is shown below in Fig. 6.2 for the Mo 3*d*, S 2*p*, Se 3*p*, W 4*f* and Se 3*d* peaks. The Mo 3*d* peak region (Fig. 6.2A) included the Mo^{4+} doublet at 229 eV and 232 eV along with the S 2*s* at 226.3 eV and the Se 3*s* at 232 eV.[21] The S $2p_{3/2,1/2}$

and Se $3p_{3/2,1/2}$ doublets were also observed at positions 160 eV, 162 eV and 163.5 eV, 166.3 eV respectively (Fig. 6.2B).[22] The Se $3d_{5/2,3/2}$ doublet peak was detected at positions 54.3 eV and 55.5 eV (Fig. 6.2D).[23,24] In the W 4*f* peak region, the W^{4+} $4f_{7/2,5/2}$ doublet was detected at 32.0 eV and 34.2 eV positions. This doublet position falls between reported W^{4+} values for 1T-phase WS_2 and the 2H-phase WS_2 thus suggesting a mixture of the two phases in the hybrid sample. For the 1T-WS_2, the W^{4+} doublet was reported at 31.9 eV and 34.0 eV, and these positions are shifted to 32.7 eV and 35.3 eV for the 2H-WS_2.[25] We also observe the W^{6+} $4f_{7/2,5/2}$ doublet due to the presence of tungsten oxides in the sample. A significant amount of oxygen was detected in the samples (Table 6.1), indicating that some of the TMD samples were oxidised during sample preparation and mechanochemical processing, leading to the formation of tungsten and molybdenum oxides.

All these peak regions correspond to reported peak positions for both MoS_2 and WSe_2 TMDs and this was also confirmed when determining the chemical composition of the mixtures. The atomic percentage of the Mo, W, Se, and S peaks were derived from the spectra, and is shown in Table 6.1 along with those of other TMD hybrids. XPS spectra of the other TMD mixtures is provided in figures 6.2-6.11. Accurate derivation of the chemical compositions of the TMDs making up the mixtures proved difficult due to the overlap of the S 2*p* and Se 3*p* peaks which made peak deconvolution a challenge. For other mixtures which have the same chalcogen atom such as MoS_2+WS_2, accurate derivation of the chemical composition of the TMDs making up the hybrid was not possible due to having the same S atom.

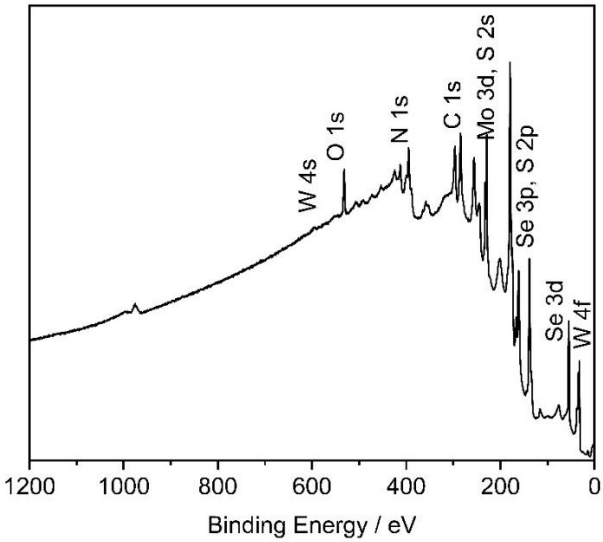

Figure 6.1. Wide area spectra of the MoS_2+WSe_2 mixture showing all the elements present in it.

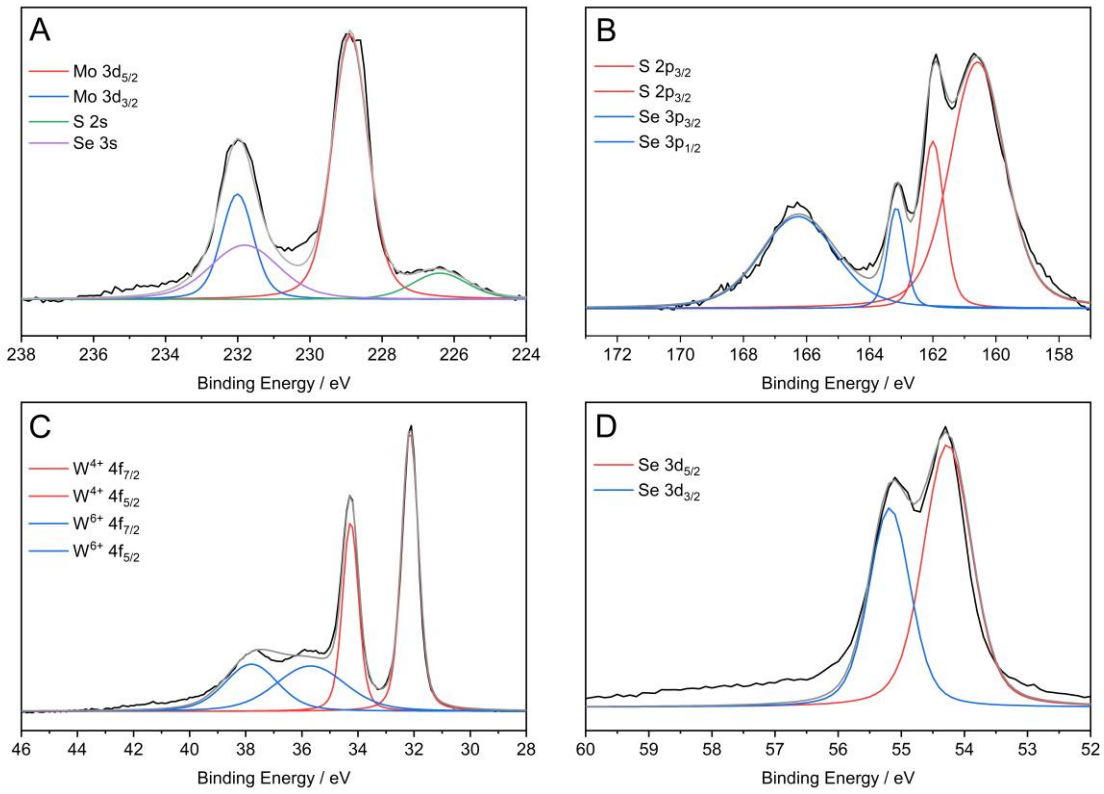

Figure 6.2. High resolution spectra of the MoS_2+WSe_2 mixture showing the **(A)** Mo 3d peak, **(B)** S 2p peak, **(C)** W 4f peak and **(D)** Se 3d peak regions from the wide area spectra. The coloured lines (red, blue, green and purple) represent the deconvolution of the peaks.

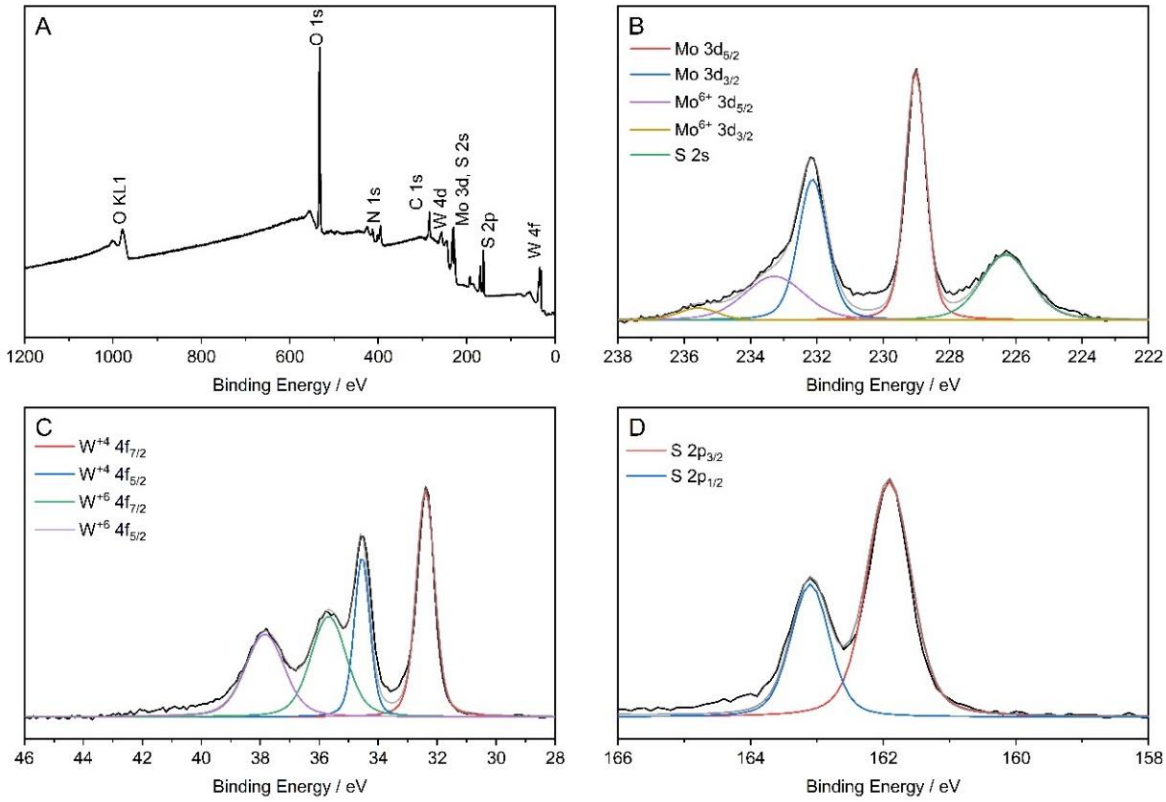

Figure 6.3. (A) Wide area spectra of the MoS_2+WS_2 mixture displaying all the elements present in it. High resolution spectra of the **(B)** Mo 3d, **(C)** W 4f and **(D)** S 2p peak regions. The coloured lines (red, blue, green, yellow and purple) represent the deconvolution of the peaks.

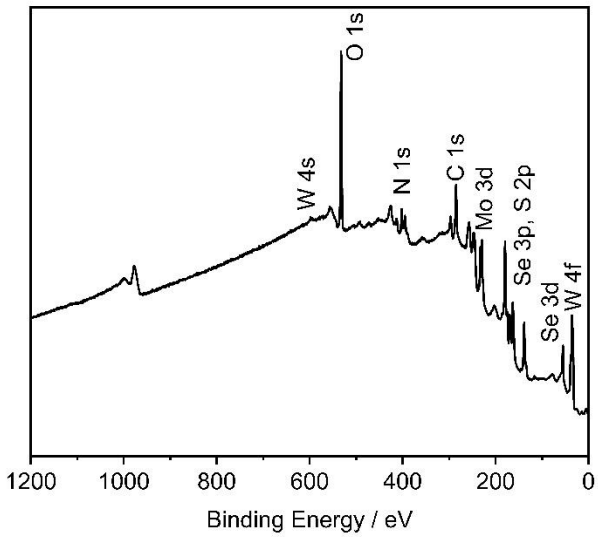

Figure 6.4. Wide area spectra of the $MoSe_2$+WS_2 sample highlighting all the elements detected in the sample.

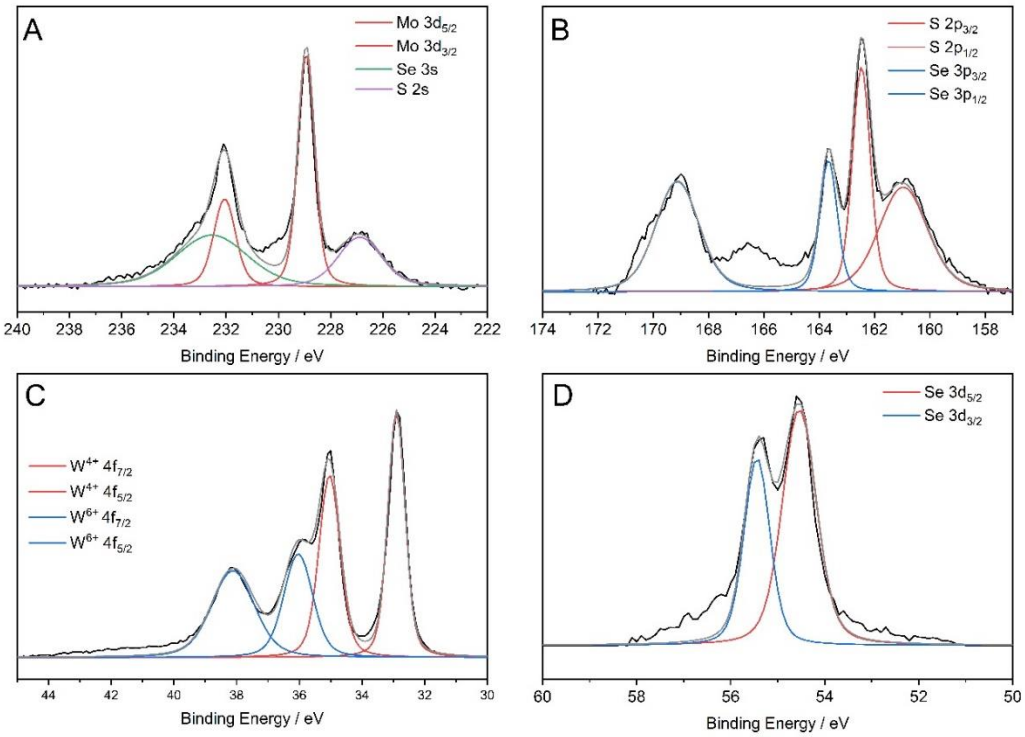

Figure 6.5. High resolution spectra of the $MoSe_2$+WS_2 mixture showing the **(A)** Mo 3d peak, **(B)** S 2p peak, **(C)** W 4f peak and **(D)** Se 3d peak regions from the wide spectra. The coloured lines (red, blue, green and purple) represent the deconvolution of the peaks.

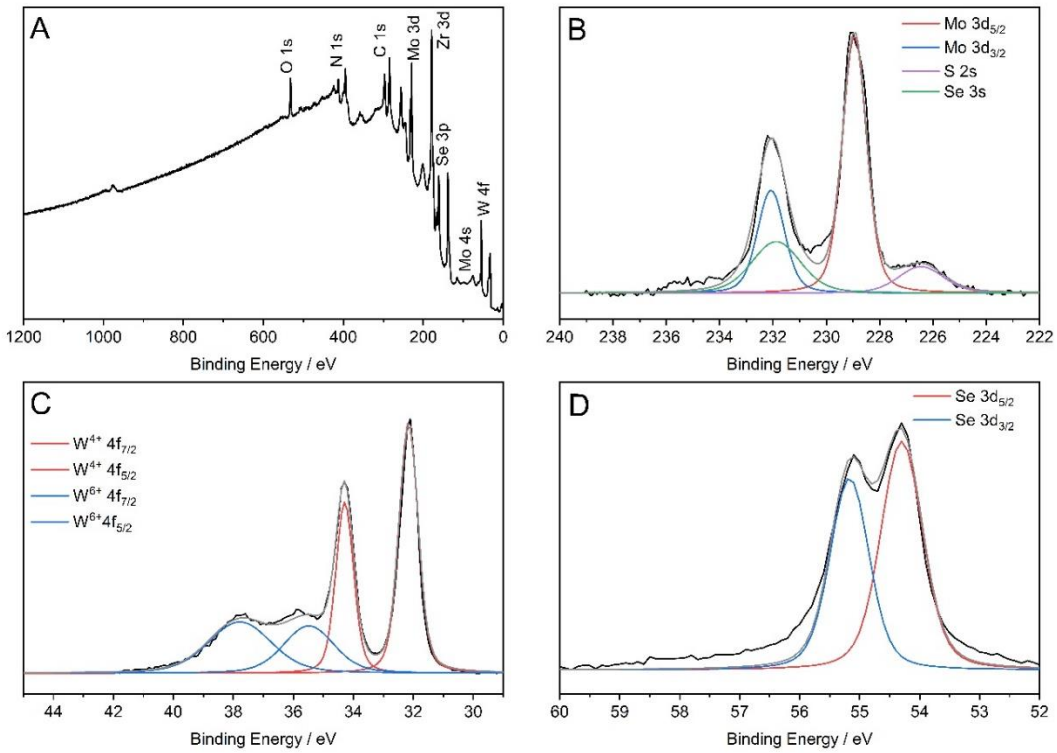

Figure 6.6. (A) Wide area spectra of the $MoSe_2$+WSe_2 mixture displaying all the elements present in it. High resolution spectra of the **(B)** Mo 3d, **(C)** W 4f and **(D)** Se 3d peak regions from the wide spectra. The coloured lines (red, blue, green and purple) represent the deconvolution of the peaks.

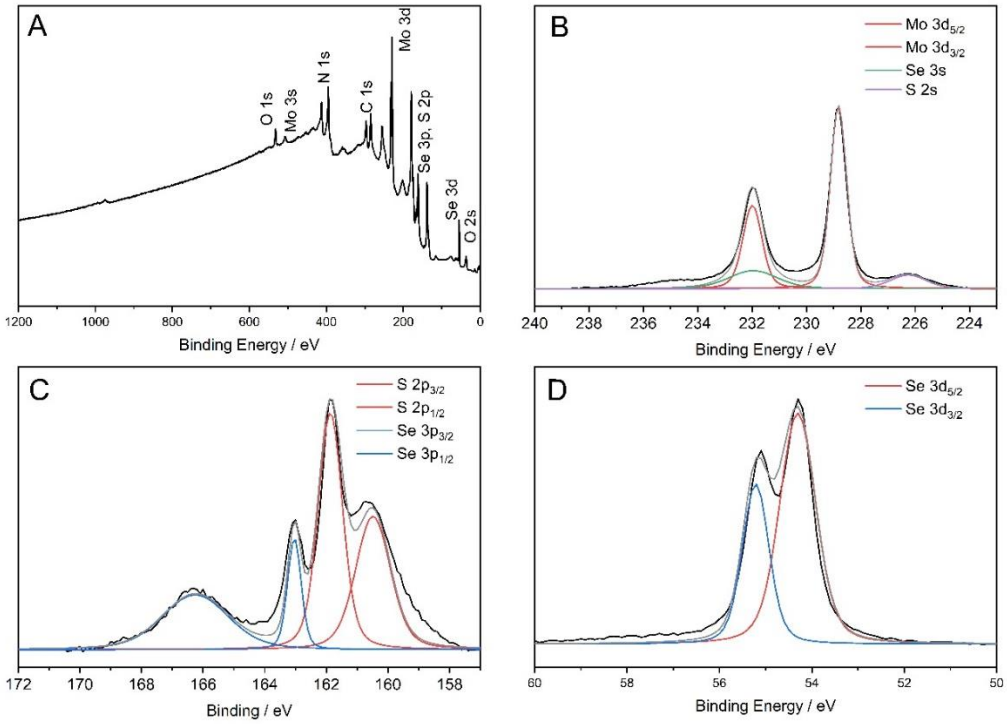

Figure 6.7. (A) Wide area spectra of the MoSSe sample showing all the elements present in it. High resolution spectra of the **(B)** Mo 3d peak, **(C)** S 2p peak and **(D)** Se 3d peak regions from the wide spectra. The coloured lines (red, blue, green and purple) represent the deconvolution of the peaks.

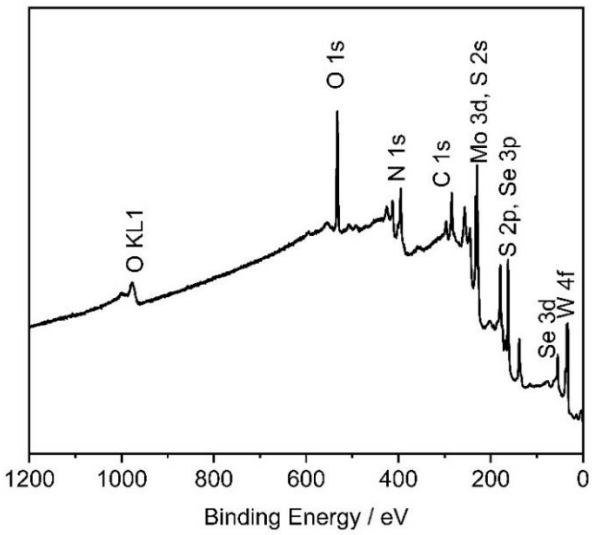

Figure 6.8. Wide area spectra of the MoS_2+$MoSe_2$+WS_2 sample highlighting all the elements detected in the sample.

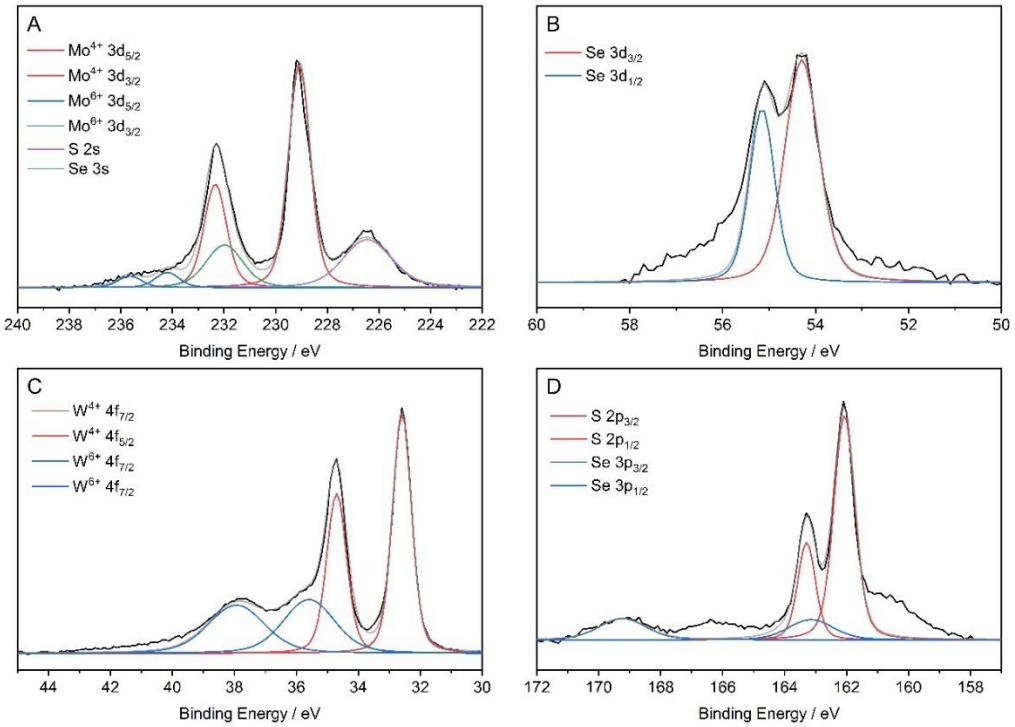

Figure 6.9. High resolution spectra of the MoS_2+$MoSe_2$+WS_2 mixture showing the **(A)** Mo 3d peak, **(B)** Se 3d peak, **(C)** W 4f peak and **(D)** S 2p peak regions from the wide spectra. The coloured lines (red, blue, green and purple) represent the deconvolution of the peaks.

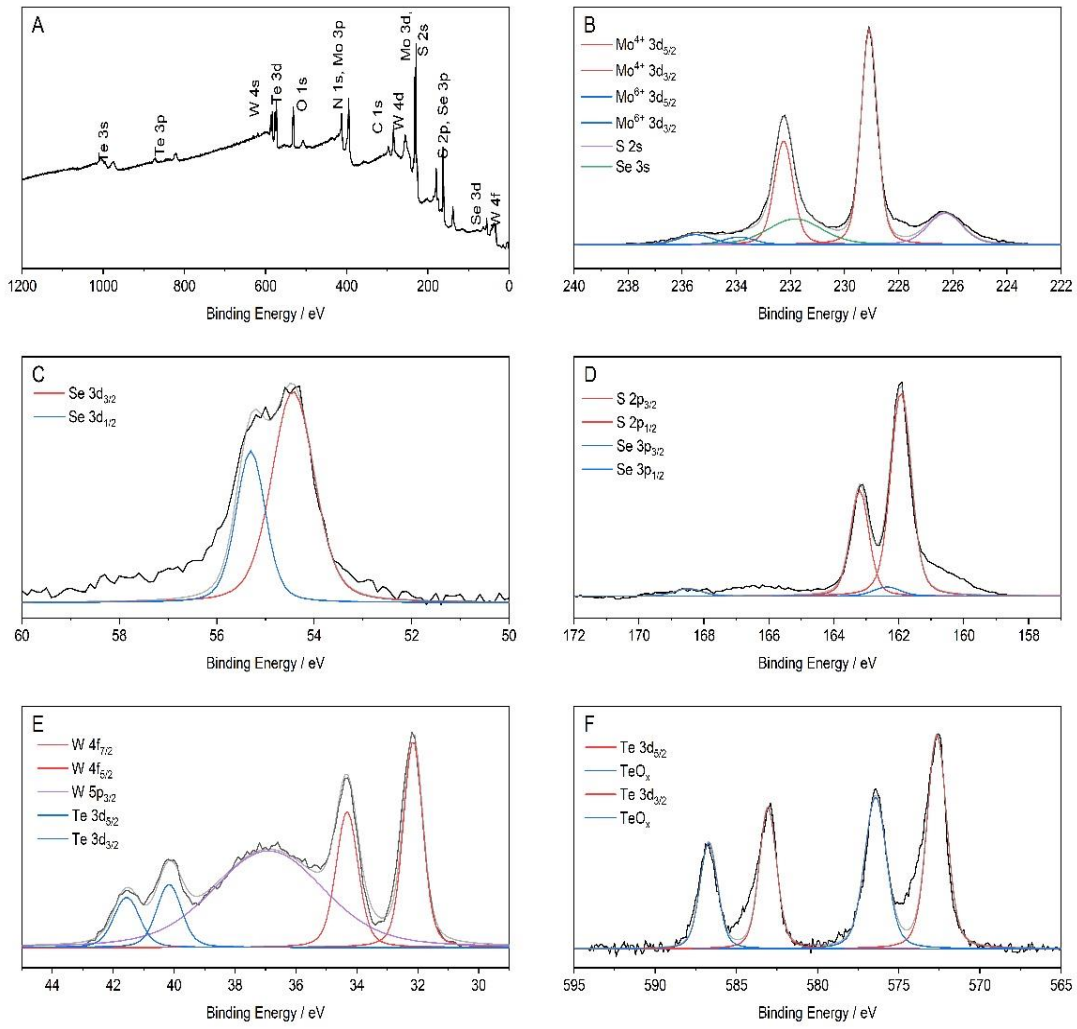

Figure 6.10. (A) Wide area spectra of the MoS_2+$MoTe_2$+WSe_2 mixture showing all the elements present in it. High resolution spectra of the **(B)** Mo 3d peak, **(C)** Se 3d peak, **(D)** S 2p peak, **(E)** W 4f peak and **(F)** Te 3d peak regions from the wide spectra. The coloured lines (red, blue, green and purple) represent the deconvolution of the peaks.

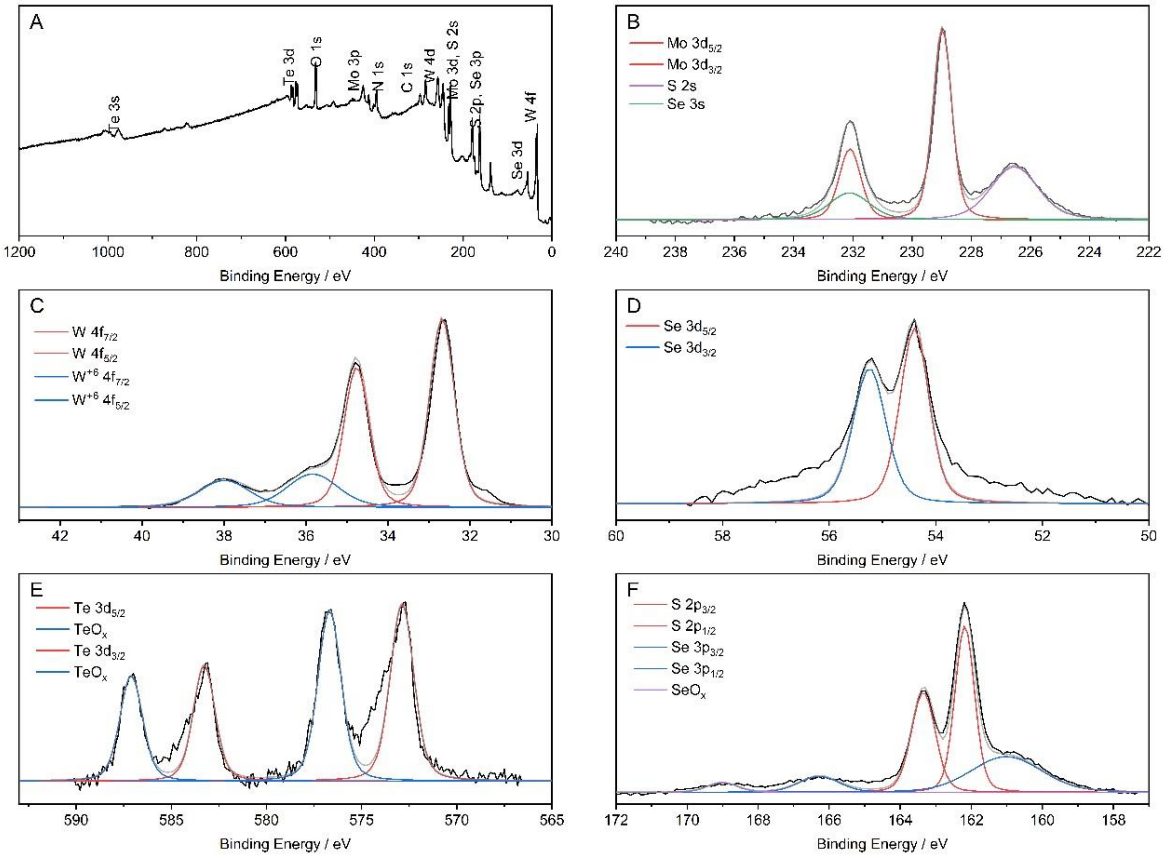

Figure 6.11. (A) Wide area spectra of the MoSSe+WTe_2+WS_2 mixture showing all the elements present in it. High resolution spectra of the **(B)** Mo 3d peak, **(C)** W 4f peak, **(D)** Se 3d peak, **(E)** Te 3d peak and **(F)** S 2p peak regions from the wide spectra. The coloured lines (red, blue, green and purple) represent the deconvolution of the peaks.

Table 6.1. Atomic percentages of the different elements in the TMD mixtures.

	XPS Atomic %						
	Binary mixture				Ternary mixture		
Element	**MoS_2+ WS_2**	**MoS_2+ WSe_2**	**$MoSe_2$+ WS_2**	**$MoSe_2$+ WSe_2**	**MoS_2+WS_2+ $MoSe_2$**	**MoS_2+$MoTe_2$ +WSe_2**	**MoSSe+WTe_2+WS_2**
Mo	18.45	19.94	16.44	20.83	25.79	17.28	9.96
W	16.04	17.93	18.17	18.13	11.26	10.05	11.92
S	44.80	34.19	30.50	-	31.18	36.61	43.39
Se	-	20.06	18.15	42.00	16.82	17.28	16.03
Te	-	-	-	-	-	13.03	6.38
O	20.71	7.88	16.74	19.04	14.95	5.75	12.28

6.2.1.2 X-ray powder diffraction

In order to obtain more information about the physical properties and crystallographic structures of the mixtures, X-ray powder diffraction was conducted on the TMD samples, and the results are displayed in Fig. 6.12. The diffraction pattern for the different TMD mixtures was essentially an overlay of the diffraction patterns of the individual TMDs with some new peaks resulting from the mechanochemical mixing and comminution. For the MoS_2+WS_2 mixture (Fig. 6.12A), the peaks observed at 14.4°, 33°, 40°, 50° and 59° correspond to the (002), (100), (103), (105) and (110) planes respectively which is typical of hexagonal phase MoS_2 and other diffraction peaks due to WS_2 at 29°, 33° and 60° corresponding to the (004), (100) and (008) planes respectively.[26-29] An extra diffraction peak was detected at 2θ value of 25.9°, which was also observed for the diffraction pattern of the $MoSe_2$+WS_2 mixture in Fig. 6.12C. This peak corresponds to the plane (004) which was not detected in the diffraction pattern of the individual TMDs making up the mixture. This shows a slight change in the crystallographic structure of the resulting from phase transformations in the TMD hybrid. Another noticeable aspect on the $MoSe_2$+WS_2 diffraction pattern is the shoulder peak on the 14.4° peak which corresponds to the (002) plane of the WS_2 sample. This caused the peak to be broader compared to the same peak on the WS_2 diffraction pattern thus suggesting a decrease in crystallinity of the hybrid TMD.

This shoulder peak on the 14.4° peak was observed on the MoS_2+WSe_2 and $MoSe_2$+WSe_2 (Fig. 6.12 B&D) diffraction patterns as well. The diffraction patterns for MoSSe and the ternary mixtures are provided in figures 6.13-6.16. For the MoS_2+$MoSe_2$+WS_2 hybrid, it is worth noting that the peaks (Fig. 6.14) are much broader than the corresponding peaks on the constituent TMD patterns. This signifies a reduction in crystallinity of the ternary hybrid. The broadening of the peaks was observed for the other ternary mixtures (Fig. 6.15 & 6.16) in relation to the diffraction patterns of their constituent TMDs.

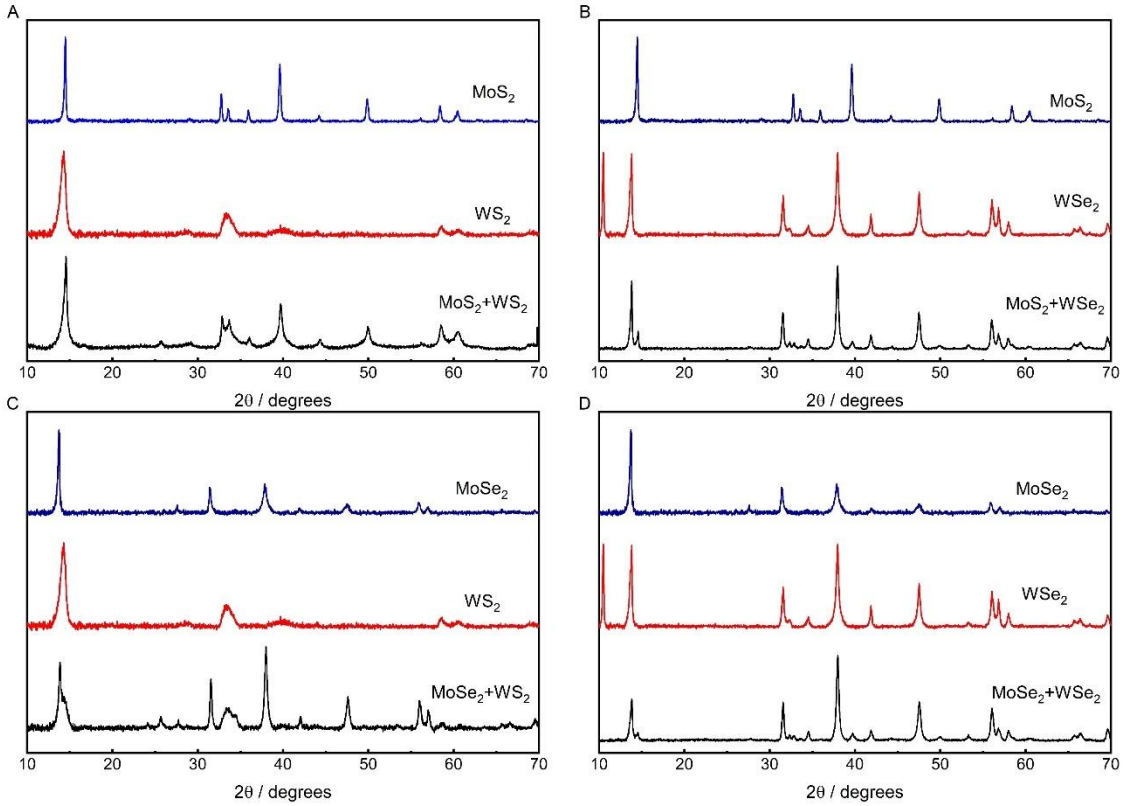

Figure 6.12. X-ray powder diffraction patterns of the binary TMD mixtures and the individual TMD components **(A-D)**.

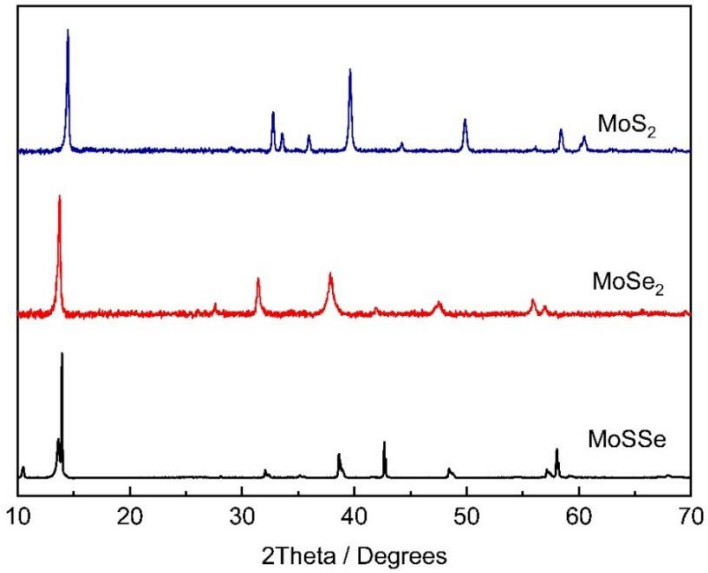

Figure 6.13. X-ray powder diffraction patterns of the MoSSe sample and the individual TMDs making it up.

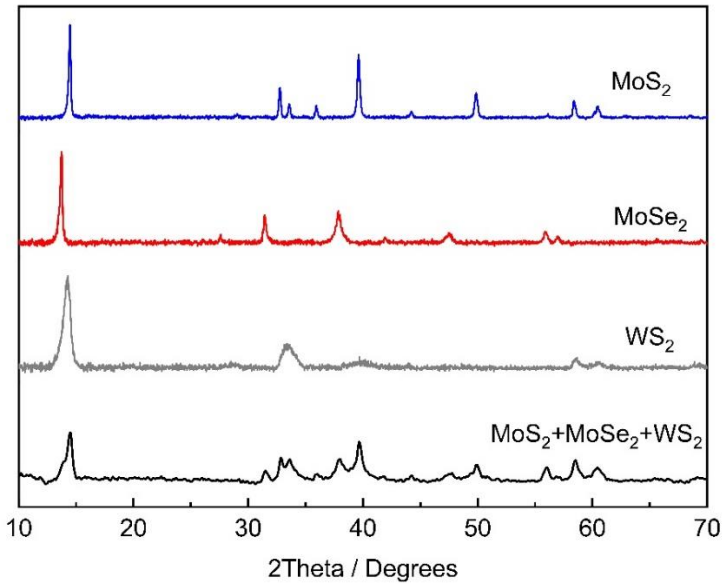

Figure 6.14. X-ray powder diffraction patterns of the MoS_2+$MoSe_2$+WS_2 mixture and the individual TMDs making it up.

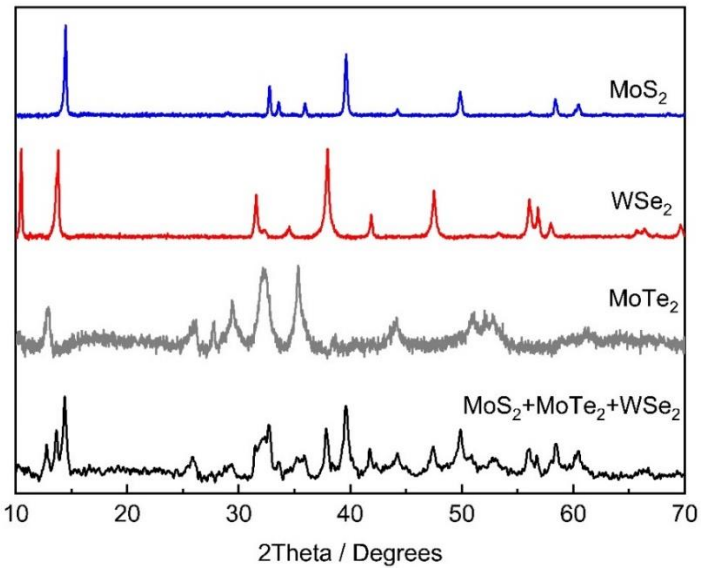

Figure 6.15. X-ray powder diffraction patterns of the MoS_2+$MoTe_2$+WSe_2 mixture and the individual TMDs making it up.

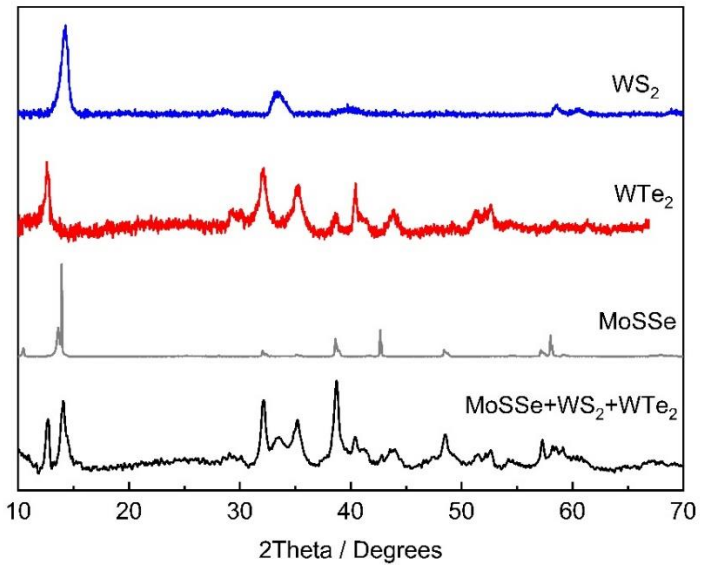

Figure 6.16. X-ray powder diffraction patterns of the MoSSe+WTe_2+WS_2 mixture and the individual TMDs making it up.

6.2.1.3 Raman spectroscopy

Raman spectroscopy was then carried out and Fig. 6.17 shows a selection of the spectroscopy results for the various TMD mixtures. Similar to the diffraction patterns, the spectrum of the TMD mixtures is a combination of the spectra of the two separate TMDs. In Fig. 3A, the MoS_2 spectrum has two peaks (vibrational modes), being the E_{2g} (in-plane) band at 385 cm^{-1} and the A_{1g} (out-of-plane) band at 405 cm^{-1}.[30] For WS_2, the E_{2g} peak is at 350 cm^{-1} while the A_{1g} peak is at 417.5 cm^{-1} which is in good agreement with literature.[31] All these peaks are still visible on the MoS_2+WS_2 spectrum and coincide with reported spectrum for WS_2/MoS_2 heterostructures.[32,33] However, it is worth noting the shift in peak positions in the spectrum which is more evident on the A_{1g} peak for WS_2, which has shifted from 417.5 cm^{-1} to 423 cm^{-1} on the MoS_2+WS_2 spectra. It has been reported that strain effects causing lattice deformations can be detected by Raman spectroscopy.[34-37] The shift in the E_{2g} peak can be attributed to the phase shift from 2H phase to the 1T phase as it has been previously reported for TMD.[38] This shift is a result of changes in bond lengths, bond angles and interlayer interactions during phase changes. The peak shifts detected on Fig. 6.17 are therefore likely to be due to a strain effect and phase transformation resulting from mechanochemical treatment during sample preparation. The MoS_2+WSe_2 spectrum on Fig. 6.17B is a combination of the MoS_2 and WSe_2 spectra which is similar to the spectrum of the reported WSe_2/MoS_2 heterolayer which was also a combination of the two TMDs.[39] The positions of the E_{2g} and A_{1g} peaks were blue-shifted by 16 cm^{-1}. This peak position shift hence shift in vibration modes is due phase transformations resulting from mechanochemical grinding and mixing of the TMD powders. The spectra for $MoSe_2$+WS_2, $MoSe_2$+WSe_2 and the ternary hybrids (Fig. 6.18 to 6.21) were also a combination of the spectra of their constituent TMDs with a slight shift in peak positions.

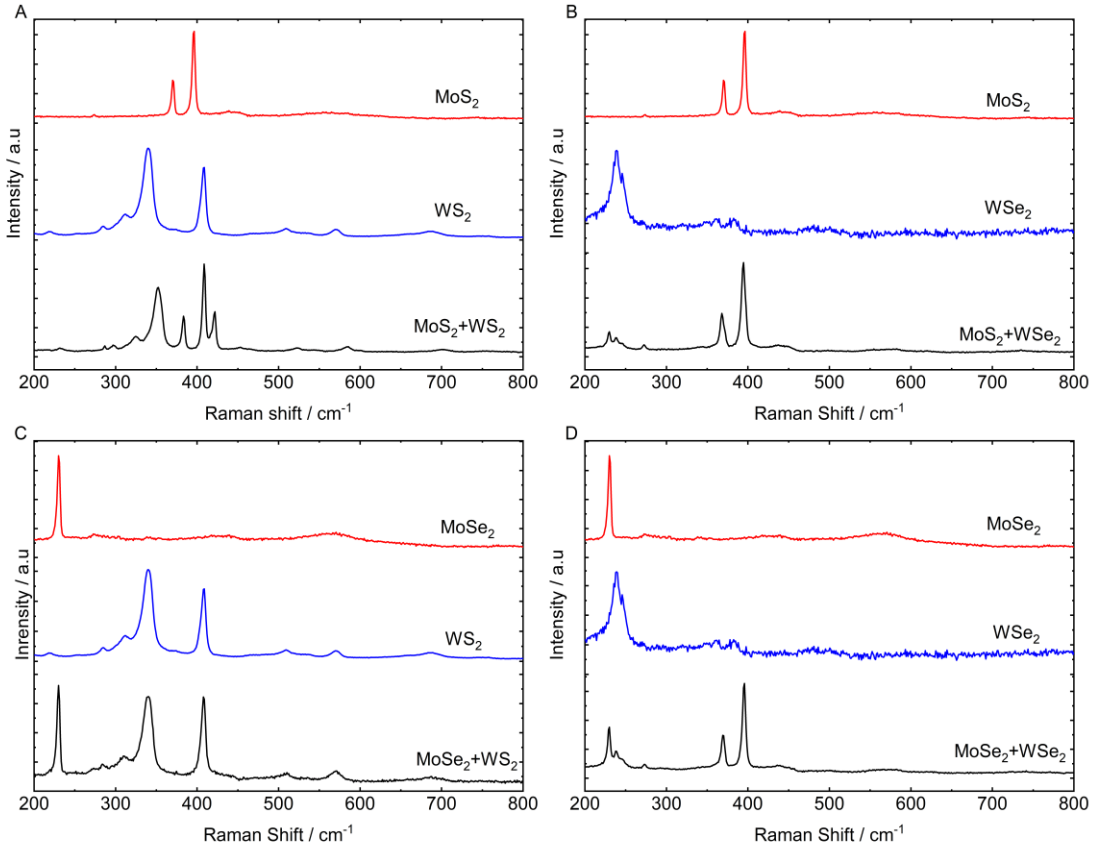

Figure 6.17. Raman spectra of the various TMD mixtures along with the spectra of individual TMD components **(A-D)**.

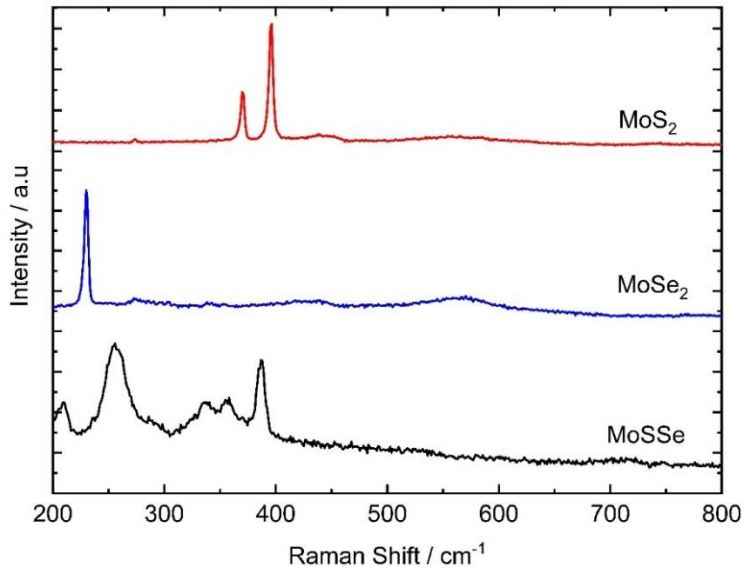

Figure 6.18. Raman spectra of the MoSSe sample along with the spectra of individual TMDs making them up.

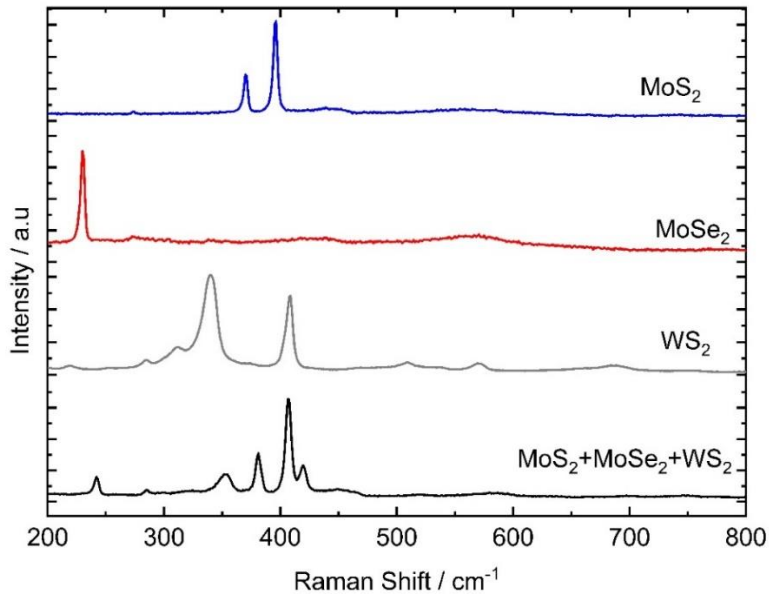

Figure 6.19. Raman spectra of the MoS_2+$MoSe_2$+WS_2 TMD mixtures along with the spectra of individual TMDs making them up.

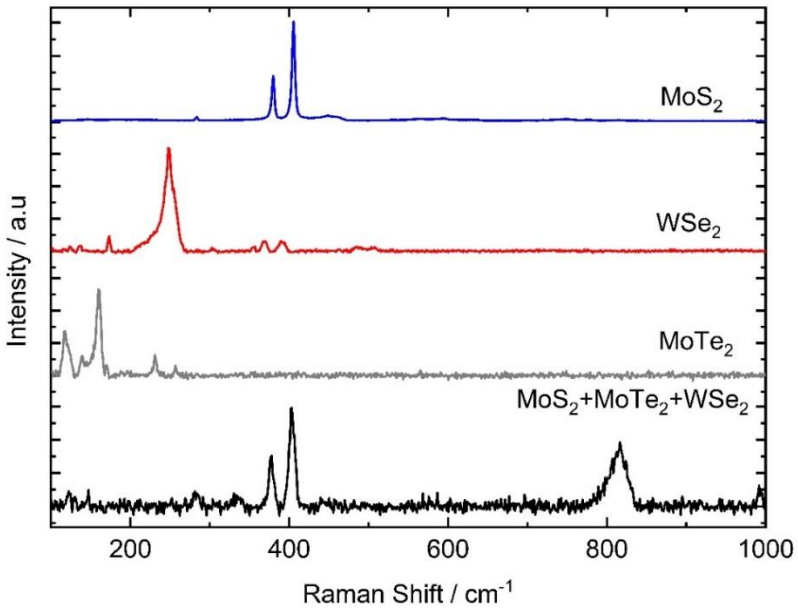

Figure 6.20. Raman spectra of the MoS_2+$MoTe_2$+WSe_2 TMD mixtures along with the spectra of individual TMDs making them up.

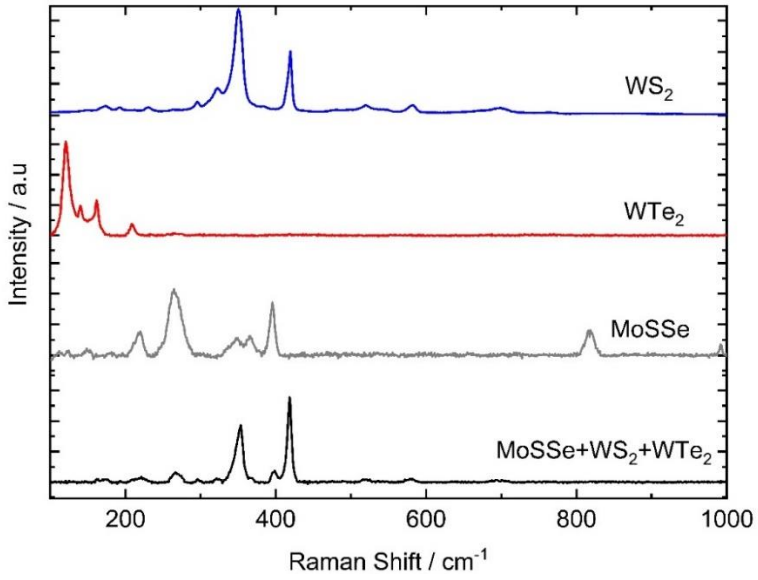

Figure 6.21. Raman spectra of the MoSSe+WTe_2+WS_2 TMD mixtures along with the spectra of individual TMDs making them up.

6.2.2 HER activity

The catalytic effects of the different TMD mixtures towards the hydrogen evolution reaction were investigated and compared to the individual TMDs. This was done by drop casting suspension of the TMD hybrids onto a glassy carbon electrode which are then used for linear sweep voltammetry in 10 mM H_2SO_4 and 0.1 M K_2SO_4 solutions at voltage scan rate of 50 mV s^{-1}. Fig. 6.22 below shows the activity of the binary TMD mixtures and how they compare to the individual TMDs with the current normalised by catalyst surface area which was approximately equal to the electrode surface area.

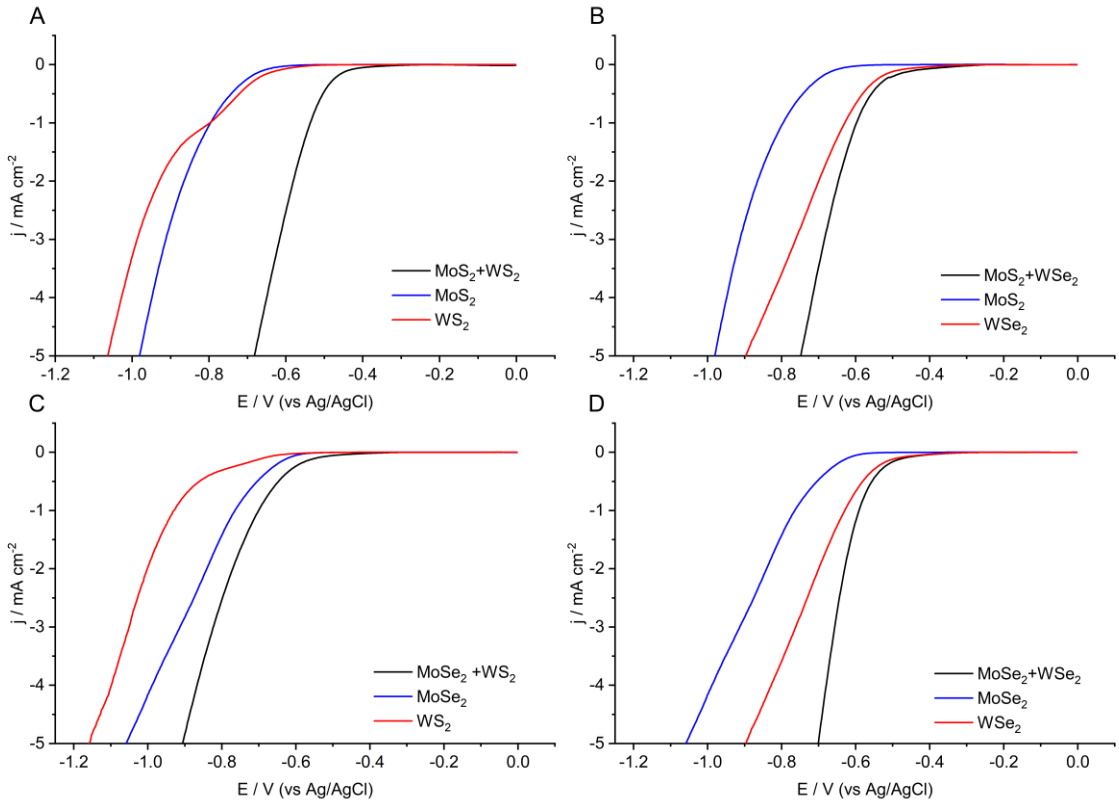

Figure 6.22. Voltammograms showing the change in onset potential between the TMD mixtures and the individual TMD components as electrocatalysts for the hydrogen evolution reaction **(A-D)**. An aqueous supporting electrolyte containing 10 mM H_2SO_4 and 0.1 M K_2SO_4 was used for the measurements with a scan rate of 50 mV s^{-1}.

An improvement in onset potential (here defined at 0.5 mA cm^{-2}) was observed for all the TMD mixtures with their onset potential becoming less negative as compared to the constituent TMDs. MoS_2+WS_2 (Fig. 6.22A) presented the greatest shift in onset potential compared to the MoS_2 and WS_2 onset potentials, highlighting the improvement brought about by the comminution and mixing of the two TMDs. This onset potential falls within the 0.33-0.50 V (vs Ag/AgCl) range of reported onset potential values for MoS_2 and WS_2 heterostructures and is thus in good agreement with literature.[40-42] Despite the different synthetic methods available to prepare TMD heterostructures and mixtures, it is clear that linking two or more TMDs, either by overlaying or mixing, enhances the HER catalytic activity. For the TMD mixtures, there has been an increase in surface area and presence of metastable phases as a result of comminution and this exposes more active edge sites for HER and this along with the combined effect of the two TMDs enhances the overall catalytic performance of the mixture towards HER. The mixed TMD powders, like the individual TMDs, were made into a suspension with deionised water which is then sonicated for 45 minutes, and it has been previously shown that sonicating the TMD the suspension has the potential to exfoliate further the nanoparticles thereby increasing the content of the more catalytically active 1T phase TMDs in the mixtures.[43-45] This could have had an effect on the improved HER activity from the mixed TMDs highlighted on Fig. 6.22.

The same improvement trend was observed for the triple mixed TMDs, that is, a shift on onset potential as compared to the individual TMDs (shown in Fig. 6.23). Onset potentials of these mixed TMDs are displayed in Table 6.2 and highlight that the MoS_2+$MoSe_2$+WS_2 sample require less applied potential for HER to occur in comparison to the other mixtures. For this mixture, this shift is possibly due to the presence of $MoSe_2$ which has been shown to have an earlier onset potential for HER compared to the other two TMDs in the mixture.

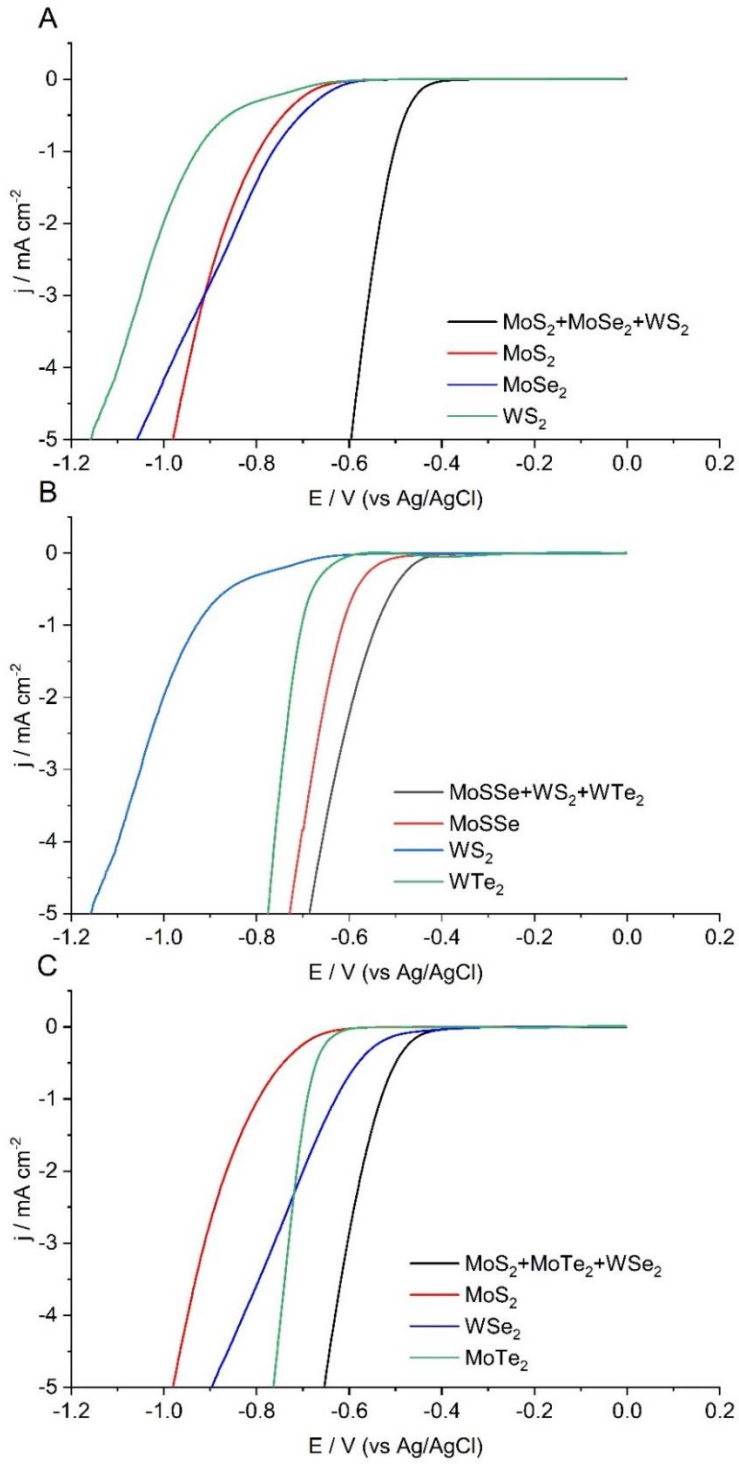

Figure 6.23. Voltammograms showing the change in onset potential between the TMD mixtures and the individual TMDs making them up as electrocatalysts for the hydrogen evolution reaction **(A-C)**. A solution of 10 mM H_2SO_4 with 0.1 M K_2SO_4 supporting electrolyte was used for the measurements with a scan rate of 50 mV s^{-1}.

Table 6.2. HER onset potentials for the various TMD mixtures used as electrocatalysts. Onset potentials were determined at a current density of 0.5 mA cm^{-2} for all materials.

TMDs	**Onset Potential (± 0.01) / V**
MoS_2+WS_2	-0.50
MoS_2+WSe_2	-0.56
$MoSe_2$+WS_2	-0.65
$MoSe_2$+WSe_2	-0.56
MoSSe	-0.58
MoS_2+$MoSe_2$+WS_2	-0.47
MoS_2+$MoTe_2$+WSe_2	-0.50
MoSSe+WTe_2+WS_2	-0.50

The various TMD mixtures were compared, and Fig. 6.24 shows the overlay of the scans and how they vary from each other in terms of overpotential and corresponding current density. Ternary mixtures had an earlier onset potential for HER as compared to the binary mixtures with the exception of the MoS_2+WS_2 sample which had an onset approximately equal to these mixtures. For all the mixtures highlighted on Fig. 6.24, there was a decrease in onset potential for hydrogen evolution reaction compared to the individual TMDs. Unfortunately, onset potential is not commonly reported in literature, making it challenging to compare some of these improvements with reported TMD heterostructures. There is, however, one study that has shown through density functional theory (DFT) calculation combined with experimental investigation that substituting tungsten (W) and other transition metals into MoS_2 activates more of the remote sulphur (S) active sites, leading to an increase in active sites and, consequently, enhanced HER activity.[46] Tungsten atoms could be incorporated into MoS_2 during mechanochemical activation, resulting in a compound with more active S sites, which would explain the improved HER activity observed in this study. Another factor contributing to the improvement in HER activity could be the introduction of strain in the TMDs during mechanochemical treatment, as observed in the Raman spectra exhibiting a shift in peak positions attributed to strain in the material. This strain can alter or modify the electronic structure of 2D TMDs, thereby enhancing their catalytic

activity.[47-49] This alteration likely contributes to the improved performance observed in these hybrids. The structural changes (exfoliation and phase transition) and strain induced by mechanochemical treatment, combined with the synergistic catalytic effects of two or more TMDs, lead to an overall improvement in the HER catalytic activity of the resulting hybrid materials and explain the shift in onset potential for HER compared to the individual TMDs.

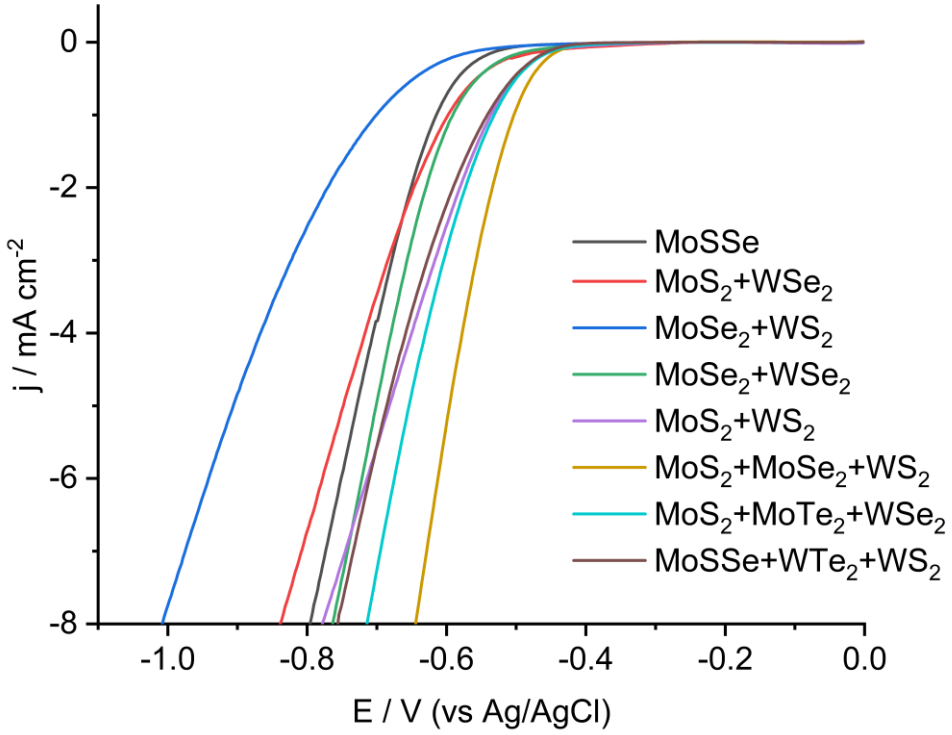

Figure 6.24. Comparison of the different TMD mixtures as electrocatalysts for HER. The conditions were kept the same for all the scans and the voltammetry was conducted in a 10 mM H_2SO_4 and 0.1 M K_2SO_4 aqueous electrolyte. The cells consisted of a Ag/AgCl (saturated KCl) reference electrode and graphite rod counter electrode along with modified glassy carbon as the working electrode.

6.2.3 Kinetic analysis

Hydrogen evolution reaction occurs in a multi-step process involving the Volmer, Tafel and Heyrovsky steps as potential rate determining steps.[50] These steps are determined by their associated Tafel slope values which are outlined in Table 6.3.[50-53]

Table 6.3. Rate determining steps in the hydrogen evolution reaction and their respective Tafel slope.

Step	**Equation**	**Tafel slope / mV dec^{-1}**
Volmer	$H_3O^+ + e^- \rightarrow H_{ads} + H_2O$	120
Heyrovsky	$H_{ads} + H_3O^+ + e^- \rightarrow H_2 + H_2O$	40
Tafel	$H_{ads} + H_{ads} \rightarrow H_2$	30

The calculated Tafel slope values obtained from the HER measurements conducted using TMD mixtures are shown in Fig. 6. The values lie between the Heyrovsky and Volmer step values with the exception of MoS_2+WSe_2 and $MoSe_2$+WS_2 which had a value more than 120 mV dec^{-1}. This suggests a mixture of both the Heyrovsky and Volmer as the rate determining steps for TMD mixtures with Tafel slope values falling between 40 and 120 mV dec^{-1}. $MoSe_2$ catalysts have been reported to have relatively high Tafel slope values ranging from 67 mV dec^{-1} to 192 mV dec^{-1},[54-57] and the calculated Tafel slope values for mixtures containing $MoSe_2$ are in good agreement with this range. Previous studies on MoS_2 electrocatalysts have shown a lower range of Tafel slope values as compared to $MoSe_2$, and these ranged from 40 to 60 mV dec^{-1}.[58-60] None of the mixtures containing MoS_2 registered a Tafel slope within that range which could be attributed to an effect from the other TMDs in that mixture resulting in an increase in Tafel slope value.

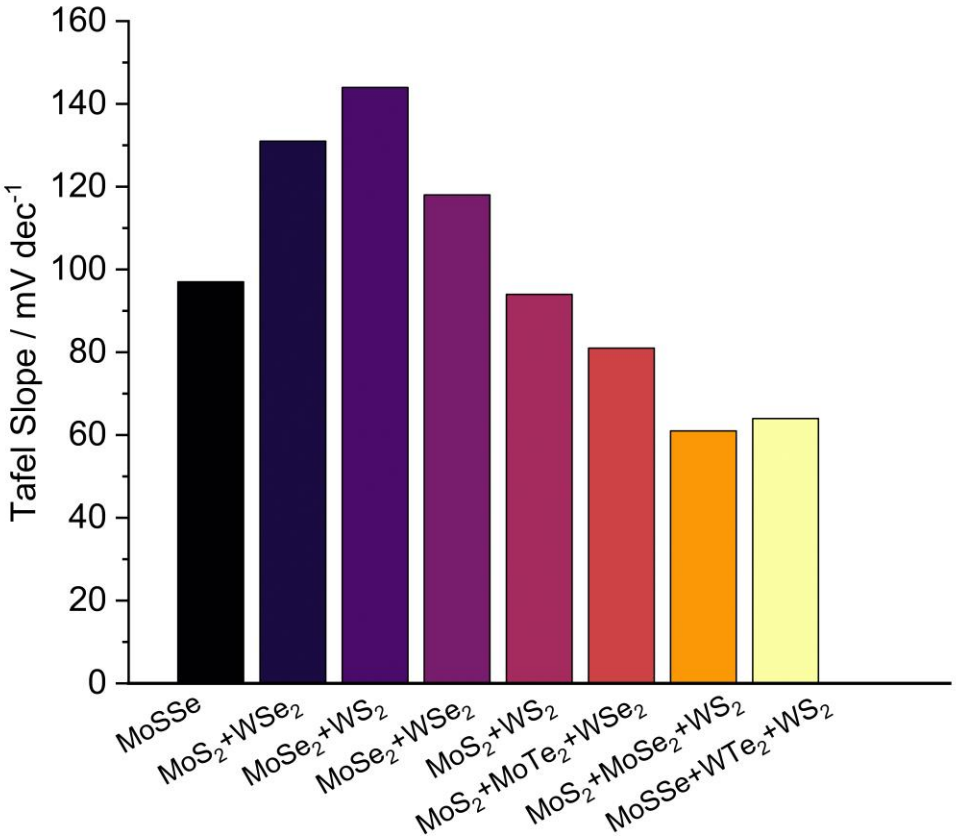

Figure 6.25. Tafel slope values for the different TMD mixtures. The Tafel slopes for the pure TMDs are: 104 mV dec^{-1} (MoS_2), 143 mV dec^{-1} (WS_2), 97 mV dec^{-1} ($MoSe_2$), 130 mV dec^{-1} (WSe_2), 66 mV dec^{-1} ($MoTe_2$) and 84 mV dec^{-1} (WTe_2).

Catalytic activity of the TMD mixtures was further investigated by modelling the reaction kinetics and extracting electrochemical rate constants for the hydrogen evolution reaction. For this voltametric study, a 33 μm carbon fibre electrode was used instead of the 3 mm glassy carbon electrode used in previous measurements. For TMD mixtures, an aliquot of 1 μL of their suspensions was drop cast onto the carbon fibre electrode surface and left to dry under a light source. These were used to run a series of linear sweep voltammograms in 10 mM H_2SO_4 and 0.1 M K_2SO_4 aqueous solution at 50 mV s^{-1} scan rate. The resulting voltammograms were then analysed to extract kinetic information by waveshape fitting the graphs using DigiElch software with a diffusion coefficient of 9.6×10^{-5} cm^2 s^{-1} and formal potential of

-0.32 V (vs Ag/AgCl).[61,62] Fig. 7 below shows a selection of the best-fit plots resulting from the waveshape fitting simulations. The electrochemical rate constants and transfer coefficients extracted from the simulations are shown in Table 6.4.

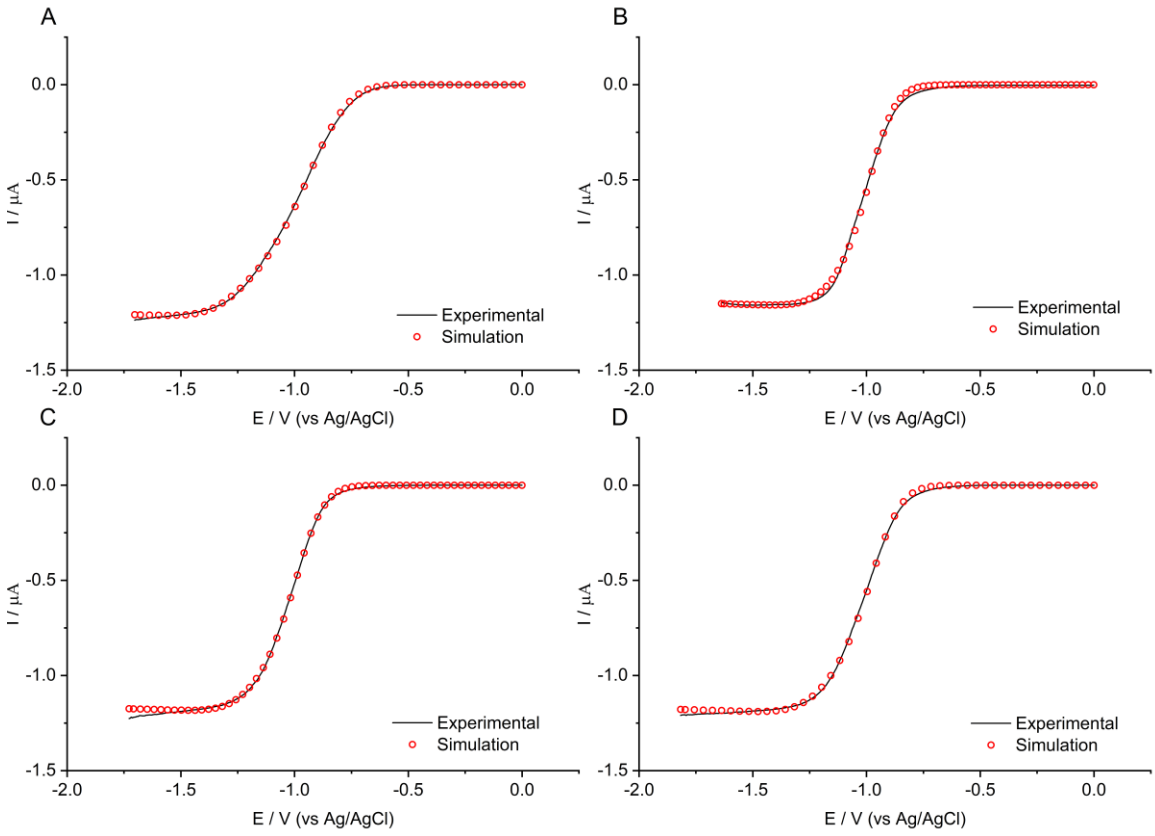

Figure 6.26. Reaction kinetics modelling of the resulting voltammograms from the HER scans using the TMD mixtures. Best-fit plot of the waveshape fitting simulation (○) and experimental data (—) for **(A)** MoS_2+WS_2, **(B)** MoS_2+WSe_2, **(C)** $MoSe_2$+WS_2 and **(D)** $MoSe_2$+WSe_2.

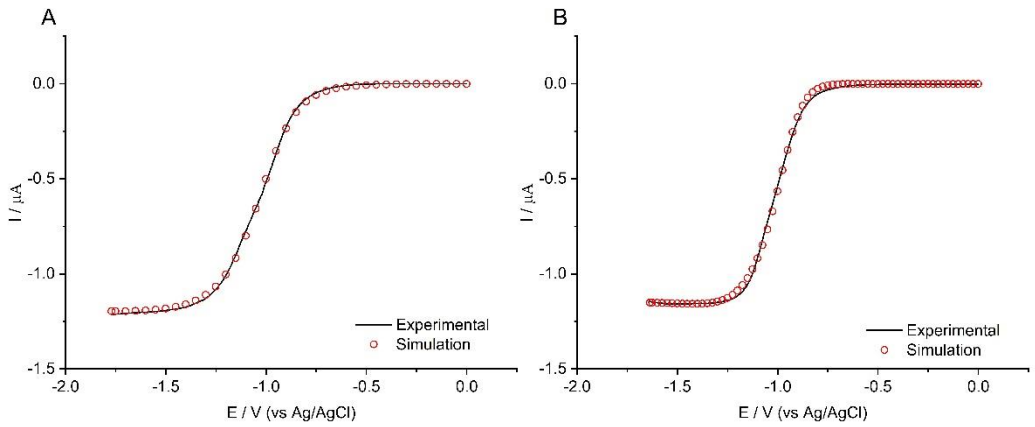

Figure 6.27. Reaction kinetics modelling of the resulting voltammograms from the HER scans using the MoS_2+WSe_2 TMD mixture. Best-fit plot of the waveshape fitting simulation (○) and experimental data (—) for two HER scans **(A-B)**.

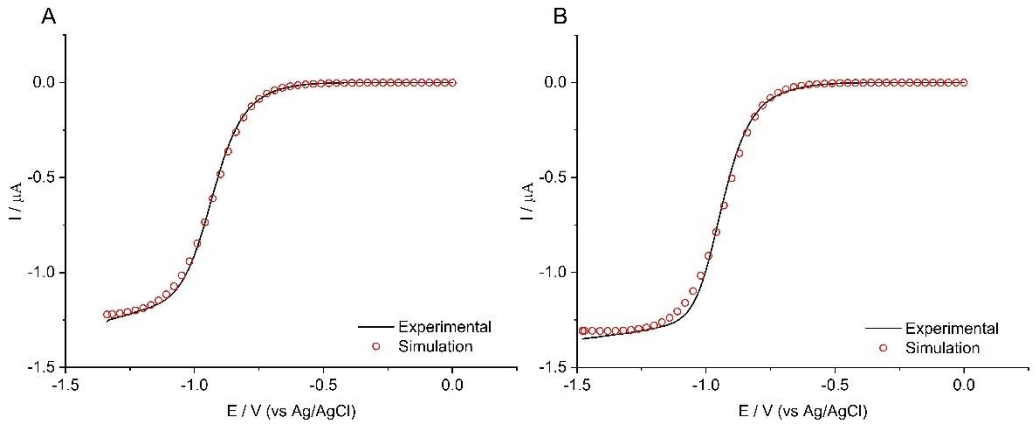

Figure 6.28. Reaction kinetics modelling of the resulting voltammograms from the HER scans using the MoS_2+WS_2 TMD mixture. Best-fit plot of the waveshape fitting simulation (○) and experimental data (—) for two HER scans **(A-B)**.

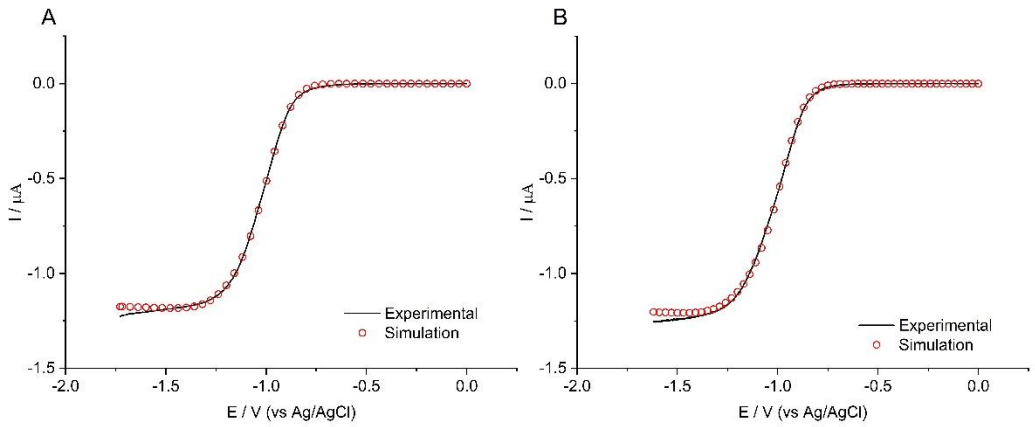

Figure 6.29. Reaction kinetics modelling of the resulting voltammograms from the HER scans using the $MoSe_2$+WS_2 TMD mixture. Best-fit plot of the waveshape fitting simulation (○) and experimental data (—) for two HER scans **(A-B)**.

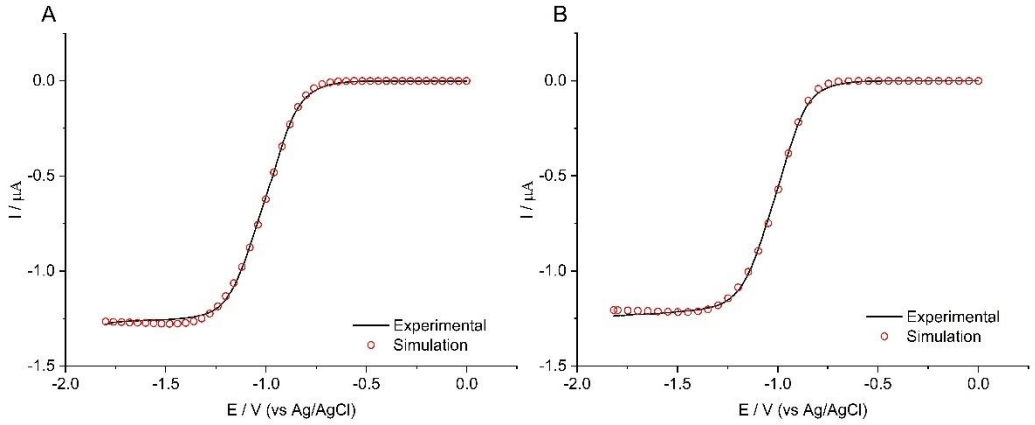

Figure 6.30. Reaction kinetics modelling of the resulting voltammograms from the HER scans using the $MoSe_2$+WSe_2 TMD mixture. Best-fit plot of the waveshape fitting simulation (○) and experimental data (—) for two HER scans **(A-B)**.

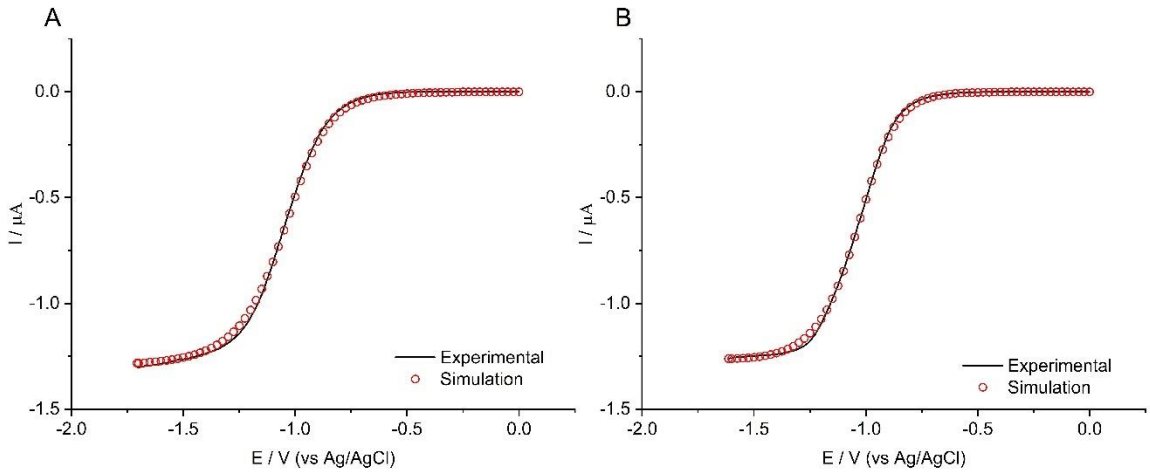

Figure 6.31. Reaction kinetics modelling of the resulting voltammograms from the HER scans using the MoS_2+$MoSe_2$+WS_2 TMD mixture. Best-fit plot of the waveshape fitting simulation (○) and experimental data (—) for two HER scans **(A-B)**.

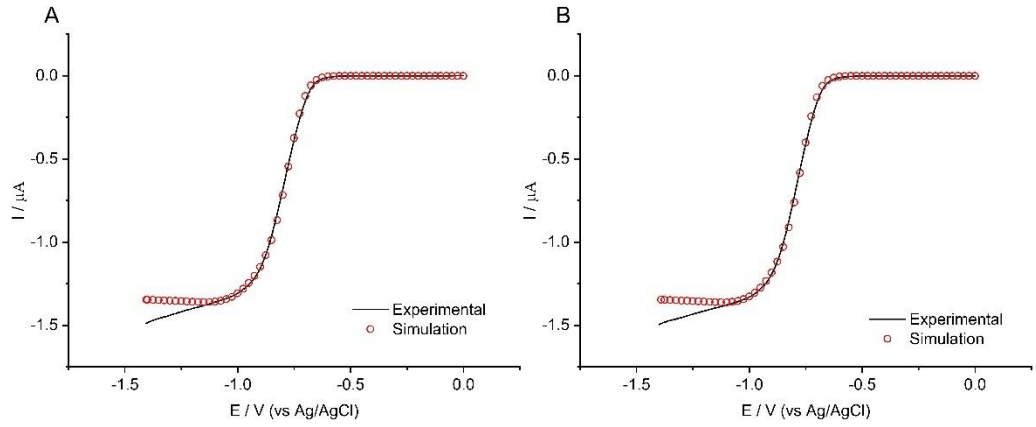

Figure 6.32. Reaction kinetics modelling of the resulting voltammograms from the HER scans using the MoS_2+$MoTe_2$+WSe_2 TMD mixture. Best-fit plot of the waveshape fitting simulation (○) and experimental data (—) for two HER scans **(A-B)**.

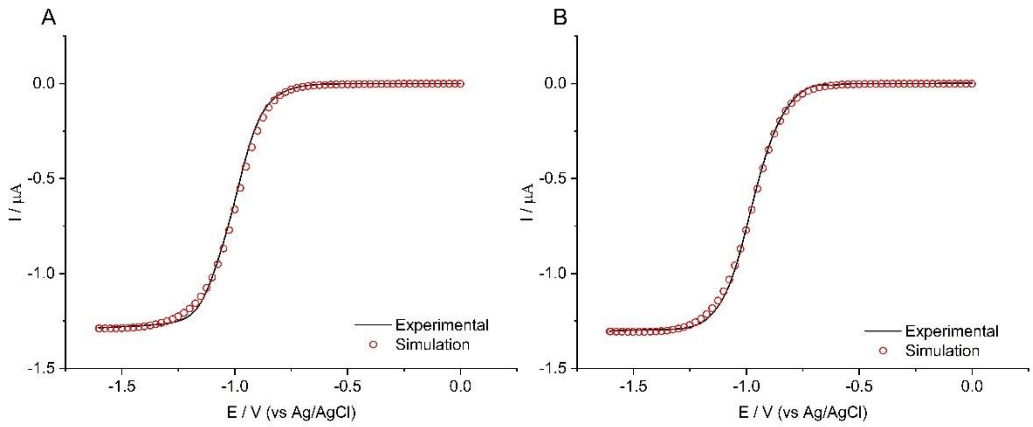

Figure 6.33. Reaction kinetics modelling of the resulting voltammograms from the HER scans using the MoSSe+WTe_2+WS_2 TMD mixture. Best-fit plot of the waveshape fitting simulation (○) and experimental data (—) for two HER scans **(A-B)**.

Electrochemical rate constants ranged from 5.2×10^{-4} cm s^{-1} to 8.2×10^{-3} cm s^{-1} for the different TMD mixtures with MoS_2+WS_2 having the lowest standard electrochemical rate constant value while $MoSe_2$+WSe_2 had the highest. On average the calculated rate constants are consistent with reported electrochemical rate constants for HER using various electrocatalyst materials. Previous studies have reported the rate constant for HER due to multi-layer MoS_2 electrocatalysts to range around 2.3×10^{-4} cm s^{-1} to 3.17×10^{-5} cm s^{-1}.[62,63] All the TMD mixtures containing MoS_2 have registered an improved electrochemical rate constant compared to the reported values which highlights the improvement in catalytic activity due to mechanochemical treatment of the different TMDs. Mixtures containing $MoSe_2$ had a higher electrochemical rate constant than the other mixtures and upon closer inspection, this could be attributed to the selenide components. This is more evident when comparing MoS_2+WS_2 and MoS_2+WSe_2 where an order of magnitude difference is observed for their rate constants with the Se containing mixture having a higher rate constant (1.5×10^{-3} cm s^{-1}) than the other. The trend was observed again when both TMDs in the mixture were selenides, that is the $MoSe_2$+WSe_2 mixture, which had an even greater rate constant of 8.2×10^{-3} cm s^{-1}. However, $MoSe_2$ has been shown to degrade easily in chapter 5 and this stability limitation is what prevents widespread application of TMDs with the Se

chalcogen. Creation of mixed TMD hybrids was in part aiming to improve the stability of the Se hybrids for enhanced HER performance. It is also worth noting the overall improved catalytic effect due to the mechanochemical comminution and mixing, which reduced the particle sizes to the nano range. This reduction increases the surface area-to-volume ratios, providing more surface area of the TMDs and thereby exposing more active sites for HER. Another effect would be the exfoliation and phase transformations of the TMD particles resulting in 1T-monolayer components which have been proved to be more catalytically active for HER.[43-45] All these effects combined with mixing different TMDs together improved the catalytic effect of the resulting mixture/compound and this is made apparent by the overall improvement in onset potential and electrochemical rate constants.

Table 6.4. The calculated standard electrochemical rate constants (k_0) and transfer coefficients (α) for HER from modelling the voltammograms using DigiElch software.

TMD	**k_0 / 10^{-3} cm s^{-1}**	**α (all values ±0.01)**	**Onset Potential (± 0.01)/ V**
MoS_2+WS_2	0.52 ± 0.01	0.33	-0.50
MoS_2+WSe_2	1.5 ± 0.5	0.25	-0.56
$MoSe_2$+WS_2	3.2 ± 0.3	0.24	-0.65
$MoSe_2$+WSe_2	8.2 ± 0.7	0.21	-0.56
MoS_2+$MoSe_2$+WS_2	1.2 ± 0.5	0.24	-0.47
MoS_2+$MoTe_2$+WSe_2	3.4 ± 0.4	0.36	-0.50
MoSSe+WTe_2+WS_2	1.0 ± 0.5	0.28	-0.50

6.3 Conclusion

Binary and ternary mixtures of transition metal dichalcogenide (TMD) materials were synthesized via mechanochemical activation and subsequently characterized to investigate their catalytic activity for the hydrogen evolution reaction (HER). Diffraction patterns of the hybrids displayed a combination of the constituent TMD patterns, with some such as MoS_2+$MoSe_2$+WS_2 and $MoSe_2$+WS_2, having broader diffraction peaks which signified a decrease in crystallinity of the TMD hybrids. For the Raman spectra,

there was a slight shift in peak positions of the A_{1g} and E_{2g} peaks for both the binary and ternary TMD hybrids thereby a shift in vibration modes as a result of mechanochemical treatment. For XPS characterization, accurate determination of the chemical compositions of the TMDs in the mixtures from the XPS spectra was challenging due to the overlap of the S 2*p* and Se 3*p* peaks. Additionally, mixtures containing the same chalcogen atom, such as MoS_2+WS_2 and $MoSe_2$+WSe_2, made peak deconvolution difficult.

These hybrids were tested in an aqueous solution of 10 mM H_2SO_4 and 0.1 M K_2SO_4, and kinetic parameters were derived from HER scans. On average, ternary hybrids exhibited better performance in terms of HER onset potential compared to binary hybrids, with the MoS_2+$MoSe_2$+WS_2 hybrid showing the lowest onset potential at -0.47 V (vs Ag/AgCl). This trend was also observed in Tafel slope calculations, where ternary hybrids had a lower range of Tafel slope values than binary hybrids. Despite these differences, both types of hybrids followed a Volmer-Heyrovsky mechanism, with the Volmer discharge step being the rate-determining step for HER.

Kinetic analysis revealed electrochemical rate constants ranging from 0.52×10^{-3} cm s^{-1} to 8.2×10^{-3} cm s^{-1} for the various TMD hybrids. The MoS_2+WS_2 hybrid had the lowest rate constant, while $MoSe_2$+WSe_2 had the highest, indicating that hybrids containing selenium generally had higher electrochemical rate constants than those without it. The overall catalytic activity of the TMD hybrids improved after mechanochemical treatment, attributed to the increased surface area of the particles and the exfoliation of the TMDs, which resulted in 1T-monolayer components known for their higher activity in HER.

6.4 References

(1) Liang, Z.; Shen, R.; Ng, Y. H.; Zhang, P.; Xiang, Q.; Li, X. A Review on 2D MoS_2 Cocatalysts in Photocatalytic H_2 Production. *J. Mater. Sci. Technol.* 2020, **56**, 89–121. https://doi.org/10.1016/j.jmst.2020.04.032.

(2) Jin, Q.; Liu, N.; Chen, B.; Mei, D. Mechanisms of Semiconducting 2H to Metallic 1T Phase Transition in Two-Dimensional MoS_2 Nanosheets. *J. Phys. Chem. C* 2018, **122**, 28215–28224. https://doi.org/10.1021/acs.jpcc.8b10256.

(3) Eftekhari, A. Molybdenum Diselenide ($MoSe_2$) for Energy Storage, Catalysis, and Optoelectronics. *Appl. Mater. Today.* 2017, **8**, 1–17. https://doi.org/10.1016/j.apmt.2017.01.006.

(4) Ambrosi, A.; Sofer, Z.; Pumera, M. 2H → 1T Phase Transition and Hydrogen Evolution Activity of MoS_2, $MoSe_2$, WS_2 and WSe_2 Strongly Depends on the MX_2 Composition. *Chem. Commun.* 2015, **51**, 8450–8453. https://doi.org/10.1039/c5cc00803d.

(5) Qian, Z.; Jiao, L.; Xie, L. Phase Engineering of Two-Dimensional Transition Metal Dichalcogenides. *Chin. J. Chem*. 2020, **38**, 753–760. https://doi.org/10.1002/cjoc.202000064.

(6) Xiao, D.; Huang, C.; Luo, Y.; Tang, K.; Ruan, Q.; Wang, G.; Chu, P. K. Atomic-Scale Intercalation of Graphene Layers into $MoSe_2$ Nanoflower Sheets as a Highly Efficient Catalyst for Hydrogen Evolution Reaction. *ACS Appl. Mater. Interfaces* 2020, **12**, 2460–2468. https://doi.org/10.1021/acsami.9b18302.

(7) Velický, M.; Dryfe, R. A. W. Electrochemistry of 2D Nanomaterials. *Front. Nanosci*. 2021; **18**, 485–536. https://doi.org/10.1016/B978-0-12-820055-1.00009-5.

(8) Li, G.; Zhang, D.; Qiao, Q.; Yu, Y.; Peterson, D.; Zafar, A.; Kumar, R.; Curtarolo, S.; Hunte, F.; Shannon, S.; Zhu, Y.; Yang, W.; Cao, L. All the Catalytic Active Sites of MoS_2 for Hydrogen Evolution. *J. Am. Chem. Soc.* 2016, **138**, 16632–16638. https://doi.org/10.1021/jacs.6b05940.

(9) Liu, X.; Li, Y.; Zeng, L.; Li, X.; Chen, N.; Bai, S.; He, H.; Wang, Q.; Zhang, C. A Review on Mechanochemistry: Approaching Advanced Energy Materials with Greener Force. *Adv. Mater*. 2022, **34**, 2108327. https://doi.org/10.1002/adma.202108327.

(10) Solares-Briones, M.; Coyote-Dotor, G.; Páez-Franco, J. C.; Zermeño-Ortega, M. R.; Contreras, C. M. de la O.; Canseco-González, D.; Avila-Sorrosa, A.; Morales-Morales, D.; Germán-Acacio, J. M. Mechanochemistry: A Green Approach in the Preparation of Pharmaceutical Cocrystals. *Pharmaceutics* 2021, **13**, 790. https://doi.org/10.3390/pharmaceutics13060790.

(11) Amrute, A. P.; De Bellis, J.; Felderhoff, M.; Schüth, F. Mechanochemical Synthesis of Catalytic Materials. *Chem. - Eur. J.* 2021, **27**, 6819–6847. https://doi.org/10.1002/chem.202004583.

(12) Grandhi, G. K.; Viswanath, N. S. M.; Cho, H. Bin; Han, J. H.; Kim, S. M.; Choi, S.; Im, W. Bin. Mechanochemistry as a Green Route: Synthesis, Thermal Stability, and Postsynthetic Reversible Phase Transformation of Highly-Luminescent Cesium Copper Halides. *J. Phys. Chem. Lett.* 2020, **11**, 7723–7729. https://doi.org/10.1021/acs.jpclett.0c02384.

(13) De Oliveira, P. F. M.; Torresi, R. M.; Emmerling, F.; Camargo, P. H. C. Challenges and Opportunities in the Bottom-up Mechanochemical Synthesis of Noble Metal Nanoparticles. *J. Mater. Chem. A*. 2020, **8**, 16114–16141. https://doi.org/10.1039/d0ta05183g.

(14) Liu, X.; Wen, H.; Guo, B.; Lv, C.; Shi, W.; Kang, W.; Zhang, J.; Yuan, R.; Zhang, C. Pan-Milling: Instituting an All-Solid-State Technique for Mechanical Metastable Oxides as High-Performance Lithium-Ion Battery Anodes. *Adv. Energy Mater.* 2021, **11**, 2100310. https://doi.org/10.1002/aenm.202100310.

(15) Musa, C.; Danjou, P. E.; Pauwels, A.; Cazier-Dennin, F.; Delattre, F. Ultrasound-Assisted Heterogeneous Synthesis of Bio-Based Oligo-Isosorbide Glycidyl Ethers: Towards Greener Epoxy Precursors. *Molecules* 2019, **24**, 1643. https://doi.org/10.3390/molecules24091643.

(16) Boulatov, R. The Liberating Force of Ultrasound. *Nat. Chem.* 2021, **13**, 112–114. https://doi.org/10.1038/s41557-020-00623-9.

(17) Cuccu, F.; De Luca, L.; Delogu, F.; Colacino, E.; Solin, N.; Mocci, R.; Porcheddu, A. Mechanochemistry: New Tools to Navigate the Uncharted Territory of “Impossible” Reactions. *ChemSusChem*. 2022, **15**, e202200362. https://doi.org/10.1002/cssc.202200362.

(18) Do, J. L.; Friščić, T. Mechanochemistry: A Force of Synthesis. *ACS Cent. Sci.* 2017, **3**, 13–19. https://doi.org/10.1021/acscentsci.6b00277.

(19) Wu, Z.; Wang, D.; Sun, A. Preparation of MoS_2 by a Novel Mechanochemical Method. *J. Alloys Compd*. 2010, **492**, L5-L7. https://doi.org/10.1016/j.jallcom.2009.11.070.

(20) Guan, J.; Wu, J.; Jiang, D.; Zhu, X.; Guan, R.; Lei, X.; Du, P.; Zeng, H.; Yang, S. Hybridizing MoS_2 and C_{60} via a van Der Waals Heterostructure toward Synergistically Enhanced Visible Light Photocatalytic Hydrogen Production Activity. *Int. J. Hydrogen Energy* 2018, **43**, 8698–8706. https://doi.org/10.1016/j.ijhydene.2018.03.148.

(21) Ambrosi, A.; Pumera, M. Templated Electrochemical Fabrication of Hollow Molybdenum Sulfide Microstructures and Nanostructures with Catalytic Properties for Hydrogen Production. *ACS Catal.* 2016, **6**, 3985–3993. https://doi.org/10.1021/acscatal.6b00910.

(22) Weber, T.; Muijsers, J. C.; Niemantsverdriet, J. W. Structure of Amorphous MoS_3. *J. Phys. Chem*. 1995, **99**, 9194-9200. https://pubs.acs.org/sharingguidelines.

(23) Sharma, M. D.; Mahala, C.; Basu, M. 2D Thin Sheet Heterostructures of MoS_2 on $MoSe_2$ as Efficient Electrocatalyst for Hydrogen Evolution Reaction in Wide pH Range. *Inorg. Chem*. 2020, **59**, 4377–4388. https://doi.org/10.1021/acs.inorgchem.9b03445.

(24) Rodriguez-Pereira, J.; Zazpe, R.; Charvot, J.; Bureš, F.; Macak, J. M. Molybdenum Diselenide Thin Films Grown by Atomic Layer Deposition: An XPS Analysis. *Surf. Sci. Spectra* 2020, **27**. https://doi.org/10.1116/6.0000354.

(25) Yang, C.; Gong, N.; Chen, T.; Li, Y.; Peng, W.; Zhang, F.; Fan, X. Enhanced Catalytic Conversion of Polysulfides Using High-Percentage 1T-Phase Metallic WS_2 Nanosheets for Li–S Batteries. *Green Energy Environ.* 2021, **7**, 1340-1348. https://doi.org/10.1016/j.gee.2021.03.001.

(26) Hu, S.; Chen, W.; Zhou, J.; Yin, F.; Uchaker, E.; Zhang, Q.; Cao, G. Preparation of Carbon Coated MoS_2 Flower-like Nanostructure with Self-Assembled Nanosheets as High-Performance Lithium-Ion Battery Anodes. *J. Mater. Chem. A* 2014, **2**, 7862–7872. https://doi.org/10.1039/c4ta01247j.

(27) Khan, M.; Kumar, S.; Mishra, A.; Sulania, I.; Nath Tripathi, M.; Tripathi, A. Study of Structural and Electronic Properties of Few-Layer MoS_2 Film. *Mater. Today: Proc.* 2022, **57**, 100–105. https://doi.org/10.1016/j.matpr.2022.01.361.

(28) Gopika, M. S.; Bindhu, B. Preparation and Characterization of Few Layered MoS_2 Nano Flakes. *Inter. J. Recent Tech. Eng.* 2019, **8**, 146–148. https://doi.org/10.35940/ijrte.B1027.0782S319.

(29) Mahler, B.; Hoepfner, V.; Liao, K.; Ozin, G. A. Colloidal Synthesis of 1T-WS_2 and 2H-WS_2 Nanosheets: Applications for Photocatalytic Hydrogen Evolution. *J. Am. Chem. Soc.* 2014, **136**, 14121–14127. https://doi.org/10.1021/ja506261t.

(30) Gołasa, K.; Grzeszczyk, M.; Bozek, R.; Leszczyński, P.; Wysmołek, A.; Potemski, M.; Babiński, A. Resonant Raman Scattering in MoS_2- From Bulk to Monolayer. *Solid State Commun*. 2014, **197**, 53–56. https://doi.org/10.1016/j.ssc.2014.08.009.

(31) Berkdemir, A.; Gutiérrez, H. R.; Botello-Méndez, A. R.; Perea-López, N.; Elías, A. L.; Chia, C. I.; Wang, B.; Crespi, V. H.; López-Urías, F.; Charlier, J. C.; Terrones, H.; Terrones, M. Identification of Individual and Few Layers of WS_2 Using Raman Spectroscopy. *Sci. Rep.* 2013, **3**, 1755. https://doi.org/10.1038/srep01755.

(32) Okada, M.; Kutana, A.; Kureishi, Y.; Kobayashi, Y.; Saito, Y.; Saito, T.; Watanabe, K.; Taniguchi, T.; Gupta, S.; Miyata, Y.; Yakobson, B. I.; Shinohara, H.; Kitaura, R. Direct and Indirect Interlayer Excitons in a van Der Waals Heterostructure of HBN/WS_2/MoS_2/HBN. *ACS Nano* 2018, **12**, 2498–2505. https://doi.org/10.1021/acsnano.7b08253.

(33) Tongay, S.; Fan, W.; Kang, J.; Park, J.; Koldemir, U.; Suh, J.; Narang, D. S.; Liu, K.; Ji, J.; Li, J.; Sinclair, R.; Wu, J. Tuning Interlayer Coupling in Large-Area Heterostructures with CVD-Grown MoS_2 and WS_2 Monolayers. *Nano Lett.* 2014, **14**, 3185–3190. https://doi.org/10.1021/nl500515q.

(34) Chiu, M. H.; Li, M. Y.; Zhang, W.; Hsu, W. T.; Chang, W. H.; Terrones, M.; Terrones, H.; Li, L. J. Spectroscopic Signatures for Interlayer Coupling in MoS_2-WSe_2 van Der Waals Stacking. *ACS Nano* 2014, **8**, 9649–9656. https://doi.org/10.1021/nn504229z.

(35) Zhu, C. R.; Wang, G.; Liu, B. L.; Marie, X.; Qiao, X. F.; Zhang, X.; Wu, X. X.; Fan, H.; Tan, P. H.; Amand, T.; Urbaszek, B. Strain Tuning of Optical Emission Energy and Polarization in Monolayer and Bilayer MoS_2. *Phys. Rev. B* 2013, **88**, 121301. https://doi.org/10.1103/PhysRevB.88.121301.

(36) Wang, Y.; Cong, C.; Qiu, C.; Yu, T. Raman Spectroscopy Study of Lattice Vibration and Crystallographic Orientation of Monolayer MoS_2 under Uniaxial Strain. *Small* 2013, **9**, 2857–2861. https://doi.org/10.1002/smll.201202876.

(37) Rice, C.; Young, R. J.; Zan, R.; Bangert, U.; Wolverson, D.; Georgiou, T.; Jalil, R.; Novoselov, K. S. Raman-Scattering Measurements and First-Principles Calculations of Strain-Induced Phonon Shifts in Monolayer MoS_2. *Phys. Rev. B* 2013, **87**, 081370. https://doi.org/10.1103/PhysRevB.87.081307.

(38) Sokolikova, M. S.; Mattevi, C. Direct synthesis of metastable phases of 2D transition metal dichalcogenides. *Chem. Soc. Rev*. 2020, **49**, 3952-3980.

(39) Fang, H.; Battaglia, C.; Carraro, C.; Nemsak, S.; Ozdol, B.; Kang, J. S.; Bechtel, H. A.; Desai, S. B.; Kronast, F.; Unal, A. A.; Conti, G.; Conlon, C.; Palsson, G. K.; Martin, M. C.; Minor, A. M.; Fadley, C. S.; Yablonovitch, E.; Maboudian, R.; Javey, A. Strong Interlayer Coupling in van Der Waals Heterostructures Built from Single-Layer Chalcogenides. *Proc. Natl. Acad. Sci.* 2014, **111**, 6198–6202. https://doi.org/10.1073/pnas.1405435111.

(40) Vikraman, D.; Hussain, S.; Akbar, K.; Truong, L.; Kathalingam, A.; Chun, S. H.; Jung, J.; Park, H. J.; Kim, H. S. Improved Hydrogen Evolution Reaction Performance Using MoS_2-WS_2

Heterostructures by Physicochemical Process. *ACS Sustain. Chem. Eng.* 2018, **6**, 8400–8409. https://doi.org/10.1021/acssuschemeng.8b00524.

(41) Lee, H. J.; Lee, S. W.; Hwang, H.; Yoon, S. I.; Lee, Z.; Shin, H. S. Vertically Oriented MoS_2/WS_2 heterostructures on Reduced Graphene Oxide Sheets as Electrocatalysts for Hydrogen Evolution Reaction. *Mater. Chem. Front.* 2021, **5**, 3396–3403. https://doi.org/10.1039/d1qm00051a.

(42) Manyepedza, T.; Auvray, T.; Friščić, T.; Rees, N. V. Electrochemically Deposited Transition Metal Dichalcogenide Heterostructures as Electrocatalysts: Accelerated Kinetics for the Hydrogen Evolution Reaction. *Electrochem. Commun*. 2024, **160**, 107678. https://doi.org/10.1016/j.elecom.2024.107678.

(43) Tan, X.; Kang, W.; Liu, J.; Zhang, C. Synergistic Exfoliation of MoS_2 by Ultrasound Sonication in a Supercritical Fluid Based Complex Solvent. *Nanoscale Res. Lett.* 2019, **14**, 317. https://doi.org/10.1186/s11671-019-3126-4.

(44) Qiao, W.; Yan, S.; He, X.; Song, X.; Li, Z.; Zhang, X.; Zhong, W.; Du, Y. Effects of Ultrasonic Cavitation Intensity on the Efficient Liquid-Exfoliation of MoS_2 Nanosheets. RSC Adv. 2014, **4**, 50981–50987. https://doi.org/10.1039/c4ra09001b.

(45) Sahoo, D.; Kumar, B.; Sinha, J.; Ghosh, S.; Roy, S. S.; Kaviraj, B. Cost Effective Liquid Phase Exfoliation of MoS_2 Nanosheets and Photocatalytic Activity for Wastewater Treatment Enforced by Visible Light. *Sci. Rep*. 2020, **10**, 10759. https://doi.org/10.1038/s41598-020-67683-2.

(46) Qu, J.; Elgendy, A.; Cai, R.; Buckingham, M. A.; Papaderakis, A. A.; de Latour, H.; Hazeldine, K.; Whitehead, G. F. S.; Alam, F.; Smith, C. T.; Binks, D. J.; Walton, A.; Skelton, J. M.; Dryfe, R. A. W.; Haigh, S. J.; Lewis, D. J. A Low-Temperature Synthetic Route Toward a High-Entropy 2D Hexernary Transition Metal Dichalcogenide for Hydrogen Evolution Electrocatalysis. *Adv. Sci.* 2023, 10, 2204488. https://doi.org/10.1002/advs.202204488.

(47) Lee, J. H.; Jang, W. S.; Han, S. W.; Baik, H. K. Efficient Hydrogen Evolution by Mechanically Strained MoS_2 Nanosheets. *Langmuir* 2014, **30**, 9866–9873. https://doi.org/10.1021/la501349k.

(48) Li, H.; Tsai, C.; Koh, A. L.; Cai, L.; Contryman, A. W.; Fragapane, A. H.; Zhao, J.; Han, H. S.; Manoharan, H. C.; Abild-Pedersen, F.; Nørskov, J. K.; Zheng, X. Activating and Optimizing MoS_2 Basal Planes for Hydrogen Evolution through the Formation of Strained Sulphur Vacancies. *Nat. Mater.* 2016, **15**, 48–53. https://doi.org/10.1038/nmat4465.

(49) Tan, Y.; Liu, P.; Chen, L.; Cong, W.; Ito, Y.; Han, J.; Guo, X.; Tang, Z.; Fujita, T.; Hirata, A.; Chen, M. W. Monolayer MoS_2 Films Supported by 3D Nanoporous Metals for High-Efficiency Electrocatalytic Hydrogen Production. *Adv. Mater.* 2014, **26**, 8023–8028. https://doi.org/10.1002/adma.201403808.

(50) Conway, B. E.; Tilak, B. V. Interfacial Processes Involving Electrocatalytic Evolution and Oxidation of H_2, and the Role of Chemisorbed H. *Electrochim. Acta* 2002, **47**, 3571-3594.

(51) Dubouis, N.; Grimaud, A. The Hydrogen Evolution Reaction: From Material to Interfacial Descriptors. *Chem. Sci*. 2019, **10**, 9165–9181. https://doi.org/10.1039/c9sc03831k.

(52) Li, Y.; Wang, H.; Xie, L.; Liang, Y.; Hong, G.; Dai, H. MoS_2 Nanoparticles Grown on Graphene: An Advanced Catalyst for the Hydrogen Evolution Reaction. *J. Am. Chem. Soc.* 2011, **133**, 7296–7299. https://doi.org/10.1021/ja201269b.

(53) Tan, S. M.; Pumera, M. Bottom-up Electrosynthesis of Highly Active Tungsten Sulfide (WS_{3-x}) Films for Hydrogen Evolution. *ACS Appl. Mater. Interfaces* 2016, **8**, 3948–3957. https://doi.org/10.1021/acsami.5b11109.

(54) Chouki, T.; Donkova, B.; Aktarla, B.; Stefanov, P.; Emin, S. Growth of $MoSe_2$ Electrocatalyst from Metallic Molybdenum Nanoparticles for Efficient Hydrogen Evolution. *Mater. Today Commun*. 2021, **26**, 101976. https://doi.org/10.1016/j.mtcomm.2020.101976.

(55) Najafi, L.; Bellani, S.; Oropesa-Nuñez, R.; Ansaldo, A.; Prato, M.; Del Rio Castillo, A. E.; Bonaccorso, F. Engineered $MoSe_2$-Based Heterostructures for Efficient Electrochemical Hydrogen Evolution Reaction. *Adv. Energy Mater.* 2018, **8**, 1703212. https://doi.org/10.1002/aenm.201703212.

(56) Chia, X.; Pumera, M. Inverse Opal-like Porous $MoSe_x$ Films for Hydrogen Evolution Catalysis: Overpotential-Pore Size Dependence. *ACS Appl. Mater. Interfaces* 2018, **10**, 4937–4945. https://doi.org/10.1021/acsami.7b17800.

(57) Kong, D.; Wang, H.; Cha, J. J.; Pasta, M.; Koski, K. J.; Yao, J.; Cui, Y. Synthesis of MoS_2 and $MoSe_2$ Films with Vertically Aligned Layers. *Nano Lett*. 2013, **13**, 1341–1347. https://doi.org/10.1021/nl400258t.

(58) Merki, D.; Fierro, S.; Vrubel, H.; Hu, X. Amorphous Molybdenum Sulfide Films as Catalysts for Electrochemical Hydrogen Production in Water. *Chem. Sci.* 2011, **2**, 1262–1267. https://doi.org/10.1039/c1sc00117e.

(59) Shin, S.; Jin, Z.; Kwon, D. H.; Bose, R.; Min, Y. S. High Turnover Frequency of Hydrogen Evolution Reaction on Amorphous MoS_2 Thin Film Directly Grown by Atomic Layer Deposition. *Langmuir* 2015, **31**, 1196–1202. https://doi.org/10.1021/la504162u.

(60) Lukowski, M. A.; Daniel, A. S.; Meng, F.; Forticaux, A.; Li, L.; Jin, S. Enhanced Hydrogen Evolution Catalysis from Chemically Exfoliated Metallic MoS_2 Nanosheets. *J. Am. Chem. Soc*. 2013, **135**, 10274–10277. https://doi.org/10.1021/ja404523s.

(61) Escalera-López, D.; Lou, Z.; Rees, N. V. Benchmarking the Activity, Stability, and Inherent Electrochemistry of Amorphous Molybdenum Sulfide for Hydrogen Production. *Adv. Energy Mater.* 2019, **9**, 1802614. https://doi.org/10.1002/aenm.201802614.

(62) Manyepedza, T.; Courtney, J. M.; Snowden, A.; Jones, C. R.; Rees, N. V. Impact Electrochemistry of MoS_2: Electrocatalysis and Hydrogen Generation at Low Overpotentials. *J. Phys. Chem. C* 2022, **126**, 17942–17951. https://doi.org/10.1021/acs.jpcc.2c06055.

(63) Li, H.; Du, M.; Mleczko, M. J.; Koh, A. L.; Nishi, Y.; Pop, E.; Bard, A. J.; Zheng, X. Kinetic Study of Hydrogen Evolution Reaction over Strained MoS_2 with Sulfur Vacancies Using Scanning Electrochemical Microscopy. *J. Am. Chem. Soc.* 2016, **138**, 5123–5129. https://doi.org/10.1021/jacs.6b01377.

7 Conclusion and Outlook

7.1 Summary

This study explored the HER electrocatalytic activity of various TMDs as well as strategies of enhancing their electrocatalytic activity. The fabrication of these TMDs was investigated and the resulting TMDs were characterized through various techniques to determine their chemical and physical properties. This was followed by electrochemical testing for HER performance as well as their stability in different media and lastly, kinetics analysis in order to compare catalytic performance between them and also to literature.

Chapter 4 commenced by looking into one of the most investigated TMDs, MoS_2 and how the different structural morphologies of it affect HER electrocatalytic activity. This chapter investigated the bulk amorphous form of MoS_2, which was synthesised via electrochemical deposition onto a glassy carbon electrode; and the nanoparticulate form of MoS_2, which was made into a suspension and drop cast onto a glassy carbon electrode for electrochemical testing and later through nanoparticle impact electrochemistry. Successful electrochemical deposition of amorphous MoS_2 film was confirmed through energy-dispersive spectroscopy and X-ray photoelectron spectroscopy characterization, from which the Mo:S ratio for this deposited film was determined to be 1:2.2. It has been reported that formation of MoS_2 through cyclic voltammetry produces a mixed composition film of MoS_2 and MoS_3 which would explain the disparity in the Mo:S ratio calculated.[1,2]

The stability of this deposited MoS_2 film was then tested in various pH solutions to ascertain the limits of not just the deposited but MoS_2 as a whole in preparation for the nanoparticle impact study. The MoS_2 film remained stable in pH 2 sulfuric acid solution, thereby suggesting that the MoS_2 nanoparticles would display the same stability under similar pH conditions. Another aim of studying the electrodeposited form of MoS_2 was to determine the onset potential for HER, which would give a rough estimate on potentials at which impacts, or current spikes should start occurring during the impact study using MoS_2 nanoparticles. This impact study was conducted to investigate the HER reaction

kinetics of MoS_2 to compare them with the drop cast MoS_2 nanoparticles and electrodeposited forms. These were observed to have varying onset potentials for HER in pH 2 sulfuric acid, with the impact study registering an onset potential of -0.10 V (RHE), compared to -0.49 V and -0.29 V (vs RHE) for the drop cast and electrodeposited MoS_2 forms, respectively.

The earlier onset potential from the impact study needed to be verified, that it is indeed due to hydrogen evolution reaction, and this led to the scale-up of the impact experiment to produce sufficient hydrogen gas to be tested via gas chromatography. The gas produced from this scale-up impact experiment was confirmed to be hydrogen gas thereby validating the earlier onset potential for HER from the impact study. The apparent absence of the -0.10 V (vs RHE) onset in the drop cast experiment is attributed to ultralow currents being masked by capacitive currents in the diffusion-only voltammogram. This hypothesis was supported by a rotating electrode experiment within the NP suspension, which suggested the presence of an onset around -0.10 V (vs RHE).

Kinetic analysis of the electrodeposited form through automated waveshape fitting MoS_2 yielded a standard electrochemical rate constant of $(3.17 \pm 0.30) \times 10^{-5}$ cm s^{-1} and a transfer coefficient of $\alpha = 0.67 \pm 0.02$ along with a Tafel slope of 45 mV dec^{-1}. For the impact study, peak current data was used to gain kinetic information and care was required to avoid effects from the electronic filtering on the transient current signals as they can greatly distort the resulting data. Due to this, minimal filtering was applied to the data for analysis. A range of k_0 values were reported ranging from 10^{-2} to 250 cm s^{-1}. Further analysis of these results suggested that "few-trilayer" fragments were responsible for the low onset potential and varying apparent electrochemical rate constants for these 1-3 trilayer fragments in line with those reported by McKelvey et al.[3] This finding was further confirmed by AFM imaging, showing the presence of nanoparticles with heights of approximately 0.65 nm and 1.30 nm, corresponding to 1 and 2 trilayers, respectively, consistent with literature.[4]

Chapter 5 expanded the study from just MoS_2 to other TMDs, specifically, their heterostructures and how they perform compared to individual TMDs in terms of HER catalytic activity. TMD

heterostructure studies are ongoing, and this study aimed to investigate a different approach to their synthesis and how this approach will affect HER performance. Two methods were employed to create the heterolayers: the first method involved drop casting a nanoparticle layer of one TMD followed by electrodepositing a different TMD on top ('NP/L'), while the second method involved sequentially electrodepositing layers of two different TMDs ('L/L'). Successfully synthesis of these heterolayers was confirmed by SEM-EDS and XPS but unfortunately, peak deconvolution proved challenging due to the overlap of the S 2*p* and Se 3*p* peaks, thereby making it difficult to deduce the chemical compositions of the heterolayers.

Evaluation of the stability and HER catalytic activity of the heterolayers in an acidic solution was conducted after characterization and it was found that heterolayers containing a film of $MoSe_2$ exhibited low stability, whereas those with a film of MoS_2 remained very stable after multiple consecutive scans. Electrodeposited MoS_2 film has been shown to be stable in a 10 mM H_2SO_4 and 0.1 M K_2SO_4 solution in chapter 5 and from reported literature,[5] hence the high stability of the heterolayers having it as the overlayer whereas a separate study has shown that $MoSe_2$ film degrades with each passing scan in the same solution. Along with their high stability, the heterolayers with a film of MoS_2 also displayed improved HER performance when compared to the constituents TMDs making them up. A rotating disk electrode was essential for the kinetics study, and due to the requirements of the rotating disk electrode, only stable heterolayers like $MoSe_2/MoS_2$ and WS_2/MoS_2, which could endure the rotation, were used in the study. They registered electrochemical rate constants of $(3.20 \pm 0.10) \times 10^{-4}$ cm s^{-1} and $(1.73 \pm 0.03) \times 10^{-4}$ cm s^{-1} for WS_2/MoS_2 and $MoSe_2/MoS_2$ heterolayers, respectively which was an overall improvement compared to reported rate constants for electrodeposited MoS_2. This further demonstrated the enhanced HER catalytic activity of the heterolayers, highlighting that there is still potential for improvement in TMDs.

The improved HER performance as a result of heterolayer creation displayed what overlaid TMDs can achieve, and this piqued interest into what two or more mixed TMDs could achieve in terms of HER catalytic activity, as investigated in chapter 6. Mechanochemical activation was used to synthesize binary and ternary mixtures of TMDs to enhance the catalytic activity of the resulting hybrids. These

hybrids were characterised by XPS, XRD and Raman spectroscopy to explore any chemical or physical changes brought about by mechanochemical activation. In the Raman spectra, there was a slight shift in the peak positions of the A_{1g} and E_{2g} peaks for both the binary and ternary TMD hybrids, indicating a change in vibration modes due to mechanochemical treatment. The diffraction patterns of the hybrids showed a combination of the constituent TMD patterns. Some hybrids, like MoS_2+$MoSe_2$+WS_2 and $MoSe_2$+WS_2, exhibited broader diffraction peaks, indicating a decrease in crystallinity.

Electrochemical testing of the hybrids for HER exhibited improved HER performance in terms of onset potential compared to the individual TMDs, and it is worth noting that the ternary mixtures displayed better performance than the binary mixtures. This trend was also evident in the Tafel slope calculations, where ternary hybrids exhibited a lower range of Tafel slope values compared to binary hybrids. Despite these differences, both types of hybrids adhered to a Volmer-Heyrovsky mechanism, with the Volmer discharge step being the rate-determining step for HER. Electrochemical rate constants of the hybrids were calculated, and they ranged from 0.52×10^{-3} cm s^{-1} to 8.2×10^{-3} cm s^{-1}, with MoS_2+WS_2 hybrid having the lowest rate constant, while $MoSe_2$+WSe_2 had the highest, indicating that hybrids containing selenium generally had higher electrochemical rate constants than those without it. The overall catalytic activity of the TMD hybrids improved following mechanochemical treatment. This enhancement was attributed to the increased surface area of the particles, exfoliation of the TMDs, which produced 1T-monolayer components known for their higher activity in HER and the synergistic effect of two or more catalytically active materials mixed together.

7.2 Future work

Transition metal dichalcogenides offer a range of possibilities to explore in order to improve or enhance their HER catalytic activity, and this study investigated some of those ways. Bulk and nanoparticulate forms of MoS_2 were studied along with TMD heterostructures and mixtures as electrocatalysts for enhanced HER activity. They displayed improved HER performance but like any other research study,

there were certain limitations which once addressed, would provide further insights about strategies to improve catalytic activity of TMDs.

Chapter 5 investigated an alternative method of creating TMD heterostructures and these displayed enhanced HER activity, with some registering low electrochemical rate constants as compared to literature. Although they showed enhanced HER activity, some such as $MoS_2/MoSe_2$ (NP/L) and $MoS_2/MoSe_2$ (L/L) had low stability in acidic solutions which makes them unsuitable for practical applications. Further investigations will need to be conducted to determine the root cause of the degradation and how to improve the stability of these heterolayers given that their MoS_2 counterparts are relatively stable in similar solutions. Another area to consider is the characterization of the heterolayers since there was a limitation with XPS characterisation to gain chemical compositions of the heterolayers. This was due to the overlap of S 2*p* and Se 3*p* spectra, which made peak deconvolution difficult. This analytical limitation emphasizes the complexity of characterizing TMD heterostructures and underscores the necessity for advanced spectroscopic techniques to resolve overlapping peaks and accurately quantify elemental compositions in these systems.

Chapter 6 explored mixed TMDs which also highlighted improved HER performance along with a range of low electrochemical rate constants from these hybrids. Characterisation was conducted on these hybrids, but more in-depth analysis is needed to fully understand the effects of mechanochemical activation on the electronic and chemical properties of the resulting hybrids and how these affected their HER catalytic activity. Another study could investigate various rates of mechanochemical activation and corresponding HER performance to determine optimum conditions for carrying out mechanochemical mixing. This could result in a hybrid that could outperform the previously reported hybrids thereby highlighting the importance of mechanochemistry to the synthesis of new TMD structures with enhanced electrocatalytic abilities. This study could be further explored by using the TMD precursors with a means to reduce them via mechanochemical activation with the aim of synthesising co-reduced TMD mixtures with enhanced HER electrocatalytic activity.

Transition metal dichalcogenides (TMDs), their heterostructures, and mixed hybrids hold strong promise for electrolyser applications. They offer scalable, cost-effective alternatives to precious metals

with tunable electronic properties and abundant active sites for application as catalysts for HER in the cathode section of the electrolyser. Synergistic effects in heterostructures and phase transformations hybrids enhance their catalytic performance, making them suitable for hydrogen evolution reactions. While challenges remain in optimizing their stability and scalability, further research could enable their widespread adoption in sustainable energy technologies.

7.3 References

(1) Merki, D.; Fierro, S.; Vrubel, H.; Hu, X. Amorphous Molybdenum Sulfide Films as Catalysts for Electrochemical Hydrogen Production in Water. *Chem. Sci.* 2011, **2**, 1262–1267. https://doi.org/10.1039/c1sc00117e.

(2) Ambrosi, A.; Pumera, M. Templated Electrochemical Fabrication of Hollow Molybdenum Sulfide Microstructures and Nanostructures with Catalytic Properties for Hydrogen Production. *ACS Catal.* 2016, **6**, 3985–3993. https://doi.org/10.1021/acscatal.6b00910.

(3) Brunet Cabré, M.; Paiva, A. E.; Velický, M.; Colavita, P. E.; McKelvey, K. Electrochemical Kinetics as a Function of Transition Metal Dichalcogenide Thickness. *Electrochim. Acta* 2021, **393**, 139027. https://doi.org/10.1016/j.electacta.2021.139027.

(4) Fan, X.; Xu, P.; Li, Y. C.; Zhou, D.; Sun, Y.; Nguyen, M. A. T.; Terrones, M.; Mallouk, T. E. Controlled Exfoliation of MoS_2 Crystals into Trilayer Nanosheets. *J. Am. Chem. Soc.* 2016, **138**, 5143–5149. https://doi.org/10.1021/jacs.6b01502.

(5) Escalera-López, D.; Lou, Z.; Rees, N. V. Benchmarking the Activity, Stability, and Inherent Electrochemistry of Amorphous Molybdenum Sulfide for Hydrogen Production. *Adv. Energy Mater.* 2019, **9**, 1802614. https://doi.org/10.1002/aenm.201802614.

8 Appendix

8.1 Electrodeposition of MoS_2

Electrochemical deposition of MoS_2 onto a glassy carbon electrode was conducted by cycling the potential between 0.4 V and -1.1 V (vs Ag/AgCl) in a 2 mM $(NH_4)_2MoS_4$ and 0.1 M $NaClO_4$ a solution at a scan rate of 50 mV s^{-1} for 50 cycles. Below is the resulting voltammogram due to the deposition:

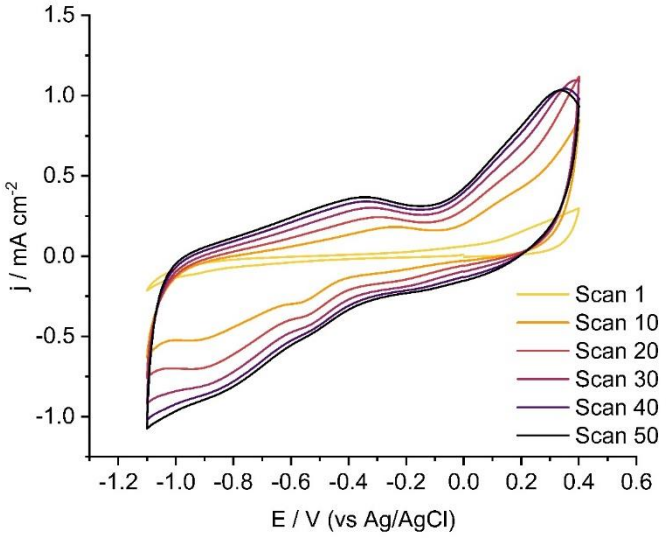

Figure 8.1. Cyclic voltammetry of the deposition of MoS_2 onto a glassy carbon electrode at a scan rate of 50 mV s^{-1} in a solution containing 2 mM $(NH_4)_2MoS_4$ and 0.1 M $NaClO_4$.

8.2 Impact Electrochemistry

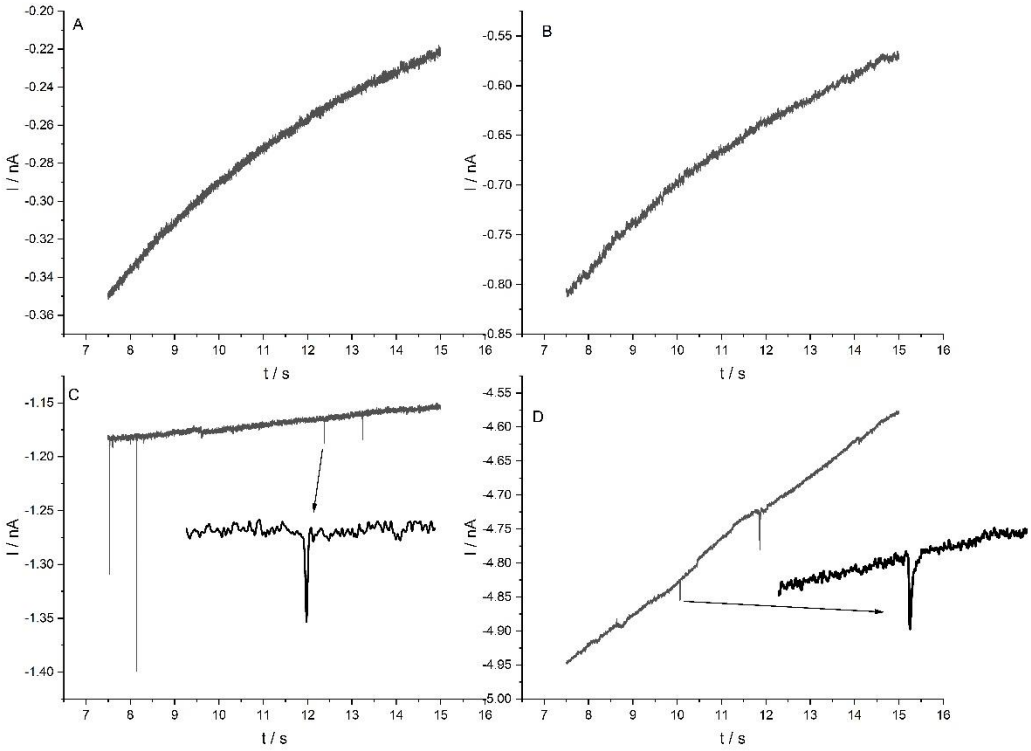

Figure 8.2. (A, B) Chronoamperometry scans without any spikes for potentials held at -0.25 V and -0.50 V (vs RHE) for 30 seconds with a pH 2 solution of 0.01 M H_2SO_4 and 0.01 M NaOH. **(C, D)** MoS_2 impact spikes for potentials held at -0.25 V and -0.50 V for 30 seconds using a 100 pM MoS_2.

8.3 Tafel analysis

Investigating the HER kinetics involved Tafel analysis and reaction rate calculations to understand and express the catalytic properties of MoS_2 towards HER. The Tafel slope for the electrodeposited MoS_2 was calculated from the voltammetry scans and was found to be 45 mV dec^{-1} while an approximate Tafel slope of 39 mV dec^{-1} was found for the fitted spike height curve (see figure 8.3 below). The Tafel equation below was used during the analysis to derive Tafel slope and the transfer coefficient (a):

$$n = \frac{-aRT}{zF}\ln(j_0) + \frac{aRT}{zF}\ln(j) \qquad (8.1)$$

$$n = c + b\log(j) \qquad (8.2)$$

$$b = \frac{2.303aRT}{zF} \qquad (8.3)$$

Where n is overpotential (V), a is the transfer coefficient, R is the gas constant (J mol^{-1} K^{-1}), T is temperature (K), F is faraday constant (C mol^{-1}), j_0 is the exchange current (A), z is the number of electrons and b is the Tafel slope.

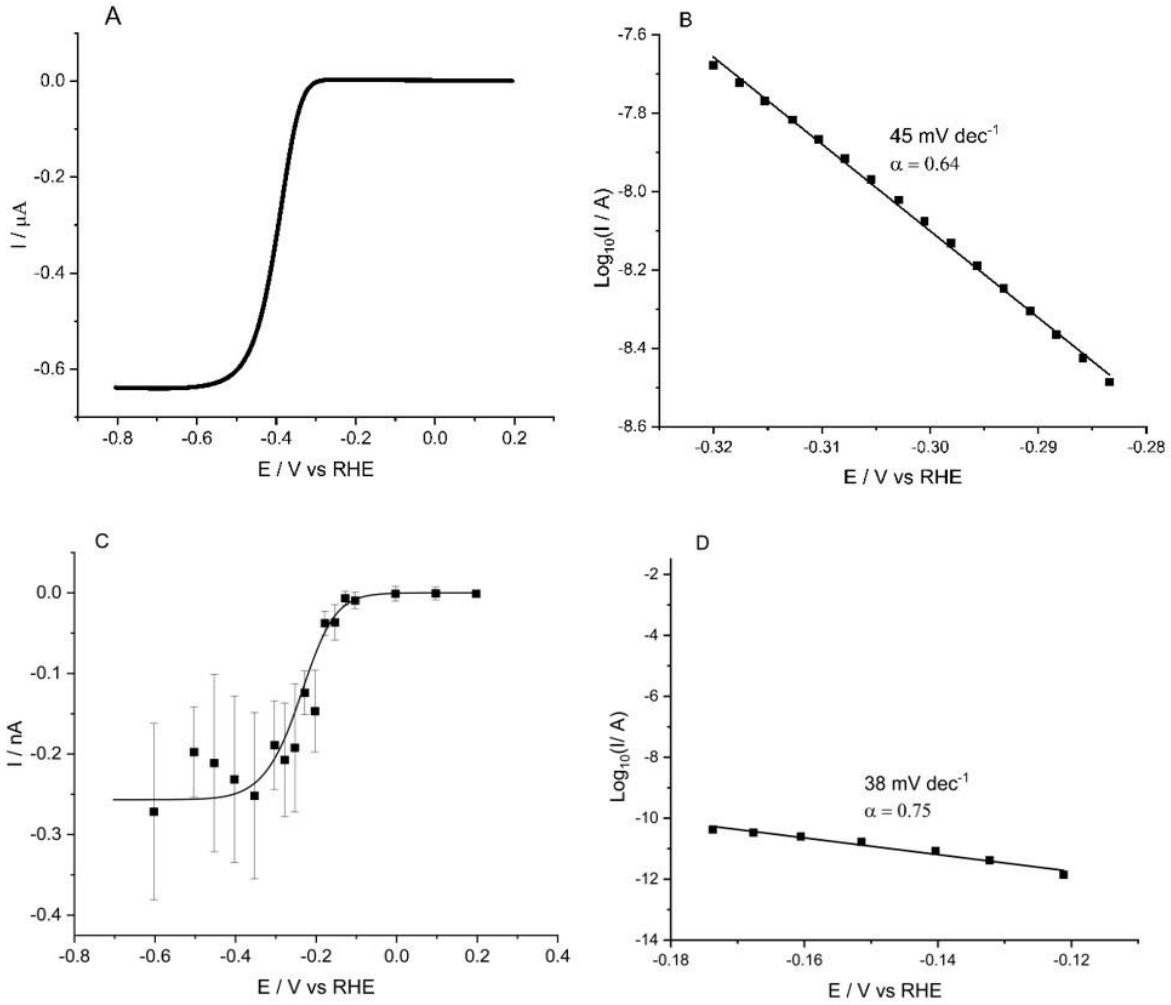

Figure 8.3. Tafel slope derivation for the electrodeposited (B) and nanoparticle (D) MoS_2 towards HER. An LSV (A) obtained using the electrodeposited MoS_2 and the nanoparticle impact height (C) scan were used for deriving the Tafel plots.

8.4 SEM characterisation of MoS_2 nanoparticles

Investigation of the nanoparticle sample via SEM revealed varying sizes of the nanoparticles with most of the visible parts being the agglomerated particles (**Fig. 8.4**). The nano powder has an average particle size of 90 nm (material specification sheet) hence the various sizes with an average size of 87±50 nm was observed in the SEM image. SEM analysis had only proved the presence of Mo and S elements in both samples and further studies were required to ascertain the chemical composition of the elements thereby resulting in XPS analysis.

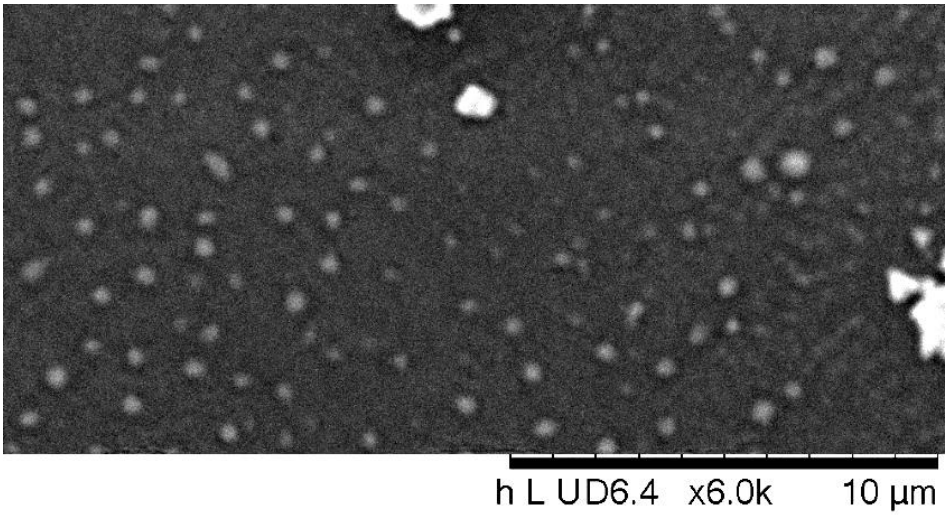

Figure 8.4. Scanning electron micrograph of MoS_2 nanoparticles. Scale bar of 10 µm.

8.5 Exfoliation of MoS_2 nanoparticles

The earlier onset of HER due to the nanoparticles was investigated to determine what was causing this effect from the nanoparticles. It is possible that more active sites on the nanoparticles are being activated by one of the processes during experimentation thus causing the shift on onset potential or the structure of the particle is being altered in some way to expose more active sites. Ultrasonic exfoliation has been outlined as one of the techniques used to exfoliate bulk MoS_2 into monolayers and even into the nanostructured form.[1] Sonicating the nanoparticle suspension in acid helped to disperse and prevent the nanoparticles from agglomerating during the impact studies. Sonicating the suspension each time before running the experiment is believed to have had an exfoliating effect on the nanoparticle structure, converting it from the 2H semiconducting phase to the 1T metallic phase form. The 1T phase of MoS_2 has a high catalytic activity towards HER as compared to the 2H form which explains the earlier onset potential for HER due to the nanoparticles.[2]

XRD analysis revealed that the MoS_2 nanoparticles are in the 2H phase form. This was the raw sample of the nanoparticles and next up, the sonicated suspension sample was analysed. This sample was sonicated then centrifuged to get supernatant, which was then then centrifuged and washed four times before drying it to get the dry solid sample for XRD characterization. The pellet was removed first to remove heavier particles that will not have the exfoliated nanosheets before subsequently centrifuging at higher velocity to remove the nanosheets as a pellet. In **Fig. 8.5**, the XRD spectra for the raw and sonicated samples are shown. The XRD spectra for the sonicated nanoparticle suspension have less peaks compared to that of the raw nanoparticle thereby indicating that a change occurred in their structure due to the sonication. The reduction in peak intensity in the ultrasonicated XRD spectra is an indication that exfoliation has occurred. This is a result of reduced layers in the 2D material resulting in weakened coherent scattering due to loss in long range order thereby causing reduced reflection intensity.[1] This change in intensity is more evident on the peak at 14.5º.

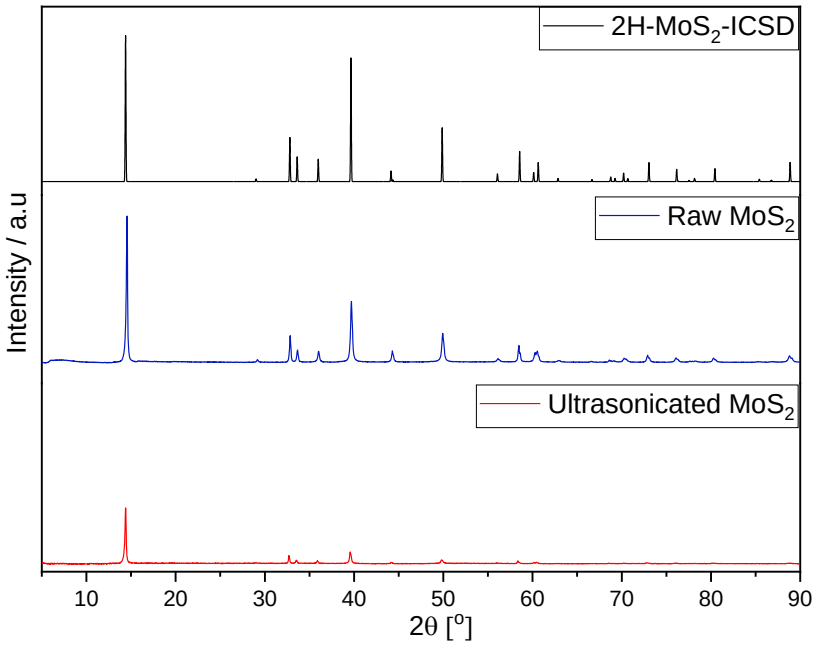

Figure 8.5. XRD spectra of the raw and ultrasonicated nanoparticles. The 2H-MoS_2 spectra from ICSD (https://icsd.psds.ac.uk/search/basic.xhtml) is also shown for comparison.

8.6 AFM Imaging of MoS_2 Nanoparticles

Atom force microscopy images were recorded of the MoS_2 particles, after ultrasonication and deposition onto a cleaved mica surface. The following are a selection of typical images.

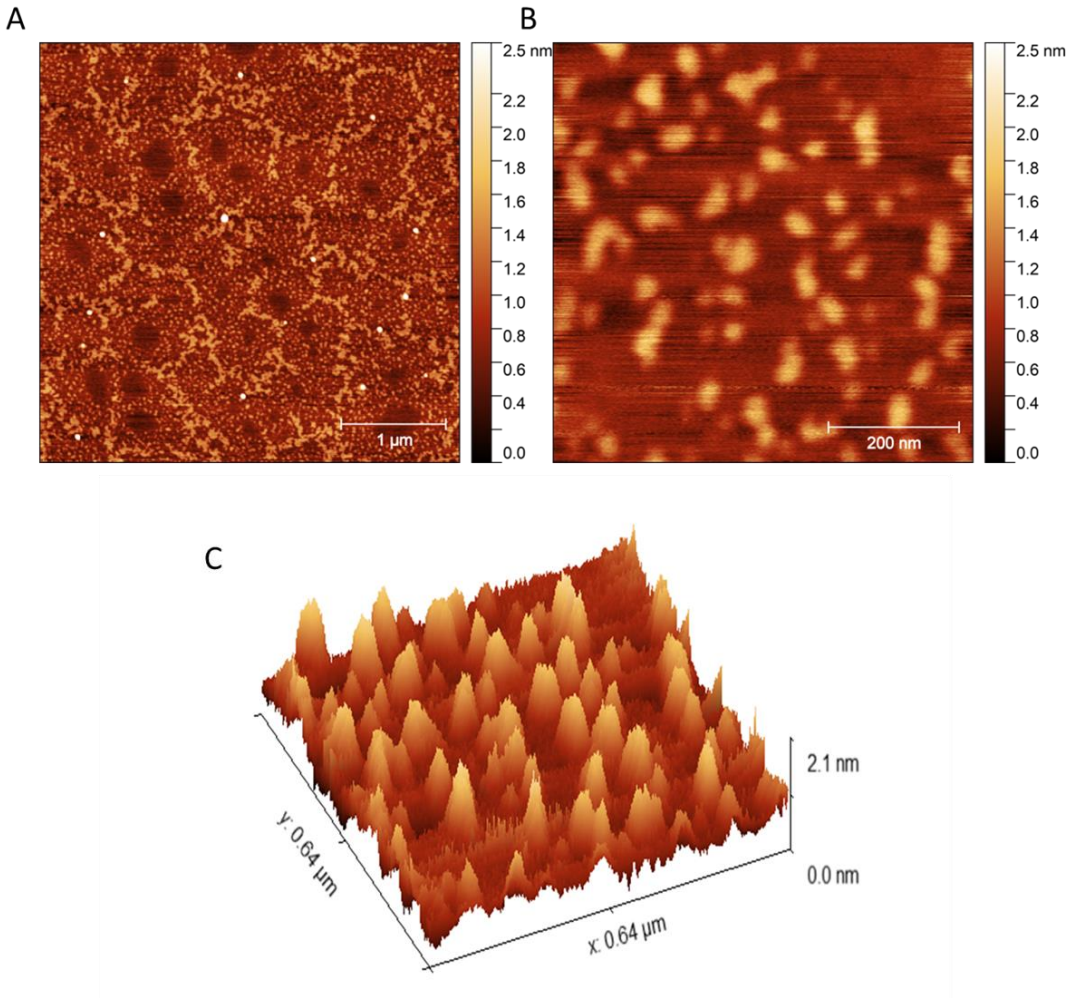

Figure 8.6. AFM image of MoS_2 on mica (A&B). (C) 3D image of the region shown in B.

8.7 References

(1) Tan, X.; Kang, W.; Liu, J.; Zhang, C. Synergistic Exfoliation of MoS_2 by Ultrasound Sonication in a Supercritical Fluid Based Complex Solvent. *Nanoscale Res. Lett.* 2019, **14**, 317. https://doi.org/10.1186/s11671-019-3126-4.

(2) Lukowski, M. A.; Daniel, A. S.; Meng, F.; Forticaux, A.; Li, L.; Jin, S. Enhanced Hydrogen Evolution Catalysis from Chemically Exfoliated Metallic MoS_2 Nanosheets. *J. Am. Chem. Soc.* 2013, **135**, 10274–10277. https://doi.org/10.1021/ja404523s.